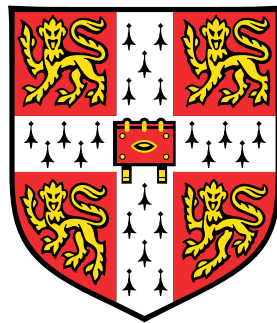


Development of a single-cell fluorescence-based sensor to investigate Myc protein stability



AstraZeneca 

Camilla Ascanelli

Department of Pharmacology
University of Cambridge

Thesis submitted for the degree of:
Doctor of Philosophy

Supervisor:

Dr Catherine Lindon

Industrial Supervisor:

Dr Karen Roberts

Girton College

28th March 2022

Declaration

I hereby declare that the contents of this dissertation are original, outside of where specific reference is made to the work of others. The work described in this thesis has not been submitted in whole or in part for consideration for any other degree or qualification in this, or any other university. It is my own work and does not contain anything resulting from work done in collaboration with others, except as specified in the text and Acknowledgements. This dissertation does not exceed the prescribed limit of 60,000 words excluding appendices, bibliography, footnotes, tables and equations.

Camilla Ascanelli

Abstract

Development of a single-cell fluorescence-based sensor to investigate Myc protein stability

The transcription factor Myc is expressed in cells in response to pro-growth signals and drives expression of a plethora of genes that promote proliferation. This pleiotropic activity renders loss of Myc regulation highly beneficial to tumour cells and, in fact, Myc is deregulated in most human cancers. While its contributions to cancer have made Myc a thoroughly studied protein and an extremely desirable drug target, over fifty years of research have failed to produce an inhibitor that has successfully reached the clinic. Drug design against Myc has been limited by its lack of a defined structure with exploitable druggable sites.

Recent strategies have been aimed at re-establishing post-translational regulation of Myc protein levels through inhibition of interacting partners that promote its accumulation in the cell. This exciting new therapeutic avenue is hindered by limited availability of high-throughput in vitro assays to measure changes in Myc stability in response to drug treatment. While many studies have been conducted to investigate regulation of Myc protein stability at the population level (for example, by immunoblotting for Myc), none have employed live imaging assays that are able to report on protein stability at the single cell level.

The work presented in this study has aimed to fill this gap in the molecular toolbox with the use of a tandem Fluorescent Protein Timer (tFT). tFTs are novel microscopy-based tools that act as sensors of protein age, and therefore stability, at a single-cell level. They make use of differing maturation kinetics of fluorophores tagged in tandem

to the protein of interest, where the ratio of the fluorescence signals of the fluorophores functions as a read-out for protein stability. This offers a high through-put assay employable in drug screening for compounds that affect Myc stability, but also allows for the investigation of single-cell regulation of Myc.

In this thesis, the generation and validation of Myc-tFT is described. Specifically, the system was challenged with known modulators of Myc stability, and the effect was assessed at the single-cell level. The functionality of Myc tagged with two fluorophores was also confirmed.

Once the ability of Myc-tFT to report on changes of Myc stability was confirmed, the assay's screening window coefficient was evaluated and the Myc-tFT sensor assay was used in a medium-throughput screen of modifiers of Myc stability. This work was undertaken at industry partner AstraZeneca where their screening pipeline was employed. This work revealed variability in the data generated by the sensor that hindered the task of identifying significant hit compounds.

With the aim of making the assay more robust, the source of the variability in tFT sensor output was investigated and identified as a cell-autonomous oscillations in Myc stability and levels. The role of cell-cycle and circadian rhythms in regulation of Myc stability and levels was investigated using Myc-tFT, and confirmed in cancer cells expressing endogenous levels of Myc. This work has revealed previously undescribed post-translational regulation of Myc by the circadian rhythm. It highlights the need to investigate single-cell regulation of Myc and account for cell-autonomous post-translational regulation that could affect and bias identification of hits during drug screening. The findings also possess implications in the importance of circadian timing of treatment with modulators of Myc stability.

Camilla Ascanelli

Dedication

I would like to dedicate this thesis to my loving parents, who are an unwavering and unconditional source of inspiration and encouragement, who believe in me even when I do not; for this I am forever indebted.

Acknowledgements

The completion of this thesis could not have been achieved without the help and support of many people, whose contributions I sincerely appreciate and gratefully acknowledge.

First of all, I would like to express my deepest gratitude to my Ph.D. supervisors, Dr. Catherine Lindon and Dr. Karen Roberts. Dr. Lindon not only offered her wealth of knowledge with which she guided me in navigating this ever-evolving project, but also great availability, support and an extremely welcoming environment. Her efforts in generating an inclusive and diverse work environment are greatly appreciated, and the diverse group of people that have been part of her team throughout the years is one of the highlights of my time in her lab. For this I am very grateful. Dr. Roberts has introduced me to the exciting world of the pharmaceutical industry and has always met my efforts and questions with earnest enthusiasm. I am lucky to have been supervised by two successful women scientists who have become role models for my future career. I would also like to thank Dr. Catherine Wilson (Department of Pharmacology, University of Cambridge) for her availability, for sharing her expertise in the Myc field and her continuous support since joining the department. I thank my funding body, AstraZeneca, for awarding me the scholarship that enabled me to undertake this work and experience both academic and industrial research. I am grateful to Department of Pharmacology for the warm environment and stimulating opportunities it presented me with, especially within the Equality Diversity and Inclusion and post-grad committees.

Special thanks must be given to all members of the Lindon lab. Dr. Anja Hagting and Dr. Begum Akman's help and support, both on a personal and a professional level,

throughout the years are immensely appreciated. I would also like to thank Richard Wang, Ahmed Abdelbaki, Siân Stockton, Roberta Cacioppo for their friendship, honesty and support. They have made my time in the lab a happy and fun time. Special thanks go to Cynthia Okoye for embarking on the EDI adventure with me. I have learned a lot about the world through knowing her and our shared adventure and had fun organising together such inspiring and fun events. Sincerest thanks must be given to my first and best friends in Cambridge, Dewi Safitri, and Winnie Ho Yan Yeun and, more recently, Aleksandra Boikova. It has been a pleasure knowing them and sharing time in and out of work. A huge thank you to my once Part II student turned friend Alex Fung, for his friendship and for dedicating much of his time in his final year at Cambridge to revising and proof-reading this thesis. It genuinely means so much to me.

I would like to extend my deepest gratitude and love to my parents, Giorgio and Stefania, without whom I would have never even dared to apply for a Ph.D. in Cambridge. Their unconditional love and encouragement, have allowed me to reach for the dream of obtaining a doctorate from such a prestigious institution, where so much of the science that I know and love has been carried out. This achievement of mine is fully dedicated to them. Finally, but not by means of importance, special thanks and recognition must also be given to Lorenzo Carnemolla, without whom I would have not pushed through the hardest moments of this journey. His love and support were a safe haven in times of doubt and insecurity both in my work and in the COVID-19 pandemic.

Grazie.

Contents

Declaration	iii
Abstract	v
Dedication	vii
Acknowledgements	ix
List of Abbreviations	xli
1 Introduction	1
1.1 Myc family proto-oncogenes and the Hallmarks of cancer	1
1.1.1 The hallmarks of cancer	1
1.1.2 The Myc family	3
1.1.3 Myc and the hallmarks of cancer	3
1.1.3.1 Myc and sustained proliferative signaling	3
1.1.3.2 Myc and growth arrest signals	5
1.1.3.3 Myc and apoptosis	6
1.1.3.4 Myc and limitless differentiation potential	7
1.1.3.5 Myc and angiogenesis	8
1.1.3.6 Myc and tissue invasion and metastasis	8
1.1.3.7 Myc and deregulated cellular energetics	9
1.1.3.8 Myc and immune system evasion	10
1.1.4 Myc Structure, Expression and Function	12

1.1.4.1	Myc Structure	12
1.1.4.2	Myc Expression	16
1.1.4.3	Myc Function	16
1.1.5	Targeting Myc	20
1.2	Post-translational modification of proteins and protein stability	26
1.2.1	The Ubiquitin-Proteasome System	27
1.2.2	Post-translational modifications regulate Myc protein's life cycle and activity	30
1.2.3	Experimental tools to assess Protein Stability	36
1.2.3.1	Classical tools for measuring protein degradation	36
1.2.3.2	Fluorescence-based assays to monitor protein stability	40
1.3	Aims and objectives	46
2	Materials and Methods	49
2.1	Materials	49
2.1.1	Molecular biology reagents	49
2.1.1.1	Cloning reagents	49
2.1.1.2	Immunoblotting and Immunofluorescence	53
2.1.1.3	Chromatin immunoprecipitation	55
2.1.1.4	mRNA extraction and quantification	57
2.1.2	Mammalian cell culture growth media	58
2.1.3	Small molecule compounds	60
2.1.4	Software used	60
2.2	Methods	61
2.2.1	Molecular Biology Techniques	61
2.2.1.1	Plasmid Generation and Cloning	61
2.2.1.1.1	Plasmid DNA manipulation and purifications.	61
2.2.1.1.2	<i>Escherichia coli</i> transformations and plasmid amplification.	62
2.2.1.1.3	Site-directed mutagenesis.	62

2.2.1.1.4	Site directed mutagenesis via round the horn PCR	67
2.2.2	Mammalian cell culture	69
2.2.2.1	Mammalian cell subculturing	69
2.2.2.2	Long-term cryostorage and cell recovery of mammalian cell lines	70
2.2.2.3	Mammalian cell transfection	70
2.2.2.3.1	Lipofectamine®.	70
2.2.2.3.2	Electroporation.	71
2.2.2.4	Generation of stable cell lines.	71
2.2.2.4.1	Giemsa's assay	72
2.2.2.5	Cell synchronisation	72
2.2.2.5.1	Cell cycle synchronisation.	72
2.2.2.5.2	Circadian rhythm synchronisation.	74
2.2.3	Cell Lysate extraction, protein quantification and Immunoblotting	75
2.2.4	Bromodeoxyuridine assay	78
2.2.4.1	Chromatin Immunoprecipitation and quantitative PCR analysis	79
2.2.5	Fluorescent imaging of live and fixed cells and image analysis. .	86
2.2.5.1	Live cell imaging	86
2.2.5.2	Fixed cells imaging	86
2.2.5.3	Imaging data collection and storage	87
2.2.6	Image analysis	87
2.2.7	Statistical analysis and curve fitting	88
2.2.7.0.1	Statistical analysis of single time-point data. .	88
2.2.7.0.2	Curve fitting of time-lapse data.	88
2.2.8	mRNA extraction and quantification by RT-qPCR	90
2.3	Materials and methods for work undertaken at AstraZeneca	90
2.3.1	Cell culture and seeding	90
2.3.2	Compound dosing	91

2.3.3	Image acquisition and analysis	91
2.3.4	Data analysis	93
3	Generation and validation of a suitable Myc Stability Sensor	95
3.1	Introduction	95
3.2	Design of Myc-tFT construct and generation of a stable cell line	98
3.2.1	Choosing the appropriate combination of Fluorophores for Myc-tFT	98
3.2.2	Generation of tFT constructs	101
3.2.3	Generation of Myc-tFT stable inducible cell lines	104
3.2.3.1	Selection of slowFP for Myc-tFT	104
3.2.3.2	Cell line generation by Flp-In ^(TM) T-Rex ^(TM) system	108
3.2.4	Validation of CMV-driven Myc-tFT expression.	112
3.3	Myc-tFT is able to report on Myc stability	117
3.3.1	MG132 treatment reveals Myc-specific changes in Myc-tFT ratio measurement	117
3.3.2	Myc-tFT half-life is similar to that of untagged endogenous Myc	120
3.4	Myc-tFT undergoes the same post-translational modifications as endoge- nous Myc	122
3.5	Myc-tFT is functional	128
3.6	Chapter Summary	131
4	Optimization and application of Myc-tFT stability sensor in a medium-throughput drug screen.	133
4.1	Introduction	133
4.2	Assay optimization	134
4.2.1	Establishing a seeding density	134
4.2.2	Nuclear labelling and image acquisition optimization.	135
4.2.3	Growth media selection for optimal imaging conditions.	138
4.2.4	Automated image analysis on HCS studio	140
4.3	Whole-field analysis of the effect of modulators of Myc-tFT ratio.	146

4.3.1	Assessing the goodness of the Myc-tFT assay through artificial stabilization of Myc	147
4.3.2	Challenging the robustness of Myc-tFT assay with with a known modulator of Myc.	150
4.4	Single-cell analysis of the effect of modulators of Myc stability on the Myc-tFT ratio.	156
4.4.1	Single-dose screening: 10 μ M	157
4.4.2	Single-dose screening: 30 μ M	161
4.5	Chapter Summary	164
5	Discovering the source of variability in the Myc-tFT assay	167
5.1	Introduction	167
5.2	Time-resolved analysis of Myc-tFT in asynchronous cells	168
5.2.1	Myc-tFT ratio exhibits cell autonomous oscillations with a periodicity of 24 hours	168
5.3	Time-resolved analysis of Myc-tFT in cells synchronised for cell cycle	174
5.3.1	Myc-tFT oscillations are independent of CDK activity	174
5.3.2	Myc-tFT oscillates robustly in S-phase arrested cells	176
5.4	Contribution of synthesis rates and post-translational regulation on Myc-tFT oscillations	177
5.4.1	Oscillations are independent of protein synthesis rates	178
5.4.2	Post-translational regulation of Myc-tFT oscillations	182
5.4.2.1	GSK3 β inhibition blocks Myc-tTF oscillation to increase Myc-tFT stability	182
5.4.2.2	T58A mutation reduces amplitude of Myc-tFT oscillations	186
5.5	Chapter summary	188
6	Circadian rhythms contribute to periodic post-translational regulation of Myc-tFT	191
6.1	Introduction	191

6.1.1	The transcriptional/post-translational delayed feedback loop (TTFL) model of the circadian cycle	192
6.1.2	The post-translational oscillator model of circadian rhythm establishment and maintenance	193
6.1.3	Myc and the circadian rhythm	194
6.2	Circadian synchronisation of U2OS FRT/TO Myc-tFT cells leads to synchronised oscillations in Myc-tFT levels	196
6.2.1	Synchronisation by Dexamethasone	196
6.2.2	Synchronisation by temperature cycling	199
6.2.2.1	Synchronised Myc oscillations are observed by immunoblotting following circadian synchronisation	203
6.3	Post-translational regulation of Myc-tFT contributes to its circadian regulation.	206
6.3.1	Myc-tFT mRNA expression	206
6.3.2	Oscillations are more robust in the presence of wild-type Myc	208
6.3.3	The oscillations in Myc-tFT appear independent of Myc-tFT activity	216
6.3.4	GSK3 β regulates Myc-tFT oscillations independently of T58	218
6.4	The variability in Myc-tFT ratio is reduced following circadian synchronisation	220
6.5	Chapter summary	226
7	General discussion and future perspectives	229
7.1	Tandem Fluorescence Timers for studying Myc stability	229
7.1.1	Myc-tFT is a novel tool for measuring Myc stability	229
7.1.2	Different methods for Myc-tFT assay image analysis	231
7.1.2.1	Manual image analysis on ImageJ	231
7.1.2.2	Semi-automated image analysis on HCS studio	232
7.2	A medium-throughput screen of modulators of Myc stability identified KN-93 as a positive modulator	234
7.3	Time-resolved analysis of the Myc-tFT signal revealed oscillating Myc-tFT levels	236

7.3.1	Myc-tFT levels are regulated by a cell-autonomous process . . .	236
7.3.2	Oscillations in Myc-tFT levels are cell-cycle independent	240
7.3.3	Myc-tFT oscillations can be synchronised by circadian synchroni- sation	241
7.3.4	Post-translational regulation of Myc-tFT contributes to its oscillat- ing levels	244
7.3.5	Circadian synchronisation reduced the variability in Myc-tFT ratios	246
7.4	Future work and concluding remarks	247

References		251
-------------------	--	------------

List of Figures

1.1	Myc and the Hallmarks of Cancer. Myc is directly (orange) and indirectly (blue) involved in allowing cells to gain any of the tumourigenic capabilities termed 'Hallmarks of Cancer'. Inspired by Hanahan and Weinberg (2011) Figure 3.	4
1.2	Myc structure and interactome. Schematic representation of the modular structure of the Myc oncoprotein. The IDR extends from the N-terminus to just after Nuclear Localisation sequence (NLS) and contains multiple disordered regions. Myc Boxes (MB), are conserved between Myc family members and are functionally important. MBI mediates contact with most regulators of Myc stability, whilst the whole transactivation domain TAD is important in mediating binding of co-activators and repressors of Myc activity. The NLS is present in the C-terminus and precedes the basic Helix-Loop-Helix Leucine Zipper (bHLH-LZ) domain of Myc which is essential for binding to MAX and DNA, as shown in the crystal structure.	13

1.3 **The transcriptional function of Myc is to drives cell cycle progression.** Myc functions by promoting cell cycle progression in different ways based on the stage of the cell cycle. In early G1, Myc induces transcription of Cyclin D Cdk4/6 and represses expression of CDKI p15. Later in G1, it induces transcription of Cyclin A, Cdk2 and represses CDKI p21 expression. In the meantime it also drives ribosome biogenesis, which promotes progression by increasing cellular size. Myc is also a key player of DNA replication during S-phase. Finally, Myc induces Cyclin B1 expression at the G2/M transition. 19

1.4	Strategies for therapeutic modulation of Myc. Myc modulation has been approached with many strategies that either aim at impairing its transcription, translation, protein function or interactions. Therapeutic categories (orange) can be indirect (dotted line) or direct (full line) inhibition/activation of regulators and interactors. Myc transcription (top left) can be inhibited by stabilising G-quadruplex DNA structures or by inhibiting bromodomain and extra-terminal (BET) proteins. Myc translation can be inhibited by decreasing its mRNA levels through the use of antisense oligonucleotides or siRNA, or by affecting translation indirectly through inhibition of eIF4E-mediated cap-dependent Myc translation. Finally, Myc protein function (bottom) can also be inhibited through hindering its binding to DNA, MAX or co-activators. Regulating post-translational modification and protein stability (bottom) can be pursued as a therapeutic option. <i>Ac</i> acetylation, <i>TF</i> Transcription Factor, <i>BET</i> bromodomain and extra-terminal motif, <i>ERK</i> extracellular signal-regulated kinases, <i>MEK</i> Mitogen-activated protein kinase kinase, <i>eIF4R</i> Eukaryotic translation initiation factor 4E, <i>4E-BPs</i> eIF4E-binding proteins, <i>mTORC1</i> mammalian target of rapamycin complex 1, <i>FBW7</i> F-box and WD repeat domain-containing 7), <i>MBI</i> Myc box , <i>Ub</i> ubiquitin, <i>PIN1</i> Prolyl isomerase 1, <i>P</i> phosphorylation, <i>DUB</i> deubiquinating enzyme, <i>PP2A</i> Protein Phosphatase 2A. Inspired by Whitfield, Beaulieu, and Soucek (2017), Figure 3 and Allen-Petersen and Sears (2019) Figure 1.	22
1.5	The Ubiquitin-Proteasome System. Degradation of proteins (exemplified by protein X in yellow) by the UPS is a multi-step process:	29
1.6	Myc protein Life cycle. The life cycle of Myc is a complex and tightly regulated process:	32
1.7	Fluorescence-based assays to monitor protein stability. There are several methods of assaying protein stability through live imaging microscopy that allow single-cell analysis:	41
1.8	Aims of this work. Graphical representation of the aims of this work: . .	47

2.1	Maps for plasmidic DNA used for site-directed mutagenesis.	63
2.2	Strategy for site-directed mutagenesis of BamHI site downstream of mRuby. Schematic representation of the cloning strategy used to remove the BamHI site following mRuby in the AurkA-tFT construct:	64
2.3	Maps for pcDNA5 FRT/TO Myc-tFT with the primers for round-the-horn mutagenesis of T58 displayed in the callout.	67
2.4	Schematic representation of double Thymidine block and release synchronisation method.	73
2.5	Schematic representation of circadian synchronisation by dexamethasone treatment or Temperature cycling.	74
2.6	Schematic representation of the BrdU protocol.	78
2.7	Schematic representation of the SimpleChIP protocol.	80
2.8	Optimization of DNA digestion by Micrococcal Nuclease and sonication. Differing amounts of Micrococcal Nuclease and sonication pulses were tested to verify which combination yielded the optimal DNA digestion. Samples were run on 1% agarose gel with 100bp-ladder.	82
2.9	Melt Curve, Amplification curve and Standard curve for CA48-F, CA49-R hCAD primers. Primer efficiency was calculated by the Applied biosystems qPCR software as 96.483%.	84
2.10	Melt Curve, Amplification curve and Standard curve for CA16-F, CA17-R CMV primers. Primer efficiency was calculated by the Applied biosystems qPCR software as 104.364%.	85
2.11	Multi_Measurement Plug In for ImageJ. Visual summary of the ImageJ tool used for image analysis. Images show steps in sequential order. Call outs show provide a closer view of the tool's ROI generation.	87
2.12	Circadian Damped Cosine wave. Shared by Dr. John O'Neill	89
3.1	tFT construct cloning strategy. Schematic representation of cloning strategy adopted for generation of tFT constructs:	101

3.2	Plasmid maps of tFT constructs: All the plasmids shown in this figure were used for this work. Plasmid Maps were generated using SnapGeneViewer.	103
3.3	Images of Myc-tFT transfected cells. U2OS cells were transfected with either Myc-mCherry-mNeonGreen (Myc-mCmN) or Myc-mRuby-mNeonGreen (Myc-mRmN) constructs and imaged under the same imaging parameters. Representative data of n=3 experiments.	105
3.4	Images of Myc-tFT transfected cells treated with MG132 or vehicle control. U2OS cells were transfected with either Myc-mCherry-mNeonGreen or Myc-mRuby-mNeonGreen constructs; treated with either MG132 (4.2 μ M) or vehicle control DMSO. Both constructs and treatments were imaged within the same experiment and under the same imaging parameters. Representative data of n=3 experiments.	107
3.5	Effect of proteasomal inhibition on slowFP/fastFP ratios. U2OS cells were transfected with either Myc-mCherry-mNeonGreen or Myc-mRuby-mNeonGreen constructs; treated with either MG132 (4.2 μ M) or vehicle control DMSO. Both constructs and treatments were imaged within the same experiment and under the same imaging parameters. Representative data of n=3 experiments. Each dot represents data from a single cell; Mean and SD are shown.	107

3.6	Flp-In^(TM) T-Rex^(TM) System. Depiction of the system as adapted from ThermoFisher. The system allows homologous recombination between the FRT sites of the host FRT/TO cell line and those present in the pcDNA5/FRT/TO plasmid transfected. This recombination is catalysed by pOGG44 (plasmid)-driven expression of Flp recombinase which is co-transfected with pcDNA5/FRT/TO X-tFT (X is the POI). This allows for the integration of the gene of interest under CMV TetO ₂ and switch in resistance from Zeocin to Hygromycin. The callout at the bottom shows the workings of the TetO ₂ promoter: two repressors bind the TetO ₂ promoter and inhibit CMV-driven transcription. Addition of tetracycline or doxycycline, which bind the repressors, releases the TetO ₂ promoters and thereby allows CMV to drive transcription.	109
3.7	tFT cell lines. Images representing the selected clones for each U2OS FRT/TO cell line expressing a tFT construct. Cells were imaged under the same imaging conditions to allow for comparison of brightness and selection of clones for further experiments.	110
3.8	Correct integration of Myc-tFT in U2OS FRT/TO leads to loss of Zeocin resistance. U2OS FRT/TO and U2OS FRT/TO Myc-tFT cells were seeded in the plate and grown for 7 days in the presence or absence of Zeocin (+ or - columns) and processed for Giemsa stain to evaluate proliferation.	111
3.9	Myc-tFT expression by the CMV promoter is Doxycycline-dependent. U2OS FRT/TO Myc-tFT Cl.8 cells were cultured in the presence or absence of Doxycycline and collected for immunoblot. Lysates were run on a polyacrylamide gel and transferred to a membrane which was cut and stained with antibodies against Myc, HA and GAPDH.	112

3.10	Serum stimulation post-serum starvation leads to a lower increase in Myc-tFT ratio. The effect of serum stimulation post serum starvation on Myc stability was evaluated by the Myc-tFT sensor in U2OS FRT/TO Myc-tFT Clone 8. Serum starved cells were treated with L15 or FBS in the presence of doxycycline and imaged before and after 4 hours of treatment. ANOVA was performed to compare the effect of serum addition to cells at each time point (n.s.=non-significant $p>0.05$; ****= $p\leq 0.0001$):	114
3.11	Serum addition leads to increased synthesis of Myc-tFT. U2OS FRT/TO Myc-tFT Cl.8 cells were cultured in the presence or absence of Doxycycline and serum starved for 18 hours, followed by addition of serum-free media (lanes 1-5) or FBS (final concentration=20%, lanes 6-8) or FBS and CHX (Cf=20 μ g). Lysates were run on a polyacrylamide gel and transferred to a membrane which was cut and stained with antibody against Myc. Ponceau staining provided a loading control.	115
3.12	A Serum Response Element can be found within the CMV promoter of pcDNA5 FRT/TO plasmids.	116
3.13	tFTs are able to report on increased stability of Myc upon proteasome inhibitor treatment. The effect of proteasome inhibitor MG132 on U2OS FRT/TO Myc-tFT Clone 8 is shown in images and relative quantification. Student's t-tests were performed to compare MG132- to DMSO-treated cells at each time point (n.s.=non-significant $p>0.05$; ****= $p\leq 0.0001$) Student's t-test on data from the 90 minute time-point mean and SD of the three replicates and displayed a p-value $p=0.0025$. :	117
3.14	tFTs are able to report on increased stability of nMyc upon proteasome inhibitor treatment. The effect of proteasome inhibitor MG132 on U2OS FRT/TO nMyc-tFT Clone 1 is shown in images and relative quantification. Student's t-tests were performed to compare MG132- to DMSO-treated cells at each time point. (n.s.=non-significant $p>0.05$; **= $p\leq 0.01$; ****= $p\leq 0.0001$):	118

3.15	Control tFT is stable and does not display increased stability after treatment with proteasome inhibitor. The effect of proteasome inhibitor MG132 on U2OS FRT/TO tFT cells is shown in images and relative quantification. Student's t-tests were performed to compare MG132- to DMSO-treated cells at each time point (n.s.=non-significant $p>0.05$; $*=p\leq 0.05$:	119
3.16	C-terminal tagging of Myc with tFTs does not affect Myc protein's half-life. cycloheximide (CHX)-chase experiments were performed in U2OS FRT/TO Myc-tFT or HeLa cells to determine and compare Myc half-life (Pooled data of n=3 experiments):	121
3.17	Inhibition of GSK3β leads to Myc-tFT accumulation by reduction of Threonine 58 phosphorylation. The effect of inhibition of GSK3 β by CHIR99021 (3 μ M) on Myc-tFT and endogenous Myc was assessed by immunoblot (Pooled data of n=3 experiments):	124
3.18	Inhibition of GSK3β by CHIR99021 leads to increased Myc-tFT ratio. U2OS FRT/TO Myc-tFT were treated with DMSO or CHIR99021 (3 μ M) and imaged over time. (Representative data of n=3 experiments):	125
3.19	Myc-tFT is more sensitive than immunoblotting for measuring increased Myc stability by TWS119 treatment. U2OS FRT/TO Myc-tFT were treated with DMSO or GSK3 β inhibitor TWS119 (3 μ M) and imaged over time. Samples were collected for parallel immunoblotting experiments (Representative data of n=3 experiments):	126
3.20	Non-phosphorylatable T58A mutant Myc-tFT is more stable than Wild-type (WT) Myc-tFT. U2OS FRT/TO WT and T58A Myc-tFT were imaged following overnight induction with Doxycycline untreated or post MG132 (4.2 μ M) or DMSO treatment (Representative data of n=4 experiments) Each dot represents data from one individual cell. Mean and SD are shown:	127
3.21	Myc-tFT is functional Myc-tFT functionality was assessed by Bromodeoxyuridine (BrdU) stain (Pooled data of n=3 experiments):	129

3.22	Myc-tFT is enriched at hCAD but not CMV promoters	Protein enrichment at promoter sites was assessed by qPCR following Chromatin Immunoprecipitation (ChIP) of U2OS FRT/TO Myc-tFT cells. hCAD is a traditional Myc target while CMV is the promoter under which the Myc-tFT is expressed.	131
4.1	Seeding density.	U2OS FRT/TO Myc-tFT cells were seeded at different seeding densities (cells per well or cc/well) in a 384-well plate in the presence of doxycycline. Representative images of mNeonGreen after overnight incubation with DOX signal are shown.	135
4.2	Different modes of dispensing Hoechst.	Representative images of 384-well plates of cells dosed with Hoechst and call out of wells. U2OS FRT/TO Myc-tFT were treated with DNA stain Hoechst (Cf=1µg/mL) with two different dispensing methods:	137
4.3	Difference in background fluorescence between Leibovitz's L15 media and DMEM without Phenol red.	U2OS FRT/TO Myc-tFT cells were seeded in either Leibovitz's L15 media (Columns 1-12) or DMEM without phenol red(Columns 13-24) (both supplemented with 10% FBS) in the presence of doxycycline. Well G13 shows a well containing DMEM that has been previously imaged, thus bleaching the autofluorescent components of the media.	139
4.4	Nuclei segmentation and object selection	Representative images of U2OS FRT/TO Myc-tFT cells with segmentation applied. Segmentation in Channel 1 generates objects selected (blue) or rejected (orange) according to mNeon threshold in Channel 2.	140
4.5	Valid Object Count versus Selected Object Count	Data of an untreated plate of U2OS FRT/TO Myc-tFT cells. The data is visualised and plotted using the Genedata Screener analyzer tool.	141
4.6	Effect of normalisation against valid Object count or Selected Object count.	Data for Channel2 (mNeonGreen signal) of an untreated plate of U2OS FRT/TO Myc-tFT cells normalised to:	143

4.7	Channel 3 and tFT Ratio normalised to Selected Object count. Data from an untreated plate of U2OS FRT/TO Myc-tFT cells normalised to Selected Object count:	144
4.8	Experimental workflow. The experimental workflow for a medium-throughput screening assay was set up as follows:	145
4.9	Establishing a stimulator control. Data from plates of U2OS FRT/TO Myc-tFT treated according to the plate layout or untreated. Representative of n=3 experiments.	149
4.10	Testing an intermediate stimulator, CHIR99021. Data from plates of U2OS FRT/TO Myc-tFT treated according to the plate layout or untreated. Representative of n=3 experiments.	151
4.11	Dose response curves for MG132 and CHIR99021. Data from plates of U2OS FRT/TO Myc-tFT treated with increasing concentrations of MG132 or CHIR99021, each in triplicate per plate. Representative of n=3 experiments.	154
4.12	Effects of MG132, CHIR99021 by student t-test. Data from plates of U2OS FRT/TO Myc-tFT treated according to the plate layout or untreated in Figure 4.10, analysed by student t-test. Each dot represents the average tFT ratio reading from a well. Representative of n=3 experiments. . . .	155
4.13	Single-dose (10μM) medium-throughput screen of modifiers of Myc stability. Scatter plot of data from a representative plate of U2OS FRT/TO Myc-tFT treated with compounds listed in table 4.3 at 10 μ M with the exception of MG132 (Cf=4.2 μ M) and AZ1 (Cf=30 μ M); analysed by One-way ANOVA for comparison with DMSO. Each dot represents the ratio for a single cell. Mean and SD are displayed. Representative of n=2 plates per experiment and n=3 experiments. n.s.= non significant p>0.05, **=p \leq 0.001, **** = p \leq 0.0001	159

4.14	Single dose (30μM) screen of modifiers of Myc stability Scatter plot of data from a representative plate of U2OS FRT/TO Myc-tFT treated at 30 μ M with the exception of MG132 (Cf=4.2 μ M), with compounds listed in table 4.3, analysed by One-way ANOVA for comparison with DMSO. Each dot represents the ratio for a single cell. Mean and SD are displayed. Representative of n=2 plates per experiment and n=3 experiments. n.s.= non significant p>0.05, * = p \le 0.05, **** = p \le 0.0001	161
5.1	Panel images of a single Myc-tFT expressing cell over time. Panel illustrating the changes in Myc-tFT levels within the life cycle of a cell. Panels are from images taken an hour apart. Images are a composite of channels 490, 550 and Differential Interference Contrast (DIC).	169
5.2	Time-resolved traces of changes in Myc-tFT ratio. Representative (of n=3) data of Myc-tFT ratios of a number of cells undergoing the cell cycle. a and b refer to daughter cells.	170
5.3	Time-resolved traces of changes in mNeonGreen over time. Representative (of n=3) data of mNeonGreen relative fluorescence units (RFU) of a number of cells undergoing the cell cycle. These are the corresponding mNeonGreen levels to the Myc-tFT ratios of the cells displayed in Figure 5.2	172
5.4	Time-resolved traces of changes in mCherry. Representative (of n=3) data of mCherry relative fluorescence units (RFU) of a number of cells undergoing the cell cycle. These are the corresponding mCherry levels to the Myc-tFT ratio and mNeonGreen signal of the cells displayed in Figure 5.2 and 5.3	173
5.5	Time-resolved traces of cells treated with RO3306 for arrest in G2. U2OS FRT/TO Myc-tFT cells were treated with RO3306 (Cf=10 μ M) to induce arrest in G2 phase:	175

5.6	Average of time-resolved traces of cells undergoing cell division or arrested in S-phase. Average curve of mNeonGreen, mCherry RFU (left Y axis) and tFT ratio (right Y axis) with standard deviation (light shading) of:	177
5.7	Time-resolved traces of cells treated with DMSO. Representative traces of mNeonGreen (left Y axis), mCherry (left Y axis, dotted line) and Myc-tFT ratio (top curves, Right Y axis) for cells that:	179
5.8	Time-resolved traces of cells treated with TORin. Representative traces of mNeonGreen (left Y axis), mCherry (left Y axis, dotted line) and Myc-tFT ratio (Right Y axis) for cells treated with mTOR inhibitor TORin (Cf=2.5 μ M) that:	180
5.9	Inhibition of protein translation rates by TORin1 does not abolish oscillations in S-phase arrested cells. Representative data of U2OS FRT/TO Myc-tFT cells synchronised in S-phase and treated with DMSO or TORin1 (Cf=2.5 μ M):	181
5.10	Time-resolved traces of cells treated with CHIR99021. Representative traces of mNeonGreen (left Y axis), mCherry (left Y axis, dotted line) and Myc-tFT ratio (top curves, Right Y axis) for cells treated with CHIR99021 (Cf=3 μ M) that:	183
5.11	Inhibition of GSK3β by CHIR99021 leads to time-dependent accumulation of Myc-tFT. Representative data of U2OS FRT/TO Myc-tFT cells synchronised in S-phase and treated with DMSO or CHIR99021 (Cf=3 μ M):	185
5.12	Mutation of T58 in Myc-tFT to non-phosphorylatable T58A dampened the oscillations. Representative data of U2OS FRT/TO WT or T58A Myc-tFT cells synchronised in S-phase:	187

6.1	Schematic representation of the transcriptional/post-translational delayed feedback loop (TTFL) (Left) and how Myc disrupts it (Right). <i>Left:</i> The TTFL model of circadian regulation describes BMAL1 and CLOCK bHLH transcription factors that upon accumulation lead to the transcription of their negative regulators Cryptochrome and Period and REV-ERB α and β which in turn inhibit BMAL1 and CLOCK activity, leading to the reduced levels of these transcription factors and of the negative regulators themselves. <i>Right:</i> Myc is shown to disrupt the TTFL in different ways. First, it occupies the CRY and PER promoters, inhibiting their transcription. It has also been reported that in embryonic stem cells, Myc impedes PER shuttling to the nucleus. Myc also amplifies expression of REV-ERB α and β , which in turn represses BMAL1 and CLOCK expression. Finally, Myc binds to MIZ-1 and antagonises MIZ-1-induced transcription of BMAL1 and CLOCK genes.	195
6.2	Cells treated with Dexamethasone displayed synchronous oscillations. Representative data of U2OS FRT/TO Myc-tFT cells whose circadian rhythms were synchronised by Dexamethasone treatment (Cf=0.1 μ M) or asynchronous in DMSO vehicle control:	197
6.3	Detrended data of Myc-tFT RFU curve-fitted with a damped cosine wave. Representative detrended RFU data of U2OS FRT/TO Myc-tFT cells whose circadian rhythms were synchronised by Dexamethasone treatment (Cf=0.1 μ M):	198
6.4	Panel images of U2OS FRT/TO Myc-tFT cells synchronised by temperature cycling. Images of the mNeonGreen signal of circadian synchronised cells which were imaged every hour for 96 hours. In this image, 3 hours lapsed between one panel and the next. To the left and right of the panels are time stamps of the first and last panels in the row.	200
6.5	Temperature cycling synchronisation yields clear oscillations of cells in a field, and of multiple fields in the same well. Representative detrended RFU data of U2OS FRT/TO Myc-tFT cells:	201

6.6	Synchronised oscillations of Myc-tFT have a period of 24h and decreasing amplitude. Average detrended RFU of curves fitted to data from experimental repeats:	202
6.7	Myc-tFT oscillations are detectable by immunoblotting following circadian synchronisation. U2OS FRT/TO Myc-tFT cells were synchronised by temperature cycling and samples were collected for lysate extraction at the described time points post-synchronisation:	204
6.8	Endogenous Myc levels of A549 cells oscillate following circadian synchronisation A549 cells (lung cancer cell line) were synchronised by temperature cycling and samples were collected for lysate extraction at the described time points post-synchronisation:	205
6.9	Myc-tFT PER2 mRNA levels in Myc-tFT cells. U2OS FRT/TO Myc-tFT cells were synchronised by temperature cycling and samples were collected for mRNA extraction at the described time points post-synchronisation. Myc-tFT mRNA from three biological repeats was evaluated using primers that bound to the mCherry sequence (designed by Roberta Cacioppo).	207
6.10	Panel images of U2OS FRT/TO Myc T58A-tFT Clone 5 cells synchronised by temperature cycling. Images of the mNeonGreen signal of circadian synchronised cells which were imaged every hour for 96 hours. In this panel, 3 hours lapsed between one figure and the next. To the left and right of the panels are time stamps of the first and last panels in the row.	209
6.11	Mutation of T58 of Myc to block phosphorylation results in oscillations of decreased amplitude but period length is maintained. Average detrended RFU of curves fitted to data from experimental repeats. Data from U2OS FRT/TO Myc-tFT (WT- grey) or two different clones of Myc T58A-tFT (Cl.9 and 5, blue and green respectively):	210

6.12	mNeonGreen levels and Myc-tFT ratios of Myc-tFT clones. Comparison of Myc-tFT constructs in asynchronous U2OS FRT/TO Myc-tFT (WT and T58A) clones (ns= non significant; ****= $p \leq 0.0001$):	211
6.13	Panel images of U2OS FRT/TO tFT Clone 1 cells synchronised by temperature cycling. Images of the mNeonGreen signal of circadian synchronised cells which were imaged every hour for 96 hours. In this panel, 3 hours lapsed between one figure and the next. To the left and right of the panels are time stamps of the first and last panels in the row.	213
6.14	Expression of tFT alone results in oscillations with a greater period than those recorded in Myc-tFT lines. Average detrended RFU of fitted curves. Data from U2OS FRT/TO Myc-tFT (WT- grey) or two different clones of Myc T58A-tFT (Cl.9 and 5, blue and green respectively) and tFT (orange):	214
6.15	CHX-chase experiments of tFT cells. U2OS FRT/TO tFT Clone 1 (Cl.1) cells were treated with Cycloheximide for the described periods, and then cells were collected for lysates. Detection of the tFT constructs was achieved with the use of an antibody against mCherry.	215
6.16	Inhibition of Myc-tFT by KJ-Pyr-9 does not affect Myc-tFT oscillations. U2OS FRT/TO Myc-tFT were treated with Myc inhibitor KJ-Pyr-9 (Cf= $10 \mu\text{M}$):	217
6.17	Inhibition of GSK3β by CHIR99021 resets oscillations of WT and T58A Myc-tFT. U2OS FRT/TO Myc-tFT (WT- light blue and orange) or Myc T58A-tFT (dark blue and orange) were circadian synchronised and imaged every hour for 96 hours. 72 hours into the movie, CHIR99021 (Cf= $3 \mu\text{M}$; orange) or DMSO (blue) were added to the wells:	219

6.18	Illustration of dosing regime in synchronised cells. U2OS FRT/TO Myc-tFT cells were synchronised by temperature cycling and Myc-tFT expression was induced. 27h and 39h post induction cells were dosed with DMSO, CHIR99021 (Cf=10µM), KN-93 (Cf=10µM) or MG132 (Cf=4.2µM). Cells were imaged at 30h and 42h post-induction to correspond to trough (30h) and peak (42h) of circadian oscillation. In parallel, Myc-tFT was induced in asynchronous cells which were also treated at the same timepoints (not shown).	221
6.19	Myc-tFT ratio is significantly lower in synchronised cells. Data from asynchronous and synchronised U2OS FRT/TO Myc-tFT cells DMSO-treated with DMSO at 30 or 42 hours post-induction. Effect of synchronisation was compared by Ordinary One-Way ANOVA. ns= non significant; ***= $p \leq 0.0001$	222
6.20	Variability in Myc-tFT read out is reduced in synchronised compared to asynchronous cells treated 30h post-induction. U2OS FRT/TO Myc-tFT synchronised or asynchronous were treated with DMSO, CHIR99021 (Cf=10µM), KN-93 (Cf=10µM) or MG132 (Cf=4.2µM) 27h post-induction and imaged 30h post-induction.	222
6.21	Variability in Myc-tFT read out is reduced in synchronised compared to asynchronous cells treated 42h post-induction. U2OS FRT/TO Myc-tFT synchronised or asynchronous were treated with DMSO, CHIR99021 (Cf=10µM), KN-93 (Cf=10µM) or MG132 (Cf=4.2µM) 39h post-induction and imaged 42h post-induction.	224
7.1	Inhibition of GSK3β in S-phase arrested cells leads to Myc-tFT accumulation and apoptosis. Myc-tFT expressing U2OS cells arrested in S-phase were treated with GSK3β inhibitor CHIR99021 (Cf=3µM), which lead to rapid increase in Myc-tFT levels and apoptosis.	230

7.2 Inhibition of mTOR in unsynchronised cells does not impede asymmetric regulation of Myc-tFT between daughter cells. Myc-tFT expressing U2OS cells were treated with mTORC1 and 2 inhibitor TORin1 (Cf=2.5 μ M) and imaged over time. At 4 hours, daughter cells of a single division at 2 hours are indicated by arrows and in remaining frames. . 239

List of Tables

2.1	Plasmids used in this study.	50
2.2	Primers used in this study. All primers were ordered from Sigma Aldrich.	51
2.3	Enzymes used in this study. most enzymes are from New England Biolabs (NEB).	52
2.4	Reagents employed for cloning in this study.	52
2.5	List of Materials and reagents required for Protein electrophoresis, immunoblot, and immunofluorescence.	53
2.6	List of Primary Antibodies. All antibodies needed for this study are listed along with supplier, catalogue number, technique and working dilution specifications.	54
2.7	List of Secondary Antibodies. All antibodies needed for this study are listed along with supplier, catalogue number, technique and working dilution specifications.	54
2.8	Materials for Chromatin Immunoprecipitation. If supplier is not stated, the material belongs to the SimpleChIP [®] Plus Enzymatic Chromatin IP Kit by Cell Signaling Technologies (CST)	55
2.9	Materials employed for qPCR analysis of ChIP products.	56
2.10	List and sequences of Primers used for qPCR of ChIP Products. hCAD primers were designed on the human CAD transcriptional start site, and the CMV primers on the CMV sequence in the Myc-tFT plasmid, using Primer3Plus (Untergasser et al., 2012).	56
2.11	Reagents for mRNA extraction and quantification utilised in this work.	57
2.12	Primers for mRNA quantification of target genes.	57

2.13	Cell lines employed in this study. List and details of cell lines used for this work.	58
2.14	Materials utilised for maintenance of mammalian cells in culture. . . .	59
2.15	Materials required for mammalian cell transfection via Lipofectamine and electroporation.	59
2.16	Small molecule compounds used in this study, their targets and function, and supplier. Where AstraZeneca is stated as the supplier, it indicates that they supplied the compounds from their own compound library.	60
2.17	Software used in this work.	60
2.18	Standard cloning buffers and reactions mixtures.	62
2.19	Site-directed mutagenesis PCR reactions set up.	66
2.20	Reagent mix for steps 2-4 in site-directed mutagenesis of BamHI.	66
2.21	Reaction mix for primer phosphorylation with T4 Polynucleotide Kinase.	68
2.22	Round the horn PCR steps.	68
2.23	Complete media recipes for all cell lines utilised in this study.	69
2.24	Recipes for immunblotting buffers utilised.	76
2.25	Recipes for ChIP buffers according to manufacturer's instructions. . . .	79
2.26	Recipes for qPCR of ChIP products based on SimpleChIP Universal qPCR Master Mix instructions. For hRPL30 primers, which come as a mix of forward and reverse primers, 2 μ L of the mix was added to the nuclease free water and the master mix.	84
2.27	Reaction set up for qPCR of ChIP products based on SimpleChIP Universal qPCR Master Mix instructions.	84
3.1	FP maturation times.	100
4.1	Myc-tFT assay goodness as assessed in a Stimulator and Neutral control setting. Table reporting representative data of n=3 experiments, referring to the plates described in Figure 4.9.	148

4.2	Myc-tFT assay goodness decreases when assessing effect of CHIR99021.	
	Table reporting representative data of n=3 experiments, referring to the plates described in Figure 4.9.	152
4.3	Compounds used in this study. List of compounds that inhibit known regulators of Myc stability and their reported effect on Myc.	157
4.4	Effect of modulators of Myc stability, dosed at 10μM, across multiple experimental repeats. List of compounds that inhibit known regulators of Myc stability and their measured effect on Myc-tFT ratio (red=decrease, green=increase). Final concentration of compounds was 10 μ M with the exception of MG132 (Cf=4.2 μ M) and AZ1 (Cf=30 μ M). Data is analysed for comparison with DMSO by One-way ANOVA. n.s.= non significant p>0.05, * = p \leq 0.05, ** = p \leq 0.01, *** = p \leq 0.001, **** = p \leq 0.0001	160
4.5	Effect of modulators of Myc stability, dosed at 30μM, across multiple experimental repeats. List of compounds that inhibit known regulators of Myc stability and their measured effect on Myc-tFT ratio (red=decrease, green=increase). Final concentration of compounds was 30 μ M with the exception of MG132 (Cf=4.2 μ M) Data is analysed for comparison with DMSO by One-way ANOVA. n.s.= non significant p>0.05, * = p \leq 0.05, ** = p \leq 0.01, *** = p \leq 0.002, **** = p \leq 0.0001	163
6.1	Descriptive statistics for cells imaged 30h post-induction. Descriptive statistics to compare the effect of treatments in asynchronous and synchronised cells on Myc-tFT ratios as calculated using GraphPad Prism or Microsoft Excel. ****= p \leq 0.0001	223
6.2	Descriptive statistics for cells imaged 42h post-induction. Descriptive statistics to compare treatments of asynchronous and synchronised cells as calculated using GraphPad Prism or Microsoft Excel. ****= p \leq 0.0001	225

List of Abbreviations

3D	Three-dimensional
β -TRCP	F-box/WD repeat-containing protein 1A
A	Alanine
ADME	Absorbance, Distribution, Metabolism, Excretion
AGT	O ⁶ -alkylguanine-DNA-alkyltransferase
Akt	Protein kinase B
AMBRA1	Autophagy and beclin 1 regulator 1
ANG-1 / -2	Angiopoietin-1 or -2
APC/C	Anaphase promoting complex
ARF	ADP ribosylation factor
ATP	Adenosine triphosphate
AurkA	Aurora kinase A
BET	bromodomain and extra-terminal
BC	O ² -benzylcytosine
BG	O ⁶ -benzylguanine
bHLH	basic Helix-loop-helix
BRD4	Bromodomain-containing protein 4
BrdU	Bromodeoxyuridine
Ca ²⁺	Calcium
CAMKII	Calcium/Calmodulin-dependent protein kinase II

CCL9	Chemokine (C-C motif) ligand 9
CD(4 / 47)	Cluster of Differentiation 4 or 47
CDK	Cyclin-dependent kinase
CDKI	Cyclin-dependent kinase inhibitor(s)
Cf	Final concentration
ChIP	Chromatin Immunoprecipitation
CHX	Cyclohexamide
CK	Casein kinase
CMV	Cytomegalovirus
CNBP	CCHC-Type Zinc Finger Nucleic Acid Binding Protein
CRY1/2	Cryptochrome 1 and 2
C-terminus	Carboxyl-terminus
DMSO	Dimethyl sulfoxide
DNA	Deoxyribonucleic acid
DOX	Doxycycline
DR	Death receptor
Drp1	dynamamin-related protein 1
DsRed	Discosoma red fluorescent protein
DUB(s)	Deubiquitinating enzyme(s)
E	Glutamic acid
E1	E1 ubiquitin-activating enzyme
E2	E2 ubiquitin-conjugating enzyme
E3	E3 ubiquitin ligase
EGFP	Enhanced GFP
EGFR	Epidermal growth factor receptor
eIF4E	eukaryotic translational initiation factor 4E
EMT	Epithelial-mesenchymal transition

ELM	Eukaryotic linear motif
ED	exponentially degraded
ERK(s)	Extracellular signal-regulated kinase(s)
FACS	Fluorescence-activated cell sorting
fastFP	fast-folding FP
FBS	Fetal bovine serum
FB(W7)	(F-box/WD repeat-containing protein 7)
Flp	Flippase recombinase
FOXO(3A / 28)	Forkhead box O3 or O28
FP(s)	Fluorophore(s)
FRET	Fluorescence resonance energy transfer
FRT	Flippase recognition target
G4-DNA	G-quadruplex DNA
GAPDH	Glyceraldehyde 3-phosphate dehydrogenase
GCN5	Histone acetyltransferase KAT2A
GFP	Green fluorescent protein
GFRB2	Growth factor receptor-bound protein 2
GSK3 β	Glycogen synthase kinase 3-beta
GTP	Guanosine-5'-triphosphate
HA-tag	Human influenza hemagglutinin-tag
HAT(s)	Histone acetyltransferase(s)
hTERT	human Telomerase reverse transcriptase
HSC(s)	Haematopoietic stem cell(s)
HUWE1 or Hect9	E3 ubiquitin-protein ligase HUWE1
IL-(1 β / 23)	Interleukin - (1-beta or 23)
IDP	Intrinsically disordered protein
IDR	Intrinsically disordered region

iPSC(s)	induced pluripotent stem cell(s)
IRES	internal ribosomal entry site
JAK	Janus kinase
JNK	c-Jun N-terminal kinases
K	lysine
Kd	Dissociation constant
LCP	Lipid Calcium Phosphate nanoparticle
LKB1	Liver kinase B11
LZ	Leucine zipper
MAPK	Mitogen-activated protein kinasw
MB	Myc Box(es)
mC	mCherry
miRNA	micro ribonucleic acid
mRNA	messenger Ribonucleic acid
mTOR	mammalian Target of rapamycin
MXI-1	Max-interacting protein 1
NED	Non-exponentially degraded
NF- κ B	nuclear factor kappa-light-chain-enhancer of activated B cells
NLS	Nuclear Localisation Signal
Npm1	Nucleophosmin
N-terminus	Amino-terminus
P	Proline
PCR	Polymerase chain reaction
p53	Tumour protein p53
PDGFR	Platelet-derived growth factor receptor
PD-L1	programmed death-ligand1
PER1/2	Period 1 and 2

PEST sequence	Proline (P), glutamic acid (E), serine (S), Threonine (T) sequence
PI(3)K	Phosphoinositide 3-kinase(s)
Pin-1	Peptidyl-prolyl cis-trans isomerase NIMA-interacting 1
PMN	Proximal Myc network
POI	Protein of Interest
PP2	Protein phosphatase 2
Pre-RC	Pre-replicative complex
PROTAC(s)	Proteolysis targeting chimera(s)
PTM(s)	Post-translational modification(s)
R.E.	Restriction Enzyme(s)
ROI	Region of Interest
RFU	Relative fluorescence unit
RFP	Red fluorescent protein
RNA	Ribonucleic acid
rRNA	ribosomal Ribonucleic acid
S	Serine
SCF	Skp1-Cullin-F-box
SCN	hypothalamic suprachiasmatic nucleus
sfGFP	superfolderGFP
SH3	SRC Homology 3 Domain
Skp1 / 2	S-phase kinase-associated protein 1 or 2
SLiM(s)	Short linear motif(s)
slowFP	slow-folding FP
SNP(s)	Single nucleotide polymorphism(s)
SRE	Serum response element
SRF	Serum response factor
STAT	Signal transducer and activator of transcription

SUMO	Small Ubiquitin-like Modifier
T	Threonine
T _{1/2}	half-degradation rate
TAD	Transactivation Domain
TBP	TATA binding protein
TCF	T-cell factor
TFIID	transcription factor IID
TTFL	transcriptional/post-translational delayed feedback loop
tFT(s)	tandem Fluorescent Timer(s)
TGCA	The Cancer Genome Atlas
TGF β	Transforming growth factor- beta
TNF	Tumor necrosis factor
TO	Tetracycline-ON
TRAIL	TNF-related apoptosis-inducing ligand
tRNA	transfer Ribonucleic acid
TRRAP	Transformation/transcription domain-associated protein
Ub	Ubiquitin
UPS	Ubiquitin-proteasome system
USP 28 / 36	Ubiquitin-specific-processing protease 28 or 36
V	Valine
VEGF(A)	Vascular endothelial growth factor (A)
WDR5	WD repeat-containing protein-5
WHO	World Health Organisation

Chapter 1

Introduction

1.1 Myc family proto-oncogenes and the Hallmarks of cancer

1.1.1 The hallmarks of cancer

Cancer is a term used to describe a group of disease whereby cells in any tissue divide uncontrollably and invade adjacent tissues, generating metastasis. The primary cause of death in cancer is extensive metastasis. According to the World Health Organisation (WHO), in 2020 nearly 10 million patients worldwide died of cancer, making cancer a prominent cause of death (*World Health Organisation - Cancer 2022*). According to the National Health Service (*Cancer - NHS 2019*), one in two people risk developing some form of cancer in their lifetime. Breast, lung, prostate and bowel cancers are the most prevalent types of cancer in the UK, with breast and lung cancer together totalling 4.47 million new cases worldwide in 2020 and lung cancer constituting the leading cause of cancer death in 2020 at a staggering 1.8 million deaths (*World Health Organisation - Cancer 2022*). While different forms of cancer arise from a multitude of causes, for example some are caused by tobacco use others by exposure to carcinogens or oncogenic infections, some common biological characteristics are shared and have been and continue to be extensively studied in order to defeat these diseases.

The effort to understand the development, progression and vulnerability of cancer began about half a century ago, bringing forth an extensive body of literature that

Chapter 1. Introduction

highlights how complex and varied this disease is. Even though the direct cause of cancer changes from one form to another, there are common capabilities that need to be acquired by cells in order to allow oncogenesis. These are the so-called 'hallmarks' of cancer and were first highlighted by Hanahan and Weinberg (2000) as the following:

1. Sustained proliferative signalling
2. Insensitivity to anti-growth signals
3. Evasion of programmed cell death (apoptosis)
4. Limitless replicative potential
5. Sustained angiogenesis
6. Tissue invasion and metastasis

These were revised and extended a decade later (Hanahan and Weinberg, 2011) with the addition of four other hallmarks:

7. Deregulation of cellular energetics
8. Avoidance of destruction by the immune system
9. Genomic instability and mutation
10. Tumour promotion and inflammation

Specifically, hallmarks 9 and 10 are enabling characteristics whereby acquisition of any of the other hallmarks is promoted by the increased chance of mutations deriving from an unstable genome and by the increase in amount of bioactive molecules (such as growth factors) available to the tumour. As noted by Hanahan and Weinberg (2000), the order in which the neoplastic cells gain these hallmark abilities varies greatly even within tumours of the same type. Finally, some oncogenic proteins play important roles in allowing the accumulation of these biological capabilities. The Myc-family of proto-oncogenes express such proteins and are the focus of this investigation.

1.1. Myc family proto-oncogenes and the Hallmarks of cancer

1.1.2 The Myc family

In humans, Myc proto-oncogenes are a class of three genes (*c-Myc*; *n-Myc*; *l-Myc*) encoding transcription factors that highly regulate cellular gene expression. *c-Myc* was first identified as the cellular homologue of retroviral *v-Myc* from the avian Myelocytomatosis virus during characterisation studies of oncogenic retroviruses (Duesberg, Bister, and Vogt, 1977; Sheiness, Fanshier, and Bishop, 1978). The protein encoded by the gene *c-Myc*, henceforth termed Myc, is the main transcription factor of the Myc class.

According to a recent computational study (Schaub et al., 2018) based on of The Cancer Genome Atlas (TCGA) (Chang et al., 2013), Myc paralogue genes are amplified in 28% of cancers and Myc pathway activity was seen in 30 of the 33 cancer types included in TCGA. This highlights the importance that Myc isoforms play in tumorigenesis.

1.1.3 Myc and the hallmarks of cancer

Myc is involved in many pathways that allow the tumour to acquire hallmark capabilities (Gabay, Li, and Felsher, 2014; Hanahan and Weinberg, 2000; Hanahan and Weinberg, 2011) or a target of pathways that act to safeguard against oncogenesis. These are depicted in **Figure 1.1** where hallmarks directly influenced by Myc are highlighted in orange and indirectly in blue. Notably, Myc alone is not sufficient to induce tumourigenesis (Beer et al., 2004; Felsher et al., 2000). Nevertheless, if cells have already acquired some permissive genetic alteration that provide them with some of the aforementioned biological capabilities, Myc activation can drive the attainment of further oncogenic hallmarks.

1.1.3.1 Myc and sustained proliferative signaling

Myc allows cells to sustain proliferative signalling (**hallmark 1**) by inducing transcription of many genes involved in cell cycle progression, DNA replication, protein biogenesis and global metabolism. This uninterrupted proliferation facilitates occurrence of mutations through inappropriate repair of DNA damage, leading to genomic

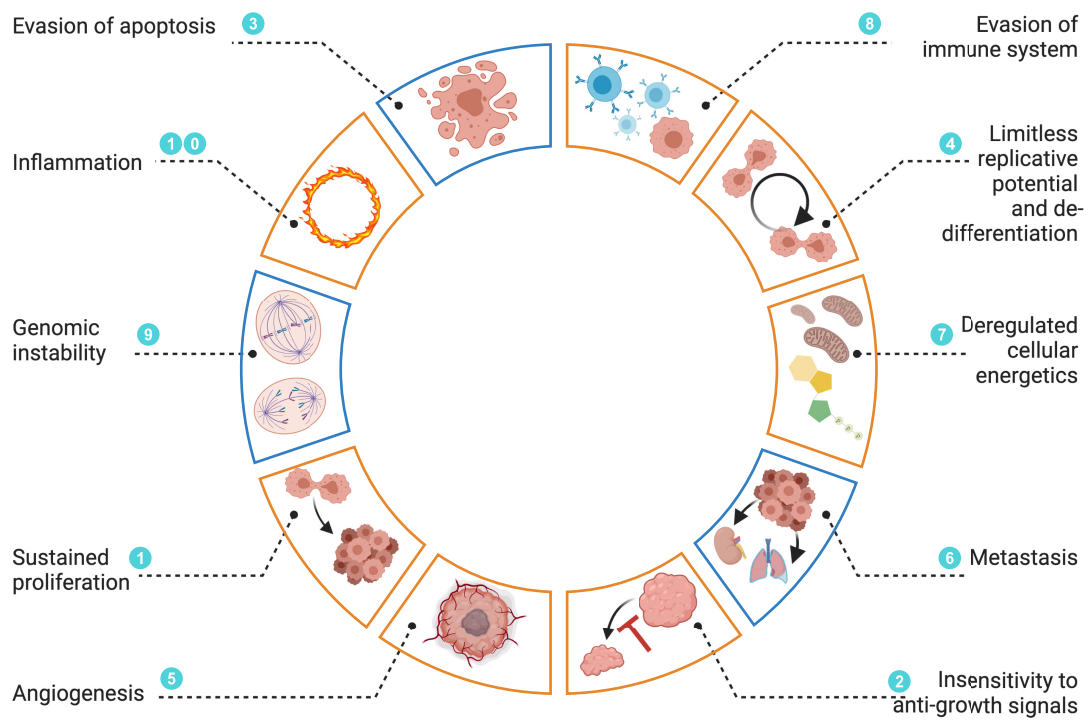


Figure 1.1: **Myc and the Hallmarks of Cancer.** Myc is directly (orange) and indirectly (blue) involved in allowing cells to gain any of the tumorigenic capabilities termed 'Hallmarks of Cancer'. Inspired by Hanahan and Weinberg (2011) Figure 3.

1.1. Myc family proto-oncogenes and the Hallmarks of cancer

instability (**hallmark 9**). Not only is Myc involved in mitogen sensing and metabolism (further discussed below), it also drives cell cycle progression through the G1 restriction point by inducing expression of cell cycle proteins cyclin D and cyclin-dependent kinase 4 (Bouchard et al., 2001; Hermeking et al., 2000). E2F transcription factors are also activated by Myc, driving progression into S phase (Dong et al., 2014). Furthermore, multiple mitogenic signalling pathways converge on Myc, highlighting the core role of Myc in promoting proliferation. An example of this is the SOS-Ras-Raf-MAPK kinase pathway, where mitogenic growth factors bind to a receptor such as the Epidermal Growth Factor Receptor (EGFR) or Platelet-derived Growth Factor Receptor (PDGFR) inducing its homodimerisation and activation of the tyrosine kinase cytoplasmic domain. This allows docking of Growth Factor Receptor-bound protein 2 (GRB2) which, together with SOS, allow binding of a Ras protein family member to GTP. GTP-bound Ras activates Raf initiating a cascade of phosphorylations that results in activation of transcription (Huynh et al., 2003; Molina and Adjei, 2006). Myc is one of the targets of this cascade: phosphorylation by MAPK stabilises the Myc protein, leading to increased levels of the transcription factor (Hayes et al., 2016; Sears et al., 1999, 2000; Vaseva et al., 2018).

1.1.3.2 Myc and growth arrest signals

Several growth arrest signals restrain Myc levels to ensure cells do not acquire insensitivity to anti-growth signals (**hallmark 2**). Firstly, controlling Myc levels is fundamental in order for cells to enter cellular quiescence. Transforming growth factor-beta (TGF β), which is involved in control of cell proliferation and differentiation, has been reported to suppress Myc expression as part of its growth arrest function through phospho-Retinoblastoma protein (pRb), the master-regulator of anti-proliferative signalling (Beijersbergen et al., 1994; Pietenpol et al., 1990). Remarkably, in carcinomas, TGF β promotes tumour progression through Endothelial-to-mesenchymal transition (EMT) (Oft, Akhurst, and Balmain, 2002). The latter is a process that results in loss of cell polarity, cell-cell adhesion, and by which cells acquire migratory capabilities. Finally,

Chapter 1. Introduction

breast cancer cells that have lost this TGF β regulation of Myc have been found to gain a survival advantage (Chen, Kang, and Massagué, 2001).

Secondly, whilst elevated Myc can drive proliferation of developing epithelial structures, this is not true in mature, quiescent epithelial structures. This was demonstrated through 3D culture, by over-expressing Myc in developing and established acinar structures. Indeed, Myc was able to drive proliferation in the former but not the latter. This growth arrest in mature epithelial structure was abolished when the Liver Kinase B1 (LKB1), an epithelial polarity protein involved in contact inhibition and epithelial tissue organisation, was knocked out (Partanen, Nieminen, and Klefstrom, 2009; Partanen et al., 2007).

Finally, Myc allows cells to avoid differentiation. Myc requires its binding partner MAX to bind DNA and exert its function (Amati et al., 1992, 1993) by recruiting transcriptional activators. MAX can also heterodimerise with Mad, a protein encoded by the *MDX1* gene, which competes with Myc for binding to MAX leading to recruitment of corepressor complexes and providing differentiation-inducing signals (Foley and Eisenman, 1999; Giardino Torchia and Ashwell, 2018; Grandori et al., 2000). An increase in Myc levels from sustained mitogenic signals will shift the balance away from the Mad-MAX interaction toward the Myc-MAX interaction which promotes immortalisation. Furthermore, Myc-deficient Haematopoietic stem cells (HSCs) cannot differentiate and cause cytopenia in mice (Wilson et al., 2004). Importantly, Myc is one of the four 'Yamanaka factors', transcription factors highly expressed in embryonic stem cells that allow the reprogramming of fully differentiated cells in induced Pluripotent Stem Cells (iPSCs) (Takahashi and Yamanaka, 2006; Takahashi et al., 2007). Overall, there is extensive evidence of the key role that Myc plays in evading growth arrest which supports the need to contain Myc levels to ensure controlled proliferation.

1.1.3.3 Myc and apoptosis

Programmed cell death, or "apoptosis", is the process that ensues following various physiological stresses, such as irreparable DNA damage, to stop uncontrolled cell

1.1. Myc family proto-oncogenes and the Hallmarks of cancer

proliferation. This precisely choreographed process leads to disruption of cellular membranes, breakdown of nuclear and cytoplasmic skeletons, cytosol extrusion, nuclear fragmentation and chromosomal degradation. Induction of apoptosis by Myc has been extensively documented. The same regulatory regions that control its ability to induce cell transformation and proliferation are also needed for its induction of programmed cell death (Evan et al., 1992). Murphy et al. (2008) proved that distinct thresholds in Myc levels are what discriminate between the proliferative or pro-apoptotic functions of Myc, with increased Myc levels required to activate the apoptotic ARF-p53 pathway. For this reason, Myc over-expression in cancer is frequently coupled with other genomic lesions such as oncogenic Ras mutations, functional inactivation of tumour-suppressor p53 (recorded in more than 50% of human cancers) and co-operation with oncogenic Bcl-2 (McMahon, 2014). In conclusion, Myc alone does not allow evasion of apoptosis (**hallmark 3**). Nonetheless, concomitant elevated expression of Myc and other oncogenic lesions drives proliferation and overcomes the apoptotic threshold of Myc.

1.1.3.4 Myc and limitless differentiation potential

The role of Myc in promoting de-differentiation, as discussed above, also supports its ability to allow cells to gain limitless replicative potential (**hallmark 4**). Additionally, human telomerase reverse transcriptase (hTERT), the rate-limiting catalytic subunit of the telomerase enzyme complex is a direct target of Myc. Telomeres are heterochromatin structures that offer chromatin stabilisation and protection, impede chromosomal fusions and recombinations, secure chromosomes within the nucleus and participate in replication. They encode thousands of repeats of a 6bp sequence that aid in safeguarding the genomic information from the 50-100bp loss of information that occurs at every round of replication. Telomerase adds these hexameric repeats to the telomeric ends to maintain them. In somatic cells, telomeres shorten with the increase of replication cycles; in germline lineage cells are immortal and have highly active telomerase. High telomerase activity correlates with tumour progression, thus Myc can also promote limitless dedifferentiation through upregulation of the hTERT gene (reviewed by Cerni,

2000).

1.1.3.5 Myc and angiogenesis

Myc promotes and sustains angiogenesis (**hallmark 5**). In fact, Baudino et al. (2002) reported that Myc plays an essential role in appropriate vasculogenesis, erythropoiesis and angiogenesis in mice and embryonic cells. Depletion of the oncogene results in a great reduction in Vascular Endothelial Growth Factor (VEGF). Additionally, mRNA levels of angiopoietin 1 and 2 (ANG-1 and -2) growth factors were high in Myc expressing cells and low in Myc null cells. Further evidence for the role of Myc in mediating of angiogenesis was provided by Shchors et al. (2006): rapid expression and release of interleukin 1 β (IL-1 β) is a consequence of Myc activation in β cells. This results in production and release of VEGF-A which drives tortuous and immature branching of vessels in the nascent tumour vasculature. Blocking of IL-1 β reduced angiogenesis making the interleukin the effector of Myc-induced angiogenesis.

1.1.3.6 Myc and tissue invasion and metastasis

The literature on the role of Myc in tissue invasion and metastasis (**hallmark 6**) is somewhat contradicting. Wolfer et al. (2010) provided evidence in support of Myc contributing to metastasis by describing how Myc coordinates the expression of 13 “poor-prognosis” cancer signatures. This study also showed that whilst Myc knockdown did not alter the kinetics of primary tumour formation in xenografts of mammary epithelial adenocarcinoma cells in mice, it greatly hindered the formation of distant metastases. This would propose a role for Myc to maintain the tissue invasion capacity rather than the proliferative and anti-apoptotic abilities of the cell line in question. Two isoforms of Myc (Myc and n-Myc) have been shown to activate miR-9, a miRNA that targets the mRNA for E-cadherin, leading to lower levels of this protein and higher cell motility and invasiveness. Upregulated miR-9 also lead to increased VEGF-A production and consequently, as previously described, angiogenesis. Finally, a

1.1. Myc family proto-oncogenes and the Hallmarks of cancer

correlation has been discovered between miR-9 and MycN amplification, tumour grade and metastasis in cancers (Ma et al., 2010). Furthermore, induced increases in Myc levels lead to tissue invasion and metastasis in a RAF-driven murine lung cancer model which would not otherwise progress to a metastatic phenotype (Rapp et al., 2009). Smith et al. (2009) provided insight into a molecular mechanism by which Myc participates in tissue invasion and metastasis: Myc and TGF β , although antagonists in non-cancerous cells, co-operate in a cancerous setting to induce transcription of *Snail* and ensuing EMT. More recently, Agarwal et al. (2019) provide another mechanism for Myc-induced invasion that is through its ability to induce a network of mitochondrial trafficking genes, such as Drp1, leading to increased mitochondria at the cortical cytoskeleton. This promotes focal adhesion dynamics, chemotaxis and tissue invasion.

Contradictingly, the following bodies of work provide evidence for the paradoxical capability of Myc to suppress tissue invasion. In the study by Liu et al. (2012), whilst Myc overexpression indeed stimulated growth and proliferation of breast cancer cells *in vitro* and *in vivo* xenografted tumours, it also inhibited motility and invasiveness in both settings. This is shown to be due to Myc-driven transcriptional repression of subunits of $\alpha v\beta 3$ integrins, reversible by exogenous expression of $\beta 3$ integrin. The inhibition of tissue invasion by Myc was investigated further by Cichon et al. (2016) who described increased sensitivity to TGF β -stimulated invasion as a consequence of Myc inhibition in basal breast cancer cells. Interestingly, one of the cell lines used in this study is the same used by Smith et al. (2009) in which Myc is reported to have a positive effect on tissue invasion through co-operation with TGF β . Finally, Myc has been reported to upregulate an inhibitor of JNK-dependent cell invasion and migration in *Drosophila melanogaster* and lung adenocarcinoma cell lines (Ma et al., 2017).

1.1.3.7 Myc and deregulated cellular energetics

In healthy cells, Myc is involved in the process of nutrient sensing and mediating cell growth in response. This is through the mammalian Target of Rapamycin (mTOR) which, as part of the mTOR Complex 1, senses nutrient availability, induces transcrip-

Chapter 1. Introduction

tion of Myc (Csibi et al., 2014) and controls the oncoprotein's stability. Specifically, during branched amino acid starvation, mTOR is inhibited and Autophagy And Beclin 1 Regulator 1 (AMBRA1) activation leads to dephosphorylation of S62 of Myc by Protein Phosphatase 2v(PP2), causing destabilisation of Myc (Cianfanelli et al., 2015). Additionally, Myc activity is inhibited and countered by Forkhead box O3 (FOXO3A) which binds and transactivates MAX-interacting protein 1 (MXI-1), an antagonist of Myc for MAX binding and repressor of Myc-target genes (Delpuech et al., 2007; Jensen et al., 2011). Again, deregulated Myc levels in cancer skew the balance toward Myc-MAX, impeding this tight regulation of Myc and its targets. Because many metabolic genes are expressed ubiquitously at basal levels, Myc can further drive their expression once activated. In fact, many metabolic target genes of Myc contain conserved consensus E-boxes in their promoter region. This is important for the biological function of Myc to drive cells into a proliferative state but once this is achieved Miz-1, MXI-1 and other regulators oppose Myc transcriptional amplification and activity (Wolf et al., 2015). Myc deregulation by chromosomal amplification, translocation and mutation bolsters Myc levels. This impedes negative feedback, promotes Myc binding to low-affinity E-boxes and enhancers, further promoting processes of macromolecule synthesis and organelle biogenesis (reviewed by Stine et al., 2015). Overall this emphasises the key role that Myc plays in supporting cancer cells to deregulate cellular energetics (**hallmark 7**).

1.1.3.8 Myc and immune system evasion

Oncogenic proteins contribute to tumourigenesis not only by driving cell-specific and host-independent functions, like pathological cellular proliferation and growth, but also by regulating host immune-mediated mechanisms (**hallmark 8**). Indeed, Myc plays a role in aiding cancerous cells in evading the immune system (reviewed by Casey, Baylot, and Felsner, 2017). The oncoprotein upregulates genes such as CD47, providing cells with an escape from phagocytosis, and PD-L1 (Programmed death-ligand 1), an immune checkpoint that allows suppression of the immune response (Casey et al., 2016). Rakhra et al. (2010) showed that upon Myc inactivation, an immunocompromised

1.1. Myc family proto-oncogenes and the Hallmarks of cancer

host is unable to maintain tumour regression following initial proliferative arrest and apoptosis. In order for sustained tumour regression through induction of cellular senescence and cessation of angiogenesis to ensue, CD4+ T-cells are required. Finally, there is recent evidence in a mouse lung model of mutant Ras and Myc for the latter's role in remodelling the tumour microenvironment through immune suppression and inflammation (**hallmark 10**). In this study, Kortlever et al. (2017) showed that lung tumours arising from long-term mutant KRas and Myc were more proliferative, invasive, angiogenic and inflammatory than those stemming from mutant KRas alone. This was mediated by Myc through up-regulation of pro-inflammatory chemokine CCL9 and cytokine IL-23.

In conclusion, the ability of Myc in aiding cancer cells into acquiring such hallmarks is crucial and many cancers become so reliant on the oncoprotein that its inactivation is sufficient to drive tumour regression, a phenomenon termed 'oncogene addiction' (Felsher and Bishop, 1999; Marinkovic et al., 2004; Pelengaris et al., 1999; Shachaf et al., 2004). This makes Myc an extremely compelling target for cancer therapy. However, efforts to develop small molecule compounds that inhibit the oncogene have been unsuccessful due to the lack of a druggable binding pocket. This will be discussed further in **section 1.1.5**.

1.1.4 Myc Structure, Expression and Function

1.1.4.1 Myc Structure

Myc is part of the Proximal Myc Network (PMN), a system of transcription factors that consolidates signals from several distinct upstream pathways into expression of thousands of target genes involved in the processes previously explained (Conacci-Sorrell, McFerrin, and Eisenman, 2014). All the members of the PMN are transcription factors that dimerize and contain a basic helix-loop-helix leucine zipper (bHLH-LZ) domain. The heterodimers can then interact with the DNA through recognition of an Enhancer box (E-box, 5'-CACGTG-3') driving recruitment of co-activators/repressors, transcriptional regulation and chromatin remodelling. This bHLH-LZ domain is present on the carboxyl-terminus (C-terminus) of Myc. The amino-terminus (N-terminus) of Myc has a large unstructured intrinsically disordered region (IDR) that contains multiple sites of interaction with regulators and interactors, as well as the phosphodegron motif required for Myc degradation and that determines its short half-life (~ 30 minutes). Recent years have seen an increased interest in IDRs as their role in protein function and regulation of protein stability are coming to light. IDRs are composed of short modular stretches of amino acids that constitute functional modules for protein-protein interactions and are termed short linear motifs (SLiMs). SLiMs are essential for allowing control of protein localization, stability, and context-dependent activity (Van Roey et al., 2014). The Eukaryotic Linear Motif (ELM) resource (Gouw et al., 2017), a repository of experimentally validated SLiMs, identifies residues 55-65 of Myc as containing the following SLiMs important for the life cycle of Myc: GSK3 β phosphorylation site; Class IV WW domain interaction motif, recognised by Pin1 (phosphorylation-dependent prolyl isomerase 1); TPxxS phospho-dependent degron, recognised by E3 FBW7 (F-box/WD repeat-containing protein 7); Proline-Directed Kinase phosphorylation site; and a motif recognised by class II SH3 domains. As shown in **Figure 1.2**, the N-terminus is key for recruitment of co-activators by Myc, which is mediated by the Transactivation Domain (TAD), a region essential for the transcriptional and cell-transforming activity of Myc (Beaulieu, Castillo, and Soucek, 2020; Kato et al., 1990). Interestingly, a version

1.1. Myc family proto-oncogenes and the Hallmarks of cancer

of Myc lacking the NLS and DNA binding domain called Myc-nick, conserves some functionality as it is able to acetylate α -tubulin through histone acetyltransferase GCN5 to promote cellular differentiation in a transcriptionally independent manner (Conacci-Sorrell, Ngouenet, and Eisenman, 2010). As this region is so important for recruitment of transactivators, more yet undiscovered SLiMs are likely to be present in this region.

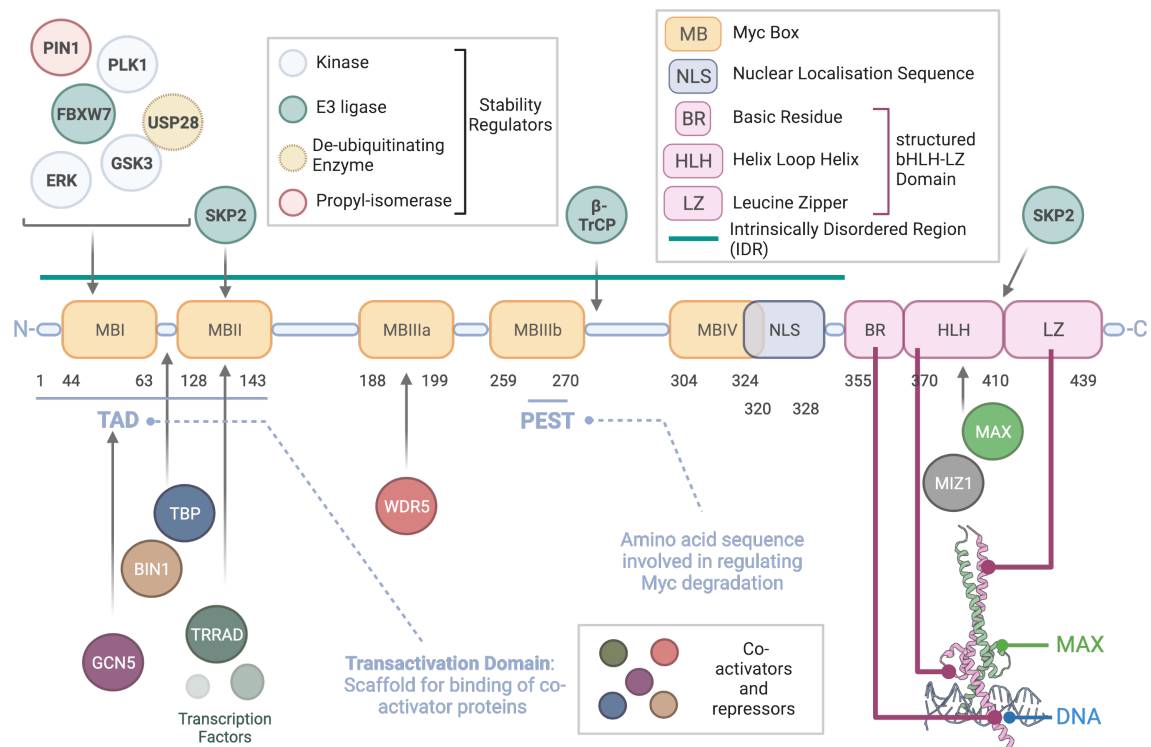


Figure 1.2: **Myc structure and interactome.** Schematic representation of the modular structure of the Myc oncoprotein. The IDR extends from the N-terminus to just after Nuclear Localisation sequence (NLS) and contains multiple disordered regions. Myc Boxes (MB), are conserved between Myc family members and are functionally important. MBI mediates contact with most regulators of Myc stability, whilst the whole transactivation domain TAD is important in mediating binding of co-activators and repressors of Myc activity. The NLS is present in the C-terminus and precedes the basic Helix-Loop-Helix Leucine Zipper (bHLH-LZ) domain of Myc which is essential for binding to MAX and DNA, as shown in the crystal structure.

All Myc family members share highly conserved transcriptional regulation elements termed Myc Boxes (MB), two of which are within the N-terminal IDR, and all

Chapter 1. Introduction

precede the more structured C-terminal bHLH-LZ domain. Indeed, the structure of the C-terminal bHLH-LZ has been studied most intensively as it presents a defined structure of an otherwise intrinsically disordered protein (IDP), and a desirable drug-gable site due to it being necessary for Myc activity. The HLH and LZ domains allow transcription factors to fold into multimeric helix bundles that allow formation of heteromers. This modular structure is key to controlling the function of the transcription factor network through regulating expression and degradation of members of the heterodimer complex. Such is the case for the PMN. Indeed, Myc alone cannot bind the DNA, but it requires MAX to do so (Amati et al., 1992, 1993). MAX is the central node of this network and it can homodimerise. Due to its lack of functional domains, MAX does not have direct transcriptional activity but rather forms transcriptionally inactive complexes that compete for binding with transcriptionally active Myc-MAX heterodimers. Therefore, MAX homodimers and heterodimers with MAX binding proteins (e.g. MNT) and dimerization proteins (e.g. MXD1) are functional antagonists to Myc (Conacci-Sorrell, McFerrin, and Eisenman, 2014). It is important to highlight the importance of residues H359, E363 and R367 of Myc for DNA binding and recognition of the canonical E-box (Nair and Burley, 2003). Furthermore, phosphorylation of T358 renders Myc unable to heterodimerize or bind to DNA (Macek et al., 2018). Additionally, the HLH domain is important for interaction with MIZ-1, a Myc binding partner that mediates its ability to repress transcription, with V394 being the key residue (Wiese et al., 2013). This will be further covered in **section 1.1.4.3**.

Because Myc has such a prominent oncogenic effect, regulation of this protein is extremely important. Indeed, Myc protein half-life is short (~ 30 minutes) and interaction sites with some of the regulators of its stability are concentrated within the TAD, specifically in Myc box I (MBI). This region is important for Pin1 binding, which facilitates Myc degradation. Importantly, MBI contains the highly conserved phosphodegron residues important for Myc degradation by FBW7 (see **section 1.2.2**). MBI is also the site of interaction of N-Myc with Aurora Kinase A (AurkA) (Richards et al., 2016). MBI and surrounding regions are also sites of interaction with co-activators

1.1. Myc family proto-oncogenes and the Hallmarks of cancer

and repressors. Specifically, Bridging Integrator 1 (Bin1), a tumour suppressor adaptor protein interacts with Myc to repress its transactivation and transformation (Sakamuro et al., 1996). Additionally, the region between MBI and MBII bind the TATA Binding Protein (TBP), a member of the Transcription Factor IID (TFIID) complex responsible for recruiting RNA Polymerase II at transcriptional start sites (Wei et al., 2019). MBII also mediates interaction of Myc with regulators of its transcriptional activity and the transcriptional machinery. One example is the transformation/transcription domain-associated protein (TRRAP) an adaptor protein for multiple chromatin-associated complexes (Conacci-Sorrell, McFerrin, and Eisenman, 2014). MBIIIa is involved in the ability of Myc to act as a transcriptional repressor. MBIIIb interacts with WD repeat-containing protein 5 (WDR5) and this is important for promoting the association of Myc with its target genes (Thomas et al., 2015). Indeed, point mutations in this domain are able to disrupt this interaction and consequent interaction with target gene sites but does not affect localisation or interaction with MAX or DNA. MBIIIb also contains the PEST sequence, a proline (P), glutamic acid (E), serine (S), and threonine (T) rich sequence that is important for Myc stability. A study by Gregory and Hann (2000) shows that deletion of this sequence leads to increased Myc levels although it does not reduce Myc ubiquitination. However, some deleted sequences upstream of the PEST do indeed affect ubiquitination. Overall the conclusion from this work is that the PEST sequence is required for Myc degradation following Myc ubiquitination and ahead of degradation by the proteasome. The first 158 amino acids and PEST sequence that were highlighted as important for Myc 26S degradation lie within the N-terminal IDR which might be required for substrate recognition by the proteasome. Indeed, protein binding to the 26S proteasome is insufficient for substrate degradation, but rather engagement of the substrate through binding of an IDR is essential (Tomita and Matouschek, 2019). Finally, MBIV is also involved in Myc activity and precedes its NLS (Beaulieu, Castillo, and Soucek, 2020). As represented schematically in **Figure 1.2**, most MB and surrounding sequences contain disordered regions (green line) as identified by the ELM resource (Gouw et al., 2017).

1.1.4.2 Myc Expression

Expression of the *Myc* gene is normally induced by several pathways (WNT, RAS/RAF/MAPK, JAK/STAT, TGF- β , NF- κ B), often deregulated in cancer, as an early response to mitogens or cytokines through activation of transcription factors that bind *Myc* enhancers and promoters. CNBP (CCHC-Type Zinc Finger Nucleic Acid Binding Protein), TCF (T-cell factor) and BRD4 (Bromodomain-containing protein 4) are examples of such transcription factors and regulators. Furthermore, non-canonical (non-B) DNA structures have also been shown to have a regulatory effect on the expression of *Myc* (Dang, 2012). Due to the key role of Myc in promoting tumourigenesis, the *Myc* gene is up-regulated in cancer through amplification, chromosomal translocations and mutation in the regulatory regions of *Myc* promoter and enhancers. Indeed, *Myc* locates within a approximately 3Mb area of chromosome 8q24 that lacks protein-coding genes. This region is frequently mutated with a considerable amount of Single Nucleotide Polymorphisms (SNPs) that are associated with cancer risk. This region of chromosome 8 contains tissue-specific long-range enhancers and super-enhancers of *Myc* that contribute to modulating *Myc* expression in normal and cancerous settings and are frequently duplicated or SNPs enriched in a multitude of cancers (Lancho and Herranz, 2018). It is important to note that Myc mRNA, which is also short-lived, is post-transcriptionally regulated by miRNAs to further modulate the overall amount of Myc protein available in the cell (Dang, 2012). Post-translational regulation of Myc will be covered in **section 1.2.2**.

1.1.4.3 Myc Function

As previously mentioned, the main function of Myc is that of a sensor, as it integrates multiple signals derived from different pathways to elicit and orchestrate expression of a great variety of genes. The roles of Myc in cancer are many as are the biological readouts of its function. As proliferation will be one of the biological outputs that will be used in this study to assess Myc function, this following section will focus on how Myc drives cellular proliferation through transcriptional activation and repression and

1.1. Myc family proto-oncogenes and the Hallmarks of cancer

non-transcriptional functions.

The function of Myc is intrinsically linked to its structure. Indeed Myc requires MAX for its transcriptional activation function. MAX is a long-lived protein, with a half-life of about 6 hours, whilst Myc is a short-lived protein with a half-life of less than an hour, making Myc rate-limiting for heterodimerization and transcriptional function (Carroll et al., 2018). On a molecular level, its transcriptional activity is linked to its ability to recruit RNA polymerase and members of histone acetylase complexes to its binding sites, with Myc target sites presenting high histone acetylation, (Conacci-Sorrell, McFerrin, and Eisenman, 2014). Additionally, Myc binds to proximal gene promoter sequences, relieving transcriptionally paused RNA Polymerase II and re-initiating transcriptional elongation. Chromatin accessibility dictates Myc targets by allowing its binding and co-operation with other transcription factors to promote or repress transcription. This allows Myc to amplify genes expressed at basal levels, such as those involved in metabolism (Stine et al., 2015). One of the key functions of Myc is to promote ribosome biogenesis, it regulates expression of core subunits of the RNA polymerase I apparatus as well as interacts with it directly to enhance pre-rRNA processing. It also enhances transcription of RNA Polymerase III subunits and cooperates with it to yield 5S RNA and tRNA production (Campbell and White, 2014). Additionally, Myc upregulates expression of genes involved in nucleotide and miRNA synthesis, as well as enzymes involved in RNA processing and capping. This function of Myc allows it to modulate cellular transcription. It also upregulates eukaryotic translational initiation factor 4E (eIF4E), catalyzing increased transcription (Stine et al., 2015). The combined modulation of both transcription and translation by Myc has the biological effect of increasing the cell mass through induction of ribogenesis and changes in cell metabolism.

MIZ-1-bound Myc is capable of transcriptional repression. MIZ-1 is a transcriptional activator when not bound to Myc and this interaction stops MIZ-1 from binding its co-activators p300 and Npm1. Furthermore, there is evidence that Myc/MIZ-1 can

Chapter 1. Introduction

recruit DNA methylases. Finally, MIZ-1 protects Myc from proteasomal degradation. Importantly, ubiquitination of Myc by Skp2 not only causes its degradation but also increases its transcriptional activity as Skp2 acts as a transcriptional co-activator. Overall, stabilization of Myc by MIZ-1, as well as the previously mentioned effects of this interaction contribute to the ability of Myc to repress transcription. Two known targets of Myc/MIZ-1's transcriptional repression are p21Cip1 and p15Ink4b, two cyclin-dependent kinase inhibitors (CDKI). For both genes, the Myc/MIZ-1 heterodimer binds the transcriptional start site, where it does not affect the basal level expression of these genes but rather their induction by anti-mitotic stimuli (Vousden, 2002; Wiese et al., 2013).

Furthermore, Myc has been shown to directly bind components of the pre-replicative complex (Pre-RC), which is necessary for DNA replication. This complex binds the origin recognition complex, which locates the origin of replication, in early G1 phase of the cell cycle. Activation of Pre-RCs to induce functional initiation of transcription requires cyclin-dependent kinases (CDK) activity. Myc directly induces expression of cyclins, CDKs and CDKIs. Specifically, Cyclin D, Cdk-4, Cdk-6 are some of the targets of Myc that drive cell cycle entry. Overall this shows its dual effect on DNA replication both by directly binding Pre-RCs and by indirectly activating them through CDK activation at G1/S transition (Dominguez-Sola and Gautier, 2014). Altogether, the effect of Myc on the cell cycle is three-fold: coupling of cell growth with cell-cycle progression, repression of cell cycle inhibitor proteins, and induction of DNA replication and of cell cycle proteins, as shown in **Figure 1.3**.

1.1. Myc family proto-oncogenes and the Hallmarks of cancer

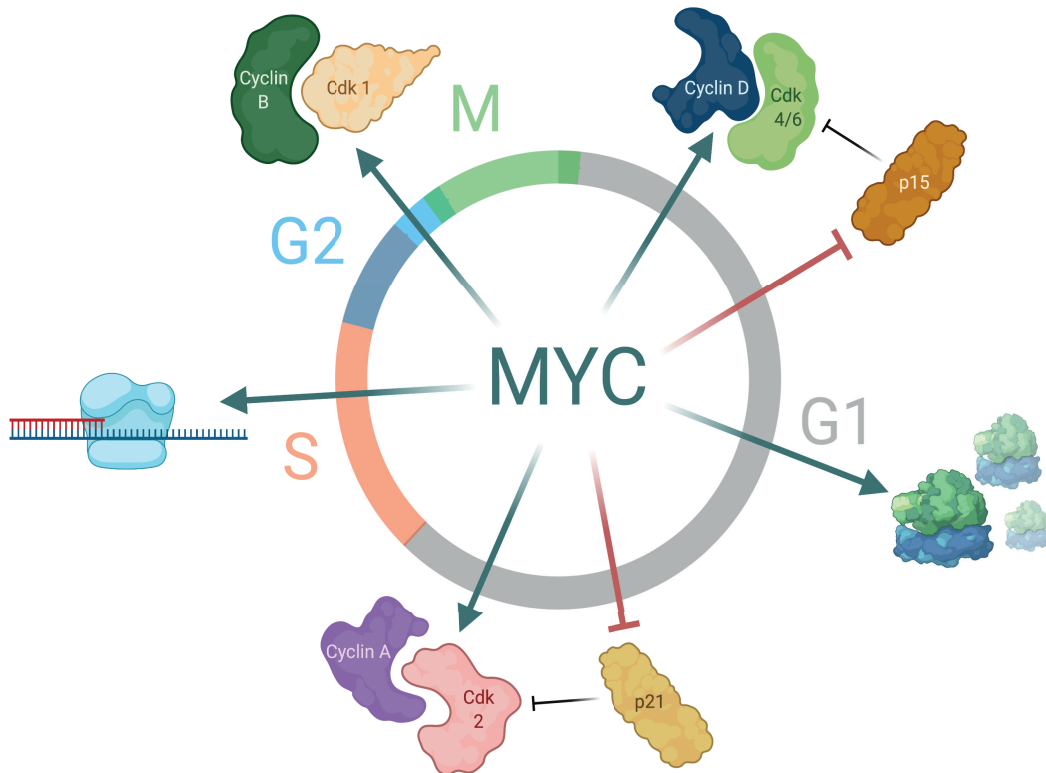


Figure 1.3: **The transcriptional function of Myc is to drive cell cycle progression.** Myc functions by promoting cell cycle progression in different ways based on the stage of the cell cycle. In early G1, Myc induces transcription of Cyclin D Cdk4/6 and represses expression of CDKI p15. Later in G1, it induces transcription of Cyclin A, Cdk2 and represses CDKI p21 expression. In the meantime it also drives ribosome biogenesis, which promotes progression by increasing cellular size. Myc is also a key player of DNA replication during S-phase. Finally, Myc induces Cyclin B1 expression at the G2/M transition.

1.1.5 Targeting Myc

The information collected so far supports the idea that Myc is an extremely appealing drug target and as such it has been studied extensively for the past three decades (Dang, 2012). However, despite such huge therapeutic potential, it has been challenging to design therapeutics against and has indeed been deemed an 'undruggable' target. Before delving deep into the efforts of targeting Myc, it is important to define an 'undruggable' cancer target. This term has been used extensively to describe desirable therapeutic targets that have been difficult to target due to either their intracellular localisation, lack of structural information or to their nature of partially or intrinsically disordered proteins. The majority of the targets for which therapies have been successfully created were once deemed 'undruggable' and advances in basic research of biological pathways and biochemical properties of these proteins has been key to designing successful therapies. About 90% of current drugs are small molecules which are challenging to design for proteins which lack structured areas and pockets. There has been a rapid expansion in the last decade of alternative drug modalities, named biologics, which include antibodies, vaccines, nucleic acid and peptide-based therapies and cell-based therapies. This unfortunately covers about 20% of potentially targetable targets (Dang et al., 2017). An 'undruggable' target for which successful therapies have been and are currently being developed is the BCL-2 family of proteins, which present no hydrophobic pockets and are localised intracellularly. Nevertheless, studies of the interactions between pro-survival (BCL-2) and pro-apoptotic (BH3-only proteins) family members yielded the BH3 mimetic drug Venetoclax which inhibits BCL-2 family members and takes advantage of the increased sensitivity of cancer cells to pro-apoptotic signals. Indeed, Venetoclax succeeded in clinical trials for refractory chronic lymphocytic leukaemia and is being tested for other malignancies (Verdine and Walensky, 2007). Overall, the term 'undruggable' should not hinder or discourage attempts at generating therapeutics against such targets, but rather should signal that more information needs to be collected to guide successful drug design and tackle this obstacle, highlighting the importance of discovery research.

1.1. Myc family proto-oncogenes and the Hallmarks of cancer

Myc falls into the 'undruggable' target category due to its largely intrinsically disordered structure and lack of a traditional binding pocket, however there has been and continues to be a large body of work dedicated to understanding and investigating several approaches to target this transcription factor. Several strategies have been employed to achieve inhibition of Myc activity and have been recently reviewed by Whitfield, Beaulieu, and Soucek (2017). These are depicted in **Figure 1.4**: direct inhibition of Myc expression, direct inhibition of Myc function through interfering with its binding to proteins or DNA, indirect inhibition of Myc and indirect targeting by synthetic lethality.

Direct therapeutic inhibition of Myc expression has been explored through G-quadruplex stabilisers, antisense oligonucleotides and siRNA. G4-DNA or G-quadruplexes are tertiary structures formed by guanine-rich sequences which are present in the NHEIII region of the Myc promoter. Chemical stabilisation of these regions by small-molecules ligands have been shown to repress Myc transcription. An example is Quarfloxin, which disrupts the interaction between nucleolin and the G4-DNA in ribosomal DNA, repressing Myc expression (Brooks and Hurley, 2010; Drygin et al., 2008). Target specificity for this therapeutic approach is unclear and was a concern that hindered further development of such strategies.

Antisense oligonucleotides offer targeted degradation of Myc mRNA as an exciting opportunity to inhibit the expression of the oncogene. Nevertheless, few of these types of molecules have reached the market. Compound INX-3280 progressed to Phase II clinical trials but failed to reach the clinic. Myc expression was also inhibited by AVI-4126 which prevents ribosomal assembly and thus mRNA translation, and seemed a promising approach that showed positive results up to Phase II trials. However, no follow up has been reported since (Whitfield, Beaulieu, and Soucek, 2017). Finally, siRNA also offers another avenue for interfering with Myc expression, with many attempts aimed at surmounting the hurdle of their rapid degradation within cells such as modified gold particles (Shaath et al., 2016) and Lipid/Calcium/Phosphate (LCP) nanoparticles (Zhang et al., 2013).

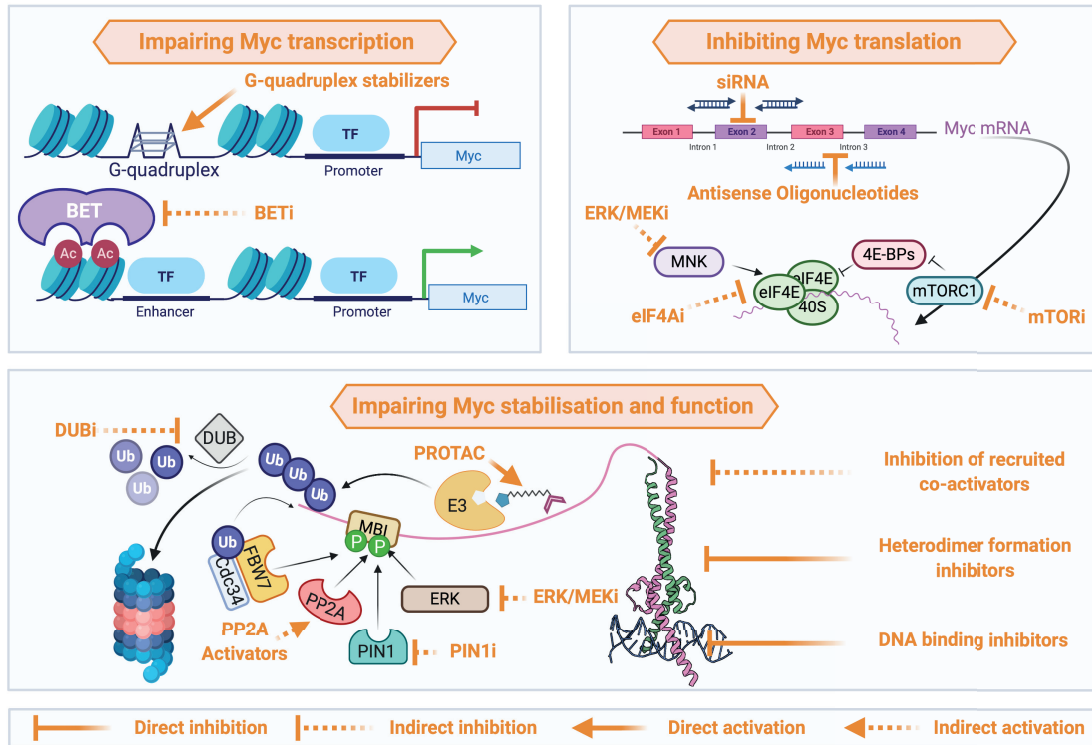


Figure 1.4: **Strategies for therapeutic modulation of Myc.** Myc modulation has been approached with many strategies that either aim at impairing its transcription, translation, protein function or interactions. Therapeutic categories (orange) can be indirect (dotted line) or direct (full line) inhibition/activation of regulators and interactors. Myc transcription (top left) can be inhibited by stabilising G-quadruplex DNA structures or by inhibiting bromodomain and extra-terminal (BET) proteins. Myc translation can be inhibited by decreasing its mRNA levels through the use of antisense oligonucleotides or siRNA, or by affecting translation indirectly through inhibition of eIF4E-mediated cap-dependent Myc translation. Finally, Myc protein function (bottom) can also be inhibited through hindering its binding to DNA, MAX or co-activators. Regulating post-translational modification and protein stability (bottom) can be pursued as a therapeutic option. *Ac* acetylation, *TF* Transcription Factor, *BET* bromodomain and extra-terminal motif, *ERK* extracellular signal-regulated kinases, *MEK* Mitogen-activated protein kinase kinase, *eIF4E* Eukaryotic translation initiation factor 4E, *4E-BPs* eIF4E-binding proteins, *mTORC1* mammalian target of rapamycin complex 1, *FBW7* F-box and WD repeat domain-containing 7), *MBI* Myc box , *Ub* ubiquitin, *PIN1* Prolyl isomerase 1, *P* phosphorylation, *DUB* deubiquitinating enzyme, *PP2A* Protein Phosphatase 2A. Inspired by Whitfield, Beaulieu, and Soucek (2017), Figure 3 and Allen-Petersen and Sears (2019) Figure 1.

1.1. Myc family proto-oncogenes and the Hallmarks of cancer

Another strategy to directly inhibit Myc function, is to **interfere with its ability to bind to proteins or DNA**. As previously discussed, MAX is required for Myc binding to DNA and to execute its transactivational function and thus inhibition of Myc can be achieved through hindering this interaction. Both small molecules and peptide drugs have been aimed at disrupting such interactions. The peptide mimetic small molecule IIA6B17 was the first inhibitor of Myc/MAX heterodimerization. The most efficient appears to be KJ-Pyr-9 which has satisfactory affinity ($K_d=6.5\text{nM}$), effectively blocks development of Myc-amplified human cancer cell xenografts, is able to penetrate the blood-brain barrier and is not acutely toxic at high doses (10mg/kg) (Hart et al., 2014). Additionally, shifting the balance towards MAX/MAX homodimers versus Myc/MAX heterodimers is an exciting alternative; a potent stabiliser of the homodimer emerged from a virtual ligand screen (Jiang et al., 2009), although over a decade ago now. Another strategy that falls into this category is to inhibit Myc/MAX binding to DNA. Indeed, compounds that block this interaction have been designed such as MYRA-A (Mo and Henriksson, 2006) which show good *in vitro* affinity but lack *in vivo* selectivity. Recently, Han et al. (2019) demonstrated effective inhibition of Myc activity and Myc/MAX dimerization by MYCi361 and MYCi975. Surprisingly, these compounds not only effectively inhibited heterodimerization, but also led to a decrease in Myc levels by increasing phosphorylation at T58 and therefore increasing phosphodegron-mediated degradation. This unexpected effect of MYCi975 combined two approaches to target Myc: Myc inhibition and destabilisation. Furthermore, the two modes of action were independent of each other so whilst the effect on Myc stability was impaired in T58A mutant Myc, the compounds were still able to impede the heterodimerization of the mutant form of Myc. Finally, peptide α -helix mimetics which recognise the heterodimer and not free Myc to disrupt DNA binding were developed, but low affinity ($K_d=13\mu\text{M}$) prevented further progress (Jung et al., 2015). OmoMyc, a drug of the miniprotein/protein domain class, was designed based on the structure of Myc and indeed is the bHLH-Zip domain of Myc with four amino acid substitutions that modify its dimerization specificity (Soucek et al., 1998). It was essential for proof of concept of the feasibility of systemic Myc inhibition. Savino et al. (2011) showed

Chapter 1. Introduction

that OmoMyc acts in multiple ways to inhibit Myc function. Firstly, it is able to bind Myc, MAX and Miz-1, leading to increased nuclear Miz-1. OmoMyc expression in cells impacts the Myc-mediated transcriptional response to serum stimulation following serum withdrawal in fibroblasts leading to downregulation of 44% of Myc-amplified genes, most of which were involved in metabolic processes. It was also shown that OmoMyc functions by directly binding to Myc binding sites so overall its effect is multiple: it stops interaction between Myc and MAX, sequesters Myc from DNA, and occupies E-boxes with transcriptionally inactive homodimers. Overall this lead to effects on proliferation and survival of cultured cells. Strikingly, it has shown minimal side-effects thus proving that a therapeutic window for Myc inhibition does indeed exist (Sodir et al., 2011; Soucek et al., 2008). The development of OmoMyc has been of great importance for the advancement of the field and has allowed studies that investigate the biological effects of switching off this tumourigenic driver (Soucek et al., 2008). Whilst the body of work generated by the invention of OmoMyc has been greatly beneficial to the understanding of Myc function as well as design of new therapies aimed at Myc, OmoMyc is not yet a therapeutic agent. Another peptide inhibitor of Myc created by structure-based design is a 14 amino acid sequence of its Helix 1 that unlike OmoMyc, does not perform well *in vivo* due to its inability to cross the nuclear membrane. However, a combination of this H1 peptide and docletaxel to prolong the period of nuclear envelope disassembly delivered in the macromolecular carrier HPMA, gave good results *in vivo* (Li et al., 2016). A final peptidic therapeutic option to target Myc could be through the bHLH-Zip of MAX. Montagne et al. (2012) showed that this spontaneously transduces into cells and through excess homodimeric MAX inhibits Myc transcription by outcompeting Myc/MAX binding.

Due to direct Myc inhibition being so challenging, indirect inhibition has been an extensively pursued avenue of therapeutic development. **Indirect inhibition** of Myc can be achieved by blocking its transcription and/or translation, regulating its stability, and via synthetic lethality. In the first instance, bromodomain and extra-terminal (BET) domain inhibitors (e.g. compound JQ1) have had some success in clinical Phase I and II

1.1. Myc family proto-oncogenes and the Hallmarks of cancer

trials but with frequent relapse (Allen-Petersen and Sears, 2019). JQ1 has been shown to displace bromodomain chromatin regulators from Myc, cause cell cycle arrest and cellular senescence (Delmore et al., 2011). Their effect might not solely rely on their effect on Myc and compensatory mutations have been recorded which limit their effect on Myc regulation (Andrieu, Belkina, and Denis, 2016). Nonetheless, BET inhibitors might provide a valid therapeutic option in combination with other Myc-targeting compounds. Blocking Myc translation has been successfully achieved with the use of mTOR inhibitors however these have multiple other targets beyond Myc (Wiegering et al., 2015). Nevertheless, these are currently approved for clinical use. Inhibition of translation can also be achieved through inhibition of eIF4E-mediated cap-dependent Myc translation through direct inhibition of eIF4E with drugs like Silvestrol or indirect inhibition of ERK1/2-MNK1, mTORC1 (Whitfield, Beaulieu, and Soucek, 2017).

Since Myc is expressed so highly in cancers, with many becoming 'addicted', targeting this indirectly through **synthetic lethality** is highly valuable especially since it provides for a safer therapeutic strategy with possibly fewer side effects. Myc-mediated synthetic lethality was first taken advantage of through the use of TNF-related apoptosis-inducing ligand (TRAIL) Death Receptor (DR) 5 agonists to which Myc sensitizes cells (Wang et al., 2004). SUMOylation enzyme SAE1/2 also emerged as a potential target from Myc synthetic lethality screens. This enzyme is essential for proper mitotic spindle function and leads to cell death in Myc-driven cancers. Recent efforts to target SUMOylation enzymes might produce valid therapeutic options. Furthermore, pharmacological inhibition and ablation of CDK2 induces senescence in fibroblasts with deregulated Myc or B-cells with activated Myc (Campaner et al., 2010; Hydbring et al., 2010). Myc-driven tumours become addicted to certain metabolic pathways, thus several metabolic genes were shown to be synthetically lethal with Myc over-expression. These genes include some involved in glycolysis, nucleotide biosynthesis, purine synthesis, lipogenesis and mitochondrial transcription (Whitfield, Beaulieu, and Soucek, 2017) and inhibition of various metabolic targets of Myc reduced tumour growth and extended survival in Myc-dependent and -inducible models (Hsieh and Dang, 2016; Whitfield, Beaulieu, and Soucek, 2017). In an shRNA screen in a

p53-altered liver cancer model, Dauch et al. (2016) showed that AurkA plays a role in mediating Myc 'addiction' in this model by stabilising Myc and promoting cell cycle re-entry. The Lindon group recently described an AurkA PROTAC (PROteolysis TArgeting Chimera) which combines a known AurkA inhibitor linked to pomalidomide, a small molecule that binds E3 ligase Cereblon, to yield targeted degradation of the mitotic kinase (Wang et al., 2021). This could offer an alternative therapeutic option in the disease context described by Dauch et al. (2016).

Another increasingly popular strategy to inhibit Myc is to target regulators of its stability. As Myc stability will be covered in **section 1.2.2**, therapeutic targeting of Myc stability will also be covered there.

1.2 Post-translational modification of proteins and protein stability

The overall cellular pool of proteins, termed the proteome, requires strict regulation to guarantee correct and efficient cellular function. This regulation, termed proteostasis or protein homeostasis, is exerted and orchestrated on several levels whereby every process that contributes to the generation of functional proteins is subject to rigorous biological controls to produce a dynamic equilibrium in protein synthesis, folding, localisation, activity and degradation. Post-translational modifications (PTMs) occur following the biosynthesis of proteins and are covalent modifications key for overseeing most proteome-regulating processes. Indeed some are important in directing the protein to a specific cellular location. Many PTMs are involved in lipidation which directs proteins to organelle membranes. Others promote protein folding, like glycosylation and phosphorylation. Phosphorylation is the most common PTM and is essential for the transduction of many signals through modulating the activity of various proteins. Other modifications, such as ubiquitination, regulate overall levels of proteins in cells by promoting degradation. Overall, PTMs are essential for orchestrating many biological process and most are under tight coordination by enzymes that add or remove them to

1.2. Post-translational modification of proteins and protein stability

yield changes to specific pools of proteins or to the whole proteome, like cleavage of proteins by active caspases during apoptosis. PTMs can also affect the pattern of cellular gene expression through epigenetic modification of histone proteins and chromatin, modifying the physiology and lineage of the cell (Deribe, Pawson, and Dikic, 2010; Serrano-Gomez, Maziveyi, and Alahari, 2016).

Protein function is intrinsically linked to a protein's ability to assume certain stable three-dimensional conformations. Some proteins can spontaneously fold and assume such conformations in the cell, but others like Myc require binding to other proteins or molecular chaperones to assume the conformation optimal for their function. Based on their function, a protein's stability is regulated as a balance of synthesis, folding and degradation, and PTMs play a key role in this process. This balance allows cells to maintain the total protein amount, remove proteins that have fulfilled their function to avoid the rise of potentially harmful effects deriving from constitutive activity. For this reason, housekeeping proteins required for basic cellular function, such as Glyceraldehyde 3-phosphate dehydrogenase (GAPDH), are more stable and have longer half-lives. Other proteins, like those that regulate cellular proliferation, are less stable and their synthesis and degradation is timed to specific cell-cycle phases and mitogenic signals. Investigating protein stability is important for understanding healthy biological process and diseases that can arise from imbalance of such systems (Clausen et al., 2019; Hartl, Bracher, and Hayer-Hartl, 2011).

1.2.1 The Ubiquitin-Proteasome System

The Ubiquitin-proteasome system (UPS) is the main protein degradation machinery of the cell and is responsible for maintaining proteostasis in the context of cellular stresses like oxidative or xenobiotic stress, cellular differentiation, variation in nutrients supply and temperature (Lindquist and Kelly, 2011). Its discovery dates to the end of the 1970s with the identification of ubiquitin, E1-E3 enzymes and deubiquitinating enzymes (DUBs) (Ciechanover, Hod, and Hershko, 1978; Hershko, Ciechanover, and Rose, 1979;

Chapter 1. Introduction

Hershko et al., 1980). Ubiquitin is a 79-amino acid protein that is bound to proteins destined for degradation by ATP-dependent 26S proteasomes. Ubiquitination is established through covalent binding of the C-terminal glycine of the ubiquitin molecule usually to the ϵ amino groups of lysine residues on the target protein. Ubiquitin chains are then extended through the same process and can have different conformations based on the lysine residue on the ubiquitin molecule that other ubiquitins are attached to. This process is schematically represented in **Figure 1.5**.

The enzymes responsible for catalysing this reaction are the ubiquitin-activating enzyme E1 (1), which activates ubiquitin in an ATP-dependent manner (2) and transfers the activated ubiquitin to an E2 carrier enzyme (3), which in turn binds an E3 enzyme bound to a substrate protein (4), and transfers the ubiquitin onto the target substrate (5). Lysine-48 (K48) or K11 ubiquitin chains are recognised by the 26S proteasome for degradation, so several rounds of this process occur to establish a ubiquitin chain and induce protein degradation (6) (Nandi et al., 2006). Importantly, in order for substrates to be bound and efficiently degraded by the UPS they require a proteasome-binding tag, usually the ubiquitin chain, and an unstructured region. Indeed the 26S proteasome recognises the degradation signal in the form of the ubiquitin tag but the substrate engagement is done through binding of IDRs in the substrate which can be N- or C-terminal but also within the protein sequence itself (Tomita and Matouschek, 2019).

Substrate specificity is brought about by E3 ligases, often multi-protein complexes, of which humans are estimated to have more than 500 (Nandi et al., 2006). An example of a multi-subunit E3 ligase complex is the SCF (Skp1-Cullin-F-box) which relies on a multitude of substrate recognition domain-containing F-box subunits to target varying substrates with great specificity (Min and Lindon, 2012). Several F-box proteins target Myc proteins to alter its stability and function. There are several types of ubiquitin chains, with K48 linkages being the best characterised, which lead to protein degradation by the 26S proteasome. Other ubiquitin chains include K6, K11, K27, K29, K33, K63, Methionine-1 and have different functions. For example, upon inhibition of

1.2. Post-translational modification of proteins and protein stability

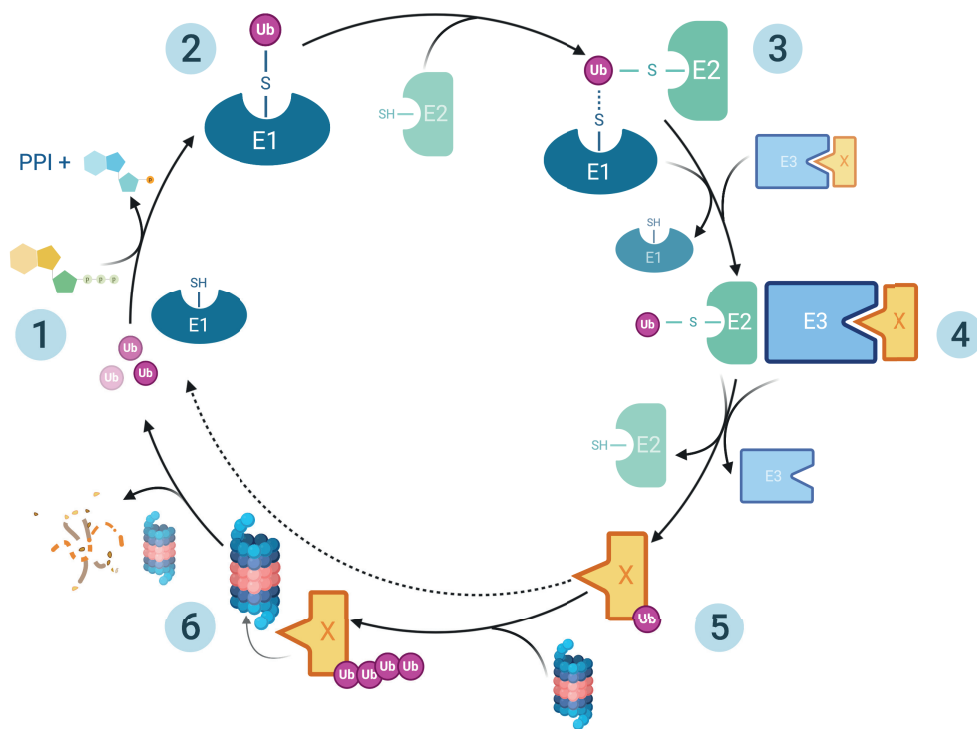


Figure 1.5: **The Ubiquitin-Proteasome System.** Degradation of proteins (exemplified by protein X in yellow) by the UPS is a multi-step process:

1. the reaction begins from a pool of free Ubiquitin (Ub), E1 ubiquitin activating enzymes and ATP;
2. in an ATP-dependent manner, an E1 enzyme activates a ubiquitin (Ub) molecule;
3. Ub is transferred onto an E2 carrier enzyme;
4. an E3 enzyme recognises protein X as substrate and brings it in proximity to an E2 enzyme with activated Ub;
5. the activate ubiquitin is transferred onto Protein X and the cycle repeats until a chain of Ub is formed on Protein X;
6. Protein X, tagged with a Ub chain is recognised by the 26S Proteasome (lid proteins in blue, core in pink), is unfolded and degraded yielding a pool of free Ub and amino acids to be used in other cycles of synthesis and degradation.

Chapter 1. Introduction

the proteasome, K6 chains do not increase suggesting that they have non-degradative roles. K63-linkages, the second-best studied types of chains have many non-degradative roles such as membrane trafficking and inflammatory signalling and NF- κ B activation. The chain composition is generally determined by the E2 ligase, for example, Ube2S, a component of the anaphase promoting complex (APC/C), is K11-specific (Min and Lindon, 2012; Swatek and Komander, 2016; Tomita and Matouschek, 2019). The best-studied process in which proteasomal degradation plays a key role is the cell cycle where ubiquitin-dependent 26S Proteasome-mediated destruction by the APC/C is essential for allowing successful sister chromatid separation and timely mitotic exit (Lindon, 2008; Lindon, Grant, and Min, 2015; Min and Lindon, 2012).

Finally, DUBs add another element of complexity as they remove ubiquitin molecules from substrates either impeding their degradation or fine-tuning the chain providing more chain specificity. Overall this highlights how the multitude of E3 ligases expressed and varying types of ubiquitin chains brings about specific and timed degradation of substrates.

1.2.2 Post-translational modifications regulate Myc protein's life cycle and activity

Myc is subject to several PTMs that not only regulate its stability but also its activity. The most important of these are phosphorylation, acetylation and ubiquitination. The first phosphorylation sites identified on Myc were within the PEST sequence and are the binding sites of casein kinase (CK2), however their role in the regulation of Myc has yet to be fully defined. Interestingly, CK2 also phosphorylates MAX, impeding its heterodimerization with Myc, homodimerization and DNA binding so it is possible that its effect on Myc also affects DNA and MAX binding.

The most important phosphorylated residues are Threonine-58 (T58) and Serine-62 (S62) within MBI. They play a key role in the life cycle of Myc, which is depicted in **Figure 1.6**, and S62 is involved in Myc stabilisation upon mitogen sensing and cell cycle re-entry when catalysed by ERK as part of the RAS/RAF/MAPK signalling

1.2. Post-translational modification of proteins and protein stability

pathway. These phosphorylations are interdependent as phosphorylated S62 (pS62) is a prerequisite for pT58 by GSK3 β . This “priming” phosphorylation interacts with a binding pocket of the kinase involved in substrate recognition. These phosphorylations occur at different time points during the cell cycle: upon mitogen sensing and cell cycle entry, the Ras/Raf/MAPK is activated and leads to Myc phosphorylation and stabilisation, as well as inhibition of GSK3 β by mediating the activation of the PI(3)K/Akt signalling pathway. This promotes early accumulation of pS62 Myc. Later in G1 phase, Akt activity declines leading to augmented GSK3 β activity, promoting the double-phosphorylated form of Myc and overall destabilising c-Myc and increasing its turnover. It is worth noting that the original reports of pS62 highlighted this PTM as stabilising for Myc upon cell cycle re-entry but these were conducted in a context of Myc adenoviral over-expression (Sears et al., 1999, 2000). Recent evidence has shown that multiple kinases phosphorylate Myc at S62 causing increased stability, supporting the original work. Myc stability is reduced by pharmacological inhibition of ERK (Hayes et al., 2016; Marampon, Ciccarelli, and Zani, 2006; Vaseva et al., 2018), and CDKs like CDK9 (Blake et al., 2019; Hashiguchi et al., 2019) and CAMKII (Gu et al., 2017), which all constitute possible avenues for indirect therapeutic inhibition of Myc.

The relevance of these PTMs in cancer is two-fold: firstly, activating Ras mutations often coincide with Myc amplification in cancer causing increased stabilisation of Myc through the promotion of in pS62 and inhibition of GSK3 β , leading to accumulation of Myc beyond its physiological threshold; secondly, T58 and surrounding amino acids are a mutation hotspot in many cancers such as Burkitt’s lymphoma (Bahram et al., 2000; Gregory and Hann, 2000) and *in vivo* the T58A mutation prevents T58 phosphorylation leading to inhibition of Myc ubiquitination and increased stability (Gregory, Qi, and Hann, 2003).

Following on from the double phosphorylation of pS62 and pT58, the life cycle continues onto a series of interactions that yield a single phosphorylated residue pT58 which is the phospho-degron motif recognised by the main E3 ligase of Myc, FBW7. As shown in step 4 of **Figure 1.6**, Pin1 catalyses the conformational change of S62-Proline

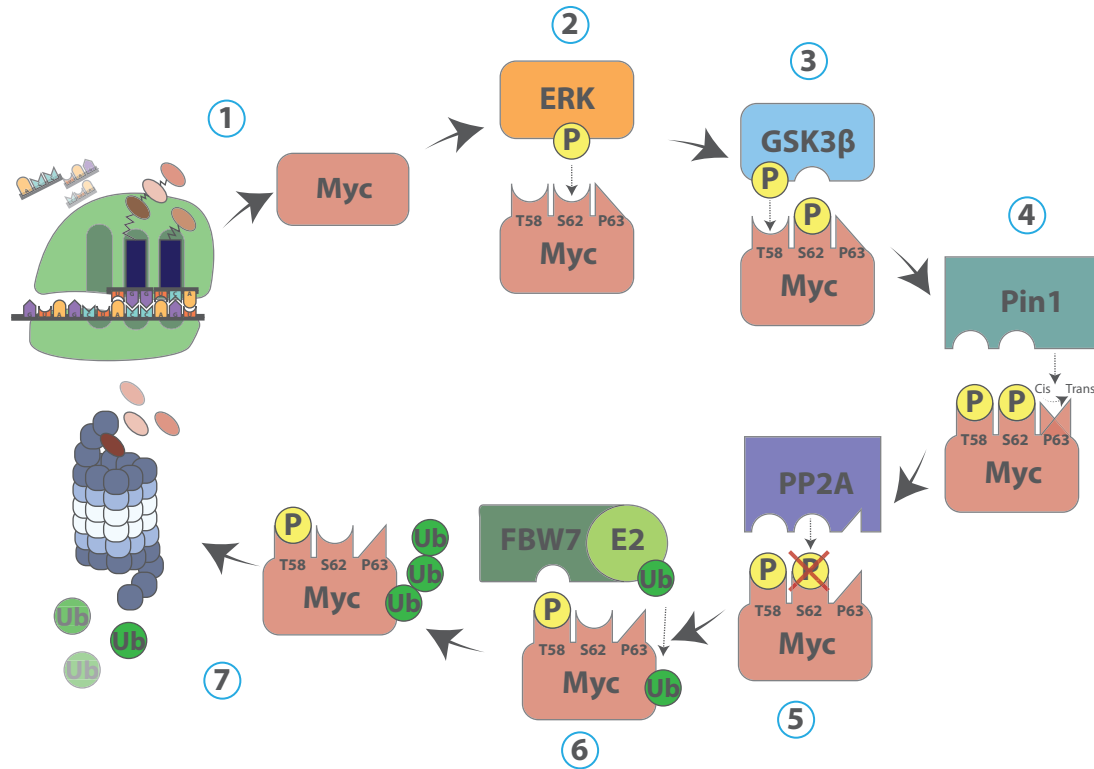


Figure 1.6: **Myc protein Life cycle.** The life cycle of Myc is a complex and tightly regulated process:

1. Myc is synthesised
2. extracellular signal-regulated kinases (ERK) phosphorylate Myc at Serine-62 (S62)
3. phospho-S62 Myc is primed for recognition and phosphorylation by Glycogen Synthase Kinase-3 β (GSK3 β) at Threonine-58(T58)
4. Peptidyl-prolyl cis-trans isomerase NIMA-interacting 1 (Pin1) mediates a conformational change of S62-P63 peptide bond from cis to trans
5. due to the conformational change of step 4, Protein Phosphatase 2A (PP2A) can bind more efficiently to Myc, dephosphorylating it at S62
6. Only the single phospho-T58 Myc is recognised by E3 ligase FBW7 which recruits an E2 to poly-ubiquitinated Myc
7. poly-ubiquitinated Myc is recognised by the proteasome for degradation

1.2. Post-translational modification of proteins and protein stability

63 (P63) peptide bond from *cis* to *trans*. This Cis-to-Trans change improves engagement of Myc by Protein Phosphatase 2A (PP2A), step 5. This phosphatase recognises a phosphorylated Threonine, Serine residues followed by a Proline and, if the peptidyl bond is in *trans* conformation its activity is greatly increased (Yeh et al., 2004). Interaction with PP2A yields a single phosphorylation at T58 which is recognised by FBW7, the F-box substrate-specificity component of the SCF ubiquitin ligase complex (step 6) (Welcker et al., 2004; Yada et al., 2004). This leads to recognition and degradation by the 26S proteasome. For their role in the Myc lifecycle, PP2A and PIN1 are appealing for pharmaceutical targeting in the form of activators and inhibitors respectively, to promote Myc degradation and bring about indirect inhibition of Myc by promoting its degradation (see **Figure 1.4**).

There are several E3 ligases that ubiquitinate Myc. FBW7 is recognised as the main E3 ligase responsible for Myc degradation and its E2 ligase has been recognised as being Cdc34 (Popov et al., 2010), and together they form K48 linkage chains on Myc, leading to its degradation and suppression of activity. USP28 and USP36 are two DUBs that oppose Myc ubiquitynation by different isoforms of FBW7 (Popov et al., 2007; Sun, Sears, and Dai, 2015; Sun et al., 2015). Pharmacological inhibition of DUBs that promote Myc stability is a potential therapeutic avenue (Wrigley et al., 2017). Notably, AurkA has been shown to protect N-Myc from FBW7-mediated degradation and inhibition of this interaction is being investigated as possible therapeutic approach, especially in neuroblastomas where the N-Myc-AurkA drives the disease (Brockmann et al., 2013; Otto et al., 2009; Richards et al., 2016). Since the pathway that leads to Myc degradation is frequently mutated in cancer, especially with either FBW7 being frequently mutated and unable to degrade Myc or with Myc levels being increased through mutations or protein-protein interactions that shield Myc from degradation by its main E3 ligase, a novel therapeutic approach that has gained some traction is that of PROTACs. These peptide or small-molecule compounds are an emerging drug class that targets proteins of interest (POIs) for degradation by the UPS by combining an entity that recruits an E3 ligase, a protein-binding element that recruits the POIs and a linker to tether the

Chapter 1. Introduction

two (Ottis and Crews, 2017; Raina et al., 2016; Toure and Crews, 2016). Since PROTACs only require binding to the POI, and lack the need for binding to an active site like most occupancy-driven pharmacological models, they are particularly appealing for drugging 'undruggable' proteins like Myc (**Figure 1.4**). This could allow re-purposing of compounds aimed at direct inhibition of the Myc protein that have previously failed during drug development for insufficient inhibition of activity. Another advantage to PROTACs is their ability to combine ADME profiles of small molecules and the benefits of knockdowns as they do not solely inhibit the POI, but deplete its pool within the cells. Finally, PROTACs are thought to have catalytic activity, whereby one PROTAC molecule could target multiple protein units within its intracellular life span. It is worth noting that in the context of neuroblastoma, PROTACs against Aurka, such as that described by Wang et al. (2021), could provide another therapeutic avenue.

Skp2 is another SCF E3 ligase that targets Myc for ubiquitination and has two binding sites on Myc, MBII and the bHLH-LZ domain (see **Figure 1.2**). Its effect on Myc is two-fold: it promotes its degradation but also acts as a co-activator (Kim et al., 2003; von der Lehr et al., 2003). The reason for this dual function is unclear but it has been suggested that a transcription-coupled proteasomal degradation mechanism is in place to ensure tight control of Myc activity. This is supported by the presence of proteasomal subunits along with Skp2 at Myc target sites (von der Lehr, Johansson, and Larsson, 2003; von der Lehr et al., 2003).

Several E3 ligases mediate non-proteolytic ubiquitination of Myc: β -TRCP, HectH9 and FBXO28. Popov et al. (2010) showed that β -TRCP, another E3 ligase of the SCF complex, binds Myc within residues 278 and 283 to promote lysine-independent ubiquitination of Myc. The E2 ligase that mediates this was shown to be UbcH5, which promotes formation of ubiquitin chains composed of K33, K48 and K63 chains. This E3 ligase was shown to antagonise FBW7 promoting differential ubiquitination of the N-terminus of Myc and stabilising it. Furthermore, this non-proteolytic ubiquitination of Myc is required for acceleration of cell cycle progression through S and G2 phases. Indirect targeting of β -TRCP by PI3K/mTOR Inhibitors is a novel option to promote

1.2. Post-translational modification of proteins and protein stability

Myc degradation (Yi et al., 2015).

Hect9 (also known as HUWE1) binds the TAD of Myc leading to generation of K63 ubiquitin chains at lysines proximal to the NLS. This allows recruitment of p300 of the p300-CBP co-activator family of Histone Acetylators (HAT), enhancing the transcriptional activity of Myc. Miz-1-bound Myc is not ubiquitinated by Hect9 and therefore has reduced transcriptional capacity (Adhikary et al., 2005). Inhibition of this E3 ligase reduced Myc-dependent transactivation in colorectal cancer through stabilisation of the inhibitory Myc-Miz1 complex (Peter et al., 2014). As previously mentioned, Myc interacts with many HATs such as CBP/p300 and GCN5 which not only are important in Myc-dependent transcriptional activation through their acetylation of histones, but also acetylate Myc itself and inhibit Myc ubiquitination resulting in overall stabilisation of Myc (Patel et al., 2004; Zhang, Faiola, and Martinez, 2005).

Overall all PTMs of Myc play a role in orchestrating Myc function and protein stability, which indeed go hand-in-hand. Phosphorylation is required for Myc ubiquitination by FBW7. Ubiquitination of Myc is important for its activation through recruitment of HATs which in turn oppose ubiquitin-dependent degradation of the transcription factor. The investigations into the “ubiquitin code” of Myc has led to the identification of the TAD region as essential in mediating both ubiquitin-mediated proteolysis and transcriptional activity. This search was extended to other transcription factors that also show an intimate overlap between activation domains and destruction elements, leading to the formulation of the “transcription factor licensing” model (Salghetti et al., 2000) which proposes that activation of some transcription factors is coupled to ubiquitination and degradation in an unexpected convergence of two very different processes to ensure efficient and specific fine-tuning of proteins that have extensive impact on the transcriptional pattern of the cell. For this reason, understanding PTMs and overall protein stability is an essential part of any investigation into a protein’s function.

1.2.3 Experimental tools to assess Protein Stability

Before describing how protein stability is assessed, it is important to define the term 'half-life', which is extensively used in the field of protein stability to indicate a protein's degradation rate and is the time it takes for a pool of protein to halve under unchanged synthesis rate. Half-lives of the components of the proteome are extremely varied, with some proteins possessing a short half-life of minutes, and others days or weeks. Additionally, the half-life and stability of most proteins is not constant but rather can fluctuate based on cell cycle stages or following circadian rhythms, or changes in response to extracellular stimuli (Eldeeb et al., 2019). Novel tools that monitor these variations in a spatiotemporal single-cell manner are emerging, allowing us to gain a deeper understanding of the regulation of protein dynamics in cells; perhaps offering novel assays and read-outs that are needed in the drug-discovery field to evaluate the efficacy of treatments aimed at changing a protein's stability.

1.2.3.1 Classical tools for measuring protein degradation

These tools described in this section constitute the most commonly used techniques to accurately evaluate protein stability in a population of cells. However, they require time-course experiments and do not offer information at the single-cell or subcellular levels.

The two main classical methods for assessing a protein's half-life in cultured cells are **Pulse-chase metabolic labelling** and **Cyclohexamide (CHX)-chase assays**. The first is divided in a pulse phase, where the cells are cultured for a determined amount of time with media containing a radioactive-labelled amino acid, such as ³⁵S labeled Cystine; and then a chase phase which consists of incubating those cells in media containing the same but unlabelled amino acid for different time intervals. Cells are collected at different timepoints, and following immunoprecipitation of the POI, the amount of radioactive amino acid at each time point is assessed to determine the rate of degradation. This technique can be coupled with mass spectrometry to allow for parallel analysis of multiple proteins (Khmelinskii et al., 2012). In the case of a

1.2. Post-translational modification of proteins and protein stability

long-lived protein, the amount of radioactive signal will not vary greatly between timepoints as any newly synthesised non-radioactive protein will not constitute much of the sample. On the other hand, if the protein is short-lived, the radioactive fraction of protein will progressively disappear from the sample as it is degraded and replaced by pools of non-radioactive protein. Whilst this technique allows accurate evaluation of endogenous or exogenous protein half-lives without interfering with any biological processes, there are some drawbacks to this technique. First of all, it is quite laborious and it requires the use of radioactive material which, due to health and safety concerns, is becoming less commonly available in laboratories. It also requires affinity reagents for isolation of the POI which are not always attainable, especially in the case of novel proteins (Eldeeb et al., 2019; Simon and Kornitzer, 2014).

CHX-chase is a less-laborious alternative to pulse-chase metabolic labelling that does not require the use of radioactive material. In this technique, the pulse phase consists of incubation with CHX, a global protein translation inhibitor that halts the process of translational elongation. Because translation is halted, the chase phase consists of collecting cells at different time points and measuring the levels of POI by western blotting at each interval to estimate the rate of decay. This is normalised to a control stable endogenous protein (such as GAPDH) to obtain the rate of degradation of the POI and its half-life, a control that is not available in the pulse-chase metabolic labelling assay. Although this assay, which will be used in this work, has largely replaced the metabolic labelling pulse-chase due to its simplicity and lack of radioactive procedures, it has some considerable pitfalls. Primarily, the main issue comes with the use of the CHX itself as blocking translation is not only cytotoxic, rendering this technique unreliable for study of long-lived proteins, but also is thought to have a negative impact on the biological systems in place to maintain homeostasis. Indeed, recent evidence suggests that components of the proteolytic apparatus of the cell are indeed short-lived proteins, which in a context of CHX would become unstable and therefore impede the degradation of the POI, resulting in an erroneous readout of stability of the latter (Eldeeb et al., 2019; Oh, Chen, and Varshavsky, 2017; Yewdell et al., 2011).

Chapter 1. Introduction

Another technique for measuring decay rates of proteins is the **ubiquitin-reference technique** which consists of transfecting cells with a plasmid containing a metabolically stable reference protein and the test protein separated by a ubiquitin moiety. When this is translated, ubiquitin hydrolases will mediate co-translational cleavage of the fusion after the last residue of ubiquitin. This will yield two separate proteins, the POI and the ubiquitin tagged protein of reference, at equimolar ratio. These proteins can then be immunoprecipitated and analysed by pulse-chase analysis. If a small tag, such as a FLAG or HA tag, is applied to the proteins, analysis by western blot would also be possible. Overall, this assay allows, through the normalization to the co-expressed reference protein, to account for the scattering of data in the conventional pulse-chase assay by compensating for differences in labelling efficiency and immunoprecipitation yields and other sample-to-sample variations.

Finally, the **promoter-reference technique** is similar to the ubiquitin-reference technique in that it allows monitoring of the level of the POI against that of a reference protein. In this system, the two proteins are co-expressed from two P_{TDH3} promoters which allow repression of both proteins by addition of tetracycline. The resulting transcribed mRNA will contain RNA aptamers in its 5' UTR (untranslated region) that fold in the presence of tetracycline preventing translational initiation. This system allows for a pulse-chase analysis where the pulse phase is created by addition of tetracycline and the chase phase by measuring the proteins at different time points followed by analysis by western blot if the proteins also contain small tags. Overall this technique offers two key advantages to traditional pulse-chase as it has an inbuilt stable reference protein and it also does not require the handling of radioactive materials or global translational inhibition as with the CHX-chase assay. Nevertheless the system is heterologous and does not allow for analysis of endogenous proteins. Furthermore, as it relies on over-expression, this might overwhelm the system in place to degrade the POI, affecting the read-out.

More recently, **mass spectrometry** has become the gold standard for assessing proteomic information such as identification of protein complexes, proteomic composition

1.2. Post-translational modification of proteins and protein stability

of a cell, and post-translational modification. Nonetheless, it is not optimal to assess short-lived or low-abundance proteins such as transcription factors that are tightly regulated on the proteomic level. Mass spectrometry is a biochemical technique that allows the discrimination of molecule based on their mass/charge ratio following ionisation of the sample. This technique is limited by different ionisation efficiencies of what is being measured. Metabolic labelling of proteins with stable-isotope amino acids has been used in combination with mass spectrometry to determine protein degradation kinetics. Much like the pulse-chase the population of metabolically labelled to unlabelled populations of the same protein can be quantified with great accuracy with mass spectrometry. Other labelling strategies have emerged to provide the ability of parallel quantification of multiple proteins in a sample. Tandem mass tag (TMT) mass spectrometry has allowed efficient tracking of protein level changes and has become a prominent tool in the study of protein degradation and the tool of choice in drug discovery to assay PROTAC activity (Eldeeb et al., 2019; Zhang and Elias, 2017). Recently, McShane et al. (2016) used a combination of pulse-chase labelling and quantitative mass spectrometry to characterise protein degradation kinetics in mammalian cells. They were able to show that proteins can be classed based on two degradation profiles: exponentially (ED) and non-exponentially degraded proteins (NED) and link this to the stoichiometry and roles of the proteins. The study proposes that more disordered proteins are ED whilst proteins with larger interaction interfaces within subunits are NED and thus degraded quickly within the first few hours of synthesis but then stabilised. Whilst this study highlights the high-throughput and complex data that these approaches can provide, it also notes the lack of information on proteins whose half-lives are shorter than an hour, like Myc, as a limitation of this technique.

All of these techniques, whilst mostly powerful and accurate in their estimation of protein degradation kinetics, have as main drawback their lack of single-cell resolution of protein kinetics and offer no information on sub-cellular localisation and regulation of the POI. They also are biased towards more stable or abundant proteins, excluding many tightly regulated proteins involved in signal transduction pathways such as transcriptional regulators. For this reasons many fluorescence and microscopy-based

Chapter 1. Introduction

assays have been developed to address cell-to-cell variability in protein regulation kinetics (Eldeeb et al., 2019; Zhang et al., 2019) and represent a better alternative for high-throughput screening of modifiers of protein stability, especially when the POI is a short-lived transcription factor like Myc.

1.2.3.2 Fluorescence-based assays to monitor protein stability

Several methods to allow the study of single-cell regulation of proteins have been developed and mostly make use of microscopy to also enable gathering of information on subcellular processing of proteins. The key advantage to fluorescent-based assays is that they do not require handling of radioactive labels or tampering with the cellular machinery as with CHX-chase assays. However, the major drawback to these techniques is the requirement for a tagged protein which may appear more stable as a consequence of the tag; and also either requires tagging of the endogenous protein, a time-consuming and difficult task, or only allows analysis of an exogenously expressed tagged POI.

Analogously to the pulse-chase assays, a **bleach-chase assay (Figure 1.7 A)** allows the evaluation of the half-life of a fluorophore (FP)-tagged POI where the pulse phase exploits the irreversible process of photo-bleaching by which a fluorophore is rendered non-fluorescent when exposed to a brief pulse of light. Following photo-bleaching the non-fluorescent population is no longer replenished and decays solely due to protein degradation kinetics. As this population may not constitute the total population of the bleached sample, the non-fluorescent component of the population is measured by subtracting the fluorescence of the bleached sample from that of the control unbleached sample. The chase phase consists in time lapse imaging to assess the replenishment of the fluorescent population in the bleached sample. The recovery time needed to replenish the fluorescent subpopulation of the bleached sample is indicated as α and it is also the rate of removal of the non-fluorescent population. In other words, the rate at which the non-fluorescent component is removed α is measured as the rate at which the bleached population recovers its fluorescence to a level comparable to that

1.2. Post-translational modification of proteins and protein stability

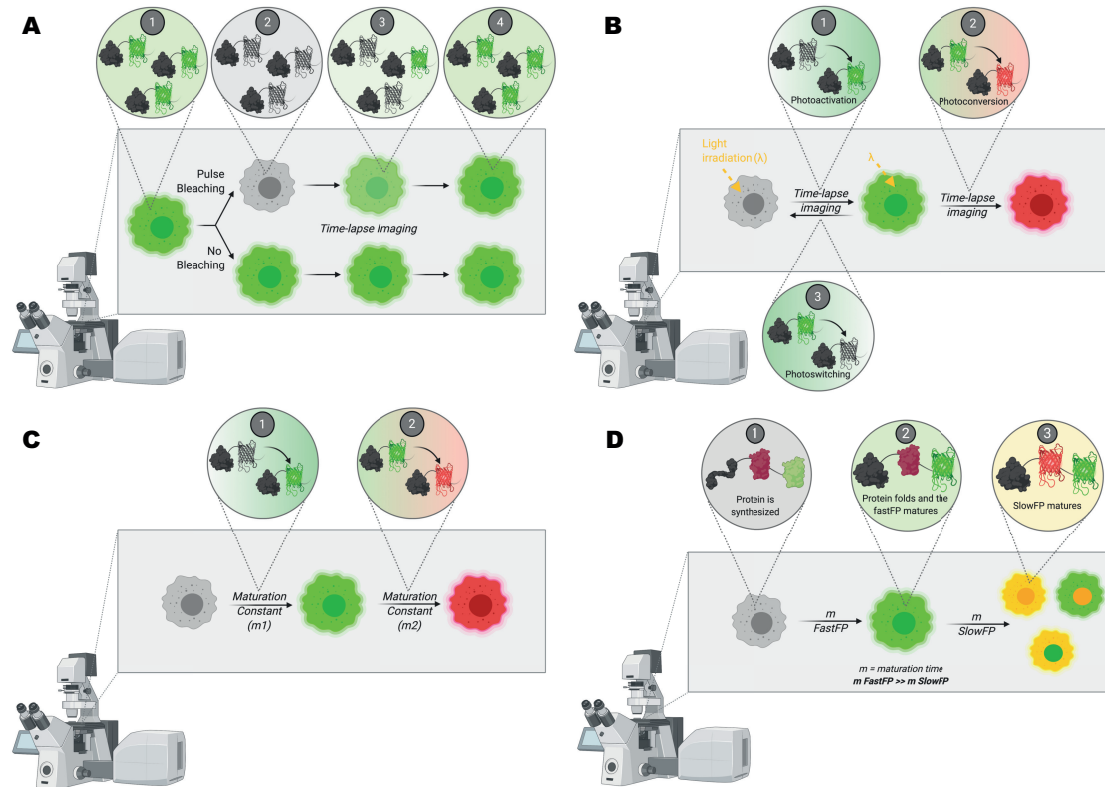


Figure 1.7: **Fluorescence-based assays to monitor protein stability.** There are several methods of assaying protein stability through live imaging microscopy that allow single-cell analysis:

- A **Bleach-Chase:** The POI is tagged with a single fluorophore (FP). After a pulse of light that photo-bleaches the FP, the sample is imaged in a time-lapse manner to estimate recovery of fluorescence and is compared to a non bleached sample;
- B **Photo-switchable FPs** allow through time-lapse microscopy to assess the protein stability of a single FP-tagged POI by measuring the fluorescent intensity of a fluorophore that
- C **Conventional fluorescent timers** consist of tagging the POI with a single fluorophore that changes its fluorescent properties according to distinct maturation times and as the protein matures, this method does not require time-lapse imaging as the ratio of the colours will determine the age of the pool of POI under steady state conditions of synthesis and degradation;
- D **tandem Fluorescent protein timers (tFTs)** are a system of the POI tagged with two fluorophores with distinct maturation times (m), whereby the difference in maturation time of the slow-foldingFP (slowFP) and fast-folding FP (FastFP) allows to assess both rate of synthesis and protein stability. This technique does not require time-lapse microscopy as the ratio of the intensity of the two FP will provide a readout for protein stability under steady-state conditions.

Chapter 1. Introduction

of an unbleached sample. In a semi-logarithmic plot, α is the slope of decay of the difference between the unbleached and bleached sample. This is then used to calculate the protein's degradation rate ($T_{1/2}$): $T_{1/2} = \ln(2)/\alpha$.

This elegant technique allows the exploitation of fluorescent timers to estimate degradation rates without the need to radio-label or causing interference with the cell's biological processes (Eden et al., 2011; Eldeeb et al., 2019).

Photo-switchable fluorophores (Figure 1.7 B) exploits the ability of some fluorescent proteins to modify their fluorescence by either acquiring, changing or losing their ability to fluoresce following experimental intervention. This assay is a fluorescence-based pulse-chase assay where the POI is tagged with a fluorophore. The pulse phase consists of light irradiation that causes photoactivation or photobleaching and the chase phase is monitoring of the fluorescence levels by time-lapse microscopy (Eldeeb et al., 2019). Specifically, the bleach chase assay exploits the irreversible effect of a brief pulse of light which renders a fluorophore non-fluorescent. This results in two differing subpopulation of fluorophore-tagged POI: fluorescent and non-fluorescent. The non-fluorescent proteins will be degraded in a POI-dependent manner. The difference in fluorescence intensity between a bleached and unbleached sample will provide a read-out for the non-fluorescent population. When this is followed through time, it is possible to extrapolate the decay rate for the non-fluorescent population and, therefore, for the POI (Eden et al., 2011). A few new labelling techniques that rely on a chemical reaction for the pulse phase have emerged. These are SNAP-Tag and CLIP-tag, which allow site-specific labelling with chemical probes. These tags function by tagging the POI with either an engineered form of O⁶-alkylguanine-DNA-alkyltransferase (AGT) that can be covalently labelled to O⁶-benzylguanine (BG) or O²-benzylcytosine (BC) derivatives (SNAP-Tag and CLIP-Tag respectively) containing a chemical probe (Cole, 2013; Gautier et al., 2008; Keppler et al., 2003). The two substrates can be used in parallel to simultaneously monitor two different POI when the chemical probe or dye differs between the two substrates. All these fluorescence-based pulse-chase assays provide multiple advantages to the classical pulse-chase metabolic assay. Mainly it provides information of subcellular protein kinetics in live cells and allows the analysis

1.2. Post-translational modification of proteins and protein stability

of single-cell data.

It is important to note that the fluorescence assays described above are pulse-chase assays in which the condition of the pulse and chase phases vary depending on the assay but nonetheless require temporal resolution in order to assess protein stability. This makes them suboptimal with regards to high-throughput screening of compounds that alter the POI's stability. The following assays are ratiometric and thus allow estimation of protein stability from a single snapshot analysis with time-lapse imaging not being required.

Conventional **Fluorescent timers** (**Figure 1.7 C**) rely on the ability of fragments of fluorescent proteins to change their colour by undergoing sequential chemical reactions, as the protein age increases. The ratio of the two colours provides a readout for protein stability with the advantage of making time-lapse imaging dispensable as a single snapshot is sufficient to evaluate the ratio. This proves advantageous when compared to photo-switchers or a protein tagged with a traditional fluorophore where the time resolution is key to assess the protein's stability. Importantly, the protein pool needs to be at steady state, whereby the rate of synthesis and degradation are constant, in order to correctly estimate the protein stability. These can be estimated theoretically by fitting the data to theoretical models where the fluorophores' maturation kinetics are previously evaluated (Eldeeb et al., 2019). A novel advancement to fluorescent timers was made by Khmelinskii et al. (2012) with the introduction of **tandem Fluorescent protein timers (tFTs)** in yeast (**Figure 1.7 D**). Instead of consisting of a single fluorophores, tFTs are a system composed of two fused distinct fluorophores constructed in tandem and possessing different maturation kinetics. The tandem consists of: a slow maturing fluorophore (slowFP, usually redFP), whose delayed folding time causes a lower-paced increase in intensity; a faster maturing fluorophore (fastFP, usually greenFP) with fast maturation time, immediate high intensity emission and whose signal plateaus at peak emission. Readout for the stability of the protein fused to the tFT system is a result of the different maturation times of the fluorophores. It is measured as the ratio of the slowFP emission signal to fastFP emission signal. For this reason the choice of

Chapter 1. Introduction

fluorophores in the tandem is key to be able to successfully measure changes in POI's stability and it is essential that the emission-excitation spectra of the two fluorophores do not overlap. The choice of fastFP depends on its maturation time, which should be as fast as possible to provide readout for protein localisation and abundance. It is also key that the slowFP is placed between the POI and the fastFP in order to ensure that if only fastFP fluorescence is detected it is because the POI has lower stability than slowFP maturation time and not because the slowFP has been cleaved from the construct.

In a follow up investigation, Khmelinskii et al. (2016) identified some limitations with the use of commonly adopted greenFPs within tFTs: these can be very stable and in part withstand proteasomal degradation leading to build-up of segments of fluorophore within the cell, thus affecting the tFT readout. In this work they report that mNeonGreen, which possesses similar molecular brightness to sfGFP under identical excitation wavelength, is a valid alternative to the latter in terms of proteasomal degradation in yeast. This was also confirmed to be true in mammalian cells by a member of the Lindon lab. The choice of slowFP should be based on the half-life of the POI, specifically, the maturation time of the slowFP should be greater than the protein's half-life to allow a wider range of ratio, but it should not be too much greater as this would result in a POI-tFT that would never reach maturation of the slowFP. This is the technique that will be used in this study to assess Myc stability. Beyond the use in yeast, tFTs have also been used in zebrafish to investigate a protein turnover in embryos (Barry et al., 2016; Donà et al., 2013); in plants to test the effect of mutations on protein stability (Zhang et al., 2019); in mammalian cells to explore cell-cycle dependent degradation rates (Alber et al., 2018).

A final fluorescence-based assay was introduced by Vaseva et al. (2018) for investigating Myc stability and further used in work by Blake et al. (2019) as part of a Myc degradation screen. Their system consists of the two fluorophores DsRed and (enhanced green fluorescent protein) EGFP fused to the N-terminus of Myc, expressed under a CMV promoter and separated by an internal ribosome entry site (IRES) so

1.2. Post-translational modification of proteins and protein stability

that both proteins arise from the same transcript. This allows the normalisation of the green EGFP intensity to that of DsRed, thus accounting for fluctuations in transcription. Changes in EGFP-Myc signal in a context of no changes in DsRed is due to changes in Myc protein stability. This system was then stably transfected in a *KRAS*-mutant line to be used for drug screening purposes by fluorescence-activated cell sorting (FACS). The limitation of this assay was the increased stability of EGFP-Myc when compared to WT in the same cells but the hits, compounds that destabilised Myc, that resulted from the screen had even stronger destabilising effects on endogenous Myc in multiple cell lines. Another drawback of this study is the inappropriate localisation of the DsRed that would have made this study hard to conduct on a microscopy-based setting.

Altogether, these techniques show that there are advantages to using single-cell fluorescent assays when assessing protein stability. The Lindon lab has previously worked to optimise the use of tFTs in mammalian cells to investigate the stability of mitotic kinases like Aurora A and B and test the assay as a screening tool that allows direct evaluation of the effects of PROTAC compounds on their stability (Richard Wang's Thesis). These proteins have a half-life of several hours outside of mitosis, so to further challenge the tFT system, this work looks at the short-lived transcription factor Myc. As published in Blake et al. (2019) during the course of this thesis, there is a need to develop high-throughput assays for drug screening of modifiers of Myc stability as this therapeutic strategy is becoming more and more promising and relevant. The use of tFTs for this purpose is ideal as they offer a microscopy-based alternative to the work previously published with the further advantage that they allow concomitant gathering of information on synthesis and stability of Myc over time.

1.3 Aims and objectives

As stated above, the principal aim of this body of work was to harness tFTs to develop a microscopy-based assay for Myc stability, generating an assay that possessed all the advantages of fluorescent-based techniques and yielding a tool that could be used in high-throughput screening for modulators of Myc stability. To achieve this several objectives are outlined hereafter and in **Figure 1.8**:

1. Generation a suitable Myc-tFT
 - (a) Design of Myc-tFT construct and generation of a stable cell line expressing it
 - (b) Verification of tFT's ability to report on Myc stability
 - (c) Confirmation that Myc-tFT was subject to the same post-translational processing as endogenous Myc
 - (d) Investigation into the functionality of Myc-tFT
2. Employment of Myc-tFT in a medium-throughput drug screen
 - (a) Optimisation of assay conditions
 - (b) Dose-response of known modifiers of Myc stability
 - (c) Single-dose screening of known modifiers of Myc stability

The use of the Myc-tFT for drug screening purposes was hindered by great cell-to-cell variability in the Myc-tFT ratio.
3. Understanding the origin of the variability in single-cell Myc-tFT readout
 - (a) Time-lapse investigation into Myc-tFT variability
4. Study of the molecular basis for Myc-tFT oscillation through time

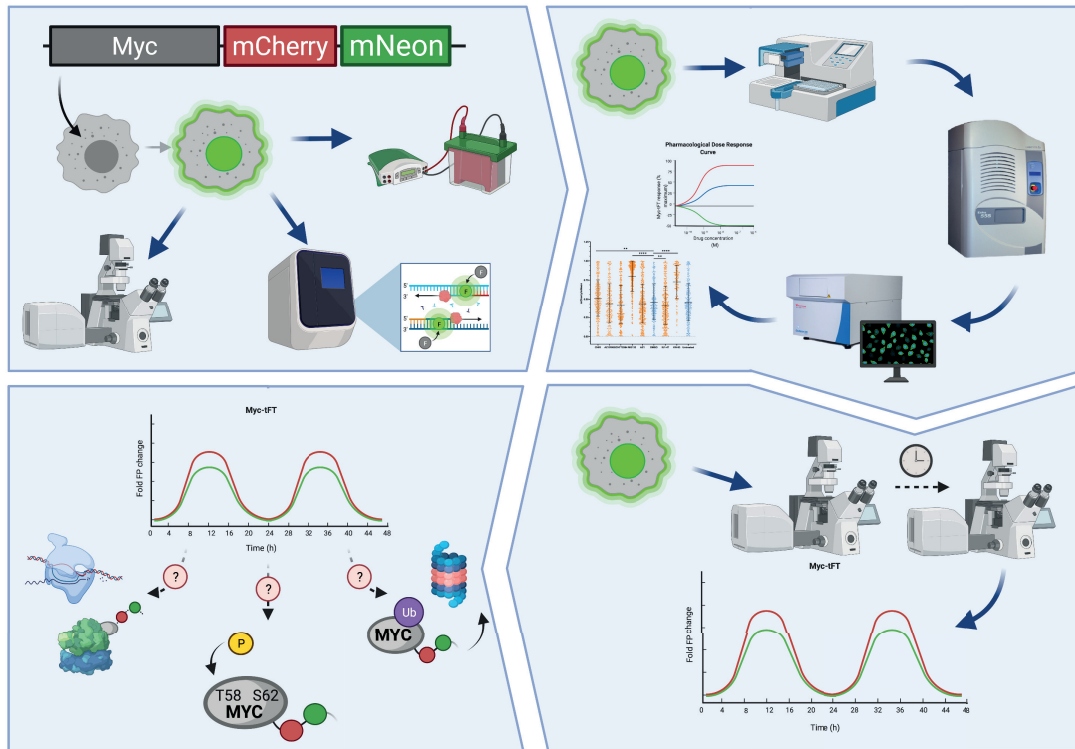


Figure 1.8: **Aims of this work.** Graphical representation of the aims of this work:

1. Design and validation of the Myc-tFT construct
2. Employment of the Myc-tFT cell line for medium-throughput a drug screen (at industrial partner AstraZeneca)
3. Investigation into the evolution of Myc-tFT signal though time
4. Elucidation of the molecular basis for the oscillations observed in (3)

Chapter 2

Materials and Methods

2.1 Materials

This chapter lists the materials and protocols of methods employed to undertake this study.

2.1.1 Molecular biology reagents

2.1.1.1 Cloning reagents

In this section the list of plasmids (**Table 2.1**), primers (**Table 2.2**), enzymes (**Table 2.3**) and reagents (**Table 2.4**) used to generate the tFT constructs are listed. Cloning strategies and techniques can be found in **Section 2.2.1.1**.

Chapter 2. Materials and Methods

Plasmid	Source	Details
pcDNA5-mRuby	Lindon Group	pcDNA5 backbone vector carrying mRuby
pcDNA5 FRT/TO mCherry-mNeonGreen	Prof. Michael Knop, ZMBH, University of Heidelberg	pcDNA5 with FRT site for Flp-In™ T-Rex™ (ThermoFisher Scientific) carrying mCherry-mNeonGreen and conferring Hygromycin resistance
pcDNA3-HA-hMYCN	Martine Roussel (Addgene 74163)	pcDNA3 vector carrying HA-tagged human nMyc
pBABE-hcMYC	Dr. Heike Laman, University of Cambridge	pBABE vector carrying human cMyc
pcDNA5 FRT/TO Myc-mCherry-mNeonGreen	Lindon Group, created by Camilla Ascanelli	pcDNA5 with FRT site for Flp-In™ T-Rex™ (ThermoFisher Scientific) carrying Myc tagged at its C-terminus with mCherry-mNeonGreen and conferring Hygromycin resistance
pcDNA5 FRT/TO nMyc mCherry-mNeonGreen	Lindon Group, created by Camilla Ascanelli	pcDNA5 with FRT site for Flp-In™ T-Rex™ (ThermoFisher Scientific) carrying nMyc tagged at its C-terminus with mCherry-mNeonGreen and conferring Hygromycin resistance
pcDNA5 FRT/TO Myc T58A-mCherry-mNeonGreen	Lindon Group, created by Camilla Ascanelli	pcDNA5 with FRT site for Flp-In™ T-Rex™ (ThermoFisher Scientific) carrying mutant (T58A) Myc tagged at its C-terminus with mCherry-mNeonGreen and conferring Hygromycin resistance
pcDNA5 AurKA-mRuby-mNeonGreen	Lindon Group, created by Richard Wang and Camilla Ascanelli	pcDNA5 with FRT site for Flp-In™ T-Rex™ (ThermoFisher Scientific) carrying mutant (T58A) AurKA tagged at its C-terminus with mCherry-mNeonGreen and conferring Hygromycin resistance. A BamHI site between fluorophores was removed.
pcDNA5 FRT/TO Myc-mRuby-mNeonGreen	Lindon Group, created by Camilla Ascanelli	pcDNA5 with FRT site for Flp-In™ T-Rex™ (ThermoFisher Scientific) carrying mutant (T58A) Myc tagged at its C-terminus with mRuby-mNeonGreen and conferring Hygromycin resistance

Table 2.1: Plasmids used in this study.

2.1. Materials

Oligo Name	Purpose	5'-3' Sequence
CA01-F	cMYC cDNA from ATG – cloning into tFT constructs. Contains KpnI tail	TCGACGGTACCATGCCCCCAACGTTAGCTTC
CA02-R	cMYC cDNA end (no Stop codon) – cloning into tFT constructs. Contains BamHI tail	CTGCGGATCCGCACAAGAGTTCCGTAGCT
CA03-F	MYC cDNA from ATG - Sequencing	ATGCCCCCAACGTTAGCTTC
CA04-R	MYC cDNA end (no Stop codon) – Sequencing	CGCACAAGAGTTCCGTAGCT
CA05-F	Primer mid MYC sequence F – Sequencing	CGTCTCGGATCTCTGCTC
CA06-R	Primer mid MYC sequence R – Sequencing	GAGCAGAGAATCCGAGGACG
CA07-F	nMYC cDNA from ATG - cloning into tFT constructs. Contains HindIII tail.	TGCACAAGCTTATGCCGAGCTGCTCCACGTC
CA08-R	nMYC cDNA end (no Stop codon) - cloning into tFT constructs. Contains KpnI tail	TCGACGGTACCCCGCAAGTCCGAGCGTGTCAATT T
CA20-F	Mutagenesis T58A Myc	GCCCCGCCCTGTCCCCTA
CA21-R	Mutagenesis T58A Myc	GGGAGCAGCTCGAATTTCTTC
Upstream BamHI-F	Amplification of CMV to mRuby region of pcDNA5-mRuby	CGTGTACGGTGGGAGGTCTATA
Upstream BamHI-R	Amplification of CMV to mRuby region of pcDNA5-mRuby. This primer contains a mutation to eliminate the BamHI site that follows mRuby	ATATCTGCGGAACCACCAGC
Downstream BamHI-F	Amplification of region of following mRuby in pcDNA5-mRuby. This primer contains a mutation to eliminate the BamHI site that follows mRuby	GCTGGTGGTCCGCAGATAT
Downstream BamHI-R	Amplification of region of following mRuby in pcDNA5-mRuby.	TTCCGCCTCAGAAGCCATA
mRuby-F	Amplification of mRuby sequence. Contains an FseI tail for cloning into pcDNA5 AurKA-mRuby-mNeonGreen	GAAGTAGGTCGACGGCCGCCACCATGAACAGCC TGATCAAAGAA
mRuby-R	Amplification of mRuby sequence. Contains an AgeI tail for cloning into pcDNA5 AurKA-mRuby-mNeonGreen	TAGCTCCTGCACCGGTAGAATTCACCACACTGGA CTAGT

Table 2.2: **Primers used in this study.** All primers were ordered from Sigma Aldrich.

Chapter 2. Materials and Methods

Enzyme	Supplier and catalogue number
AgeI-HF	NEB (R3552)
Alkaline Phosphatase (CIP)	NEB (M0290)
BamHI-HF	NEB (R3136)
DpnI	NEB (R0176)
FseI	NEB (R0588)
HindIII-HF	NEB (R3104)
KpnI-HF	NEB (R314)
Q5 High-Fidelity DNA Polymerase	NEB (M0491)
T4 DNA Ligase	NEB (M0202)
T4 Polynucleotide Kinase	ThermoFisher (EK0031)

Table 2.3: **Enzymes used in this study.** most enzymes are from New England Biolabs (NEB).

Reagent / Material	Supplier and catalogue number
NEB® 5-alpha Competent E coli (High Efficiency)	NEB (C29871)
LB agar, Miller microbiologically tested	Sigma (L3027-250G)
Fisher Bioreagents™ LB Broth, High Salt, Granulated	Fisher Bioreagents™ (12801660)
Bacterial plates	BD Biosciences (351029)
Ampicillin sodium salt	FisherScientific (10419313)
Midori Green Advance DNA Stain	Geneflow (S6-0022)
Hi-Res Standard Molecular Biology Grade Agarose	Geneflow (A4-0700)
Quick load Purple 1kb ladder	NEB (N0552S)
Monarch® DNA Gel Extraction Kit	NEB (T1020S)
Monarch® PCR DNA Cleanup Kit	NEB (T1030)
Monarch® Gel Extraction Kit	NEB (T1020)
GeneRuler 100 bp Plus DNA Ladder	ThermoFisher (SM0321)
1 kb DNA ladder	NEB (N3232)
QIAGEN Plasmid Midi Kit	Qiagen (12145)
QIAprep Spin Miniprep Kit	Qiagen (27104)

Table 2.4: **Reagents employed for cloning in this study.**

2.1.1.2 Immunoblotting and Immunofluorescence

The equipment required for immunoblotting and Immunofluorescence experiments are listed in **Table 2.5**, and the antibodies utilised in **Tables 2.6 and 2.7**.

Reagent / Material	Supplier and catalogue number
96well plates	Starstedt (83.3924)
Bovine serum albumin (BSA)	Sigma (A9647)
Bovine serum albumin (BSA) Standard Ampules, 2 mg / mL	ThermoFisher (23209)
Bio-Rad Protein Assay Dye Reagent Concentrate	Bio-Rad 5000006
CLARIOstar® Plus plate reader	BGM Labtech
cOmplete™ EDTA-free protease inhibitor cocktail	Roche (11836170001)
Dithiothreitol (DTT)	Sigma (10197777001)
Duolink® In Situ Mounting Medium with DAPI	Sigma (DUO82040)
Ethanol (EtOH)	Sigma (32221)
Filter paper (8cm X 13.5cm)	ThermoFisher (84784)
Glass cover slips	Academy (400-02-16)
Hydrochloric acid (HCl) 1.16 (32%)	Fisher Chemicals (H/1050/P1317)
Immobilon Western® chemiluminescent HRP substrate	Millipore (WBKLS0100)
Immobilon-FL PVDF membrane	Millipore (IPFL00010)
Methanol	Sigma (32213)
NOVEX® Sharp Pre-stained ladder	ThermoFisher (LC5800)
NuPage® LDS Sample buffer (4X)	ThermoFisher (NP0007)
NuPage® MOPS SDS Running Buffer (4X)	ThermoFisher (NP0001)
NuPAGE® Novex® 4-12% Bis-Tris Protein Gels (10, 12, 15 well)	ThermoFisher (NP0321, NP0322, NP036)
1-STEP Transfer Buffer	ThermoFisher (84731)
PageRuler Pre-stained ladder	ThermoFisher (26616)
Pierce™ G2 Fast Blotter	ThermoFisher (62288)
PhosSTOP™ phosphatase inhibitor	Roche (4906845001)
Sodium dodecyl sulphate (SDS)	FisherScientific (S/P530/53)
SuperFrost microscope slides	VWR (631-0912)
Tris-HCl	FisherScientific (BP1757)
Triton X-100	Prolabo (28 817 .295)
Tween® 20	Sigma (P1379)

Table 2.5: List of Materials and reagents required for Protein electrophoresis, immunoblot, and immunofluorescence.

Chapter 2. Materials and Methods

Antibody Target	Supplier and catalogue number	Species	Working dilution
BrdU	Abcam (ab6326)	Rat monoclonal IgG [BU1/75 (ICR1)]	IF 1:200
BMAL1	Abcam (ab3350)	Rabbit polyclonal IgG	IB 1:200
c-Myc (D84C12)	CST (5605)	Rabbit monoclonal IgG	IB 1:1000
c-Myc (phospho T58)	Abcam (ab185655)	Rabbit monoclonal IgG [EPR17923]	IB 1:1000
GAPDH	Cell Signalling Technology (14C10)	Rabbit monoclonal IgG	IB 1:3000 – 1:4000
GAPDH	Proteintech (6004-1-Ig)	Mouse monoclonal IgG	IB 1:3000 – 1:4000
mCherry	Abcam (ab167453)	Rabbit polyclonal IgG	IB 1:1000

Table 2.6: **List of Primary Antibodies.** All antibodies needed for this study are listed along with supplier, catalogue number, technique and working dilution specifications.

Antibody	Supplier and catalogue number	Species	Working dilution
Anti-rabbit HRP linked	Dako (P0448)	Goat IgG IB	IB 1:5000
IRDye® 680RD anti-rabbit	Li-Cor (926-68071)	Goat IgG	IB 1:20,000
IRDye® 800RD anti-mouse	Li-Cor (926-32210)	Goat IgG	IB 1:10,000
Cy3™ conjugated AffiniPure F (ab') ₂ Anti-Rat	Jackson ImmunoResearch Laboratories (112-166-072)	Goat Anti-Rat IgG	IF 1:400

Table 2.7: **List of Secondary Antibodies.** All antibodies needed for this study are listed along with supplier, catalogue number, technique and working dilution specifications.

2.1.1.3 Chromatin immunoprecipitation

Chromatin Immunoprecipitation (ChIP) was carried out by utilising the SimpleChIP[®] Plus Enzymatic Chromatin IP Kit (with magnetic beads) by Cell Signaling Technologies (CST). Full details of the materials and reagents included and supplementary to the kit can be found in **Table 2.8**.

Reagent/Material	Supplier and catalogue number
Buffer A (4x)	7006
Buffer B (4x)	7007
c-Myc Rabbit Antibody	9402
ChIP Buffer (10x)	7008
ChIP Elution Buffer (2x)	7009
ChIP-Grate Protein G Magnetic Beads	9006
DNA Binding Buffer	1007
DNA Elution Buffer	1009
DNA Purification Columns	10010
DNA Wash Buffer	1008
DTT (Dithiothreitol)	7016
DYNAL [™] /DynaMag [™] Magnetic separation rack	ThermoFisher (12320D)
EDTA 0.5M	7011
Formaldehyde Solution, ACS reagent, 37%	Sigma Aldrich (252549)
Glycine Solution (10x)	7005
Histone H3 (D2D12) XP Rabbit mAb (ChIP Formulated)	406020
Micrococcal Nuclease	10011
NaCl 5M	7010
Normal Rabbit IgG	2729
Protease Inhibitor Cocktail (200x)	7012
Proteinase K (20mg/mL)	10012
RNase A (10mg/mL)	7013
Soniprep 150	MSE

Table 2.8: **Materials for Chromatin Immunoprecipitation**. If supplier is not stated, the material belongs to the SimpleChIP[®] Plus Enzymatic Chromatin IP Kit by Cell Signaling Technologies (CST)

Chapter 2. Materials and Methods

qPCR following ChIP was carried out using SimpleChIP® Universal qPCR Master Mix according to manufacturer instructions with the materials details in **Table 2.9** and with the primers listed in **Table 2.10**.

Reagent/Material	Supplier and catalogue number
SimpleChIP Universal qPCR Master Mix	Cell Signalling Technologies (88989)
UltraPure DNase/RNase-Free Distilled Water	Thermo Fisher Scientific (10977035)
StepOne™ Real-Time PCR System	Applied Biosystems™ (4376357)
MicroAmp™ Fast Optical 96-Well Reaction Plate with Barcode, 0.1 ml	Thermo Fisher Scientific (4346906)
MicroAmp™ Optical Adhesive Film	Thermo Fisher Scientific (4360954)

Table 2.9: **Materials employed for qPCR analysis of ChIP products.**

Oligo Name	Purpose	5'-3' Sequence
CA48-F	ChIP qPCR – hCAD	CTTCCCGCTTCTCCGTACTC
CA49-R	ChIP qPCR – hCAD	CTTGCTTACCCACTTCCCGG
CA16-F	ChIP qPCR – CMV	ATAGCGGTTTGACTCACGG
CA17-R	ChIP qPCR – CMV	GGCGGAGTTGTTACGACATT
SimpleChIP hRPL30 Exon 3 Primers 1	ChIP	N/A: from Cell Signalling Technologies (CST) SimpleChIP® Human RPL30 Exon 3 Primers #7014

Table 2.10: **List and sequences of Primers used for qPCR of ChIP Products.** hCAD primers were designed on the human CAD transcriptional start site, and the CMV primers on the CMV sequence in the Myc-tFT plasmid, using Primer3Plus (Untergasser et al., 2012).

2.1.1.4 mRNA extraction and quantification

Reagent / Material	Supplier and catalogue number
CFX Opus 384 Real-Time PCR System	BioRad (12011452)
Hard-Shell PCR plates, 384-well, thin wall.	BioRad (HSP3805)
Luna Universal One-Step RT-qPCR Kit	NEB (E3005S)
Microseal ® 'B' seal Seals	BioRad (MSB1001)
NanoDrop™ Lite Spectrophotometer	Thermo Fisher (ND-LITE-PR)
Monarch® Total RNA Miniprep Kit	NEB (T2010S)
RNaseZap	Sigma Aldrich (R2020)

Table 2.11: Reagents for mRNA extraction and quantification utilised in this work.

Oligo Name	Source	5'-3' Sequence
hActin-F	Dr. Catherine Wilson	CATGTACGTTGCTATCCAGGC
hActin-R		CTCCTTAATGTCACGCACGAT
hPER2-F	Altman, Brian J. et al. 2015, Cell Metabolism, Volume 22, Issue 6, 1009 - 1019	GGATGCCCCGCCAGAGTCCAGAT
hPER2-R		TGTCCACTTTCGAAGACTGGTCGC
mCherry-F	Roberta Cacioppo, Lindon Lab	CCGACATCCCCGACTACTTGAAGC
mCherry-R		CACCTTGTAGATGAACTCGCCGTCC

Table 2.12: Primers for mRNA quantification of target genes.

Chapter 2. Materials and Methods

2.1.2 Mammalian cell culture growth media

The following cell lines were generated and/or employed for this study:

Cell line	Source	Details
HeLa FRT/TO (Flp-In™)	Professor Jonathon Pines, ICR London	HeLa line with an integrated FRT site for Flp- In™ T-Rex™ (ThermoFisher Scientific) tetracycline-inducible expression of a gene of interest
U2OS FRT/TO (Flp-In™)	Dr. Adrian Saurin, University of Dundee	U2OS line with an integrated FRT site for Flp- In™ T-Rex™ (ThermoFisher Scientific) tetracycline-inducible expression of a gene of interest
U2OS FRT/TO Myc-mCherry-mNeonGreen (tFT)	Lindon Group, created by Camilla Ascanelli	Expresses Myc-mCherry-mNeonGreen under a tetracycline-inducible CMV promoter that is selected for with hygromycin
U2OS FRT/TO Myc T58A-mCherry-mNeonGreen (tFT)	Lindon Group, created by Camilla Ascanelli	Expresses mutant (T58A) Myc-mCherry-mNeonGreen under a tetracycline-inducible CMV promoter that is selected for with hygromycin
U2OS FRT/TO mCherry-mNeonGreen (tFT)	Lindon Group, created by Camilla Ascanelli	Expresses mCherry-mNeonGreen under a tetracycline-inducible CMV promoter that is selected for with hygromycin
A549	Dr. Catherine Wilson, University of Cambridge	Lung carcinoma line

Table 2.13: **Cell lines employed in this study.** List and details of cell lines used for this work.

The materials required for cell culture are as follows:

For transfection of mammalian cells, the following reagents and materials were used:

2.1. Materials

Reagent / Material	Supplier and catalogue number
10 cm tissue culture plate	Nunc (150350)
6-well tissue culture plate	Nunc (140675)
8 -well chamber slide	Ibidi (IB-80826)
Antibiotic antimycotic solution (100x)	Merk Life Science (A5955)
Cell scraper	Greiner Bio-One (541070)
Dulbecco's modified Eagle's medium (DMEM)	Gibco (41966-029)
Foetal bovine serum (FBS)	Sigma (F9665)
Hygromycin B	Sigma (H0654)
L-Glutamine	Sigma (G7513)
Leibovitz's L-15 (no phenol red)	Gibco (21083-027)
Phosphate-buffered saline	Severn Biotech (207410)
Roswell Park Memorial Institute (RPMI) 1640 Medium	Gibco (31870-025)
Trypsin EDTA 10X	PAA laboratories (L11-001)

Table 2.14: **Materials utilised for maintenance of mammalian cells in culture.**

Reagent / Material	Supplier and catalogue number
Hanks buffered saline solution (HBSS) with calcium, magnesium, and no Phenol Red	Invitrogen (14025-050)
Lipofectamine 3000	Invitrogen (L3000-008)
Neon™ Transfection system	ThermoFisher Scientific (MPK5000)
Neon™ Transfection system Electrolytic Buffer E2	ThermoFisher Scientific (MPK10025E)
Neon™ Transfection system 100uL	ThermoFisher Scientific (MPK10025)
Neon™ Transfection system pipette	ThermoFisher Scientific (MPP100)
Neon™ Transfection Tubes	ThermoFisher Scientific (MPT100)
OptimemI (1x)	Gibco (31985-062)

Table 2.15: **Materials required for mammalian cell transfection via Lipofectamine and electroporation.**

Chapter 2. Materials and Methods

2.1.3 Small molecule compounds

Compound Name	Target/Function	Supplier (Catalogue number)
AZ1	USP25/28 inhibitor	AstraZeneca
AZ ERK inhibitor	ERK1/2 inhibitor	AstraZeneca
Bromodeoxyuridine (BrdU)	Thymidine analogue	Sigma Aldrich (B9285)
CHIR 99021	GSK3 β inhibitor	AstraZeneca
Cycloheximide	Inhibitor of translocation during translation	Life technologies (01810-1G)
Dexamethasone	Glucocorticoid (circadian rhythm synchronisation)	Tocris Bioscience (1126/100)
Dimethyl Sulfoxide (DMSO)	Vehicle	ChemCruz (sc-358801)
Doxycycline hydrochloride (DOX)	Tetracycline repressor (induction of tFT constructs)	Sigma (D3447)
IU1-47	USP14 inhibitor	AstraZeneca
KN-93	CAMKII inhibitor	AstraZeneca
MG132	Proteasome inhibitor	Alfa Aesar (J63250)
RO-3306	CDK1 inhibitor (G2 arrest)	Tocris Bioscience (4181/10)
SCH772984	ERK1/2 inhibitor	AstraZeneca
Thymidine	DNA replication (S-phase arrest)	Sigma (T1895)
TORin-1	mTOR inhibitor	Strattech (A8312)

Table 2.16: **Small molecule compounds used in this study, their targets and function, and supplier.** Where AstraZeneca is stated as the supplier, it indicates that they supplied the compounds from their own compound library.

2.1.4 Software used

Software	Reference/Source
Adobe Illustrator	Adobe Inc. https://adobe.com/products/illustrator
Adobe Photoshop	Adobe Inc. https://adobe.com/products/photoshop
BioRender	www.biorender.com
Excel	Microsoft Corporation https://office.microsoft.com/excel
Fiji	(Schindelin et al., 2012) https://imagej.net/Fiji
Image Studio™ Lite	LI-COR Biosciences https://www.licor.com/bio/image-studio-lite/
Micro-Manager	(Edelstein et. Al 2014) https://micro-manager.org
Prism 9.3.1	GraphPad Software www.graphpad.com

Table 2.17: **Software used in this work.**

2.2 Methods

2.2.1 Molecular Biology Techniques

2.2.1.1 Plasmid Generation and Cloning

The following steps were undertaken to generate the plasmids described in this work. The overarching cloning strategy and resulting plasmids maps are depicted in **Chapter 3.2.2**.

2.2.1.1.1 Plasmid DNA manipulation and purifications. In order to insert Myc isoforms in pcDNA5 mCherry-mNeonGreen, the backbone was digested with appropriate enzymes (KpnI and BamHI for Myc, HindIII and KpnI for n-Myc). Myc and n-Myc coding sequences were amplified by PCR using the primers listed in **Table 2.2**. The resulting amplification product was purified using Monarch[®] PCR DNA Cleanup Kit and digested with the enzymes mentioned above (details of enzymes can be found in **Table 2.3**). Digestions were carried out in 20 μ L reaction volumes for 1 hour at 37°C according to the restriction enzymes' manufacturer instructions, and backbones were subject to 30 min 37°C calf intestinal phosphatase (10U) treatment prior to ligation. DNA was separated in 1% agarose gel (1 μ L MidoriGreen per 20mL agarose to allow DNA visualisation) by electrophoresis in TAE buffer at 100V. DNA fragments were excised and purified using Monarch[®] DNA Gel Extraction Kit according to manufacturer's instructions. Digested DNA fragments (Myc and n-Myc) and vector were ligated using T4 Rapid DNA Ligation kit according to manufacturer's instructions. Ligation products were then transformed into DH5 α *E. coli* (product by New England Biolabs, NEB5 α). Recipes and reaction mixtures are detailed in **Table 2.18**.

Chapter 2. Materials and Methods

Buffer or reaction mixture	Ingredients
PCR	0.5 μ g DNA, 1X Q5 Reaction buffer, 1X Q5 High GC Enhancer, 200 μ M dNTPs, 0.5 μ M Forward and Reverse primers, 0.02 U/ μ L Q5 High-Fidelity DNA Polymerase
Restriction digest mixture	2 μ g DNA, 10U restriction enzyme, 1X restriction enzyme buffer, ultrapure water
Ligation reaction mixture	3:1 DNA insert:backbone vector (w/w), 2.5 U T4 DNA ligase, T4 DNA ligation buffer
TAE buffer (1X)	40 mM Tris acetate pH 8.4, 1 mM EDTA, ultrapure water

Table 2.18: Standard cloning buffers and reactions mixtures.

2.2.1.1.2 *Escherichia coli* transformations and plasmid amplification. Per each plasmid to be transformed, 50 μ L NEB5 α E. coli was used for transformation with 500ng of DNA. Bacteria were kept on ice for 15 minutes, heat-shocked at 42C for 60 seconds, and incubated in 800 μ L Luria Broth (LB) for 1 hour. Transformants were then plated onto Luria Broth agar with an appropriate antibiotic (Ampicillin 100 μ g/mL). Colonies were picked and expanded in 3mL LB (in the presence of antibiotic) overnight. For transformation of existing and validated plasmids, the 3mL of culture was transferred into 50mL LB with antibiotic prior to DNA extraction by midi-prep. For transformation of newly-ligated plasmids, 1mL of the 3mL was used for plasmid extraction via mini-prep and diagnostic digestions and/or sequencing. The remaining 2mL of the culture of the colony with successful amplification of novel plasmid, was then transferred to 50mL of LB with antibiotic prior to DNA extraction by midi-prep. QIAfilterTM Plasmid Midi kit and Qiaprep[®] Spin Miniprep kit were used respectively for midi- and mini-prep of plasmid DNA, according to manufacturers' instructions.

2.2.1.1.3 Site-directed mutagenesis. The process to generate Myc-tFTs with mRuby as slowFP resulted more complicated. Since the plasmid backbone with the mRuby-mNeonGreen tFT (pcDNA5 FRT/TO AurkA-mRuby-mNeonGreen) contained BamHI sites upstream and downstream of mRuby, this site could not be used for cloning. To address this I performed site-directed mutagenesis to remove the BamHI site after

mRuby. Maps illustrating the plasmids used are shown in **Figure 2.1**. The cloning strategy to address this, which was designed by a previous Ph.D. student in the Lindon lab (Dr. Richard Wang), is schematised in **Figure 2.2**.

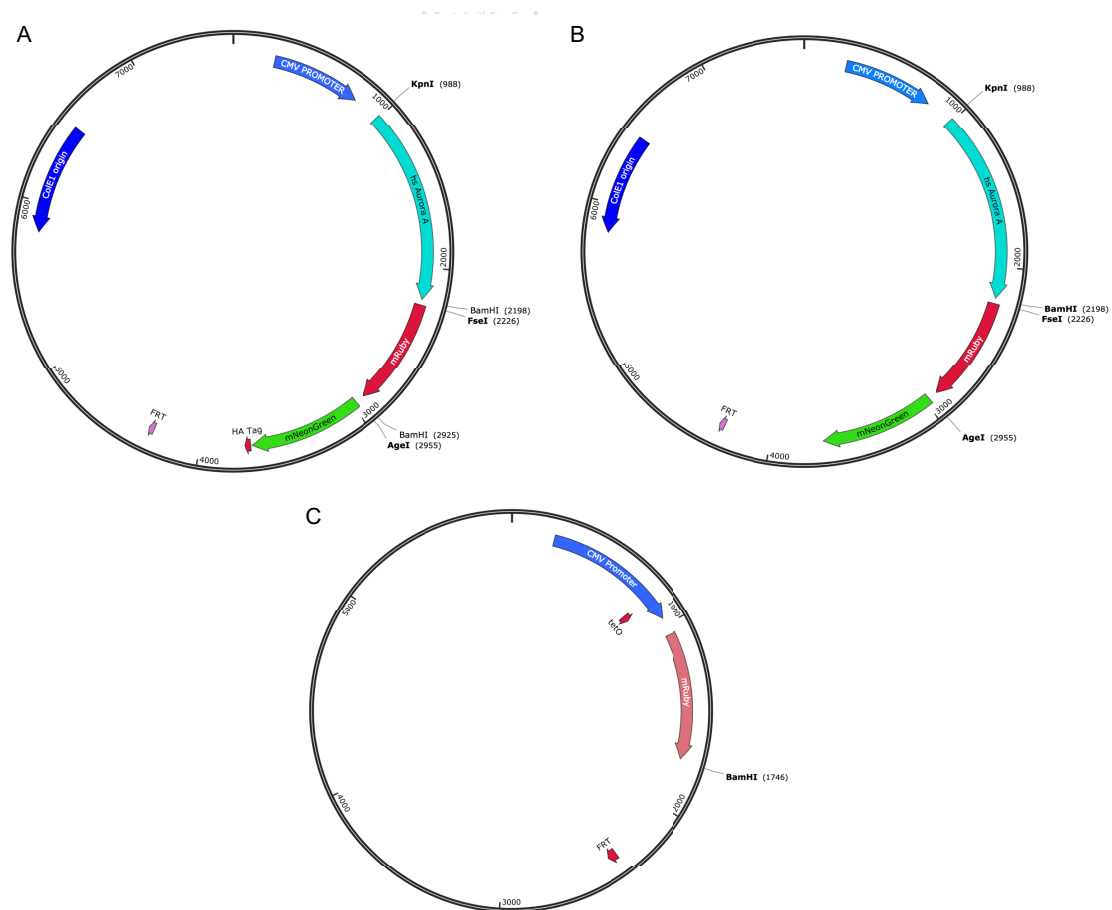


Figure 2.1: Maps for plasmidic DNA used for site-directed mutagenesis.

- A pcDNA5 Aurka-mRuby-mNeonGreen containing two BamHI sites (one upstream and one downstream of mRuby).
- B pcDNA5 Aurka-mRuby-mNeonGreen containing only one BamHI site (upstream of mRuby). Final product of site-directed mutagenesis.
- C pcDNA5 mRuby

Briefly, from the pcDNA5-mRuby plasmid, two fragments with sequences upstream and downstream of the BamHI site are amplified using primers that contain a mutated BamHI site in the tails (Step 1). The PCR was undertaken using Upstream BamHI (forward and reverse) and Downstream BamHI (forward and reverse) according to the

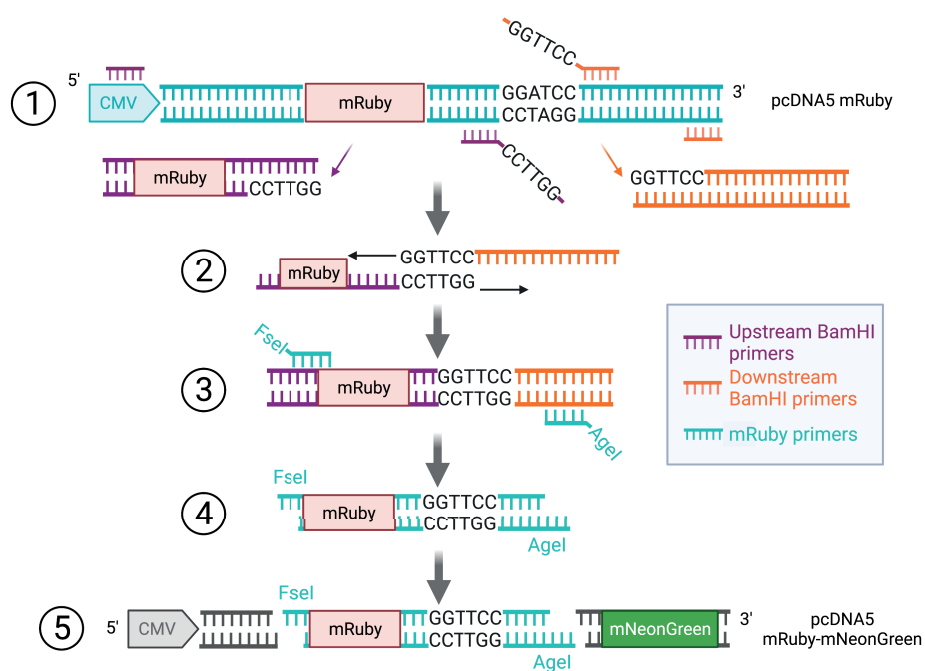


Figure 2.2: **Strategy for site-directed mutagenesis of BamHI site downstream of mRuby.** Schematic representation of the cloning strategy used to remove the BamHI site following mRuby in the Aurka-tFT construct:

1. Design primers for segments upstream and downstream of BamHI site with tails with mutated BamHI sequence (GGATCC to GGTTCC). Anneal and amplify upstream and downstream segments.
2. Denature and align the upstream and downstream segments. Amplify resulting combined fragment.
3. Design primers for segments amplifying from mRuby to just downstream of BamHI site, these include tails with R.E. sites for integration into tFT plasmid (FseI and AgeI).
4. Amplification by PCR and digestion with FseI and AgeI.
5. Generation of recombinant plasmid by ligating the digested fragment and backbone to yield the new pcDNA5 Aurka-mRuby-mNeonGreen plasmid.

PCR reaction mix and steps described in **Table 2.18 and 2.19 A**). Next, these fragments are denatured (Step 2) for 2 minutes at 98C to produce single strands (reaction contents **Table 2.20**), and annealed on the only common section of the sequence, the modified BamHI sequence, by 2 minutes incubation on ice (Step 3). Amplification of the annealed fragment by nested PCR follows (Step 4) according to the reaction detailed in **Table 2.19 B**. The primers used in this reaction flank mRuby and the newly modified BamHI site and contain FseI and AgeI restriction enzymes sites. These restriction enzymes are also present in pcDNA5 FRT/TO AurkA-mRuby- mNeonGreen, construct previously generated in the lab, specifically FseI is located between AurkA and mRuby and AgeI is between mRuby and mNeonGreen but after the problematic BamHI site that follows mRuby. Both the new mRuby fragment and pcDNA5 FRT/TO AurkA-mCherry-mNeonGreen are digested with AgeI and FseI and then ligated together (Step 5) resulting in a new pcDNA5 AurkA-mRuby-mNeonGreen plasmid that does not contain a BamHI site between the FPs. DNA purification by gel extraction or PCR clean up were carried out at each step in order to yield the final product.

Once the BamHI site was removed from pcDNA5 AurkA-mRuby-mNeonGreen, I was able to excise AurkA from this newly generated plasmid using KpnI and BamHI and replace it with the Myc fragment digested with the same enzymes utilising the process described in the previous paragraph.

Chapter 2. Materials and Methods

A			B		
Step	Temperature (°C)	Time (s)	Step	Temperature (°C)	Time (s)
1	98	30	1	98	30
2	98	10	2	98	10
3	45	30	3	50	30
4	72	30	4	72	30
5	Repeat steps 2-4 3 times		5	Repeat steps 2-4 3 times	
6	98	10	6	98	10
7	58	10	7	65	30
8	72	30	8	72	30
9	Repeat steps 6-8 17 times		9	Repeat steps 6-8 17 times	
10	72	5	10	72	5
Hold	4	-	Hold	4	-

Table 2.19: Site-directed mutagenesis PCR reactions set up.

- A PCR reaction set up to yield Upstream and Downstream BamHI fragments. PCR Mix set up according to Table 2.18 and with Upstream BamHI (-F and -R) and Downstream BamHI (-F and -R) primers.
- B PCR reaction set up to yield the mRuby with the mutated BamHI site. PCR Mix set up according to Table 2.20.

Steps	Reagents	Volumes (μL)
1	dH ₂ O	19.5
	5X Q5 High GC Enhancer	10
	5X Q5 Reaction buffer	10
	Upstream Fragment	1
	Downstream Fragment	3
2	10mM dNTPs	1
	Q5 polymerase	0.5
3	mRuby Fwd primer	2.5
	mRuby Rev primer	2.5

Table 2.20: Reagent mix for steps 2-4 in site-directed mutagenesis of BamHI.

2.2.1.1.4 Site directed mutagenesis via round the horn PCR To generate the T58A mutation in Myc, Round the horn mutagenesis cloning strategy was applied to pcDNA5 FRT/TO Myc-tFT (mCherry-mNeonGreen).

Firstly, primers CA20-F and CA21-R (see **Table 2.2** for sequence) were designed in order to mutate the codon coding for Threonine 58 (ACC) into one coding for Alanine (GCC). Indeed the Forward primer anneals at the Threonine codon but with G instead of A. The reverse primer anneals from the base just upstream of the ACC codon. This is shown in **Figure 2.3**. These primers together allow for amplification of the whole plasmid with the mutation at the Threonine site.

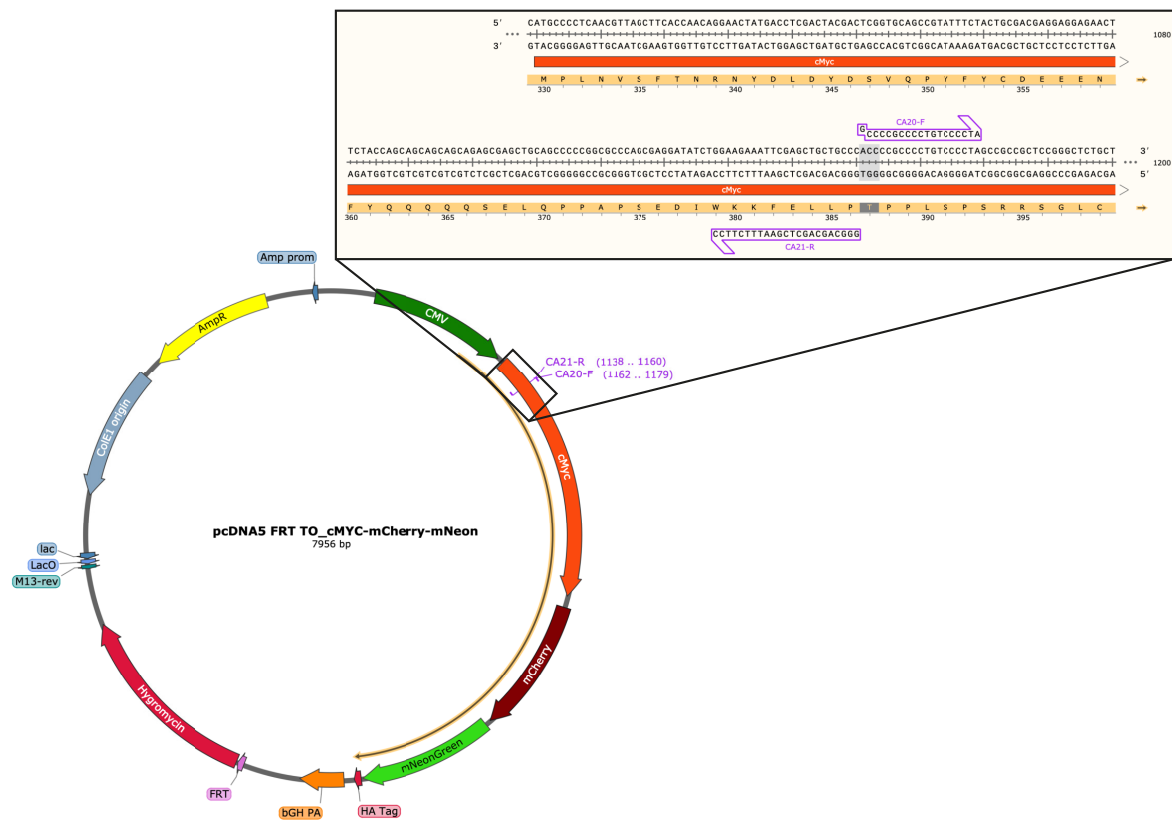


Figure 2.3: Maps for pcDNA5 FRT/TO Myc-tFT with the primers for round-the-horn mutagenesis of T58 displayed in the callout.

Primers were resuspended in ultrapure water (100 μ M) and each primer was phosphorylated with T4 Polynucleotide Kinase (PNK) according to the reaction listed in **Table 2.21**. The reaction was carried out at 37°C for 60 minutes and then PNK was heat-

Chapter 2. Materials and Methods

inactivated at 75°C for 10 minutes. Phosphorylated primers were diluted in ultrapure water to a final working stock concentration of 10 μ M.

Reagent	Volume (μ L)
PNK buffer A	2
10mM ATP	2
100 μ M Primer	15
PNK	1

Table 2.21: Reaction mix for primer phosphorylation with T4 Polynucleotide Kinase.

Mutant DNA amplification was achieved by PCR with Q5 High-Fidelity DNA Polymerase according to manufacturer's instructions and reaction details listed in Table 2.22.

Step	Temperature (°C)	Time (s)
Initial Denaturation	98	30
Amplification 25-30 cycles of:	98 (Denaturation)	30
	68 (Annealing Temperature)	30s
	72 (Amplification)	5 min (30s/kb of plasmid length + 1min)
Final Extension	72	10
Hold	4	-

Table 2.22: Round the horn PCR steps.

To the cooled PCR reaction, 10 U of DpnI were added and incubated at 37°C overnight. Digestion with DpnI results in degradation of methylated parental plasmid DNA from the PCR mix. The resulting DNA was run on a 0.7% agarose gel and the band of the correct size (linearised mutant plasmid) was excised and purified by gel extraction. The linearised plasmid was then ligated. To 100nM of linearised plasmid, 0.5 μ L of T4 ligase and T4 ligation buffer were added and final volume was adjusted with water to a final volume of 5 μ L. The ligation reaction was carried out at room temperature for 45 minutes. The ligation reaction product was then transformed into *E. coli* as previously described and colonies were grown overnight at 37°C on LB agar plates with Ampicillin. Next, colony PCR was carried out whereby 5 colonies were picked (some colony was left on the plate for future expansion) and added to a PCR tube containing Q5 Polymerase reaction mix with primers CA01-F and CA02-R (see Table 2.2) and to a 3mL tube containing LB and Ampicillin for overnight culture. Colony

PCR amplification of Myc was verified by DNA electrophoresis, all 5 colonies displayed amplification of a product of the correct size. Plasmids were extracted from the 3mL culture of each colony by Qiaprep[®] Spin Miniprep and sequenced. This confirmed that 3 of 5 colonies had correctly mutated Myc at the T58 site and no other mutation was generated. The PCR product from the colony PCR of one of the positive clones was digested with KpnI and BamHI restriction enzymes (the primer tails contained these sites), and ligated into pcDNA5 FRT/TO mCherry-mNeonGreen (digested with the same enzymes) to yield pcDNA5 FRT/TO Myc(T58A)-mCherry-mNeonGreen. Unspecified reactions of PCR, digestion with restriction enzymes and ligation followed the details outlined in **Table 2.18** and manufacturer's instructions.

2.2.2 Mammalian cell culture

2.2.2.1 Mammalian cell subculturing

The cell lines listed in **Table 2.13** were grown in the cell media compositions listed in **Table 2.23** and in an incubator at 37° and 5% CO₂.

Cell line/purpose	Media composition
A549	RPMI, 10% V/V FBS, 2 mM L-Glutamine, 1X Antibiotic antimycotic solution
U2OS FRT/TO, HeLa FRT/TO	DMEM, 10% V/V FBS, 2 mM L-Glutamine, 1X Antibiotic antimycotic solution
Filming medium	Leibovitz's L-15 (no phenol red), 10% V/V FBS, 1X Antibiotic antimycotic solution
Freezing medium	90% FBS, 10% DMSO

Table 2.23: Complete media recipes for all cell lines utilised in this study.

U2OS FRT/TO Myc-tFT, Myc (T58A)-tFT, nMyc-tFT, tFT were clonally selected for with hygromycin B (150 µg/mL). In these cells, construct expression was achieved by addition of doxycycline 0.1µg/mL in the medium. U2OS FRT/TO tFT cells were cultured with the appropriate medium with the selective pressure of hygromycin B (150 µg/mL) to preserve the expression of the constructs. Cells passaging procedures were common across cell lines. Firstly, old media was removed and a PBS wash was performed. PBS was removed and 500µL of trypsin (2.5X diluted in PBS) was added to

Chapter 2. Materials and Methods

the culture dish. Cells were incubated with trypsin at 37°C and 5% CO₂ for 3-5 minutes to ensure cell detachment. Once cells were detached, these were resuspended in at least 3mL of media and re-plated into a new plate with 10mL fresh media. Appropriate dilutions were made. If specific cell density was needed for experimental procedures, cells were counted with a haemocytometer after being resuspended in media and plated accordingly.

2.2.2.2 Long-term cryostorage and cell recovery of mammalian cell lines

For long-term storage, cells at ~80% confluency were detached with trypsin as described above. Following incubation with trypsin, cells were resuspended in freezing media and placed divided between several cryo-vials. Two cryo-vials were obtained from a 10cm dish and 4 from a 15cm dish. These were then placed in a freezing container (either Mr. Frosty, Nalgene® or a polystyrene box) and placed at -80°C for a few days and then transferred to -140°C for long-term storage.

Frozen cells were recovered from cryostorage by incubating the vials at 37°C for a few minutes (until the majority of the volume in the vial was thawed) and then by addition of 1mL of fresh culturing media to the vial, cells were gently resuspended and seeded in a plate. Once cells had attached to the dish, media was refreshed in order to eliminate any traces of DMSO in the culture medium.

2.2.2.3 Mammalian cell transfection

Two different methods for transfection of mammalian cells were used.

2.2.2.3.1 Lipofectamine®. For lipofectamine treatment of cells with Myc-mCherry-mNeonGreen or Myc-mRuby-mNeonGreen, 40,000 U2OS FRT/TO cells were seeded in filming media in each well of an Ibidi dish a day prior to the transfection. Lipofectamine 3000 reagent was diluted in Opti-MEM medium at 1µL to 25µL per condition or well. This constitutes solution A. DNA was also diluted in Opti-MEM to make up Solution B, at 1µg of plasmid DNA in 25µL of Opti-MEM and 2µL of p3000 reagent per condition. The diluted Lipofectamine of solution A was combined with the diluted DNA of

solution B at a 1:1 ratio and incubates for 5 minutes at room temperature. This mixture was then added to the cells. Transfected cells were incubated at 37° and 5% CO₂ for 24h prior to use in imaging.

2.2.2.3.2 Electroporation. Transfections by electroporation were carried out utilising the Life Technologies Neon® system. The day prior to electroporation, cells were passaged to ensure at least 80% confluency on the day of electroporation. One 80% confluent 10cm dish was used for each electroporation condition or a 15cm dish was used for three conditions using a 100µL transfection tip. Cells were detached by trypsinisation as described in **section 2.2.2.1**, pooled, and washed once in PBS and once in pre-warmed HBSS. Cells were centrifuged at 600 rcf for 3 minutes in between washes to pellet cells before removal of the supernatant by aspiration. After the HBSS wash, the cell pellet was resuspended in fresh HBSS in a volume equal to 120µL per number of electroporation conditions. To separate 1.5mL microcentrifuge tubes containing the plasmid DNA, 120µL of the cells in HBSS was added. Importantly, the volume of DNA should be no more than 5% of the volume of cells to be electroporated (100 µL) to limit cell death. The electroporation chamber was filled with 3mL of Buffer E (supplied with the Neon® system). The solution of cells and DNA in HBSS was then electroporated according to the manufacturer's instructions with electroporation settings previously optimised in the lab (1150 V, 2 pulses with 30 milliseconds width). Electroporated cells were then placed in 1mL of fresh medium to recover, until all electroporations were completed. The cells are then centrifuged at 3000 rpm for 90 seconds, the pellet resuspended in fresh media and plated in either 10 cm plates or Ibidi dishes. Transfected cells were allowed to recover by incubation at 37° and 5% CO₂ for 24h prior to use in other experimental procedures.

2.2.2.4 Generation of stable cell lines.

To create cell lines, U2OS FRT/TO Flp-in cells were transfected by electroporation with the pcDNA5 FRT/TO plasmids containing the POI-tFT construct as described in **Section 2.2.2.3.2**. For each MYC construct, two 90% confluent 10cm dishes were transfected

Chapter 2. Materials and Methods

with two electroporations. One 90% confluent 10cm dish was electroporated for the mCherry-mNeonGreen empty vector. In both cases, 3 μ g total DNA per electroporation was used at 9:1 ratio pOG44:construct. Cells for each condition were pooled and seeded on Ibidi microscopy dishes, to check the efficiency of the transfection, and into three 10cm dishes. Once established that the electroporation had worked, clones were generated by selective pressure with Hygromycin-B (Cf=150 μ g/mL) until clones emerged. Ten clones were picked per Myc- and nMyc-tFT constructs, five for the empty vector construct. Overall, 70% of Myc- and nMyc-tFT expressed the construct correctly, as well as 100% of the empty vector clones. Selective antibiotic pressure was maintained in the U2OS FRT/TO tFT clones when cultured in order to avoid loss of construct. This was not required with any of the Myc (both isoforms and mutant) constructs.

2.2.2.4.1 Giemsa's assay This assay was performed to show loss of Zeocin resistance upon integration of the Flp-In constructs in U2OS FRT/TO cells. For this 20,000 cells were seeded in each well of a 6-well-plate. After 24 hours Zeocin antibiotic was added at a final concentration of 50 μ g/mL to the treatment wells. On day 4 after initial treatment, media was changed and antibiotic pressure was added again to the treated wells. After 7 days of antibiotic incubation, treated and untreated cells were washed in PBS, which was then removed completely, and fixed in 70% EtOH by 10 minute incubation at room temperature. After the incubation, EtOH was removed and wells were rinsed with ultrapure water. Giemsa's stain (BDH, 350864X; stock diluted 1:20) was added to the wells (1mL/well) and incubated for 20 minutes at room temperature. Next, the stain was removed and the wells were rinsed with ultra-pure water. Finally, the water was removed and the stained cells were left to air dry overnight.

2.2.2.5 Cell synchronisation

Several synchronisation protocols were utilised in this work to synchronise cells to the same phase of the cell cycle or to the circadian rhythm.

2.2.2.5.1 Cell cycle synchronisation. Two synchronisation methods were performed to arrest cells in G2 phase or in S-phase. In the first protocol, cells (seeded in Ibidi

dishes) were treated at the start of the imaging experiment with CDK1 inhibitor RO-3306 (Cf=10 μ M).

For the second arrest (depicted in **Figure 2.4**), cells were synchronised by double Thymidine block and release. Briefly, cells were seeded at a density of 20,000 cells/well with growth media supplemented with 2mM Thymidine. After 24h Thymidine treatment, arrested cells were released by washing twice in PBS (5 minutes each wash) and once filming media (15 minutes in length), then, the wash was replaced with 300 μ L of filming media and released for 12 hours in an incubator at 37°C, 5% CO₂. After 12 hours, Doxycycline (Cf=0.1 μ M) and Thymidine (Cf=2mM) were added to each well to induce Myc-tFT expression and further enrich for cells in S-phase arrest. The ibidi dish was then placed on the microscope at 37°C for 4 hours prior the start of imaging experiment to allow Myc-tFT expression to detectable levels.

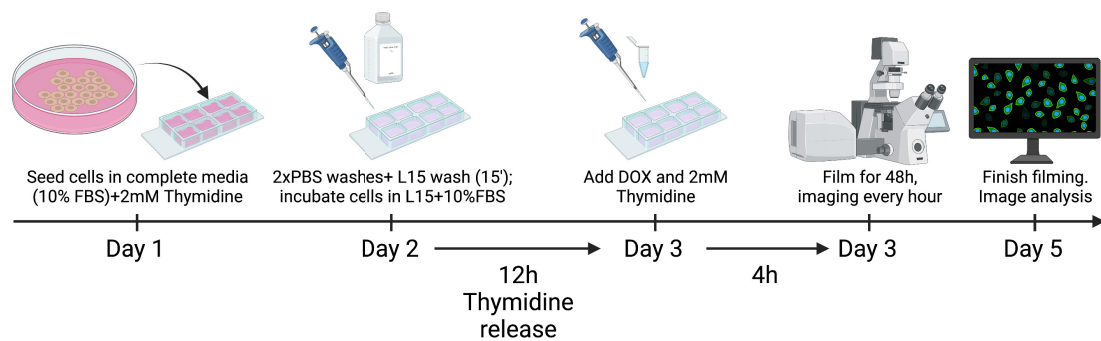


Figure 2.4: Schematic representation of double Thymidine block and release synchronisation method.

Chapter 2. Materials and Methods

2.2.2.5.2 Circadian rhythm synchronisation. Two methods of circadian synchronisation were used in this work, both based on synchronisation protocols from Dr. John O'Neill (Laboratory of Molecular Biology, University of Cambridge), and illustrated in **Figure 2.5**. The first was dexamethasone treatment, where cells (at seeding density near confluency of 80,000cc/well) are first seeded in growth media and left overnight to attach. The cells were seeded in the central wells of an ibidi dish where less evaporation of media occurs; PBS was placed in the external wells to maintain humidity during filming. The next day cells were washed twice with PBS and media was changed to filming media with reduced serum (1% instead of 10% FBS to reduce the rate of proliferation) and with dexamethasone ($C_f=0.1\mu\text{M}$) and Doxycycline. Cells are placed on the microscope at 37°C for 4 hours while Myc-tFT signal begins to develop prior to imaging for 96 hours. It was worth noting that dexamethasone synchronisation only achieves synchronisation of a proportion cells in the field ($\sim 60\%$).

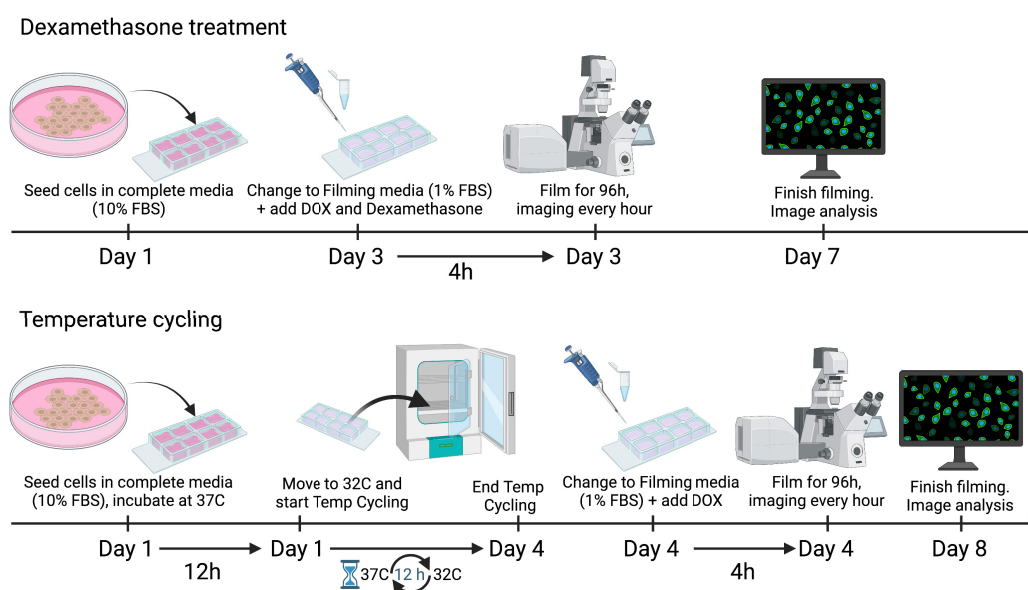


Figure 2.5: Schematic representation of circadian synchronisation by dexamethasone treatment or Temperature cycling.

The second protocol consists of synchronisation by exposing cells to 12 hour alternating cycles at 37°C and 32°C in $5\% \text{CO}_2$ for 4 days. While programmable incubators with active coolings allow automation of this process, none were available in our lab so cells were manually moved every 12 hours between two incubators set at the two

different temperatures. Overall, the protocol required seeding cells to be confluent by the end of the synchronisation process. Cells grow slower due to the oscillating temperature so 40,000 cells were seeded in complete media in the central wells of an ibidi dish to yield a confluent density of 80,000 cells by the fourth day. Again, PBS was placed in the outer wells to maintain humidity during filming. Cells were then placed in an incubator at 37°C, 5% CO₂, for 12 hours starting the temperature cycling process. The cells were then moved to the incubator at 32°C for the following 12 and so on and so forth. On the fourth day, when cells were to be moved to 37°C, they were washed twice in PBS and then filming media with reduced serum (1% FBS) and supplemented with Doxycycline was added to the cells. The microscope dish was then moved to the microscope where temperature was set at 37°C and imaging was started after 4h. If the experiment required sample collection, cells were seeded (at 200,000 cc/well) in 6cm dishes (one per each time point). Cells were temperature cycled as described above and on the fourth day, time 0 cells were collected by trypsinisation (see method in **Section 2.2.3**). The other cells were washed with PBS and media was changed to low serum media. They were then placed into the 37°C incubator for the remaining time of the experiments. Cells were collected by trypsinisation at the time points required by the experiment and pellets of all time points were frozen at -20°C for protein extraction. Overall, this protocol results in synchronisation of all cells in the field to the circadian rhythm.

2.2.3 Cell Lysate extraction, protein quantification and Immunoblotting

Cells were harvested for lysis either by scraping in PBS with a cell scraper or by trypsinisation. In the latter case, trypsin was inactivated with addition of media and cells were centrifuged at 3000rpm for 90 seconds, and then washed with PBS. In both cases, cells in PBS were centrifuged at 3000rpm for 90 seconds and PBS was aspirated. Cellular pellet was either frozen at -20°C or resuspended in lysis buffer (recipe in **Table 2.24** with all other buffers needed for this technique). In the case of time-course experiments, pellets were frozen until all timepoints were collected and then thawed and lysed at the same time with the same lysis buffer solution. Lysis buffer was freshly made for each

Chapter 2. Materials and Methods

application. Pellets from 6-well plate wells were resuspended in 50 μ L of lysis buffer, ones from 10cm petri dishes were resuspended in 100 μ L. Cell pellets were lysed with lysis buffer on ice for one hour and then centrifuged at 4°C, 14000 rcf for 15 minutes. The supernatant was collected and frozen at -20°C until further use.

Buffer	Composition
Blocking solution	5% (w/v) BSA in PBST or TBST
Fluorescence buffer	5% (w/v) FBS, 0.01% (w/v) SDS, PBST
Lysis Buffer	1% Triton X-100, 150 mM NaCl, 10 mM Tris-HCl at pH 7.5, EDTA-free protease inhibitor cocktail, and PhosSTOP™ phosphatase inhibitor, ultrapure MQ water
PBST	0.1% (v/v) Tween-20, PBS 1X
TBS (pH 7.6) 10x	152.2 mM Tris-HCl, 46.2 mM Tris base, 1500 mM NaCl
TBST	0.1% (v/v) Tween-20, TBS 1X

Table 2.24: Recipes for immunblotting buffers utilised.

Lysate protein concentrations were assessed by the colorimetric Bradford assay which was carried out in 96-well plates. Briefly, BSA (2mg/mL stock) was diluted in ultrapure MQ water to generate a standard curve (final concentrations: 0; 5; 10; 15; 20; 25 μ g/mL; final well volume=80 μ L). Lysates were diluted 1:10, 5 μ L of which were added to a well with 75 μ L of ultrapure MQ water. Each sample of standard concentration was repeated in triplicate. Once all samples were loaded, 20 μ L of Bradford reagent was then added to yield a final volume of 100 μ L per well. The plate was incubated on a shaker at room temperature for 10 minutes shielded from light to allow the reagent to develop. The plate was then read on a CLARIOStarPlus plate reader for absorbance at 595nm. Standard curve extrapolation from absorbance values and quantification of unknown concentration of experimental samples was carried out on Excel.

Prior to protein gel electrophoresis, 30-50 μ g of lysates, with the addition of NuPage™ LDS Sample buffer (4X) with 10mM DTT, were heated at 95°C for 10 minutes to yield protein denaturation. Denatured proteins and molecular weight ladders were then separated by protein electrophoresis using SDS-PAGE using 4-12% pre-cast NuPage®gels. Protein extracts were run in 1X MOPS SDS Running buffer at 150 V for 90 min. Proteins were then transferred to Immobilon-FL membrane, which was pre-activated by 2

minute incubation in 100% EtOH and then equilibrated in 1-Step transfer buffer for 5 min at room temperature. The transfer was carried out in 1-Step transfer buffer using a semi-dry PierceTM G2 Fast Blotter which allows transfer at 25V, 1.3A (constant) in 12 minutes (optimised protocol) according to the manufacturer's instructions. After transfer, membranes were blocked whilst on a roller in blocking buffer for 1 hour at room temperature. Blocking solution was made up in TBST if blotting for phosphorylated proteins. Membranes were then treated with primary antibodies diluted in the same composition blocking solution for 1 hour at room temperature (GAPDH) or overnight at 4°C on a roller to ensure even spread of the antibody on the membrane. Following 3 washes with PBST or TBST, each lasting 5 min, secondary membranes were incubated for an hour at room temperature on a roller with antibodies diluted in blocking buffer (HRP-linked) or fluorescence secondary buffer according to the dilutions listed in **Table 2.7**. This was followed by another 3, 5-minute washes in PBST or TBST prior to addition of chemiluminescent HRP substrate (HRP-linked antibodies only) and visualised by chemiluminescence or fluorescence with an Odyssey®Li-COR Imaging System (LI-COR Biosciences). Resulting images were analysed on ImageStudioLite by measuring the fluorescence intensity in a region of interest (ROI) around the specified band and subtracting the intensity reading of a ROI of the same size in an area of background.

2.2.4 Bromodeoxyuridine assay

To evaluate the effect of Myc induction on proliferation, integration of Bromodeoxyuridine (BrdU) in DNA during S-phase was used. This assay allows to measure progression in S phase by labelling cells that undergo DNA replication. The method is described below and illustrated in **Figure 2.6**.

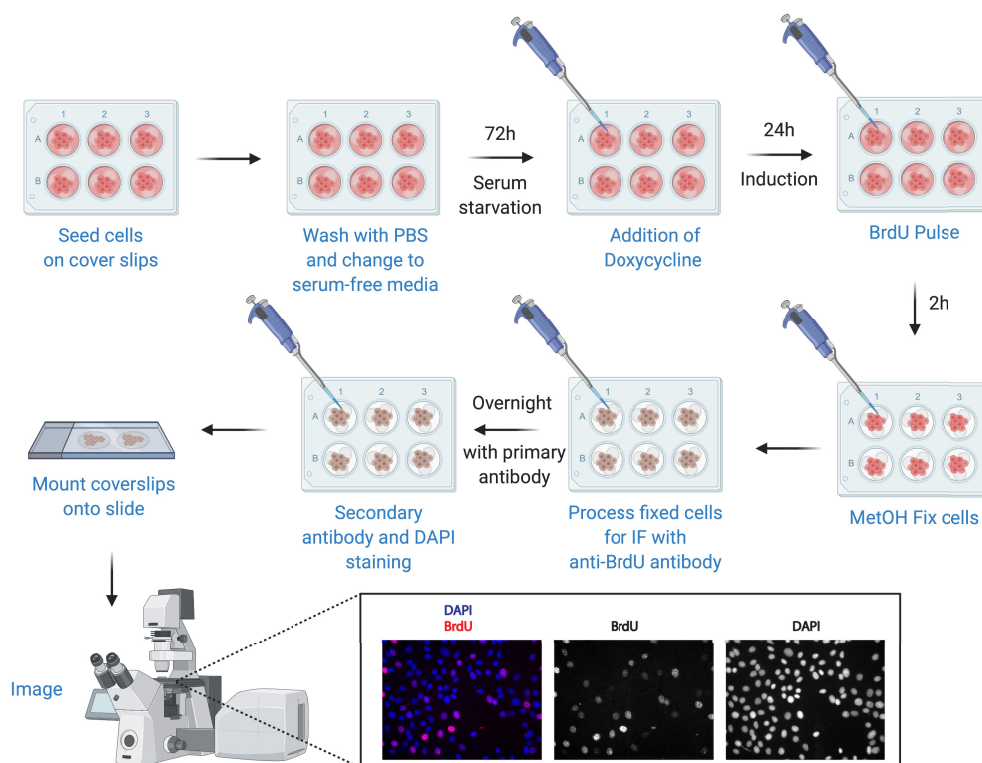


Figure 2.6: Schematic representation of the BrdU protocol.

Briefly, cells were seeded on coverslips (3 per well of 6-well plate) at a density of 100,000 cells (cc)/well in fully supplemented media. The following day, adherent cells were washed three times with PBS and media without any serum was added; cells were serum starved for 72 hours. Doxycycline (DOX) or water vehicle control, was added and incubated for 24h to yield induction of any construct expressed under the control of doxycycline repressor in U2OS FRT/TO. After 24h, cells were incubated for 2 hours with BrdU (Cf=10 μ M), at the end of which they were washed once in PBS and fixed in cold MetOH (stored at -20°C). Coverslips were stored for a few hours at -20°C.

After MetOH removal, fixed cells on coverslips were rehydrated in PBS for 10 minutes. DNA denaturation was achieved by 30 minute incubation with 2M Hydrochloric Acid (HCl) in PBS 0.1% Tween. Coverslips were washed three times for 5 minutes with PBS and incubated for 30 minutes in blocking solution (3%BSA in PBS 0.1% Triton). This was followed by another step of 3, 5 minute washes, in PBS 0.1% Triton and then the coverslips are incubated in a humidity chamber with anti-BrdU antibody diluted in blocking solution (see **Table 2.6**) overnight at 4°C. The following day, coverslips were washed three times for 5 minutes in PBS 0.1% Triton and incubated for 45 minutes with an anti-rat secondary antibody (see **Table 2.7**) in blocking solution. Next, coverslips were washed for 5 minutes once in PBS 0.1% Triton, once in PBS and once in ultrapure MQ water. These were then mounted on microscope slides with mounting media containing DAPI. Slides were stored short term at 4°C and long term at -20°C.

2.2.4.1 Chromatin Immunoprecipitation and quantitative PCR analysis

Chromatin Immunoprecipitation (ChIP) experiments were carried out to assess enrichment of Myc-tFT at the promoter of Myc target gene Carbamoyl-Phosphate Synthetase 2, Aspartate Transcarbamylase, And Dihydroorotase (CAD). To do so, SimpleChIP®Plus Enzymatic Chromatin IP Kit (with Magnetic Beads), from Cell Signaling Technologies, was employed. List of materials required for this protocols can be found in **Table 2.8** and buffer recipes in **Table 2.25**.

Buffer (Vf/condition)	Ingredients per condition
1x Buffer A (1mL)	250µL 4X Buffer A, 750µL ultrapure water, 0.5µL 1M DTT, 5µL 200X PIC
1x Buffer B (1.1mL)	275µL 4X Buffer A, 825µL ultrapure water, 0.55µL 1M DTT
1xChIP Buffer (100µL)	10µL 10X ChIP Buffer, 90µL ultrapure water, 0.5µL 200X PIC
1X ChIP Elution buffer (150µL)	75µL 2X ChIP Elution Buffer, 75µL ultrapure water
High salt wash (1mL)	100µL 10X ChIP Buffer, 70µL 5M NaCl, 900µL ultrapure water
Low salt wash (3mL)	300µL 10X ChIP Buffer, 2.7mL ultrapure water

Table 2.25: Recipes for ChIP buffers according to manufacturer's instructions.

The workflow of the experiment is illustrated in **Figure 2.7** and was carried out

Chapter 2. Materials and Methods

according to manufacturer's instructions.

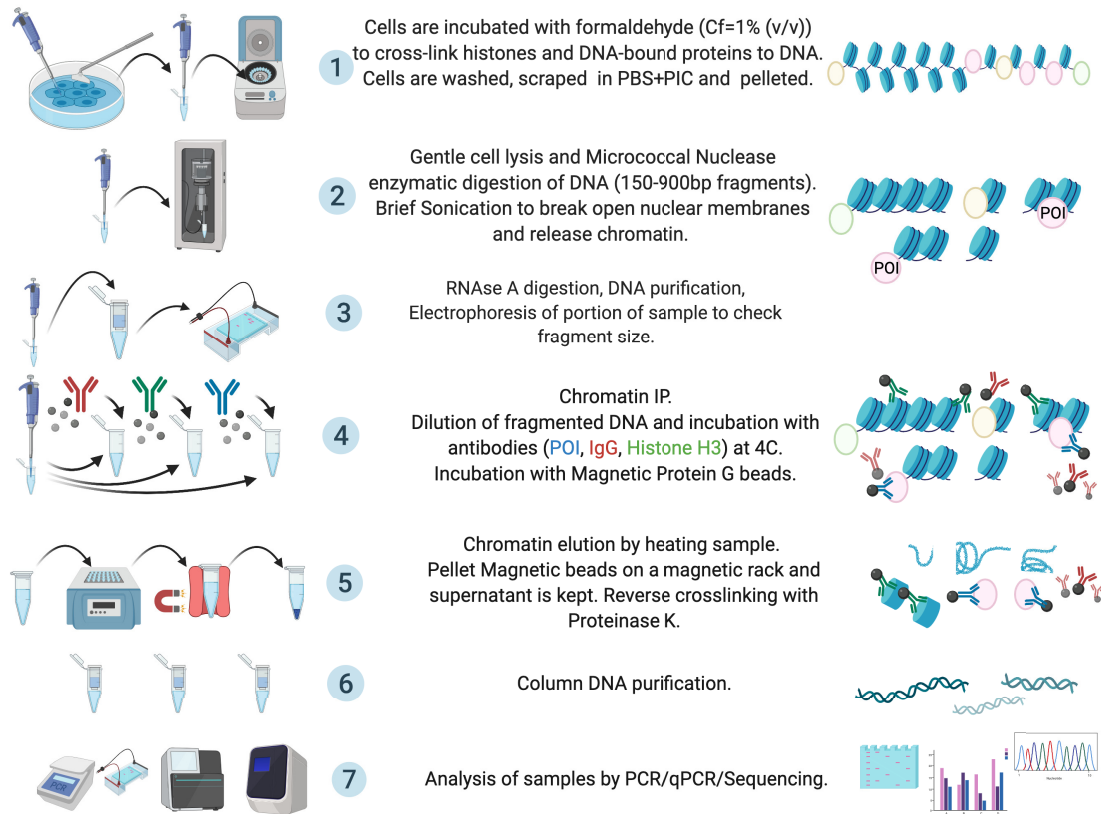


Figure 2.7: Schematic representation of the SimpleChIP protocol.

The protocol is as follows:

- 1. Cell culture cross-linking and sample preparation:** One 90% confluent 15cm dish of cells (Vf=20mL media) were used per immunoprecipitation condition. To each plate, firstly, 540 μ L of 37% (v/v) PFA (Cf=1%) was added and incubated for 10 minutes at room temperature. A 5 minutes incubation with 1X Glycine followed. Cells were washed twice with 20mL PBS (supplemented with protease inhibitor cocktail (PIC) and pre-chilled on ice) and scraped into 5mL of pre-chilled PBS with PIC and collected in a tube. The plates were washed with another 5mL of pre-chilled PBS with PIC, which then collected and added to the same cell suspension (Vf=10mL of cells in PBS+PIC), to ensure collection of as many cells as possible. Cells were pelleted by centrifugation at 4°C, 2000rcf for 5 minutes.

2. **Nuclei preparation and chromatin digestion:** Cellular pellet was resuspended in 1X Buffer A (supplemented with DTT and PIC ; 1mL per condition) and incubate 10 minutes on ice with mixing by inversion to allow cell lysis. Nuclei were pelleted from lysates by centrifugation at 4°C, 2000rcf for 5 minutes. Nuclei were resuspended in 1X Buffer B with DTT (1mL per condition) and the centrifugation step was repeated. The pellet was resuspended in 100 μ L of 1X Buffer B with DTT per prep, and transferred to a 1.5mL microcentrifuge tube. To yield digested DNA of 150-900 basepair (bp) fragments (1 to 5 nucleosomes), nuclear lysates were treated with Micrococcal Nuclease by adding 0.25 μ L of the nuclease per IP to the samples in Buffer B and incubating them at 37°C for 20 minutes. Digest was stopped by addition of 10 μ L of 0.5M EDTA per prep and incubating on ice for 2 minutes. Nuclei were pelleted by centrifugation at 4°C, 16000rcf for one minute after which supernatant was removed and pellets were resuspended in 100 μ L of 1X ChIP Buffer (with PIC) and incubated on ice for 10 minutes. Nuclei were then sonicated on ice by 3 sets of 20 seconds pulses (30second incubation in between pulses) at sonicator settings 6/20. Lysates were clarified by centrifugation at 4°C, 9400rcf for 10 minutes. Supernatant was transferred to a new 1.5mL tube and stored at -80°C. For analysis of chromatin digest, 50 μ L of digested DNA from the +DOX condition (the more abundant one) were stored separately at -20°C overnight and processed according to the next step.

Micrococcal Nuclease optimisation was carried out by cross-linking 2×10^7 U2OS FRT/TO Myc-tFT cells and processing them according to the steps described above and step 3 below. No digest, 0.25, 0.5, 0.75 and 1 μ L of micrococcal nuclease were tested along with differing number of sonication pulses (**Figure 2.8**). The best digested DNA, with fragments ranging from 150-900bp resulted from 0.25 μ L micrococcal nuclease with three sonication pulses.

3. **Analysis of chromatin digestion and concentration:** This step is undertaken on the 50 μ L for DNA analysis. Firstly, RNA in the sample was degraded by RNase reaction, which was undertaken by addition of 100 μ L nuclease-free water, 6 μ L 5M NaCl, 2 μ L of RNase and incubation for 30 minutes at 37°C. Protein degradation

Chapter 2. Materials and Methods

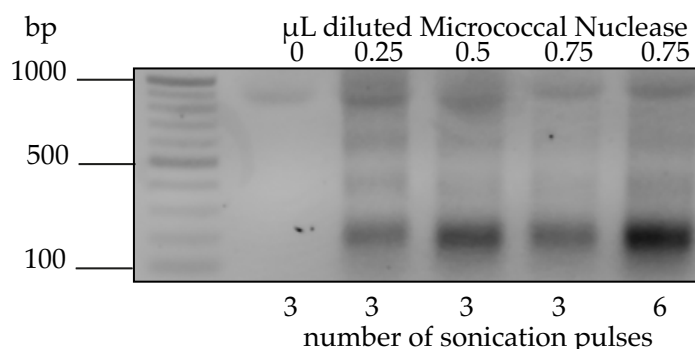


Figure 2.8: **Optimization of DNA digestion by Micrococcal Nuclease and sonication.** Differing amounts of Micrococcal Nuclease and sonication pulses were tested to verify which combination yielded the optimal DNA digestion. Samples were run on 1% agarose gel with 100bp-ladder.

was achieved by Proteinase K treatment by addition of $2\mu\text{L}$ of the enzyme to the RNase-digested sample. Samples were incubated for 2 hours at 65°C . Resulting DNA was extracted with DNA purification spin columns included in the kit, according to manufacturer's instructions. A portion of the purified DNA was run on 1% agarose gel and DNA concentration was determined using a Nanodrop spectrophotometer.

- 4. Chromatin Immunoprecipitation (IP):** Frozen chromatin from step 2 (the one stored at -80°C) was thawed and $10\mu\text{g}$ of it was added to 1X ChIP Buffer (with PIC) to yield diluted chromatin to a volume of $500\mu\text{L}$ per IP condition. From one IP condition, $10\mu\text{L}$ were removed and stored in a separate tube at -20°C until the next step; as the 2% input. For each IP condition, $500\mu\text{L}$ of chromatin were added to a fresh tube together with an antibody (c-Myc, Histone H3 or IgG 1:50; details in **Table**) and incubated overnight at 4°C with rotation. The following morning, the ChIP-Grade Protein G Magnetic Beads were resuspended by gentle vortexing and $30\mu\text{L}$ of these were added to each tube containing chromatin and antibody and incubated at 4°C with rotation for two hours. Magnetic beads were then pelleted by placing tubes on a magnetic separation rack until the solution clears. The supernatant is then removed and the beads were washed three times with 1mL per condition with the low salt wash, each wash lasting 5 minutes and with samples placed on ice with mixing by inversion. Beads were pelleted on the

magnetic rack in between each wash. Another wash step, in 1mL of high salt wash with the same incubation details as previous washes.

5. **Elution of Chromatin from antibody/Protein G Magnetic Beads and reversal of cross-links:** Immediately following on from the previous step, beads were pelleted, wash removed and 150 μ of 1X ChIP Elution buffer were added to each IP sample and to the thawed 2% input. The chromatin was then eluted from the beads by incubation for 30 min at 65°C in a heated water bath with mixing. Magnetic beads were pelleted on the magnetic separator rack and the supernatant containing the eluted chromatin was transferred to a new tube. To the eluted chromatin and the 2% input, 2 μ L of Proteinase K and 6 μ L NaCl were added and incubated at 65°C for 2 hours with the use of a shaking water bath or shaking heat-block.
6. **Column DNA purification:** Following on immediately, the reverse cross-linked chromatin was then purified using DNA purification columns according to manufacturer's instructions. Purified DNA was stored at -20°C.
7. **Quantification of DNA by quantitative PCR (qPCR):** This step was carried out using the SimpleChip®Universal qPCR Master Mix with SYBR®Green detection and other materials listed in **Table 2.9**, primers used are detailed in **Table 2.10**. Briefly, per each well of a 96-well plate, 2 μ L of DNA for each IP or water for non template control (NTC) was added to 18 μ L of qPCR mix (**Table 2.26**). Once all the samples were loaded, the plate was sealed and a brief centrifugation ensure liquid collection at the bottom of wells. The plate was maintained on ice until loaded onto the qPCR machine where the qPCR reaction was set up according to **Table 2.26**. Melt, amplifications and standard curve of the primers used can be found in **Figure 2.9** for CAD primers and **Figure 2.10** for CMV primers.

Chapter 2. Materials and Methods

Reagent	Volume for 1 PCR reaction (18 μ L)
Nuclease free water	6 μ L
Forward Primer (5 μ M)	1 μ L
Reverse Primer (5 μ M)	1 μ L
SimpleChIP Universal qPCR Master Mix	10 μ L

Table 2.26: Recipes for qPCR of ChIP products based on SimpleChIP Universal qPCR Master Mix instructions. For hRPL30 primers, which come as a mix of forward and reverse primers, 2 μ L of the mix was added to the nuclease free water and the master mix.

Step number	Step description	Temperature ($^{\circ}$ C)	Time (s)
1	Initial denaturation	95	3
2	Denaturation	95	15
3	Annealing an extension	60	60
4	Repeat steps 2-3 for 40 cycles		
5	Melt curve from 60-95 $^{\circ}$ C		
6	Hold	4	-

Table 2.27: Reaction set up for qPCR of ChIP products based on SimpleChIP Universal qPCR Master Mix instructions.

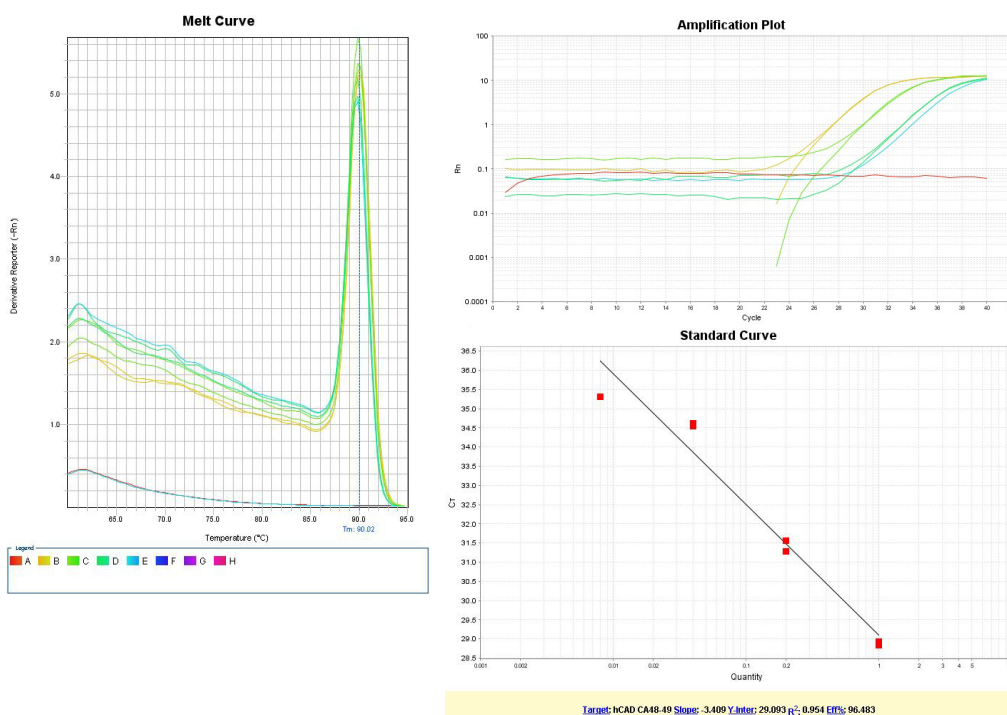


Figure 2.9: Melt Curve, Amplification curve and Standard curve for CA48-F, CA49-R hCAD primers. Primer efficiency was calculated by the Applied biosystems qPCR software as 96.483%.

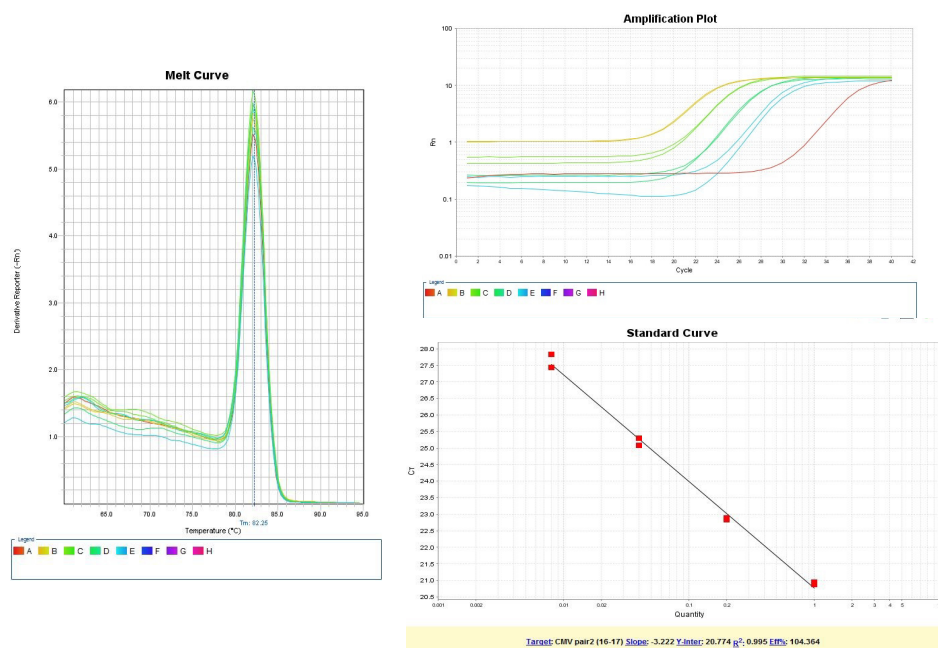


Figure 2.10: **Melt Curve, Amplification curve and Standard curve for CA16-F, CA17-R CMV primers.** Primer efficiency was calculated by the Applied biosystems qPCR software as 104.364%.

2.2.5 Fluorescent imaging of live and fixed cells and image analysis.

2.2.5.1 Live cell imaging

Cells were seeded onto 8-well Ibidi chamber slides in appropriate growth media, if the experiment required synchronisation, or in filming media for single-time point experiments or time lapse experiments without synchronisation. In the former, growth media was removed and replaced with filming media with doxycycline on the day of filming. In the latter, doxycycline was either added the day before filming, when the cells were seeded (such is the case in experiments described in Chapter 3), or at the beginning of the time lapse (unsynchronised time lapsed assays). For short time lapse movies or for single time point imaging data, the final volume in each well was 200 μ L. Drugs that needed to be added were diluted in 50 μ L Leibovit's L15 media (without FBS) at an intermediate dilution so that the final dilution step would be 1:100 and DMSO concentration in wells was 0.1%. Imaging was carried out on an Olympus CellR platform composed of an Olympus IX81 motorised inverted microscope with a 40X NA 1.3 oil immersion objective lens, a Hamamatsu ORCA-CCD Camera, a motorised stage (Prior Scientific), CoolLED- pE-4000 LED illumination system, and a 37°C incubation chamber (Solent Scientific). Micro-Manager was used to acquire and manage the images. A binning of 2 was used for image acquisition, and for all experiments, exposure was set at 150ms (YFP 490 and RFP 550, 70% laser power). Images were acquired as a stacked TIFF format for downstream analysis. For short time-lapse assays, positions of cells were selected under the microscope and time-lapse images were acquired every 15 mins. For longer time-lapse assays images were acquired every hour for 48-96 hours.

2.2.5.2 Fixed cells imaging

Coverslips on microscopy slides were imaged using an Olympus IX83 motorized inverted microscope with a 20X air lens, Spectra-X multi-channel LED widefield illuminator (Lumencor), Optospin filter wheel (Cairn Research), CoolSnap MYO CCD camera (Photometrics), automated XY stage (ASI) and climate chamber (Digital Pixel). Micro-Manager was used to acquire and manage the images. A binning of 1 was used

for image acquisition, and in BrdU experiments DAPI and RFP channels were used; the exposure and intensity of the excitation laser was adjusted accordingly in each experiment to avoid saturating the signal measured.

2.2.5.3 Imaging data collection and storage

All images were collected in the .tiff format and stored together with the metadata files as acquired in dated files on an external hard-drive that remained in the Lindon lab when not in use.

2.2.6 Image analysis

Time-lapse and single time-point images of tFT constructs, were analysed in FIJI using the Multi_Measure macro, a bespoke macro developed previously in the lab by Andrew Ying. As illustrated in **Figure 2.11**, for each cell at each time-point, the macro generates a circular region of interest (ROI) centered on two points manually selected by the user, of 60 pixel diameter, around points traced with the selection tool. The first ROI is in the nucleus and the second in the background outside the cell. The macro then calculates the area, mean, and total fluorescent intensities in all channels for the first ROI after subtracting the values in the third ROI as background.

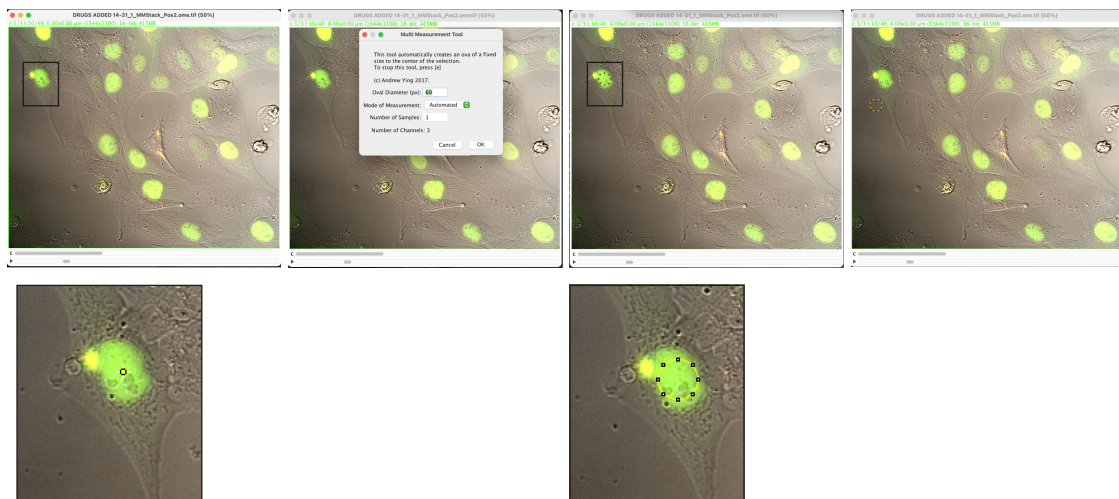


Figure 2.11: **Multi_Measurement Plug In for ImageJ**. Visual summary of the ImageJ tool used for image analysis. Images show steps in sequential order. Call outs show provide a closer view of the tool's ROI generation.

Chapter 2. Materials and Methods

For time-lapse analysis, changes in fluorescence of each single cell analysed were followed through time. The measured values were imported into Excel and the tFT ratio for the nucleus was computed by dividing the total fluorescent intensities of the ROI in the red mCherry and the green mNeonGreen channel. For single time-point analysis, ROIs for all cells in the field were manually generated with the macro and tFT ratios were calculated in excel. Whole-field analysis of time-lapse imaging was performed by first splitting channels and selecting the mNeonGreen channel, then generating a whole-field ROI. The minimum value across timepoints was then averaged and used for background correction of mean values of the whole field, to generate relative fluorescence units (RFU).

BrdU immunofluorescence images were analysed by manual scoring BrdU-positive cells over DAPI-positive cells.

2.2.7 Statistical analysis and curve fitting

2.2.7.0.1 Statistical analysis of single time-point data. Data generated from the image analysis was statistically tested in GraphPadPrism (www.graphpad.com). Normality of the data was assessed using the D'Agostino Pearson test. Data were analysed using Student's t-test or Mann-Whitney U-test for parametric or non-parametric data respectively. Ordinary One-way ANOVA was utilised for multi-group data, where the mean of each column was compared to the mean of the DMSO column. Based on their p-value score, significant results are indicated as $p < 0.05$ (*), $p \leq 0.01$ (**), $p \leq 0.001$ (***) or $p \leq 0.0001$ (****).

2.2.7.0.2 Curve fitting of time-lapse data. Time-resolved data of experiments described in Chapters 5 and 6 were analysed for fold-change analysis of mNeonGreen and mCherry signal and for non linear regression curve fitting. In both cases, data analysis was conducted in Microsoft Excel and visualisation and curve fitting was performed in GraphPad Prism. Specifically, in the first instance data from each cell was normalised to its relative fluorescence unit in the first time-point to yield fold-change increase in stability. Data from multiple cells was then then plotted as replicate values. For analysis

of circadian-synchronised cells, the analysis pipeline was adapted from that used by Dr. John O’Neill’s lab (LMB) for bioluminescence data of circadian-synchronised cells. mNeonGreen imaging data is first analysed in Microsoft Excel. The 24-hour rolling average is calculated from background-corrected data (starting from the 12 hour time-point) by averaging the RFU of the 12 time-points prior and the 12 following. Briefly, the 24-hour rolling average was removed from the RFU data to yield detrended data. This was then imported into Prism and non-linear regression curve fitting was applied. Specifically, a circadian damped cosine wave (without a baseline) was used (**Figure 2.12**) where the only constraint was that the period should be greater than 18. The range of data used for curve fitting was, if needed, adjusted per each curve in order to obtain the most accurate curve fitting. In other words, if noise in the data was recorded toward the end of the movie, the curve was fitted until the last time point before the start of the noise. From the curve fitting, the period of the oscillation was generated. The data from the resulting curve was analysed by defining the Area Under the Curve (AUC) to yield X and Y values for all the peaks in the curve. The Y values were plotted as amplitude. The average curve with standard error of the mean was then generated.

$$Y = ((m * X) + C) + amplitude * exp(-k * X) * cos(((2 * pi * (X - phase)) / period))$$

Figure 2.12: **Circadian Damped Cosine wave.** Shared by Dr. John O’Neill

X: Time

Y: Signal

Amplitude: Height of top of wave, at the beginning;

Wavelength: Time it takes for a complete cycle, in units of X

Frequency: Number of cycles per time unit (inverse units of X)

k: Rate constant of decay

PhaseShift: First time when Y=0, in time units of X axis.

HalfLife: How long it takes (in units of X) to decay to half the original amplitude

2.2.8 mRNA extraction and quantification by RT-qPCR

For analysis of mRNA levels of hPER2 and Myc-tFT constructs, post circadian synchronisation, cells were temperature cycled according to the previously described protocol and extracts were made at 0, 12, 18, 24, 30, and 36 hours by trypsinisation. Cell pellets were frozen until all samples were made; mRNA extraction from the cell pellets was carried out utilising the Monarch® Total RNA Miniprep Kit (reagents listed in **Table 2.11**). mRNA yields were assessed by NanoDrop™ Lite Spectrophotometer and stored at -80°C. RNase Zap was used throughout any mRNA handling procedure to ensure mRNA integrity. Changes in hPER2 and Myc-tFT mRNA over time were assessed by One-Step qPCR (according to manufacturer instructions) with the primers listed in **Table 2.12** and utilising the CFX Opus 384 Real-Time PCR System. Ct values were exported and $\Delta\Delta C_t$ values were calculated on Microsoft Excel and visualised on GraphPad Prism.

2.3 Materials and methods for work undertaken at AstraZeneca

Work described in Chapter 4 was undertaken during a 6 month placement at AstraZeneca's Darwin site in Cambridge. As detailed in Chapter 4, the tFT assay for Myc stability measurement was adapted to a higher-throughput platform. The materials and methods utilised are described in this section.

2.3.1 Cell culture and seeding

The Myc-tFT cell line was maintained according to the same method described in previous section with these differences: cells were cultured in T75 flasks (Corning®, CLS430641) and in media (DMEM) lacking antibiotic and antimycotic additives to conform to AstraZeneca's standard cell culture requirements. Experimental work required upscaling of the format of the assay to 384-well plates with a semi-automated processes of cell counting and seeding. Specifically, cells were counted and viability was assessed using the Vi-CELL XR Cell Viability Analyzer (Beckman Coulter, 731196) and seeded using a Multidrop™ Combi liquid dispenser (ThermoFisher, 5840300)

2.3. Materials and methods for work undertaken at AstraZeneca

into Greiner CELLSTAR®384 well plates (flat bottom clear polystyrene wells with lid and micro-clear bottom, sterile; Sigma Aldrich, M1937). Cells were seeded in either DMEM without phenol red (Sigma Aldrich, D4947) supplemented with GlutaMAX™ (ThermoFisher, 35050061) or Leibovit's L15 (as detailed above), both with 10% Foetal Bovine serum (FBS) and Doxycycline (final concentration as previously detailed). Cells were maintained in an incubator at 37°C, 5% CO₂, 95% humidity.

2.3.2 Compound dosing

Compounds used in this study and DNA stain Hoechst 33342 (20mM, Thermo Fisher, 62249) were dosed directly into the destination cell plate via acoustic dosing with a Labcyte Echo Acoustic Droplet Ejection (Echo555 Liquid Handler). All compounds or DMSO for the medium-throughput assays were dispensed from source plates directly into cell assay plates using an Echo 555 Acoustic dispenser (Labcyte Inc™). To generate compound dose curves, source plates were prepared by the Compound Management group in AstraZeneca with 10mM compound stocks diluted 1:100 using DMSO to give four intermediate dilutions (10mM, 100µM, 1µM, 10nM). This intermediate plate was then used by the Echo to dispense compounds and DMSO directly into the cell plates with a 12 point dose range (30, 10, 3.125, 1.25, 0.3, 0.1, 0.03125, 0.0125, 0.003, 0.001, 0.0003125, 0.00003 µM). Where required, all compound dispenses were also backfilled with 100% DMSO to maintain a fixed total DMSO concentration in each well of 0.3%.

2.3.3 Image acquisition and analysis

Cells were imaged on a CellInsight™ CX5 High Content Screening (HCS) Platform utilising the Compartmental Analysis.V4 protocol with a 10X air objective, binning 4x4, and three channels (BGFR 386, 485, 549). Exposure time was set at 50% Target Exposure on DMSO control wells. Each plate was given a barcode prior to the start of the image acquisition to allow for cross-reference between software. Imaging and analysis of each image was done in parallel using HCS Studio. Specifically, assay parameters were set up with the help of Mr. Philip Hopcroft, in HCS studio as follows:

- **Image Processing:** 3D Background removal for all 3 channels was performed.

Chapter 2. Materials and Methods

- **Primary object identification, validation and selection:** Primary objects were identified in Channel 1 (Hoechst staining) by applying smoothing (value 1), thresholding (isodata, value -0.1), and segmentation (Shape, value 3); and validated, whereby objects at the border were removed (Object.borderObjectCh1 was selected), as well as those with small or very large area (Object.Area.Ch1 low=41.46, high=220.14), and those with odd shapes (Object.ShapeP2A.Ch1 low=1.07, high=1.36). Selected objects were then identified to exclude nuclei that did not express detectable Myc-tFT from analysis. Selection of primary objects was carried out in Channel 2 (mNeonGreen; Object.AvgIntensityCh2, low=300 high=16000) and Channel 3 (mCherry; Object.AvgIntensityCh2, low=0 high=16000).
- **Spot identification and primary object filtering:** This function identified spots or rings or circles of intensities above the parameters set. Spot identification for Channel 2 and 3 was turned on according to thresholding values, according to which all positive objects were full of spots.

The image features stored for analysis were:

- **Cell Features:** These refer to the stored features for each individual cell (or object) identified in the field. The features chosen to save were: average intensity of mNeonGreen signal (CircAvgIntenCh2), mCherry signal (CircAvgIntenCh3) and the tFT ratio of each cell (CircAvgIntenRatioCh3Ch2).
- **Well Features:** The features chosen to save were: percentage of selected objects, mean (of the field) average intensity of the cells in Channels 2, 3 and ratio of 3/2 (MEANCircAvgIntenCh2 and 3 and MEANCircAvgIntenRatioCh3Ch2). In addition to these, additional features are automatically saved: number of Hoechst-positive cells (valid object count0), number of mNeonGreen positive cells (selected object count).

2.3.4 Data analysis

Whole-field analysis of well feature data was carried out using Genedata Screener software. This integrated the images and data from each plate (identified by a barcode) and offered a multitude of data analysis and visualisation tools. This software could not however, be used for analysis of single-cell data which was analysed with GraphPad PRISM. Ordinary One-way ANOVAs were utilised to assess the significance of any effect the compounds had when compared to DMSO.

Chapter 3

Generation and validation of a suitable Myc Stability Sensor

3.1 Introduction

The MYC oncogene encodes a transcription factor that binds to open chromatin by recognising a six-base sequence called an E-box (5'-CACGTG-3') that is found in gene promoter regions throughout the genome. The ease of target gene binding and the vast array of targets allows Myc to drive transcription of a plethora of genes involved in many aspects of cellular proliferation and metabolism (Conacci-Sorrell, McFerrin, and Eisenman, 2014). For this ability it has been referred to as “a master regulator of transcription” and its over-expression is highly beneficial to cancerous cells that harness the pleiotropic activity of Myc to divide uncontrollably, avoid programmed cell death (apoptosis) and evade the host’s immune system. Indeed Myc is a converging node that cannot be bypassed for multiple pathways that promote proliferation, making Myc a highly desirable drug target. There are many ways by which Myc levels are increased in cancer cells and while the gene is often amplified or translocated to more active loci, the otherwise tight control of the protein, achieved in healthy cells through protein-protein interactions and post-translational modifications (PTMs), is often lost. This leads to an increased half-life of the oncogenic protein that is short-lived (half-life of ~30 minutes) in normal physiological conditions (Dang, 2012; Soucek and Evan, 2010). The highly

Chapter 3. Generation and validation of a suitable Myc Stability Sensor

unstructured nature of this oncogenic protein, which lacks an exploitable enzymatic binding pocket for compound binding, has made targeting it through traditional pharmacological approaches very challenging. Some of the inhibitors that rely on protein-protein interaction interfaces typically have low binding affinities and display inhibition only at high concentrations *in vitro*. Furthermore, potent inhibition **in vitro** often does not translate to potent inhibition *in vivo*. For this reason, no Myc inhibitor has yet made it to the clinic. Recent approaches have focused on restoring regulation of Myc at the protein level, through indirect inhibition of interacting partners that promote its accumulation and stability (Dang et al., 2017). This exciting new therapeutic avenue is hindered by the lack of high-throughput *in vitro* assays to measure changes in Myc stability in response to drug treatment.

While many studies have been carried out to investigate Myc protein stability, none have done so with the use of single-cell live imaging assays that are able to report on protein stability. We believe that such an approach will not only be beneficial for the development of a higher throughput assay to perform drug screening for compounds that affect Myc stability, but also might allow for the identification of regulatory mechanisms of Myc stability at the single-cell level that would otherwise not be recorded with techniques that look at cell populations. Therefore, we propose the use of tandem Fluorescent Timers (tFTs) in the investigation of Myc stability and in this chapter specifically I will discuss the generation and validation of a suitable Myc-tFT construct.

Developed by Michael Knop's lab (Khmelniskii et al., 2012), tFTs are a novel microscopy-based tool to assess protein age and stability at a single-cell level. tFTs exploit the differing maturation kinetics of various fluorophores (FPs) tagged in tandem to the protein of interest (POI). To understand how tFTs function, it is important to understand the concept of FP maturation: for a FP to be functional (i.e. fluoresce), the newly-synthesised peptide must undergo a series of chemical processes within its chromophore. Prior to the completion of maturation processes, the FP, although synthesised, is not fluorescent (Olenych et al., 2007). FP maturation varies between FPs and is quantified by the maturation half-life (the time needed for the FP to reach

half its maximum fluorescence), which is a key determinant in the choice of FPs in the tFT system. This be explored in section **Sections 3.2.1 and 3.2.3.1**. Because in the tFT FPs are tagged in tandem at the C-terminal end of the POI, both are translated at the same time. The difference in maturation kinetics of the FPs, one faster and one slower, provides temporal information and allows for an estimation of the age of the POI. This can be measured as the ratio between the fluorescent signal of the slowFP (slow-maturing FP) to that of the fastFP (fast-maturing FP).

Several key studies have demonstrated the versatility of tFTs for the study of protein dynamics. The Knop lab demonstrated so in a proof-of-concept study carried out in *S. cerevisiae* whereby they utilised tFTs to investigate how nuclear pore complexes were trafficked at the sub-cellular level (Khmelninskii et al., 2012). In a high-throughput single-time point screen they were able to identify components of the N-end rule pathway responsible for changes in the stability of their POI. Firstly, they investigated the differential inheritance of spindle pole body (SPB) protein Spc42 pools between mother and daughter cells. Tagging of Spc42 with fast folding sfGFP (superfolder GFP) and slower folding mCherry in tandem revealed age-dependent segregation of the SPB between mother and daughter cells during mitotic division, with the older pool of Spc42 (with higher mCherry/sfGFP ratio) being directed to the daughter cell. To further characterise the accuracy of the tFT readout they generated a tFT (mCherry sfGFP-based) with a degron (degradation signal) at the N-terminus of mCherry. Variations of this N-degron showed differing protein stability as read out by the tFT ratio which matched the predicted stability of the construct: the more destabilising the N-degron motif, the lower the tFT ratio. Finally, they demonstrated that tFTs were a viable tool for screening for modifiers of protein stability by utilising various N-degron-tFTs with the same combination of FPs transfected in a genome-wide library of yeast gene deletion mutants. With the use of a plate-reader Khmelninskii et al. (2012) were able to capture whole-colony fluorescence intensities in a robust and high-throughput manner, leading to identification of components of known yeast degradation pathways. In a follow up study Donà et al. (2013) applied tFTs to investigate cell migration during embryogenesis

Chapter 3. Generation and validation of a suitable Myc Stability Sensor

in zebrafish. Previous studies had shown that during zebrafish embryogenesis, a stripe of chemokine Cxcl12a drives the migration of over 100 cells. While the process by which this self-generated gradient is formed was previously unclear, this work elucidated the process by proving that polarised ligand-receptor internalisation drives the gradient process. In more detail, through the use of tFTs they were able to measure Cxcr7 receptor turnover which is determined by Cxcl12a chemokine gradient. In other words, the higher the chemokine concentration, the more rapid the internalisation of the receptor, and the shorter the receptor lifetime. With this they could for the first time prove *in vivo* that self-generated chemokine gradient is able to direct cell migration. In a subsequent publication Khmelinskii et al. (2016) demonstrated that sfGFP resistant to degradation and therefore a poorer choice for reporting on cellular protein turnover than another other fastFP mNeonGreen.

3.2 Design of Myc-tFT construct and generation of a stable cell line

3.2.1 Choosing the appropriate combination of Fluorophores for Myc-tFT

When designing a tFT there are several parameters that influence the choice of FPs to be used in combination.

Firstly, the FPs must be different colours with non-overlapping spectra. Secondly, the FPs must be chosen according to their maturation kinetics as the optimal choice will allow reporting with highest sensitivity of the changes in stability of the POI. More specifically, the maturation time of the two FPs should be different:

1. **The fastFP should have as fast a maturation time as possible in order to report on the pool of the POI.** This allows discerning between lack of maturation and fast degradation in case the fastFP's maturation is slower than the half-life of the protein. FastFPs often emit in the green spectrum.
2. **The slowFP should have a similar but slightly longer maturation time than**

3.2. Design of Myc-tFT construct and generation of a stable cell line

the half-life of the POI. If the the slowFP's half-maturation time is faster then the POI's half-life, it would not allow for detection of slowing degradation rates. However, if the slowFP maturation time exceeded the POI's half-life greatly, the former would never mature and produce a fluorescent signal detectable for use in the tFT. SlowFPs often emit in the red or orange spectra.

3. The larger the difference between slow and fast, the greater the dynamic range of the sensor.

Another aspect that greatly influences the choice of FPs is the possibility of overlap in their emission and excitation spectra. Indeed, if these overlap there is distance-dependent excitation by a donor FP of an acceptor FP, a process known as fluorescence resonance energy transfer (FRET). The process of FRET between the slowFP (donor) and fastFP (acceptor) would lead to an incorrect estimation of protein age as it could lead to an increase in tFT ratio. Brightness of the FPs is another influencing factor. These should have a good signal-to-noise ratio to ensure appropriate measurement of FP intensity. This is determined not only by the FP itself but also by the equipment used to image the tFTs. Oligomerisation of the FPs in tandem should be evaluated as it can influence the localisation and, therefore, function and protein-protein interactions of the POI. Consequently, oligomerised FPs may produce a read-out of protein stability that does not reflect that of the endogenous POI. A screen of differing combinations of FPs will highlight the optimal pairing of FPs. It is important to verify appropriate localisation of the POI once in tandem with the chosen FPs and that the half-life of the POI-tFT construct is not significantly different to that of untagged POI due to the presence of the FP tags themselves. Of final note, pH fluctuations can also influence the tFT readout so the choice of FPs should also be determined based on the pH conditions they would be utilised under.

Information on candidate FPs previously utilised in tFTs in the Lindon lab can be found in **Table 3.1**. These were all considered suitable in terms of pH and brightness under our imaging conditions by other members of the Lindon Lab. In the Knop lab's follow-up study, Khmelinskii et al. (2016) highlight that degradation of sfGFP

Chapter 3. Generation and validation of a suitable Myc Stability Sensor

is incomplete due to the fast-folding conformation which also makes it resistant to unfolding at the proteasome. This hinders appropriate measurement of protein turnover by tFT and therefore mNeonGreen is advised as a more appropriate fastFP choice. Given this information, and the knowledge of the half-life of Myc is ~ 30 minutes (Dang, 2012; Soucek and Evan, 2010), I decided to generate two Myc-tFT constructs: Myc-mCherry-mNeonGreen and Myc-mRuby-mNeonGreen. Due to the closer timing of mCherry maturation time to the half-life of Myc, compared to mRuby, the prediction is that mCherry is better suited for reporting on Myc stability, however both FPs were tested to confirm this hypothesis. Assessment of oligomerisation, stabilisation and hindrance to functionality of Myc by the tags will be addressed in **Sections 3.3, 3.4 and 3.5**.

FP name	λ_{ex} (nm)	λ_{em} (nm)	Maturation time (min)	kDa
sfGFP	485	510	5.6	26.7
mNeonGreen	506	517	10	26.7
mVenus	515	527	17	26.9
TagRFP	555	584	100	27.6
mRuby	558	605	168	25.2
mRuby2	559	608	150	26.5
mRuby3	558	592	130	26.6
FusionRed	580	608	130	25.6
mCherry	587	610	~ 40	26.7
mKate2	588	633	20	26.1

Table 3.1: **FP maturation times.** Table illustrating common features for available FPs. Values reported are from Balleza, Kim, and Cluzel (2018), Khmelinskii et al. (2016), and Lambert (2019).

λ_{ex} : excitation wavelength in nanometers (nm)

λ_{em} : emission wavelength in nanometers (nm)

kDa : protein molecular weight (MW) in kilo-Daltons

3.2. Design of Myc-tFT construct and generation of a stable cell line

3.2.2 Generation of tFT constructs

The cloning strategy for the generation of Myc-tFT constructs is outlined in **Figure 3.1** and all primers and plasmids mentioned in this section can be found in the **Methods Section**.

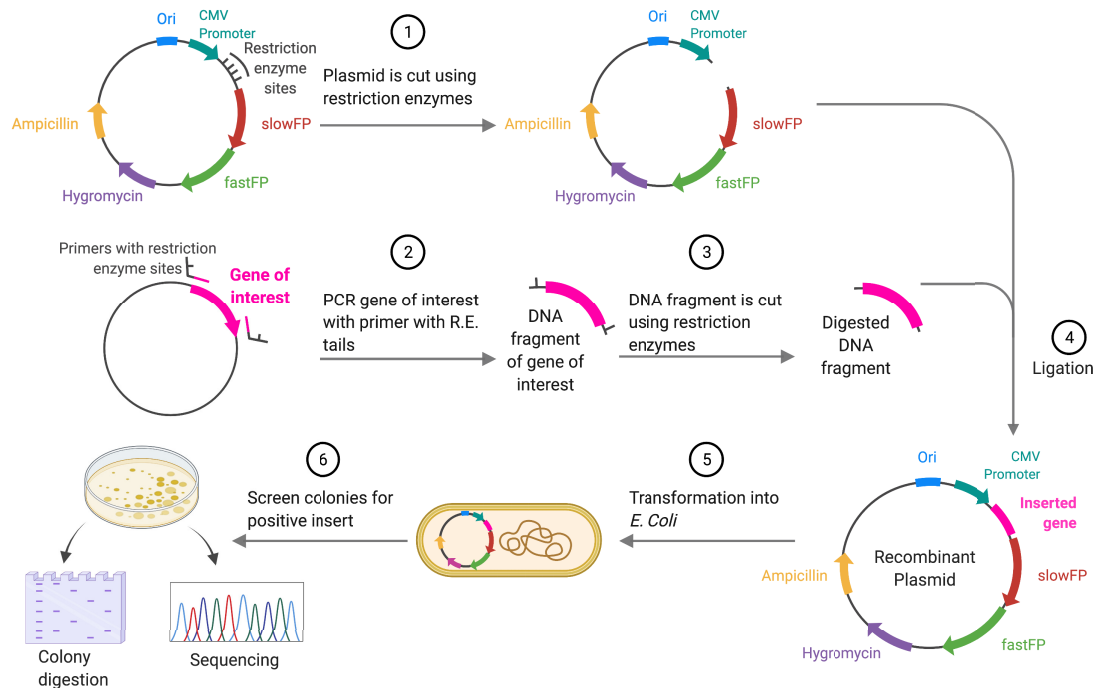


Figure 3.1: **tFT construct cloning strategy**. Schematic representation of cloning strategy adopted for generation of tFT constructs:

1. The tFT backbone plasmid is cut with two differing restriction enzymes (R.E.) selected from a list of common R.E. that do not cut within the sequence of the gene of interest
2. In parallel, the gene of interest is cloned out of another plasmid by PCR with primers that contain tails with R.E. (corresponding to those chosen in 1.) sites flanking the 5' and 3' end of the plasmid
3. The resulting amplified DNA fragment is cut using the same R.E. present in the tails and in the backbone generating a digested DNA fragment containing the gene of interest
4. The digested DNA fragments (plasmid backbone and gene of interest) are ligated together to generate a recombinant plasmid with the desired gene flanked at the 3' by the slowFP and fastFP
5. The recombinant plasmid is transformed into *E. coli* bacteria strain DH5 α to amplify the plasmid
6. Bacterial colonies are screened by colony digestion and by sequencing for the correct insert.

Chapter 3. Generation and validation of a suitable Myc Stability Sensor

Firstly, based on the available cloning sites on the tFT backbone, I checked for restriction enzymes that did not cut within the gene of interest (KpnI and BamHI for Myc and HindIII and KpnI for n-Myc). Next, I designed primers to amplify both Myc isoforms (Myc and n-Myc) with tails containing the restriction enzymes sites, and performed the polymerase chain reaction (PCR) required to generate such fragments. The plasmids used to amplify the Myc isoforms are listed in the Methods section. Both the backbone and fragment containing the gene of interest are then digested with the appropriate R.E. and ligated to form a recombinant POI-tFT plasmid. This is then cloned into *E. coli* and colonies are screened by restriction enzyme digest and sequencing to find a plasmid with the correct construct. This strategy was followed to insert Myc isoforms in a pcDNA5 mCherry-mNeonGreen backbone. To summarise four Myc-tFT constructs were generated: Myc-mCherry-mNeonGreen; nMyc-mCherry-mNeonGreen and Myc-mRuby-mNeonGreen. A mutant version of Myc (T58A) was constructed and its use will be discussed in **Section 3.4**. Maps of all the plasmids generated for this work can be found in **Figure 3.2**.

3.2. Design of Myc-tFT construct and generation of a stable cell line

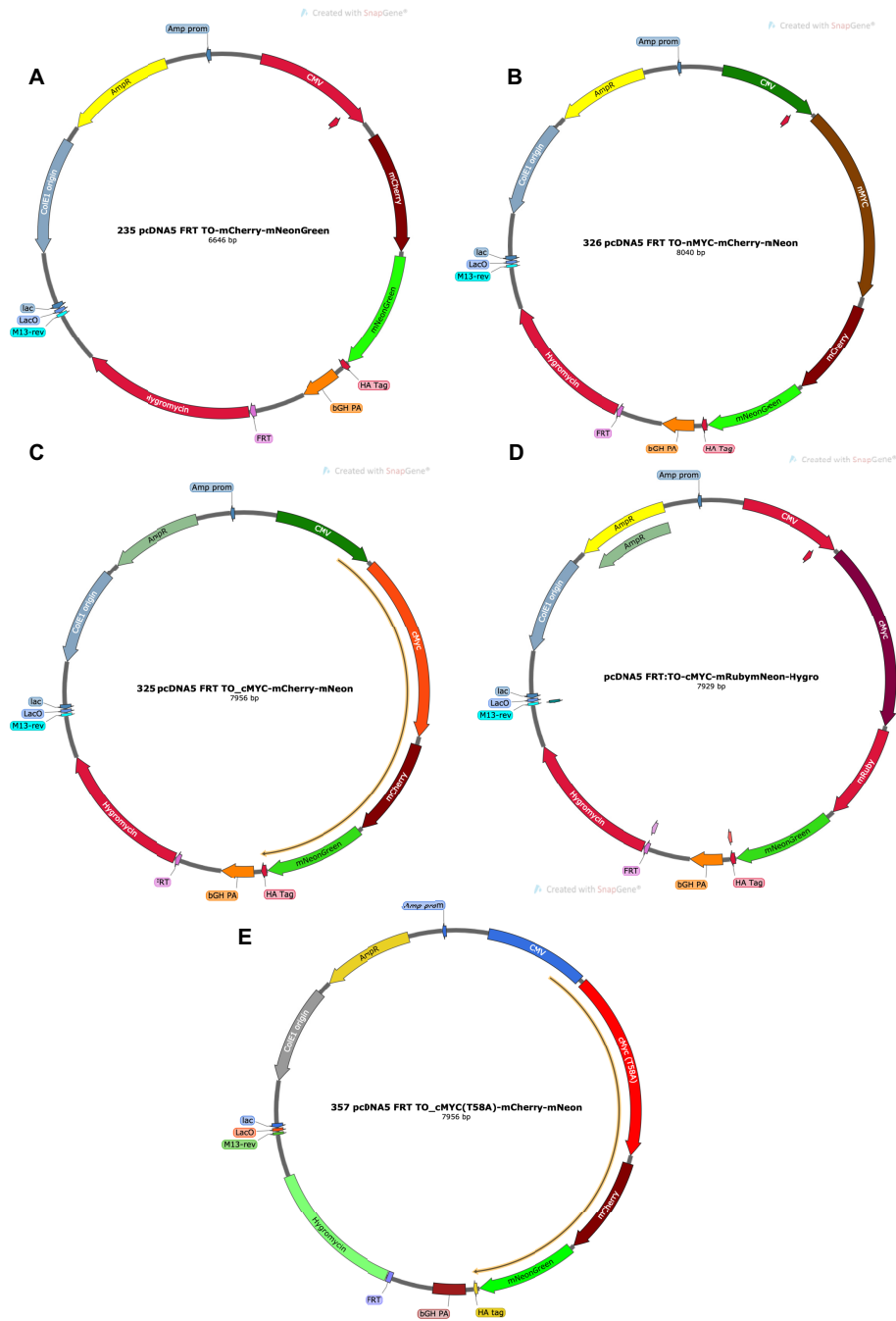


Figure 3.2: **Plasmid maps of tFT constructs:** All the plasmids shown in this figure were used for this work. Plasmid Maps were generated using SnapGeneViewer.

- A Original tFT plasmid used to generate the other versions of the tFTs used in this work
- B nMyc-mCherry-mNeonGreen
- C Myc-mCherry-mNeonGreen
- D Myc-mRuby-mNeonGreen
- E Mutant Myc(T58A)-mCherry-mNeonGreen

3.2.3 Generation of Myc-tFT stable inducible cell lines

3.2.3.1 Selection of slowFP for Myc-tFT

The Myc constructs were transiently transfected in U2OS (osteosarcoma immortalized cell line) cells to confirm which slowFP is best at reporting on Myc stability and that the presence of the tags at its C-terminus does not disrupt its localisation. The FRET signal between the two combinations of FPs had been previously assessed in the lab and no FRET had been found to occur with our imaging set up (data not shown). The possible effect of the tags on the function of Myc will be addressed in **section 3.5**.

Myc-mCherry-mNeonGreen and Myc-mRuby-mNeonGreen constructs were transfected with lipofectamine into U2OS, and imaged the following day. The result of the transfection can be seen in **Figure 3.3 A** where a snapshot image of both constructs is shown expressed in a cell. Appropriate nuclear localisation is apparent for both Myc constructs thus demonstrating that C-terminal tagging of Myc-tFT with either combination of fluorophores does not alter localisation. From **Figure 3.3 A** it appears that in cells with similar levels of mNeon signal, the slowFP signal is lowest in the mRuby-based tFT. To quantify this observation, background-corrected slowFP was plotted against fastFP and linear regression was performed. Representative data and the linear regression equation of one of n=3 experiments is displayed in **Figure 3.3 C**. The slope of the linear regression of the mCherry-based construct is greater than that of the mRuby-mNeonGreen, although the former construct had more cells with brighter fastFPs. To account for this, I repeated the analysis on cells with a fastFP signal of fewer than 600 fluorescence intensity units over background and confirmed that for similar fastFP fluorescence levels, the slowFP signal is higher in the Myc-mCherry-mNeonGreen constructs (**Figure 3.3 D**). This supports the earlier prediction as the half-life of Myc is much shorter than the half-maturation time of mRuby.

The greater pool of protein fluorescing in the slowFP recorded in the mCherry-based construct should, according to the tFT model, yield a higher tFT ratio than the mRuby version. This was demonstrated in the analysis of live cell imaging experiments (**Figure**

3.2. Design of Myc-tFT construct and generation of a stable cell line

3.3 B).

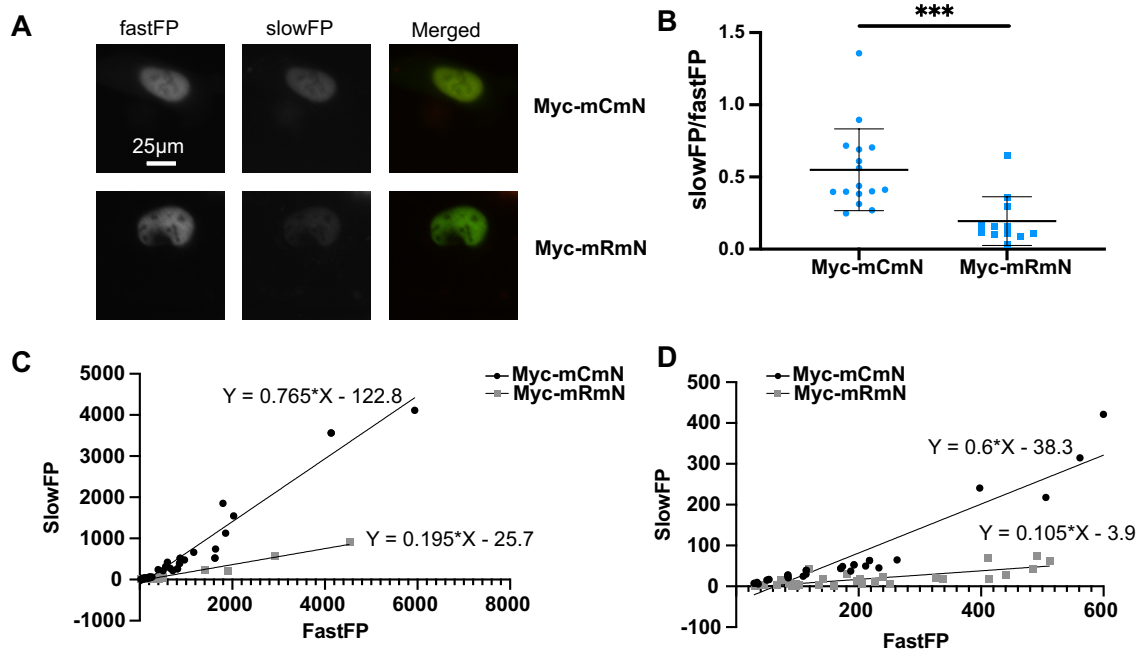


Figure 3.3: **Images of Myc-tFT transfected cells.** U2OS cells were transfected with either Myc-mCherry-mNeonGreen (Myc-mCmN) or Myc-mRuby-mNeonGreen (Myc-mRmN) constructs and imaged under the same imaging parameters. Representative data of n=3 experiments.

- A Single-channel and merged images representing a U2OS cell transfected with either Myc-mCherry-mNeonGreen or Myc-mRuby-mNeonGreen. Acquisition settings were set as the same to allow comparison of brightness between the constructs.
- B Quantification (mean+SD) of the tFT ratio of slowFP/fastFP for cells transfected with either construct and acquired in parallel, representative data of n=3. P of n=3: * p=0.0485
- C,D Each point represents the background-corrected slowFP versus fastFP of a cell (only cells with fastFP ≤ 600 are plotted and used for analysis in D). This was plotted alongside linear regression (equation displayed on chart). Myc-mCherry-mNeonGreen (black circle), Myc-mRuby-mNeonGreen (grey square).

The images were analysed using an ImageJ plug-in designed by a previous student in the lab (Andrew Ying). This plug-in is based on the point tool on imageJ and will construct a circular region of interest (ROI) of a specified pixel radius around the point selected. For my analysis, I set the radius to a pixel size that allows me to cover most of the nucleus, which varies in size depending on acquisition settings. I select a point in the middle of the nucleus (signal) and one in an area with no signal close to the cell (background). The plug-in will generate pairs of ROIs (signal and background),

Chapter 3. Generation and validation of a suitable Myc Stability Sensor

measure the average intensity of each ROI in all the channels present in the image and then subtract the average background intensity from the average signal intensity to output an average background-corrected intensity signal for the cell nucleus. The background value is also displayed in the output to allow monitoring of background noise throughout the image or time-course. This process is repeated for each cell in the field.

Another determining factor for slowFP selection is that it should be sensitive to stabilisation of the protein. To test this, cells expressing either construct were treated with proteasomal inhibitor MG132, which leads to overall protein accumulation and stabilisation, or its vehicle control DMSO. This allowed me to evaluate which construct best reports rapid changes in Myc-tFT stability. Cells were imaged every at 0, 60 and 120 minutes post-treatment.

Representative images of cells expressing either construct and treated with MG132 or DMSO are shown in **Figure 3.4**. The results of this experiment (**Figures 3.4 and 3.5**) demonstrate that increased Myc stability, achieved through inhibition of the proteasome by MG132, is better measured by the mCherry version of the tFT than the mRuby.

Interpretation of the data is complicated by the differential baseline tFT ratio between the two tFTs in DMSO control. To mitigate this, fold changes in ratios were used to compare the effects of treatments within constructs. Furthermore, there is an appreciable increased stability over time in the DMSO control over time, as shown in **Figure 3.5 A**, which will be further investigated in a later chapter. The effect of MG132 on tFT ratios becomes more apparent at the single-cell level, in data where each cell's tFT measurement through time is normalised to its ratio at the beginning of the experiment. This yields fold changes in tFT ratio and allows appropriate comparison of changes in stability through time. Normalised data (**Figure 3.5 B**) highlights that Myc-mCmN, and not Myc-mRmN can measure the greater increase in Myc stability that is expected under MG132 versus DMSO treatment and confirms that tFTs can indeed be used to measure changes in Myc protein stability at the single-cell level.

3.2. Design of Myc-tFT construct and generation of a stable cell line

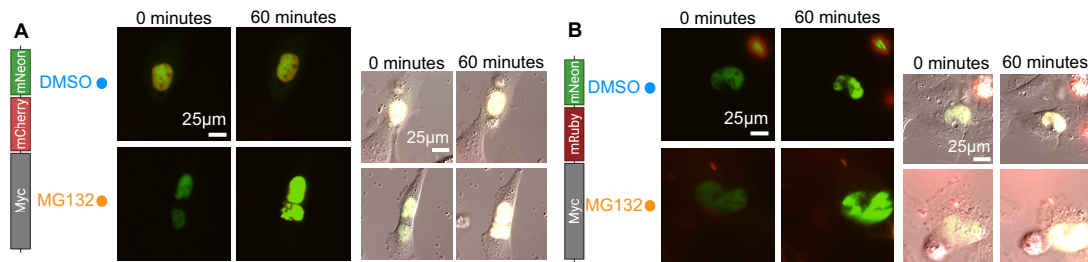


Figure 3.4: **Images of Myc-tFT transfected cells treated with MG132 or vehicle control.** U2OS cells were transfected with either Myc-mCherry-mNeonGreen or Myc-mRuby-mNeonGreen constructs; treated with either MG132 (4.2 μ M) or vehicle control DMSO. Both constructs and treatments were imaged within the same experiment and under the same imaging parameters. Representative data of n=3 experiments.

- A Representative image of a U2OS cell transfected with Myc-mCherry-mNeonGreen treated with MG132 or DMSO. Merged image of the slowFP and fastFP channels (left panel); merged image of slowFP, fastFP and brightfield (right panel)
- B Representative image of a U2OS cell transfected with Myc-mRuby-mNeonGreen treated with MG132 or DMSO. Merged image of the slowFP and fastFP channels (left panel); merged image of slowFP, FastFP and brightfield (right panel)

mCherry was selected to create tFTs for nMyc, Myc and empty vector (tFT only) cell lines.

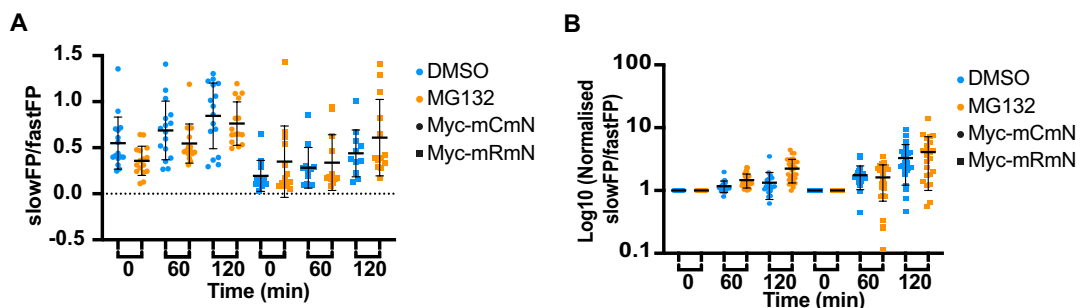


Figure 3.5: **Effect of proteasomal inhibition on slowFP/fastFP ratios.** U2OS cells were transfected with either Myc-mCherry-mNeonGreen or Myc-mRuby-mNeonGreen constructs; treated with either MG132 (4.2 μ M) or vehicle control DMSO. Both constructs and treatments were imaged within the same experiment and under the same imaging parameters. Representative data of n=3 experiments. Each dot represents data from a single cell; Mean and SD are shown.

- A tFT ratio (slowFP/fastFP) measurement for each construct [Myc-mCherry-mNeonGreen (circle); Myc-mRuby-mNeonGreen (square)] over time in either DMSO (blue) or MG132 (orange) conditions.
- B Log₁₀ of fold change in tFT ratio. Single-cell measurement for each construct [Myc-mCherry-mNeonGreen (circle); Myc-mRuby-mNeonGreen (square)] in DMSO (blue) and MG132 (orange) conditions were normalised to their 0 min value.

3.2.3.2 Cell line generation by Flp-In^(TM) T-Rex^(TM) system

Having established mCherry-mNeon as the most appropriate tFT for Myc in transient transfection experiments, I made stable cell lines that would be inducible for expression of Myc-mCmN. A cell line stably expressing the construct is essential in order to obtain more homogenous expression levels, which is crucial for its use in drug screening assays. Inducible expression allows for controlled Myc expression which is needed to limit its transformative abilities. Cell line generation was achieved by utilising the Flp-In^(TM) T-Rex^(TM) (ThermoFisher) system a in Flp-In^(TM) T-Rex^(TM) host cell line which expresses the tetracycline repressor, allowing for tetracycline(Tet)/doxycycline(Dox)-inducible expression of what is integrated in the FRT site following recombination (system depicted in **Figure 3.6**). Briefly, the Flp-In^(TM) T-Rex^(TM) system works by homologous recombination between the FRT sites of the host cell line and those present in the transfected pcDNA5/FRT/TO plasmid. This recombination is catalysed by pOGG44 (plasmid)-driven expression of Flp recombinase which is co-transfected with the previously mentioned plasmid. The pcDNA5/FRT/TO plasmid contains, downstream of the FRT site, a promoter composed of CMV (cytomegalovirus) and two TetO₂ response elements to control expression of the gene of interest (in this case any of the tFT constructs) and a hygromycin resistance cassette.

The choice of host cell line for the previously described integration of tFTs was between the following available cell lines: human U2OS (osteosarcoma line), RPE-1 (retinal pigment epithelium immortalised line) and HeLa (ovarian cancer line). U2OS cells were chosen as they had been previously shown to have low levels of endogenous Myc (Altman et al., 2015; Walz et al., 2014) and because they are particularly well-suited for imaging experiments.

Cell lines expressing each of the constructs (Myc-tFT, n-Myc-tFT and tFT only) were generated according to the protocol described in the Methods section. The brightest clones for the Myc isoforms tFTs and least bright tFT only clone, displayed in **Figure 3.7**, were used for the following experiments described in this work. It is worth noting the tFT with no POI at its N-terminus does not solely localise to the nucleus, confirming

3.2. Design of Myc-tFT construct and generation of a stable cell line

that the nuclear localisation of Myc-tFTs is Myc-driven.

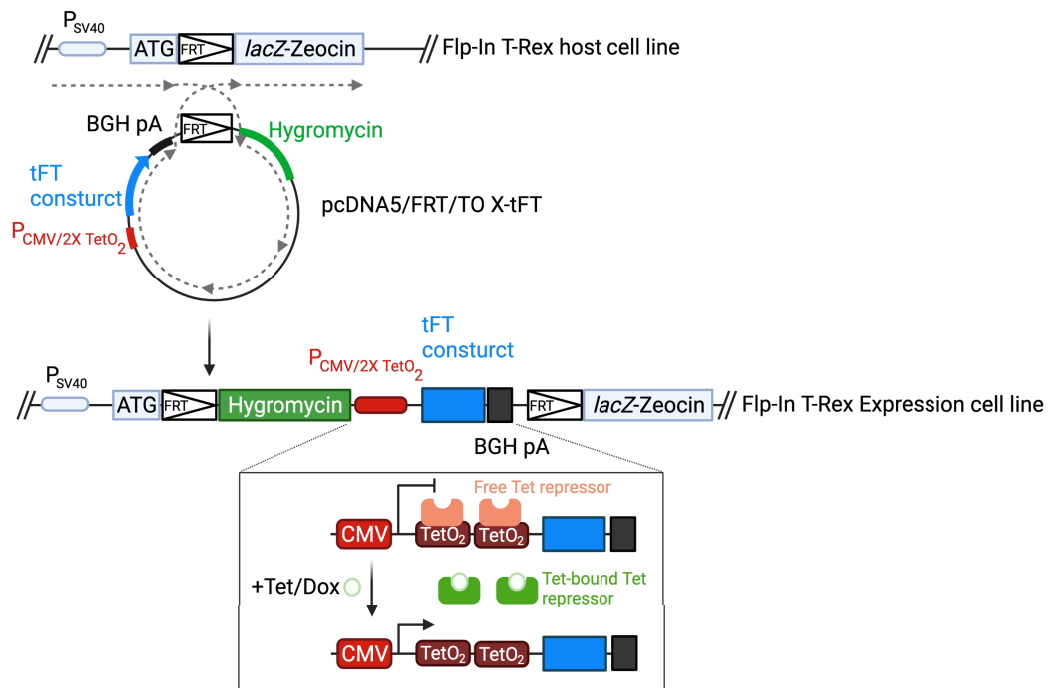


Figure 3.6: **Flp-In^(TM) T-Rex^(TM) System.** Depiction of the system as adapted from ThermoFisher. The system allows homologous recombination between the FRT sites of the host FRT/TO cell line and those present in the pcDNA5/FRT/TO plasmid transfected. This recombination is catalysed by pOGG44 (plasmid)-driven expression of Flp recombinase which is co-transfected with pcDNA5/FRT/TO X-tFT (X is the POI). This allows for the integration of the gene of interest under CMV TetO₂ and switch in resistance from Zeocin to Hygromycin. The callout at the bottom shows the workings of the TetO₂ promoter: two repressors bind the TetO₂ promoter and inhibit CMV-driven transcription. Addition of tetracycline or doxycycline, which bind the repressors, releases the TetO₂ promoters and thereby allows CMV to drive transcription.

ATG Translation initiation codon.

FRT FRT site.

P_{CMV/2xTetO₂} Promoter containing a CMV sequence and two TetO₂ elements to which the Tetracycline (Tet) repressors can bind when not sequestered by tetracycline (Tet) or doxycycline (Dox).

BGH pA Bovine Growth Hormone polyadenylation signal; termination sequence for eukaryotic protein expression.

Chapter 3. Generation and validation of a suitable Myc Stability Sensor

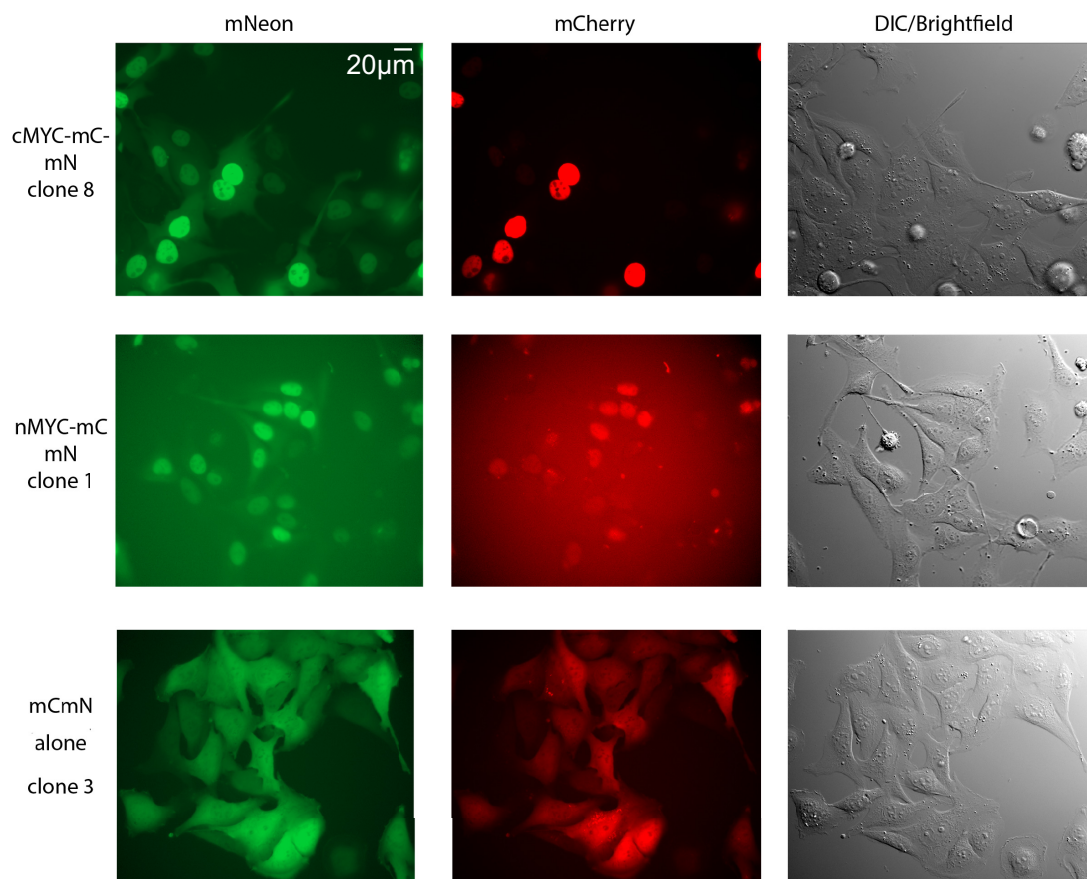


Figure 3.7: **tFT cell lines.** Images representing the selected clones for each U2OS FRT/TO cell line expressing a tFT construct. Cells were imaged under the same imaging conditions to allow for comparison of brightness and selection of clones for further experiments.

3.2. Design of Myc-tFT construct and generation of a stable cell line

To confirm correct integration of the Myc-tFT in the FRT site of clone 8, I performed a proliferation assay under Zeocin pressure. If correct integration occurred, then cells would be Hygromycin positive (confirmed by selection of clones) and Zeocin sensitive while the parental line is Zeocin sensitive. For this experiment I seeded 20,000 cells (U2OS FRT/TO or U2OS FRT/TO Myc-tFT) in each well of a 12-well plate and 24-hours post-seeding I added Zeocin (Cf= 50 $\mu\text{g}/\text{mL}$). Zeocin pressure was kept for 3 days and repeated on day 4 of treatment. At day 7 of treatment cells were fixed in EtOH (ethanol) and processed for Giemsa stain, which stains nucleic acids of the fixed cells purple. This provides qualitative estimation of proliferation or lack thereof. Results for this experiment are shown in **Figure 3.8**, where parental U2OS FRT/TO cells proliferate regardless of Zeocin treatment and U2OS FRT/TO Myc-tFT cells do not proliferate in the presence of Zeocin but do in the absence of the antibiotic. This confirms correct integration of the Myc-tFT construct in U2OS FRT/TO.

From this point onward, Myc-tFT will refer to the Myc-mCherry-mNeon constructs stably expressed in U2OS FRT/TO, specifically in clone 8.

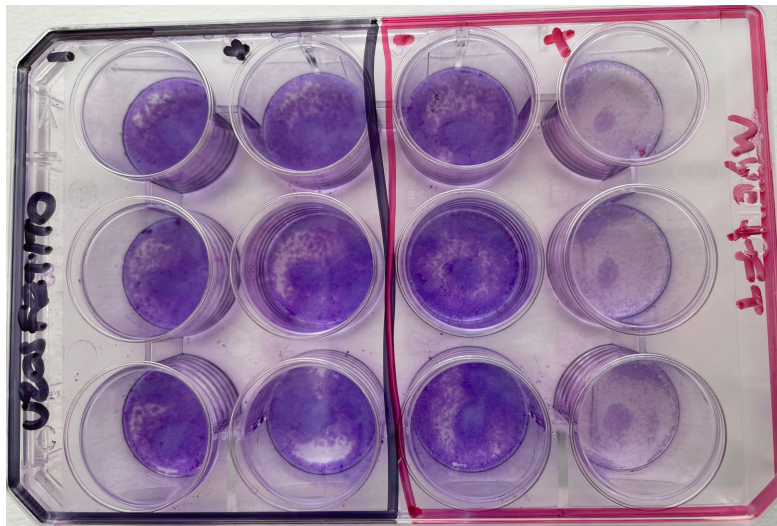


Figure 3.8: Correct integration of Myc-tFT in U2OS FRT/TO leads to loss of Zeocin resistance. U2OS FRT/TO and U2OS FRT/TO Myc-tFT cells were seeded in the plate and grown for 7 days in the presence or absence of Zeocin (+ or - columns) and processed for Giemsa stain to evaluate proliferation.

3.2.4 Validation of CMV-driven Myc-tFT expression.

Prior to use in experimental set up, validation of CMV-driven Myc-tFT expression needed to be carried out. Firstly, responsiveness of U2OS FRT/TO Myc-tFT Cl.8 to Doxycycline was assessed by culturing cells in the presence or absence of Doxycycline for 12h. The cells were then harvested and lysated for immunoblotting. Analysis of lysates by immunoblot can be found in **Figure 3.9** Myc-tFT can be detected only in the lysates of cells cultured in the presence of Doxycycline. To confirm that the band detected with the Myc antibody was indeed the Myc-tFT construct, which also contains an HA tag at the C-terminus of mNeonGreen, the lysates were processed again for immunoblotting and the membrane was probed for HA. This confirmed that indeed Myc-tFT expression could only be detected upon Doxycycline addition to relieve CMV-driven expression from transcriptional repression by the Tet repressor.

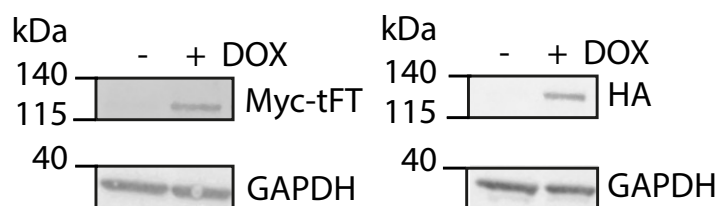


Figure 3.9: Myc-tFT expression by the CMV promoter is Doxycycline-dependent. U2OS FRT/TO Myc-tFT Cl.8 cells were cultured in the presence or absence of Doxycycline and collected for immunoblot. Lysates were run on a polyacrylamide gel and transferred to a membrane which was cut and stained with antibodies against Myc, HA and GAPDH.

Sears et al. (1999) first described Ras-driven stabilisation of Myc in cells subject to serum deprivation stimulated with serum addition. Following mitogen sensing, the Ras/Raf/MAPK kinase lead to Myc stabilisation of an ectopically expressed Myc, under the control of the CMV promoter. This phosphorylation led to an increase in the half-life of Myc as measured by pulse-chase metabolic labelling. This effect was later described to be mediated by ERK-driven phosphorylation of Myc at S62 (Sears et al., 2000; Vaseva et al., 2018).

Based on this knowledge, an analogous experiment in the Myc-tFT system was set up. To investigate the effect of mitogen activation on the Myc-tFT ratio, U2OS

3.2. Design of Myc-tFT construct and generation of a stable cell line

FRT/TO Myc-tFT cells were seeded on an imaging dish and left overnight to equilibrate at 37°C, 5% CO₂. The next day, cells were washed three times with sterile PBS and serum-free media was added. Cells were incubated in serum-free media, supplemented with Doxycycline to induce Myc-tFT expression, for 18 hours. Serum starvation media was replaced with Leibovitch's L15 media, for imaging purposes, without FBS and with doxycycline. Cells were placed on the microscope and either FBS (fetal bovine serum, final concentration 20%) or L15 were added to the media, with additional Doxycycline to maintain its final concentration. Cells were imaged prior (0h time point) and 4 hours following the addition of FBS or L15.

A time-dependent significant increase in Myc-tFT ratio, shown in **Figure 3.10 A**, was recorded 4 hours following the addition of L15 and FBS. Surprisingly, the increase in ratio measured upon addition of serum was significantly lower than that measured upon addition of L15. To understand the contribution of synthesis and degradation to the ratio, changes in background-corrected mNeonGreen and mCherry were plotted, **Figure 3.10 B and C**, respectively. In cells treated with L15 and supplemented with Doxycycline, the mNeonGreen fluorescence did not change significantly ($p=0.6088$), and neither did the mCherry fluorescence which did increase sufficiently to generate and increased ratio, but not significantly ($p=0.0766$). What this illustrates is that whilst the changes in mCherry and mNeonGreen Individual are not significant, the small increase in mCherry is sufficient to increase the tFT ratio read-out. Contrastingly, addition of serum resulted in a significant increase in mNeonGreen fluorescence ($p<0.0001$) but in a less significant increase in mCherry fluorescence ($p=0.0326$). The greater increase in mNeonGreen levels upon serum addition responsible for a diminished ratio and is indicative of an increase in synthesis.

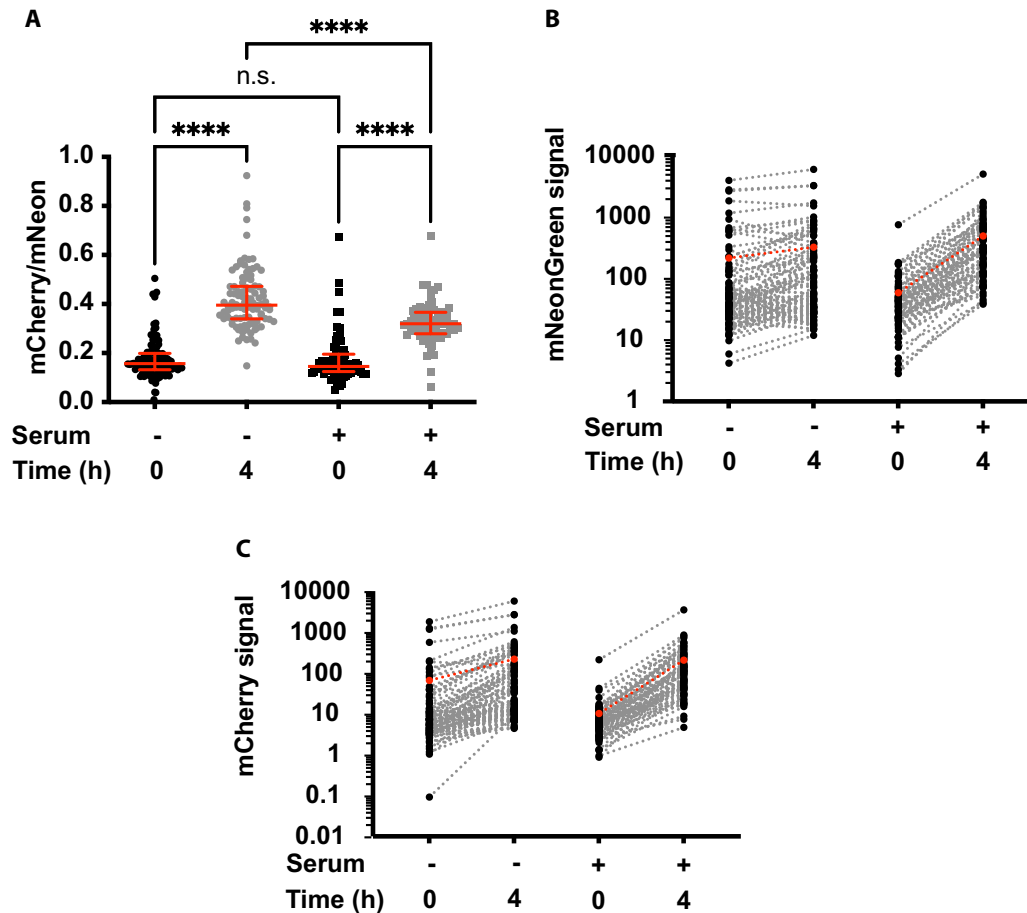


Figure 3.10: **Serum stimulation post-serum starvation leads to a lower increase in Myc-tFT ratio.** The effect of serum stimulation post serum starvation on Myc stability was evaluated by the Myc-tFT sensor in U2OS FRT/TO Myc-tFT Clone 8. Serum starved cells were treated with L15 or FBS in the presence of doxycycline and imaged before and after 4 hours of treatment. ANOVA was performed to compare the effect of serum addition to cells at each time point (n.s.=non-significant $p > 0.05$; ****= $p \leq 0.0001$):

- A Quantification of tFT ratio in U2OS FRT/TO Myc-tFT Clone 8 cells previously serum starved and with or without serum addition. Each point represents the tFT ratio of an individual cell.
- B Quantification of mNeonGreen background-corrected signal in U2OS FRT/TO Myc-tFT Clone 8 cells serum starved and with the addition of FBS (+) or L15 (-) supplemented with Doxycycline. Each point represents a reading from an individual cell at time 0 and 4 hours. Average mNeonGreen levels are shown in red.
- C Quantification of mCherry background-corrected signal in U2OS FRT/TO Myc-tFT Clone 8 cells serum starved and with the addition of FBS (+) or L15 (-) supplemented with Doxycycline. Each point represents a reading from an individual cell at time 0 and 4 hours. Average mCherry levels are shown in red.

3.2. Design of Myc-tFT construct and generation of a stable cell line

To further validate the effect of serum starvation and stimulation on Myc-tFT levels and the contribution of synthesis to the effects of serum induction, a complementary experiment was run where cells were serum starved and serum was added in the presence or absence of cyclohexamide for 2, 4 and 6 hours. The result from this preliminary investigation (**Figure 3.11**) display an increase in Myc-tFT levels following addition of serum (comparison of lanes 1-4 and 6-8) which was lost by co-treatment of serum and translational inhibitor cycloheximide (CHX, lanes 9-10).

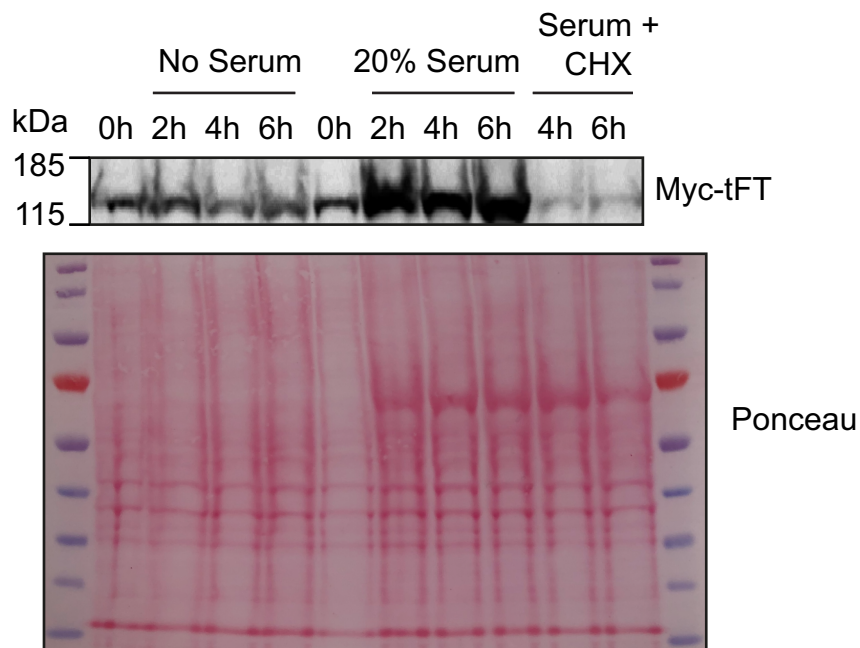


Figure 3.11: **Serum addition leads to increased synthesis of Myc-tFT.** U2OS FRT/TO Myc-tFT Cl.8 cells were cultured in the presence or absence of Doxycycline and serum starved for 18 hours, followed by addition of serum-free media (lanes 1-5) or FBS (final concentration=20%, lanes 6-8) or FBS and CHX (Cf=20 μ g). Lysates were run on a polyacrylamide gel and transferred to a membrane which was cut and stained with antibody against Myc. Ponceau staining provided a loading control.

Chapter 3. Generation and validation of a suitable Myc Stability Sensor

Taken together these data suggested that serum addition affected CMV-driven Myc-tFT expression. Upon further inspection of the CMV sequence, the core binding site motif of the serum response element (SRE) which allows for Serum Response Factors (SRF) binding (Treisman, 1992), was found. This motif, which consists of CC(A/T)₆GG, and its placement within the CMV promoter are displayed in **Figure 3.12**. Whilst no further characterisation was carried out to demonstrate SRF binding to the SRE identified within the CMV promoter, further experiments were carried out without addition of FBS prior to imaging experiments to avoid altering Myc-tFT synthesis rate.

Finally, some non-canonical (CANNTG, where N is any nucleotide) E-boxes were found on the CMV promoter, also depicted in **Figure 3.12**. The ability of Myc-tFT to bind these non-canonical E-boxes will be addressed in a later section (**Section**)



Figure 3.12: A Serum Response Element can be found within the CMV promoter of pcDNA5 FRT/TO plasmids.

3.3 Myc-tFT is able to report on Myc stability

3.3.1 MG132 treatment reveals Myc-specific changes in Myc-tFT ratio measurement

Generation of cell lines with stable, inducible expression of tFTs allows for better application of the tFT system and verification of the tFT's ability to report on the stability of the Myc isoforms. In transient and stable expression, tFTs should report on increased Myc stability when cells are treated with MG132 versus DMSO. Indeed proteasomal inhibition led to rapid increase in the pool of Myc with both FPs matured and, consequently, increased tFT ratio of Myc-tFT (**Figure 3.13**). The difference in stability measurement between DMSO and MG132 treated cells was highly statistically significant ($p \leq 0.0001$ in $n=3$ experiments) when assessed by Student's t-test (**Figure 3.13 B**).

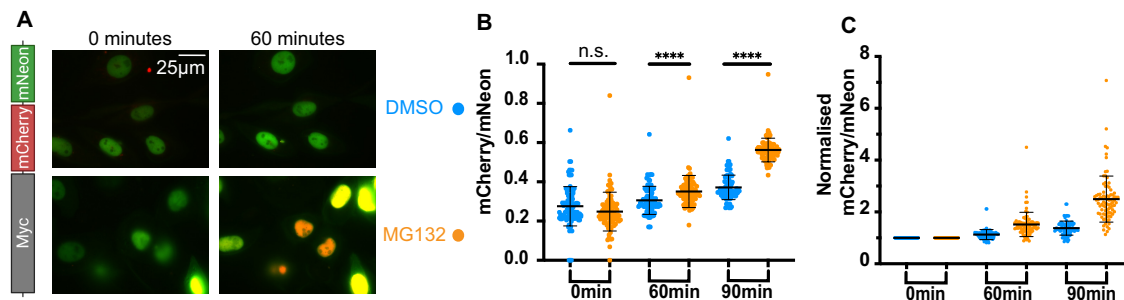


Figure 3.13: tFTs are able to report on increased stability of Myc upon proteasome inhibitor treatment. The effect of proteasome inhibitor MG132 on U2OS FRT/TO Myc-tFT Clone 8 is shown in images and relative quantification. Student's t-tests were performed to compare MG132- to DMSO-treated cells at each time point (n.s.=non-significant $p > 0.05$; ****= $p \leq 0.0001$) Student's t-test on data from the 90 minute time-point mean and SD of the three replicates and displayed a p-value $p=0.0025$.

- A Effect of MG132 on live U2OS FRT/TO Myc-tFT Clone 8 cells. Fluorescent images of merged mNeon and mCherry signals at time 0 and 60 min of treatment.
- B Quantification of tFT ratio in MG132- or vehicle control (DMSO)-treated U2OS FRT/TO Myc-tFT Clone 8 cells. Each data point represents a single cell. Mean and SD are shown. Representative data from one of $n=3$ experiments.
- C Quantification of fold change in tFT ratio in MG132- or vehicle control (DMSO)-treated U2OS FRT/TO Myc-tFT Clone 8 cells. Each data point represents a single cell. Mean and SD are shown. Representative data from one of $n=3$ experiments.

Analogous experiments were conducted in the nMyc-tFT expressing cell line: a

Chapter 3. Generation and validation of a suitable Myc Stability Sensor

rapid and statistically significant increase in mCherry/mNeon ratios was recorded, **Figure 3.14**. Interestingly, the tFT ratio reveals a greater stability of nMyc (1.2 average mCherry/mNeon ratio in DMSO at 0 min - **Figure 3.14 B**) than Myc (0.3 average mCherry/mNeon ratio in DMSO control at 0 min - **Figure 3.13 B**). Consistently with this difference in stability, the increase in Myc-tFT stability upon MG132 treatment was greater than that of nMyc-tFT, with 2.5-fold (**Figure 3.13 C**) and 2.0-fold (**Figure 3.14 C**) increase respectively. In both cases, MG132 produced a significant increase in stability at 60 and 90 minutes-post treatment compared to DMSO control.

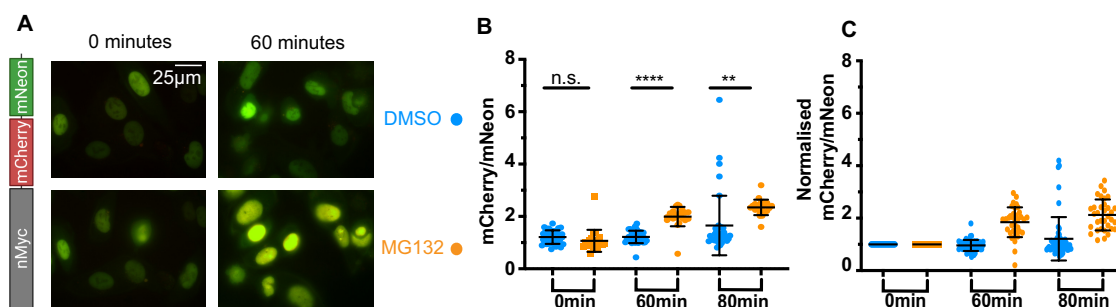


Figure 3.14: tFTs are able to report on increased stability of nMyc upon proteasome inhibitor treatment. The effect of proteasome inhibitor MG132 on U2OS FRT/TO nMyc-tFT Clone 1 is shown in images and relative quantification. Student's t-tests were performed to compare MG132- to DMSO-treated cells at each time point. (n.s.=non-significant $p > 0.05$; **= $p \leq 0.01$; ****= $p \leq 0.0001$):

- A Effect of MG132 on live U2OS FRT/TO nMyc-tFT Clone 1 cells. Fluorescent images of merged mNeon and mCherry signals at time 0 and 60 min of treatment.
- B Quantification of tFT ratio in MG132- or vehicle control (DMSO)-treated U2OS FRT/TO nMyc-tFT Clone 1 cells. Representative data from one of $n=3$ experiments. Each data point represents a single cell. Mean and SD are shown.
- C Quantification of fold change in tFT ratio in MG132- or vehicle control (DMSO)-treated U2OS FRT/TO nMyc-tFT Clone 1 cells. Representative data from one of $n=3$ experiments. Each data point represents a single cell. Mean and SD are shown.

To verify that changes in tFT ratios measured in **Figures 3.13 and 3.14** are driven by effects on Myc and not the FPs themselves, I applied the same experimental and imaging conditions to the control cell line expressing tFT with no POI tagged at its N-terminus (**Figure 3.15**). This construct is very stable (mCherry/mNeon ratio of 2.7 at the beginning of the experiment in the DMSO condition) and unaffected by MG132 treatment of short duration, as reported by the lack of fold-change increase in

3.3. Myc-tFT is able to report on Myc stability

mCherry/mNeon ratio of each cell over time.

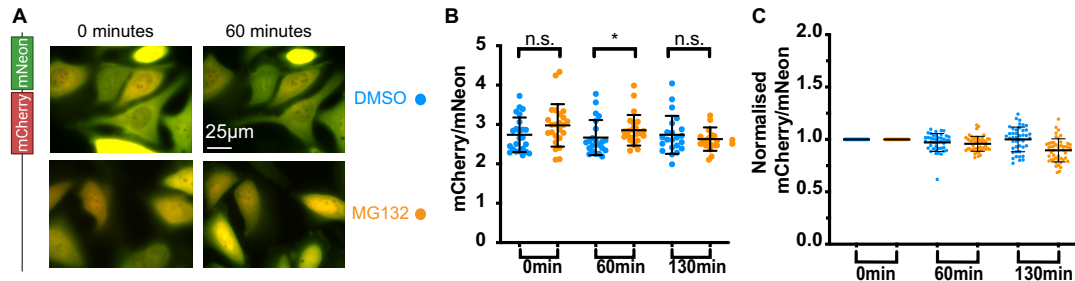


Figure 3.15: **Control tFT is stable and does not display increased stability after treatment with proteasome inhibitor.** The effect of proteasome inhibitor MG132 on U2OS FRT/TO tFT cells is shown in images and relative quantification. Student's t-tests were performed to compare MG132- to DMSO-treated cells at each time point (n.s.=non-significant $p > 0.05$; $* = p \leq 0.05$):

- A Effect of MG132 on live U2OS FRT/TO tFT Clone 3 cells. Fluorescent images of merged mNeon and mCherry signals at time 0 and 60 min of treatment.
- B Quantification of tFT ratio in MG132- or vehicle control (DMSO)-treated U2OS FRT/TO tFT Clone 3 cells. Each data point represents a single cell. Mean and SD are shown. Representative data from one of $n=3$ experiments.
- C Quantification of fold change in tFT ratio in MG132- or vehicle control (DMSO)-treated U2OS FRT/TO tFT Clone 3 cells. Each data point represents a single cell. Mean and SD are shown. Representative data from one of $n=3$ experiments.

Overall, these results demonstrate that the tFT ratio varies depending on the stability of the POI that the FPs are attached to: untagged tFT is very stable, while Myc isoforms are very unstable and sensitive to proteasomal inhibition. It can be concluded that tFTs are able to report on changes in Myc stability.

3.3.2 Myc-tFT half-life is similar to that of untagged endogenous Myc

The previous experiments highlight the rapid change in Myc-tFT stability upon proteasomal inhibition, which is to be expected for a protein with a short half-life like Myc. However, in order for Myc-tFT to act as a faithful reporter on Myc stability, it is important that the tFT tag itself should not affect the stability of Myc. In other words, the half-life of the tagged exogenous protein should be as close as possible to that of the endogenous and untagged protein. To test this, I performed cycloheximide (CHX)-chase experiments, a commonly used method for determining protein stability, to compare the half-lives. As described in the introduction, cells are incubated with CHX, a global protein translation inhibitor. Halted translation stops the replenishing of the Myc pool, allowing the measurement of its rate of decay by collecting cells at different timepoints post CHX treatment, in this experiment, every half-hour. Following protein extraction, cells were processed for immunoblotting and Myc levels were normalised to a control stable endogenous protein (GAPDH) to obtain the rate of Myc degradation and its half-life. Myc-tFT (which has a higher molecular weight than endogenous due to the presence of the tags) rapidly decayed when treated with CHX, **Figure 3.16 A**. To confirm the reduction in protein pool levels are due to degradation of Myc by the ubiquitin-proteasome system, rather than alternative degradation pathways, I co-treated with CHX and MG132. Protein degradation was inhibited by presence of MG132 indicating that rapid decay of Myc and Myc-tFT are caused by proteasomal degradation. Due to the low expression of endogenous Myc in U2OS (Altman et al., 2015; Walz et al., 2014), I compared the rate of decay of Myc-tFT in U2OS FRT/TO to that of endogenous Myc in HeLa cells, which express detectable and not deregulated Myc (**Figure 3.16 B**). Extrapolation of Myc half-life in the two cell lines yielded very similar half-lives: 39 minutes for Myc-tFT in U2OS FRT/TO cells and 44 minutes for endogenous Myc in HeLa cells (**Figure 3.16 C**).

These results confirm that the presence of the FPs at the C-terminus of Myc does not disrupt its degradation pathways and that changes in Myc stability recorded in the previous section reflect changes in stability of a protein that is very rapidly turned over in cells.

3.3. Myc-tFT is able to report on Myc stability

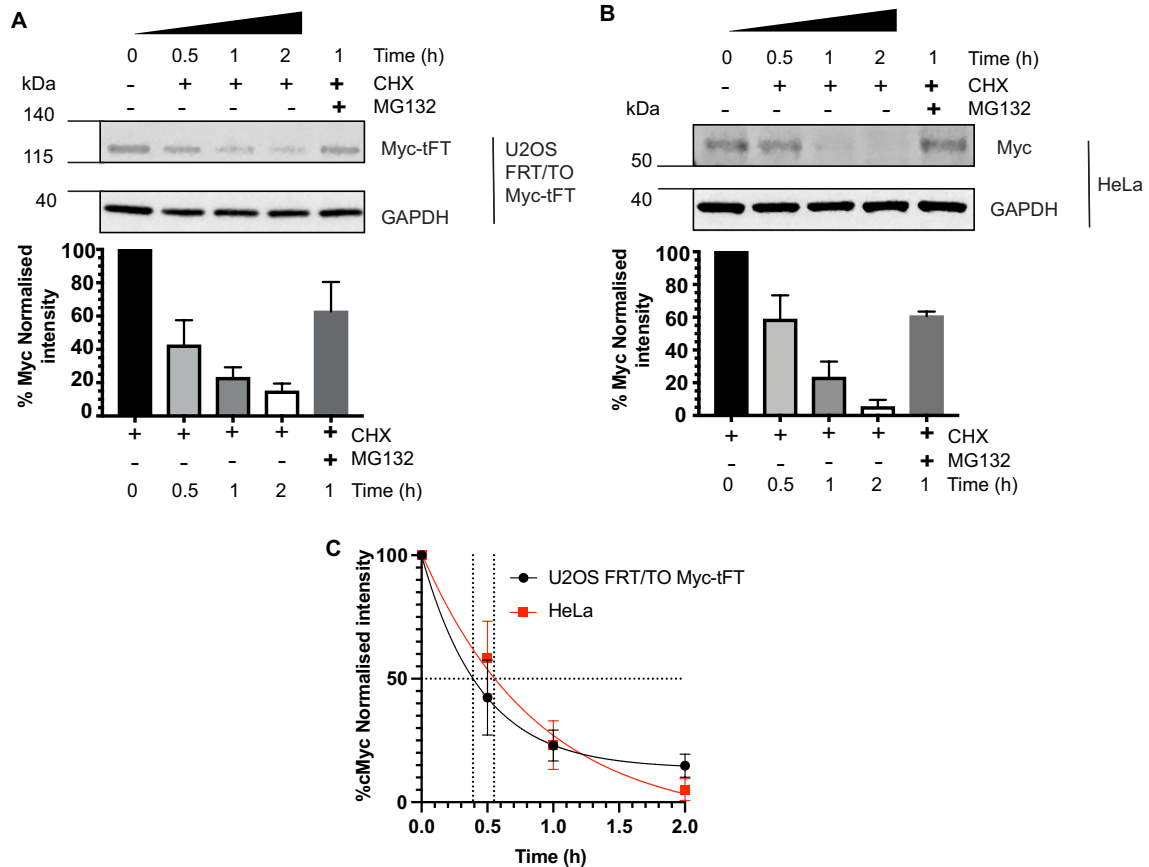


Figure 3.16: **C-terminal tagging of Myc with tFTs does not affect Myc protein's half-life.** cycloheximide (CHX)-chase experiments were performed in U2OS FRT/TO Myc-tFT or HeLa cells to determine and compare Myc half-life (Pooled data of n=3 experiments):

- A U2OS FRT/TO Myc-tFT cells were treated with CHX in the presence or absence of MG132. Cells were collected at the timepoints depicted and lysed. Lysates were processed for immunoblotting and stained for Myc or GAPDH. Myc staining intensity was normalised to housekeeping control GAPDH (quantification below) to evaluate Myc rate of decay.
- B HeLa cells were treated with CHX in the presence or absence of MG132. Cells were collected at the timepoints depicted and lysed. Lysates were processed for immunoblotting and stained for Myc or GAPDH. Myc staining intensity was normalised to housekeeping control GAPDH (quantification below) to evaluate Myc rate of decay.
- C Percentage of normalised Myc intensity is plotted against time and a non-linear curve was fitted to extrapolate the half-life of Myc (39min in U2OS FRT/TO Myc-tFT and 44 min in HeLa cells).

3.4 Myc-tFT undergoes the same post-translational modifications as endogenous Myc

The results in the previous section confirm that Myc-tFT degradation timing is unaffected by FP tags. Although I've shown that the half-lives are very similar, I wanted to verify that the Myc-tFT degradation is controlled by the same signalling pathways as endogenous Myc.

While there are several pathways to Myc degradation, the most prominent and best characterised pathway relies on post-translational modification (PTM) of Threonine 58 (T58) by phosphorylation. Briefly, in response to mitogenic signalling, Myc accumulation is not only achieved through increased expression, but also protein stabilisation. Several phosphorylation steps are required for timely Myc accumulation yielding cell proliferation, and degradation leading to cessation of this pro-growth signalling once cell cycle re-entry has been achieved. Serine 62 is firstly phosphorylated by ERKs (Extracellular signal-regulated kinases) and this PTM is in turn recognised by another kinase, GSK3 β (Glycogen synthase kinase 3-beta), that phosphorylates T58. A series of isomerase and phosphatase enzymes manipulate this double phosphorylated Myc to yield Myc phosphorylated only at T58. This single phosphorylation is recognised by a member of the proteasomal degradation pathway, an E3 ligase called FBW7 (F-box/WD repeat-containing protein 7) which terminates the transcriptional activity of Myc by causing its degradation (Sears et al., 1999, 2000; Yada et al., 2004). T58 is a mutation hot-spot in Burkitt's lymphoma resulting in a stable Myc that is degraded more slowly and, therefore, accumulates to oncogenic levels becoming the oncogenic driver of this tumour type (Gregory and Hann, 2000).

3.4. Myc-tFT undergoes the same post-translational modifications as endogenous Myc

Based on the well-documented importance of T58 in Myc degradation, and the endogenous-like half-life of Myc-tFT, I set out to investigate if Myc-tFT is indeed processed post-translationally at this key residue. Experimentally, I adapted the CHX-chase experiment shown previously, to measure changes in Myc levels upon treatment with GSK3 β inhibitor, CHIR99021 (CHIR). U2OS FRT/TO Myc-tFT cells were treated with DMSO (vehicle control), CHX, CHX and CHIR or CHX and MG132 for one hour and then cells were harvested for lysis. Immunoblotting of the lysates (**Figure 3.17 A**), confirm that Myc-tFT is indeed phosphorylated at pT58 when stained with a phospho-specific antibody. This staining decreased in the presence of CHIR. In the same sample, reduction in phosphorylation at T58 by CHIR leads to an increase in Myc-tFT levels, confirming that Myc-tFT's stability is regulated by GSK3 β and FBW7. Cells were co-treated with CHX and MG132 to offer a positive control rescue of Myc-tFT levels from protein degradation.

Relative quantifications of Myc-tFT and Myc-tFT pT58 are displayed in **Figure 3.17 B**. The experiment was done in parallel in HeLa cells to confirm that the trends in Myc-tFT phosphorylation and overall levels were comparable to that of endogenous Myc of similar half-life (**Figure 3.17 C,D**).

Chapter 3. Generation and validation of a suitable Myc Stability Sensor

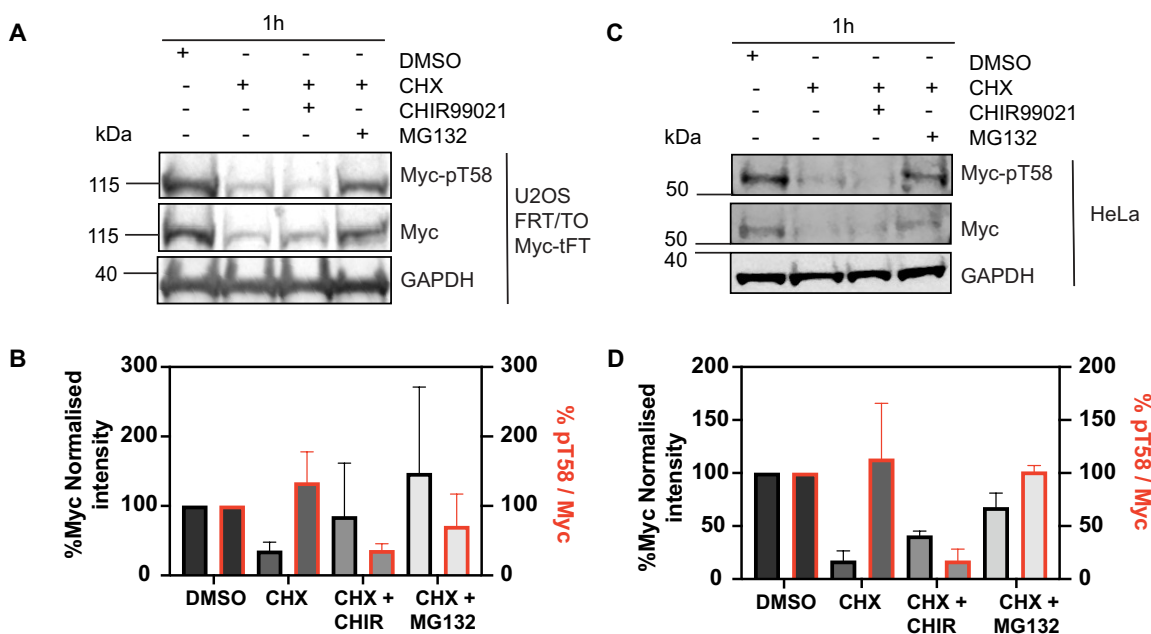


Figure 3.17: **Inhibition of GSK3 β leads to Myc-tFT accumulation by reduction of Threonine 58 phosphorylation.** The effect of inhibition of GSK3 β by CHIR99021 (3 μ M) on Myc-tFT and endogenous Myc was assessed by immunoblot (Pooled data of n=3 experiments):

A,C U2OS FRT/TO Myc-tFT [A] or HeLa [C] cells were treated with DMSO or CHX in the presence or absence of CHIR99021 (3 μ M) and MG132 and collected and lysed after one hour. Lysates were processed for immunoblotting and stained for Myc, phosphorylated Myc (Myc-pT58) or GAPDH.

B,D Quantification of Immunoblot staining of UOS FRT/TO Myc-tFT [B] an HeLa [D] lysates: Percentage of Myc staining normalised to housekeeping control GAPDH to evaluate treatment's effect on overall Myc levels (grayscale with black border); Myc-pT58 staining was normalised to total levels of Myc in the same sample to assess the percentage of phosphorylated/total Myc (grayscale with red border).

3.4. Myc-tFT undergoes the same post-translational modifications as endogenous Myc

Having confirmed the effect of GSK3 β inhibition by CHIR on a population of Myc-tFT expressing cells, its effect on single-cell tFT readouts for Myc stability was tested. Live cell imaging of U2OS FRT/TO Myc-tFT was conducted and cells were treated with either DMSO or CHIR99021. Cells were imaged at 0, 60 and 120 minutes post-treatment. Images were analysed not by following cells through time but by measuring FP intensity and calculating tFT ratios for all cells in the field for each timepoint. Treatment conditions were then compared to vehicle control for each timepoint. While this analysis method does not allow for time-resolved analysis of fold-changes in ratio, it reproduces the analysis that would be used in a medium-throughput drug screen where cells would be treated and imaged at a set time after treatment and compared to control. Each treated condition was compared to its corresponding DMSO control by Student's t-test. Results displayed in **Figure 3.18** highlight the statistically significant increase in stability, as measured by an increased tFT ratio, after short treatment with CHIR99021. Relative frequency distribution shows a clear overlap between control curves and CHIR99021 data at time 0min, with a shift in distribution towards a more stable tFT ratio after one hour of CHIR treatment.

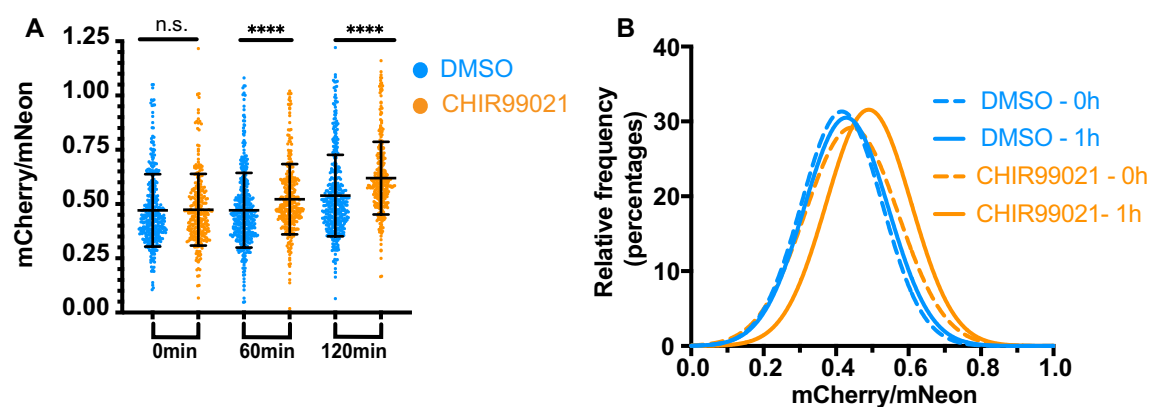


Figure 3.18: Inhibition of GSK3 β by CHIR99021 leads to increased Myc-tFT ratio. U2OS FRT/TO Myc-tFT were treated with DMSO or CHIR99021 (3 μ M) and imaged over time. (Representative data of n=3 experiments):

- A Snapshot analysis of acquired images was plotted in a scatter plot (each dot represent reading from an individual test) and Student's t-test was carried out to assess statistical significance between treatment and control (n.s.=non-significant $p>0.05$; ****= $p\leq 0.0001$). Mean and SD are shown.
- B Relative frequency distribution of control or treated cells at experiment start and one hour post-treatment

Chapter 3. Generation and validation of a suitable Myc Stability Sensor

Given the promising results, I decided to challenge the system with another GSK3 β inhibitor TWS119. From **Figure 3.19 A** it is apparent that TWS119 treatment does not provide the same degree of increased Myc stability that CHIR does (**Figure 3.19**), but significant increase in Myc stability was recorded nonetheless. This is possibly due to the fact the the half-inhibitory concentration (IC₅₀) of TWS119 is higher than that of CHIR99021 (TWS119 IC₅₀=30nM, CHIR99021 IC₅₀=7nM), thus resulting in a weaker inhibition of GSK3 β at 3 μ M. Surprisingly, no increase in Myc levels were detected by immunoblotting from parallel experiments in which Myc-tFT-expressing cells were treated with DMSO or CHIR, TWS119, MG132 (co-treated with CHX). Results in **Figure 3.19 B** confirm increased Myc levels upon GSK3 β inhibition by CHIR but not TWS119, suggesting that more modest increases in Myc stability would be otherwise overlooked if assessed by immunoblotting instead of our new Myc-tFT assay.

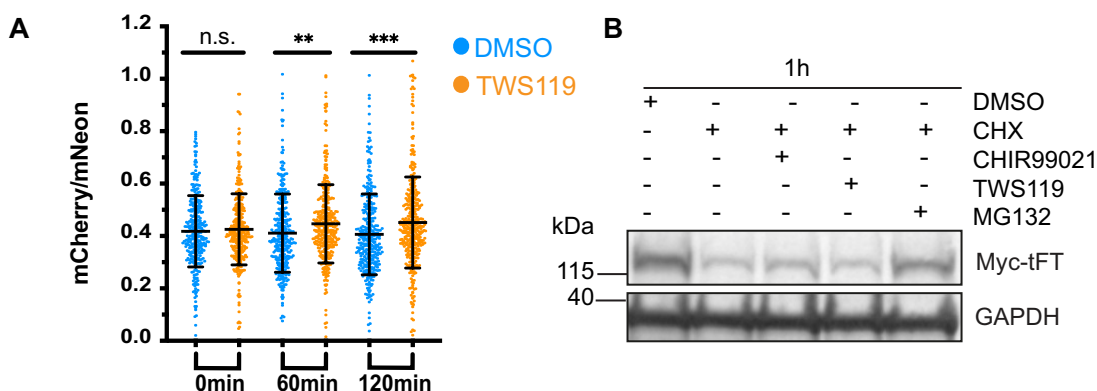


Figure 3.19: Myc-tFT is more sensitive than immunoblotting for measuring increased Myc stability by TWS119 treatment. U2OS FRT/TO Myc-tFT were treated with DMSO or GSK3 β inhibitor TWS119 (3 μ M) and imaged over time. Samples were collected for parallel immunoblotting experiments (Representative data of n=3 experiments):

- A Snapshot analysis of acquired images was plotted in a scatter plot and Student's t-test was carried out to assess statistical significance between treatment and control (n.s.=non-significant $p > 0.05$; **= $p \leq 0.01$, ***= $p \leq 0.001$). Each point represents the ratio of an individual cell. Mean and SD are shown.
- B Immunoblot experiment to compare increase in Myc levels upon GSK3 β inhibition by TWS119 (3 μ M) or CHIR99021 (3 μ M). Unless otherwise stated all cells were treated with CHX to measure changes in protein amounts following pharmacological action. MG132 provided a positive control to increased Myc levels.

3.4. Myc-tFT undergoes the same post-translational modifications as endogenous Myc

As final proof of the ability of the tFTs to report on Myc stability changes, I generated a version of Myc-tFT that is non-phosphorylatable by GSK3 β and that cannot interact with FBW7: Myc T58A-tFT. This mutant reproduces the stabilisation of Myc recorded in Burkitt's lymphoma (Bahram et al., 2000; Gregory and Hann, 2000) and has been used to stabilise Myc by reducing its recognition by FBW7 and ubiquitination (Gregory, Qi, and Hann, 2003; Sears et al., 2000; Wang et al., 2011). I then generated a U2OS FRT/TO cell line expressing this construct according to the method previously described. I first compared the tFT ratio of Wild-type (WT) Myc-tFT and the mutant Myc T58A-tFT in untreated cells (**Figure 3.20 A**) which confirmed a strong increase in tFT ratio in the mutant line. Short-term (1 and 2 hour) proteasomal inhibition by MG132 showed a greater change in tFT ratio of WT than mutant Myc-tFT (2.5 and 1.9 fold-change in ratio respectively), consistently with the fact that the mutant is more stable (**Figure 3.20 B,C**).

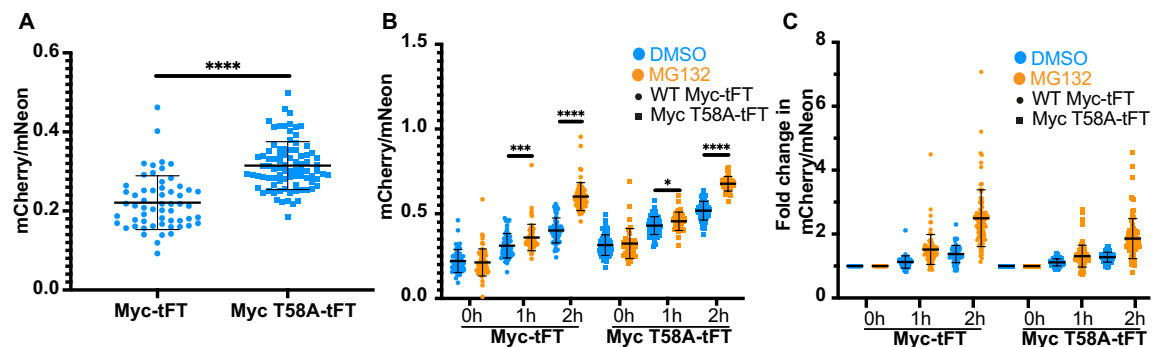


Figure 3.20: Non-phosphorylatable T58A mutant Myc-tFT is more stable than Wild-type (WT) Myc-tFT. U2OS FRT/TO WT and T58A Myc-tFT were imaged following overnight induction with Doxycycline untreated or post MG132 (4.2 μ M) or DMSO treatment (Representative data of n=4 experiments) Each dot represents data from one individual cell. Mean and SD are shown:

- A Snapshot analysis of untreated WT (Circle) or T58A (Square) Myc-tFT was plotted in a scatter plot and Student's t-test was carried out to assess statistical significance between treatment and control (n.s.=non-significant $p > 0.05$; *= $P \leq 0.05$, **= $p \leq 0.001$, ****= $p \leq 0.0001$). p value for n=4: * $p = 0.0186$
- B Quantification of tFT ratio in MG132- or vehicle control (DMSO)-treated U2OS FRT/TO Myc-tFT Clone 8 (Circle) or U2OS FRT/TO Myc T58A-tFT Clone 9 (square) cells.
- C Quantification of fold-change in tFT ratio in MG132- or vehicle control (DMSO)-treated U2OS FRT/TO Myc-tFT Clone 8 cells or U2OS FRT/TO Myc T58A-tFT Clone 9 cells.

Chapter 3. Generation and validation of a suitable Myc Stability Sensor

In conclusion, these experiments confirm that the tFT assay is more sensitive and better suited to higher-throughput screening than canonical tools for measuring Myc stabilisation as a consequence of changes in PTM and protein-protein interactions.

3.5 Myc-tFT is functional

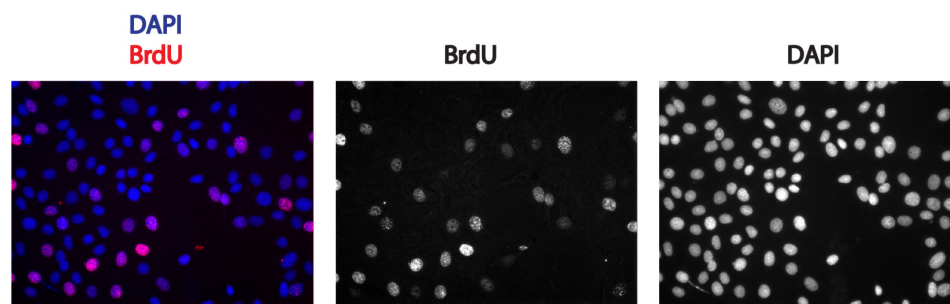
As the final step in validating Myc-tFTs, I wanted to assess Myc-tFT's functionality. As discussed in the introduction, addition of the tags to the C-terminus of a protein of interest might lead to loss of function. Therefore, Myc function was assayed by rate of S-phase entry following serum starvation, and by quantifying the amount of Myc-tFT bound to promoters of a canonical Myc target gene.

S-phase entry is most accurately measured by Bromodeoxyuridine (BrdU) labelling which assesses incorporation of BrdU, a thymidine analogue, into the DNA during DNA replication in S-phase. For this, I seeded cells on coverslips and after one day I started serum starvation of the cells by replacing media supplemented with 10% FBS with media without FBS. Cells were left in serum-free media for 72h after which Doxycycline (DOX) or water (vehicle control for DOX) was added for 24h following which cells were incubated with BrdU for two hours. Cells were then fixed in Methanol and coverslips were processed for immunofluorescence (IF) staining of BrdU and DAPI (4',6-diamidino-2-phenylindole), a DNA marker. Coverslips were then imaged and BrdU-positive cells were scored against DAPI-positive cells to assess the fraction of cells that have entered S-phase. I performed these experiments in three different cell lines in parallel: U2OS FRT/TO (parental cell line), U2OS FRT/TO Myc-tFT and U2OS FRT/TO tFT (control cell line which will express the tFT construct upon addition of DOX). Representative images for this technique are shown in **Figure 3.21**. The results of the BrdU experiment, **Figure 3.21 B** provide a large amount of information, allowing multiple conclusions to be drawn. Firstly, and most importantly for this research, induction of Myc-tFT by DOX leads to a significant increase in BrdU-positive cells. This is true when comparing + and - DOX conditions in Myc-tFT, but also when comparing the induction of Myc-tFT to that of tFT or to no construct at all in the other cell lines. Induction of tFT or addition of DOX in the parental cell line did not yield any increase

3.5. Myc-tFT is functional

in rate of S-phase entry. Finally, even the -DOX condition of Myc-tFT expressing cells displayed higher proportion of BrdU-positive cells than other -DOX controls. This suggests that some leakage of the expression of the construct in uninduced condition from the CMV promoter is occurring. It can be safely concluded that Myc-tFT induction promotes cell cycle re-entry following serum starvation, a known downstream effect of Myc.

A



B

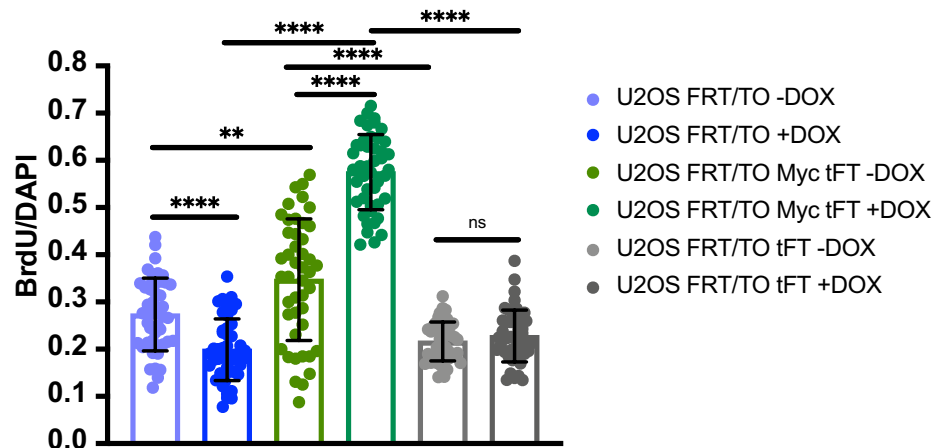


Figure 3.21: **Myc-tFT is functional** Myc-tFT functionality was assessed by Bromodeoxyuridine (BrdU) stain (Pooled data of n=3 experiments):

A Representative images of BrdU staining.

B The number of BrdU positive/DAPI positive cells was assessed by immunofluorescence in the indicated cell lines following 72h serum-starvation, 24h +/- DOX and 2h BrdU pulse (n.s.=non-significant $p > 0.05$; **= $p \leq 0.01$, ****= $p \leq 0.0001$).

Chapter 3. Generation and validation of a suitable Myc Stability Sensor

Although BrdU assessment demonstrated that Myc-tFT induction promoted a downstream effect of Myc, to confirm Myc-tFT is functional through *direct* evidence, I conducted ChIP experiments. These consisted of cross-linking proteins to DNA, digesting and extracting the DNA with proteins bound to it, and then performing an immunoprecipitation (pull-down of proteins with the use of antibodies) of Myc and Histone H3 (positive control) with the DNA that these proteins are attached to. The DNA is then purified and the yielded DNA quantified by real-time quantitative PCR. In other words, if Myc-tFT is functional, its binding will be enriched at certain genomic sites, and so immunoprecipitation with a Myc antibody would yield more DNA from that site than in any of the controls. Controls for this experiment are the amount of DNA that was incubated with an antibody (2% input); DNA pulled down with Histone H3, a protein ubiquitously bound to DNA; incubation with an antibody that does not recognise any DNA-binding protein (IgG); -DOX conditions of pulldown with a Myc antibody. This is indeed what is measured by qPCR when assessing the amount of hCAD (a known Myc target gene) promoter DNA present in the samples. As evident in **Figure 3.22**, there is great enrichment of hCAD DNA in the samples of cells expressing Myc-tFT and immunoprecipitated for Myc (Myc +DOX sample). I also wanted to investigate if Myc-tFT bound to its own promoter, the CMV promoter, as some non-canonical E-boxes are present in its sequence. No enrichment of Myc at this site was recorded, indicating that Myc-tFT cannot directly promote its own transcription.

From the combination of BrdU and ChIP experiments I can conclude that Myc-tFT does indeed function as a transcription factor to produce cell cycle re-entry and progression and binding to a canonical Myc target. Therefore, the presence of the FPs does not seem to interfere with the ability of Myc to bind to DNA and execute its transcriptional regulatory function.

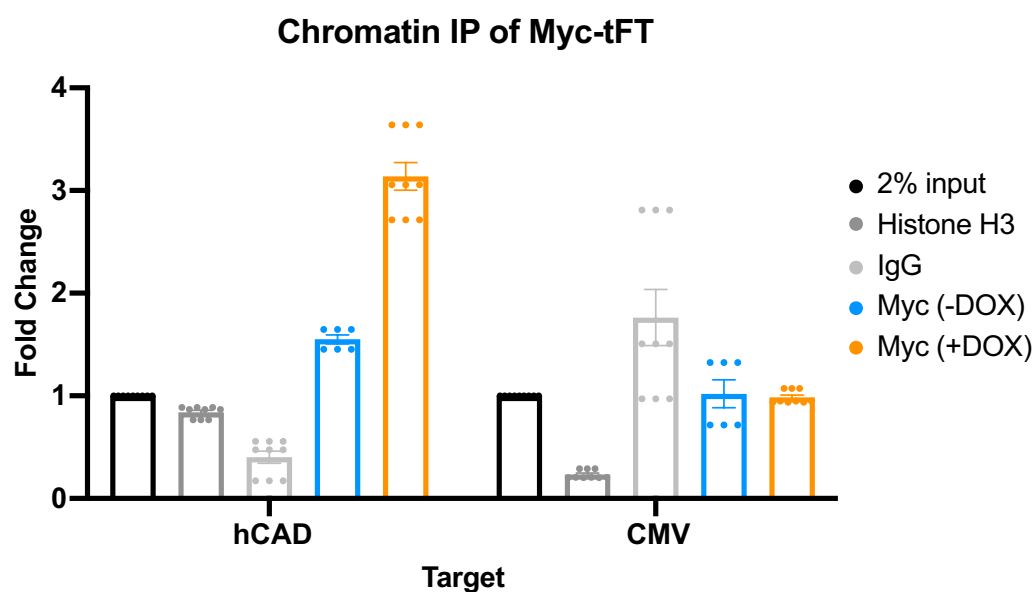


Figure 3.22: **Myc-tFT is enriched at hCAD but not CMV promoters** Protein enrichment at promoter sites was assessed by qPCR following Chromatin Immunoprecipitation (ChIP) of U2OS FRT/TO Myc-tFT cells. hCAD is a traditional Myc target while CMV is the promoter under which the Myc-tFT is expressed.

3.6 Chapter Summary

To summarise, the findings of the chapter are concluded as follows:

- **Tandem fluorescent timer tags can be used to assess Myc stability:** specifically, the combination of mCherry and mNeonGreen as the two FPs for this assay is well suited for relative measurement of Myc stability and does not affect Myc localisation.
- **Myc-tFT has the same half-life and is processed post-translationally like endogenous Myc:** I first demonstrated that Myc-tFT has comparable half-life to endogenous Myc expressed in physiological levels. This is a very good feature of our tFT when compared to previously used FP-tagged Myc (like Myc-eGFP) where the half-life is increased by the presence of the tag. Work by Blake et al. (2019) where they demonstrate the use of a fluorescent based assay for Myc degradation based on GFP-tagged Myc, shows stabilisation of Myc by their choice

Chapter 3. Generation and validation of a suitable Myc Stability Sensor

of FP. The assay I generated in this work would, therefore, more accurately reflect changes in Myc stability and offers increased sensitivity when applied to a compound screen.

- **Myc-tFT is more sensitive than traditional tools used to assess Myc stability:** There are many advantages to an imaging-based assay for protein stability compared to traditional tools like cycloheximide-chase assay. For example, it is better suited to high-throughput screening and it does not require use of metabolic labelling or inhibition of key biological processes. They also offer single-cell resolution which is otherwise hard to achieve. The tFT assay offers all these advantages to the study of Myc stability and, as I have demonstrated in this chapter, displays increased sensitivity over that of traditional cycloheximide-chase experiments. In the next chapter I will modify and validate this assay for a medium-throughput compound screen of modifiers of Myc stability.
- **Myc-tFT is functional:** This concluding finding is very impactful as it will allow me to investigate downstream effects of stabilisation and destabilisation of Myc by inhibitors of proteins that interact with and affect Myc.

Chapter 4

Optimization and application of Myc-tFT stability sensor in a medium-throughput drug screen.

4.1 Introduction

Following the generation and validation of the Myc stability sensor, Myc-tFT, I set out to use this assay at a larger scale in a medium-throughput drug screen. This work, described in this Chapter, was conducted during a placement at industry partner AstraZeneca and under the supervision of Dr. Karen Roberts and Mr. Phil Hopcroft.

The key aims of this section are:

1. **Assay optimisation.** The optimal automated imaging and image analysis conditions need to be elucidated in order reproduce most accurately the manual image and data analysis described in the previous chapter, while applying miniaturisation of the assay in a 384-well format.
2. **Whole field analysis experiments.** The assay's robustness is to be tested through analysis of whole fields of cells and across multiple wells and plates. Dose-response curves for modulators of Myc stability will be produced.

Chapter 4. Optimization and application of Myc-tFT stability sensor in a medium-throughput drug screen.

3. **Single-cell analysis experiments.** The effect of known modulators of Myc stability is to be assessed at the single-cell level.

4.2 Assay optimization

In order to generate a higher throughput version of the Myc-tFt assay from the manual version described in the previous chapter, these changes needed to be implemented: 384-well format, compatibility with an automated HCS platform which allows for simultaneous imaging in multiple channels and software-based image analysis, a robust readout that responds uniformly to modulation of the target. The steps undertaken to meet these parameters and adapt the assay to higher-throughput screening, are described in this section.

4.2.1 Establishing a seeding density

The first step in adapting this assay to a higher throughput setting was to define seeding density for the well format to be used, 384-well plate. U2OS FRT/TO Myc-tFT cells were seeded at different seeding densities in DMEM without phenol red and in the presence of doxycycline (DOX) and left overnight to grow. Cells were imaged using the CellInsight™ CX5 High Content Screening (HCS) platform with a 10x air objective. Representative images are shown in **Figure 4.1**. In all conditions of less than 2000 cc/well (cells per well) cells were too sparsely seeded. In concentrations above 3000cc/well sufficient number of cells were present for analysis (>100cc/well) and not too densely seeded that background could not be detected. For this reason, 5000cc/well was selected as the appropriate seeding density.

Segmentation of nuclei expressing Myc-tFT was attempted but the variability in brightness between cells made segmenting all nuclei impossible, generating a bias for brighter or dimmer cells based on the segmentation parameters. To solve this issue, a nuclear stain that would result in even masking of all cells in the field was tested.

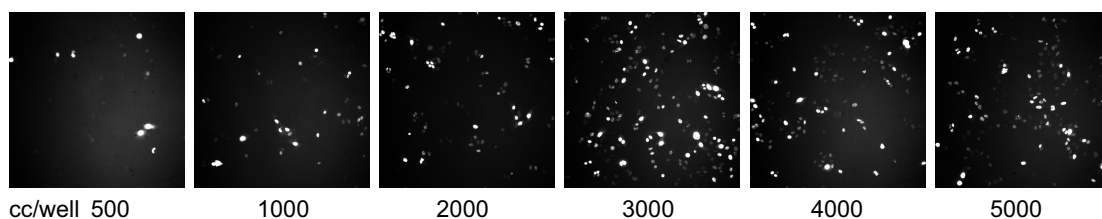


Figure 4.1: **Seeding density.** U2OS FRT/TO Myc-tFT cells were seeded at different seeding densities (cells per well or cc/well) in a 384-well plate in the presence of doxycycline. Representative images of mNeonGreen after overnight incubation with DOX signal are shown.

4.2.2 Nuclear labelling and image acquisition optimization.

Nuclei of live cells can be stained with the use of Hoechst 33342, a cell permeable DNA dye that binds to Adenosine and Thymidine-rich (A-T) regions and has an excitation wavelength range of 361/497nm, emitting in blue light. In the first instance, Hoechst (at a final concentration of $1\mu\text{g}/\text{mL}$) was dosed with the use of a MultidropTM Combi reagent dispenser. Volume wise, $5\mu\text{L}$ of Hoechst were added to wells containing $40\mu\text{L}$ of cells and media. In order for this additional volume to not further dilute any drug treatments that would have been carried out, and therefore affect the output of the treatment, Hoechst was added five minutes prior to imaging. However, image acquisition time was extremely long, with each plate requiring more than an hour to image due to the fact that the Hoechst staining in the top part of the plate was really weak, which in turn caused the autofocus to fail and increasing acquisition time of each well. In a medium-throughput setting, multiple repeats of each compound treatment would be distributed throughout the plate. A long acquisition time would mean that the time elapsing in between imaging of repeats would be too long and treatments with the same compound would develop for different lengths of time, invalidating the repeats and the assay. To remedy this, Hoechst staining was performed 30 minutes ahead of imaging and acquisition parameters were changed so that binning was increased from 2x2bin to 4x4bin. This reduced acquisition time to around 40 minutes. Nevertheless, the brightness of Hoechst staining was persistently low in the upper part of the plate when compared to wells in the bottom half of the plate. This is evident in **Figure 4.2 A** where callouts for wells A3 and P24 show a marked difference in intensity of Hoechst staining.

Chapter 4. Optimization and application of Myc-tFT stability sensor in a medium-throughput drug screen.

In order to be able to dose Hoechst with minimal addition of volume to the wells, dosing by acoustic liquid handler Echo555, was tested. This liquid handler allows for accurate dosing of compounds in nanoliters volumes and is routinely used at AstraZeneca to dispense compounds in plates of small well format (Roberts et al., 2016). This is advantageous as Hoechst can be dosed for longer time prior to imaging without altering the final volume in the well, and thus the final concentration of compounds in the wells. Indeed, Hoechst was dosed at 100nL/well (final concentration was maintained) with the acoustic dispenser 30 minutes prior to imaging. This resulted in more even Hoechst staining across the plate, as shown in **Figure 4.2 B**, and a reduction of imaging time to less than 15 minutes. Finally, Hoechst incubation time was extended to 1 hour to increase brightness of the signal, allowing optimal segmentation of nuclei.

Overall, nuclear segmentation based on Hoechst offered the advantage of segmentation of the whole nucleus, as opposed to the manual analysis method used in the previous chapter whereby the mean signal intensity of a circular area, which covered the majority of the nucleus, is used as a proxy for nuclear intensity.

4.2. Assay optimization

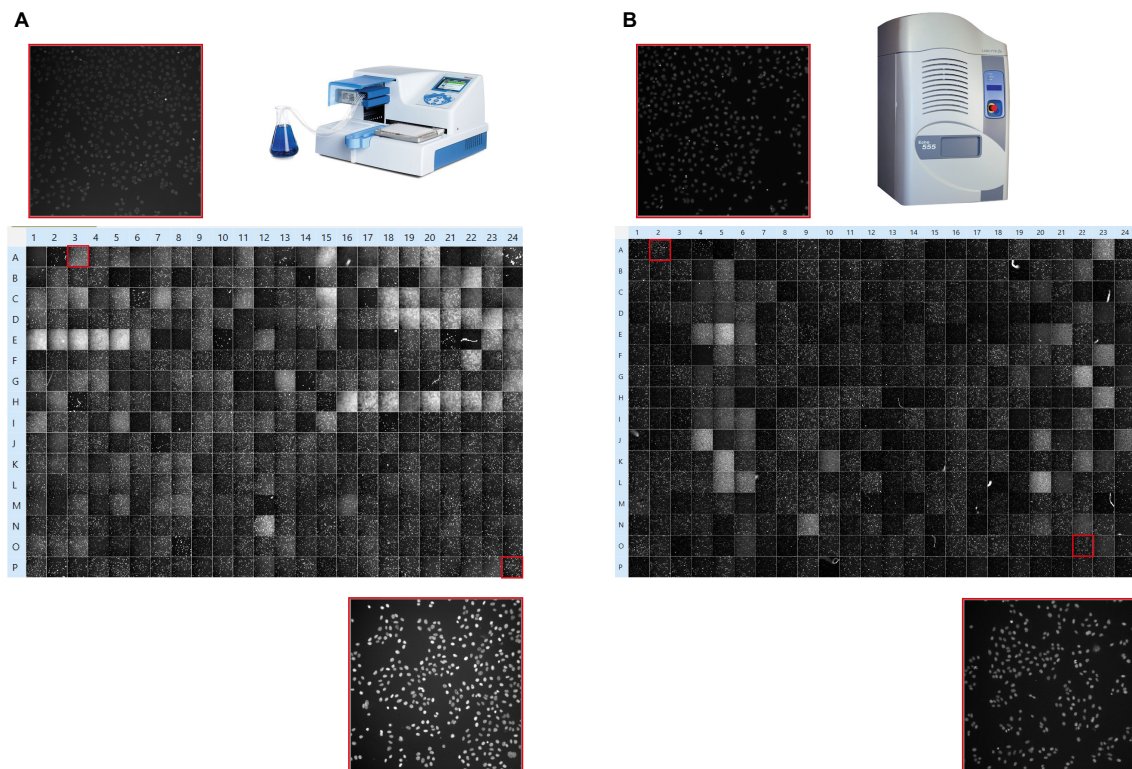


Figure 4.2: **Different modes of dispensing Hoechst.** Representative images of 384-well plates of cells dosed with Hoechst and call out of wells. U2OS FRT/TO Myc-tFT were treated with DNA stain Hoechst ($C_f=1\mu\text{g}/\text{mL}$) with two different dispensing methods:

- A Hoechst was dispensed using a MultidropTM Combi reagent dispenser at $5\mu\text{L}/\text{well}$ ($40\mu\text{L}$ initial volume in the well)
- B Hoechst was dispensed using an Echo555 Acoustic Liquid Handler at $100\text{nL}/\text{well}$

Chapter 4. Optimization and application of Myc-tFT stability sensor in a medium-throughput drug screen.

4.2.3 Growth media selection for optimal imaging conditions.

An additional technical imaging issue arose when binning was increased to yield brighter Hoechst signal. Cells were imaged in the three channels: Channel 1 (386) to acquire Hoechst signal, Channel 2 (485) to acquire mNeonGreen signal; Channel 3 (549) to acquire mCherry signal. Increased binning resulted in increased background signals in Channel 2 and Channel 3 that could be bleached by a prior excitation in the 485 channel. It is known that flavins, like riboflavin, and other metabolites produced by cells and present in some cell growth media can cause autofluorescence when excited at certain wavelengths (Bartolomé and Abramov, 2015). Suspecting autofluorescence of metabolites present in the media, I decided to compare the imaging media routinely used in Dr. Lindon's lab, Leibovitz's L15 media, to that which I had been using at AstraZeneca, DMEM (Dulbecco's Modified Eagle Medium) without phenol red (a media commonly used for imaging assays in AstraZeneca). U2OS FRT/TO Myc-tFT cells were seeded in Leibovitz's L15 media (columns 1-12) or DMEM without phenol red (columns 13-24) and DOX and left overnight in an incubator at 37C 5% CO₂. Cells were imaged in the three channels the following day. **Figure 4.3** shows the resulting fluorescence acquisition in Channel 2, 485, where it is evident that the well containing DMEM display high degrees of autofluorescence that are not seen with Leibovitz's L15. Well G13 is a well containing DMEM that had been imaged during the acquisition set up and where the autofluorescence had been bleached.

In order to avoid issues with autofluorescence, subsequent experiments were performed with cells cultured in Leibovitz's L15 media.

4.2. Assay optimization

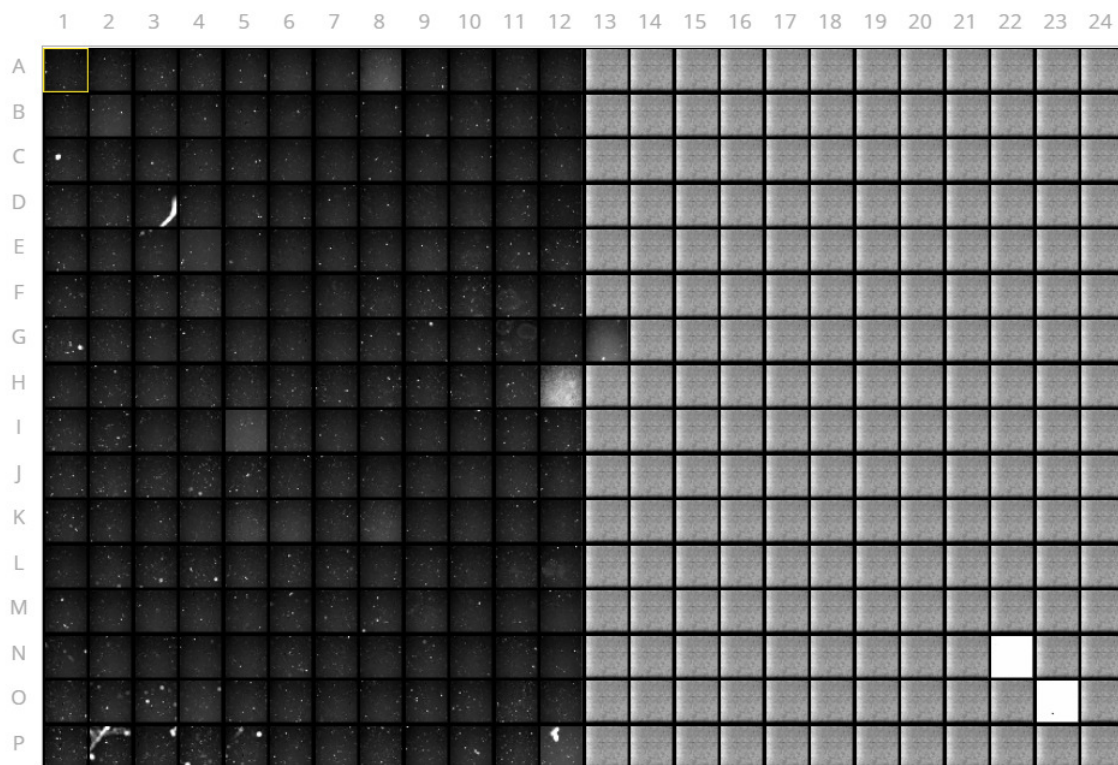


Figure 4.3: **Difference in background fluorescence between Leibovitz's L15 media and DMEM without Phenol red.** U2OS FRT/TO Myc-tFT cells were seeded in either Leibovitz's L15 media (Columns 1-12) or DMEM without phenol red (Columns 13-24) (both supplemented with 10% FBS) in the presence of doxycycline. Well G13 shows a well containing DMEM that has been previously imaged, thus bleaching the autofluorescent components of the media.

Chapter 4. Optimization and application of Myc-tFT stability sensor in a medium-throughput drug screen.

4.2.4 Automated image analysis on HCS studio

Having established appropriate image acquisition conditions, I proceeded to set up image analysis parameters within HCS studio. Firstly, 3D background subtraction was applied to each channel image. As explained above, Hoechst staining is acquired in Channel 1 and offers an even staining for cell nuclei in the field that can be segmented, as in **Figure 4.4 A**. Those segmented nuclei are classified by HCS Studio as “Valid Objects”. From these, the nuclei that are not positive for mNeonGreen signal are then excluded (segmentation in orange - average object intensity is less than 100 over background) to generate Selected Objects category (segmentation in blue) of nuclei positive in both Channel 1 and Channel 2. **Figure 4.4 B, C** displays Channel 2 signal for the same well with (B) and without (C) segmentation overlaid.

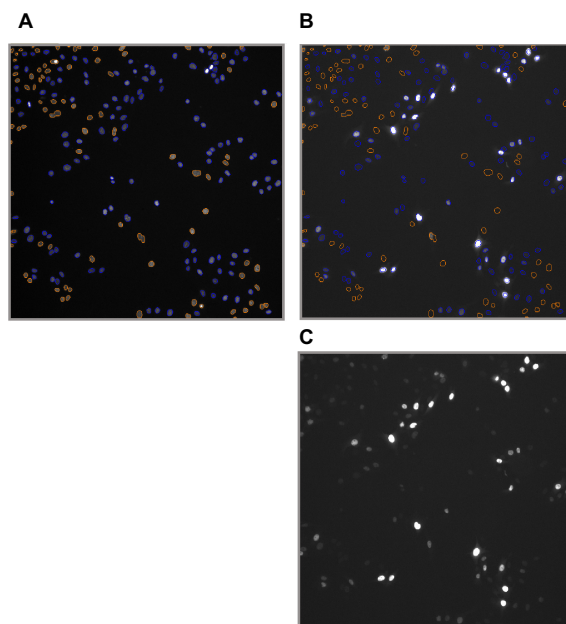


Figure 4.4: Nuclei segmentation and object selection Representative images of U2OS FRT/TO Myc-tFT cells with segmentation applied. Segmentation in Channel 1 generates objects selected (blue) or rejected (orange) according to mNeon threshold in Channel 2.

- A Hoechst staining in channel 1 is used to segment nuclei of cells in the field. All nuclei segmented are then selected for positivity in Channel 2.
- B mNeonGreen signal in channel 2 is used to exclude cells that do not express Myc-tFT at the moment of imaging.
- C mNeonGreen signal as above but without mask displaying segmentation for better visualisation of weakly expressing cells.

4.2. Assay optimization

Valid Object count is, therefore greater than Selected Object count, as shown in **Figure 4.5**. The data, visualised and plotted using the Genedata Screener analyzer tool, reveals a plate edge effect where there are a reduced number of objects in the wells at the perimeter of the plate, which is clear in **Figure 4.5 A**, and slightly reduced in **Figure 4.5 B** following restriction of Channel 2 positive objects. Plate edge effects are common in cell-based 06- or 384-well plate assays and are due to differences in temperature and gas exchange between the centre and edges of the plate.

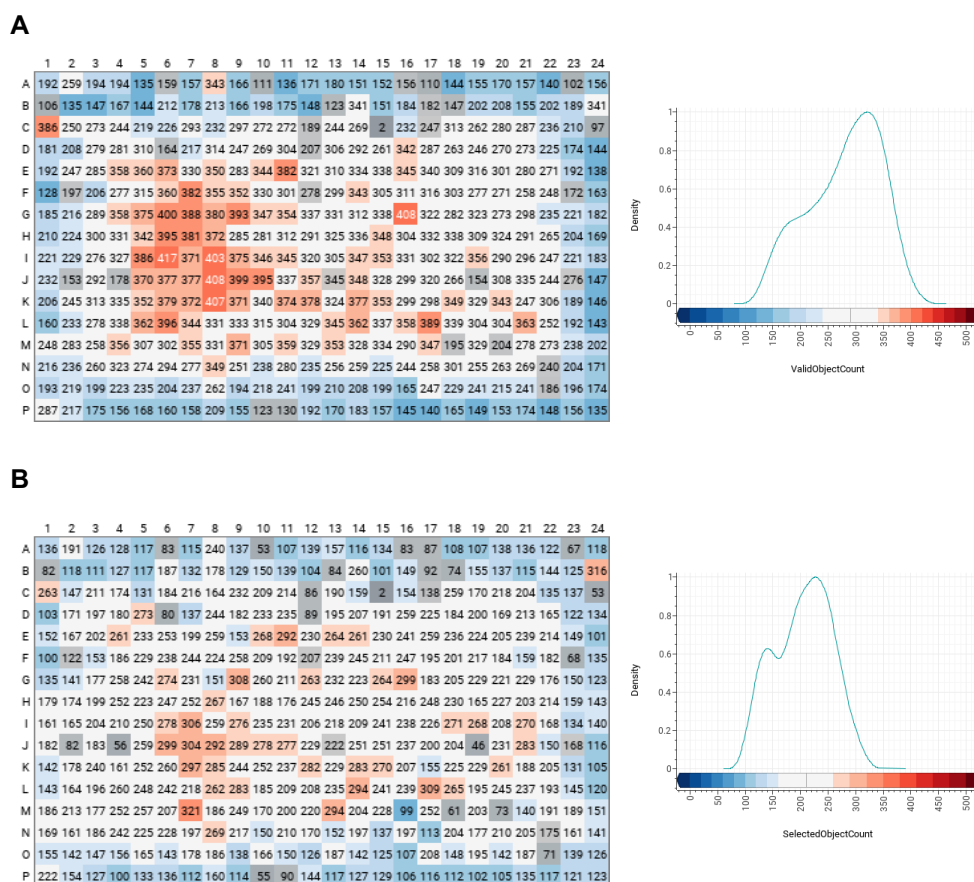


Figure 4.5: Valid Object Count versus Selected Object Count Data of an untreated plate of U2OS FRT/TO Myc-tFT cells. The data is visualised and plotted using the Genedata Screener analyzer tool.

- A Valid Object count per well in plate layout (left) and distribution and colour gradient scale (right).
- B Selected Object count per well in plate layout (left) and distribution and colour gradient scale (right).

These parameters become important in the context of whole field analysis of the

Chapter 4. Optimization and application of Myc-tFT stability sensor in a medium-throughput drug screen.

fluorescent signal, where the average intensity recorded for Channels 2 and 3 is averaged against the number of objects in the field. This normalisation is important and needed to account for edge effects and to discriminate between wells where there are very few but very bright cells that can be excluded from analysis if the selected Object count is very low (less than 100). The effect is evident in **Figure 4.6** where the average intensity of each well is divided by the number of Valid Objects (**Figure 4.6 A**) or Selected Objects (**Figure 4.6B**) resulting in a higher mean intensity Channel 2 (MEAN_CircAvgIntenCh2) reading in the latter. This is also apparent in the distribution of the data, specifically the value where the centre of the distribution curve lies is about double in the data normalised to the Selected Object count.

4.2. Assay optimization

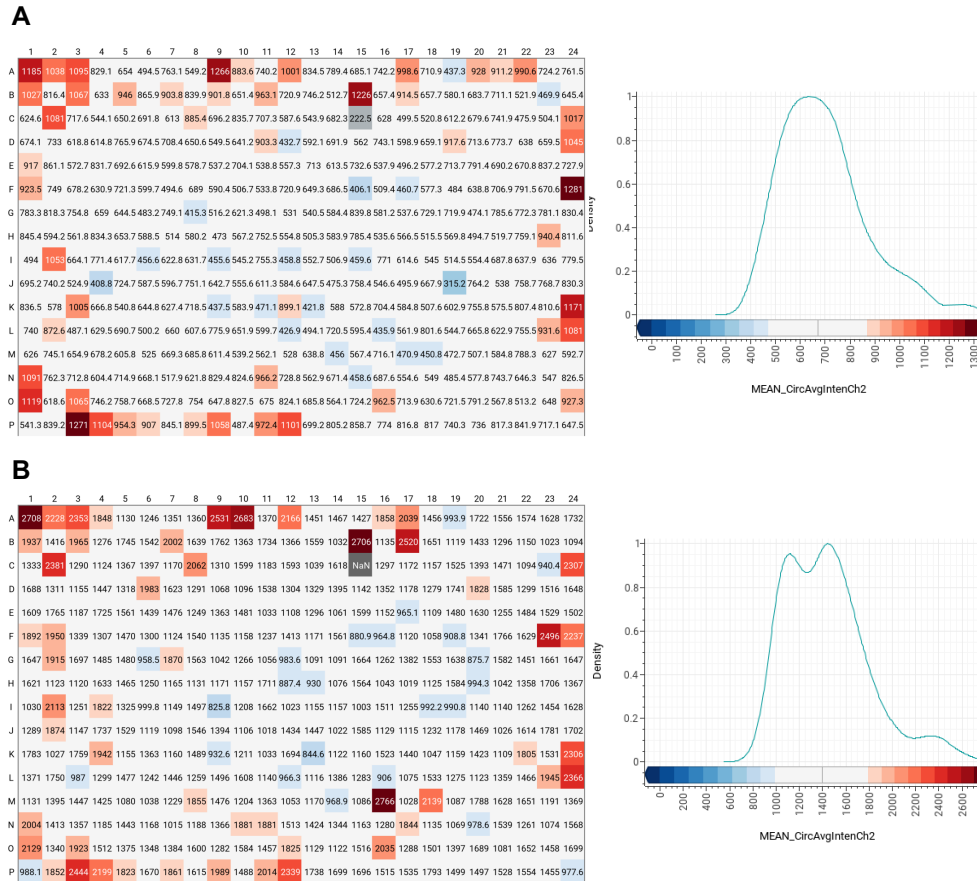


Figure 4.6: Effect of normalisation against valid Object count or Selected Object count. Data for Channel2 (mNeonGreen signal) of an untreated plate of U2OS FRT/TO Myc-tFT cells normalised to:

- A Valid Object count. The average Channel 2 intensity of each well is normalised to the number of Hoechst-positive nuclei.
- B Selected Object count. The average Channel 2 intensity of each well is normalised to the number of Hoechst- and mNeonGreen-positive nuclei.

Chapter 4. Optimization and application of Myc-tFT stability sensor in a medium-throughput drug screen.

Once the selected Object number is calculated for each well, and the average intensity of Channel 2 and 3 signals is normalised against it, this analysis method generates a mean well intensity (Figure 4.6 B, 4.7 A). Per well, the average intensity of each nuclei in Channel 3 is divided by that of Channel 2 generating the tFT ratio. These values are then normalised to the number of Selected Objects giving a mean value for Channel3/Channel2 (MEAN_CircAvgIntenRatioCh3Ch2, Figure 4.7 B).

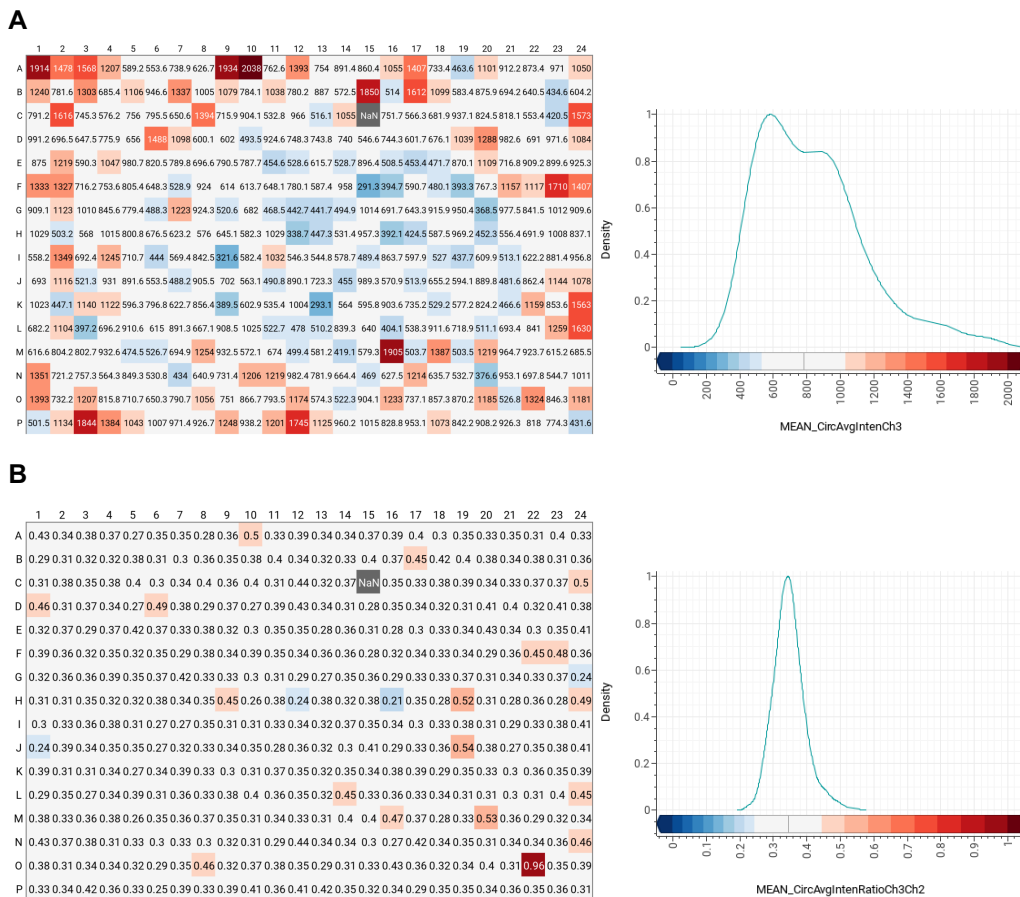


Figure 4.7: Channel 3 and tFT Ratio normalised to Selected Object count. Data from an untreated plate of U2OS FRT/TO Myc-tFT cells normalised to Selected Object count:

- A Channel 3 (mCherry signal). The average Channel 3 intensity of each well is normalised to the number of Hoechst- and mNeonGreen-positive nuclei.
- B Channel 3 to Channel 2 ratio (tFT ratio). The average ratio of Channel 3 to Channel 2 intensity of each well is normalised to the number of Hoechst- and mNeonGreen-positive nuclei.

4.2. Assay optimization

Finally, to summarize, the workflow set up for this medium-throughput assay was created, as illustrated in **Figure 4.8**.

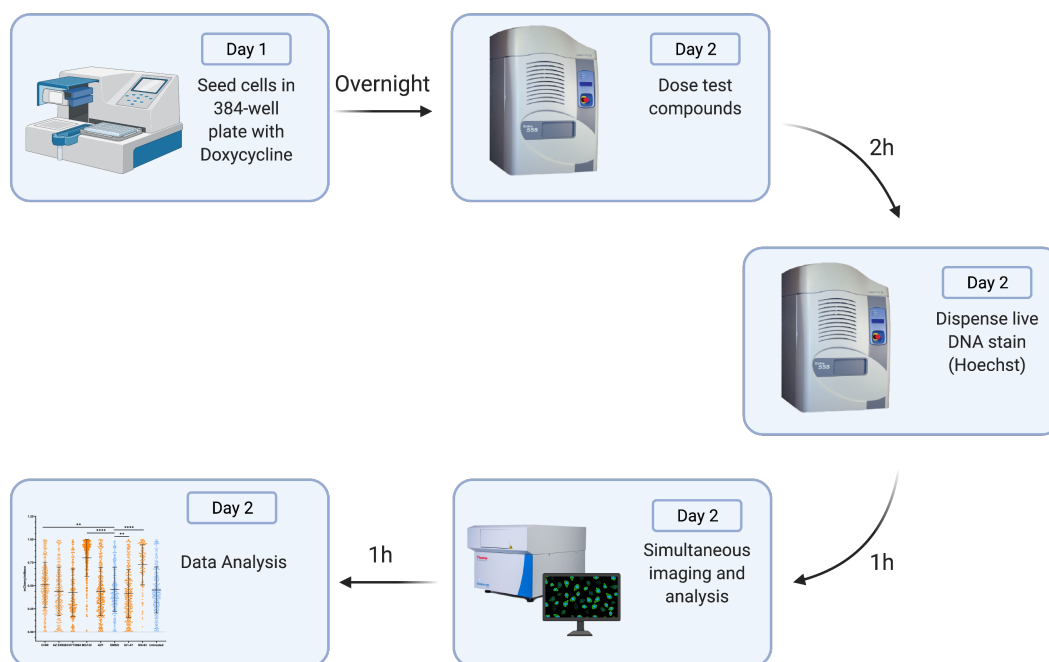


Figure 4.8: Experimental workflow. The experimental workflow for a medium-throughput screening assay was set up as follows:

- On the afternoon of Day 1 cells are seeded (500cc/well) in a 384-well plate using Leibovitz's L15 media with Doxycycline
- On Day two, three hours prior to imaging compounds are dosed using an acoustic dispenser and incubated at 37C, 5%CO₂
- One hour prior to imaging, the plate is dosed with Hoechst DNA dye using an acoustic dispenser.
- Cells are imaged using a CellInsight™ and image analysis is performed concurrently to image acquisition on the HCS studio software.
- Data is analysed using Genedata Screener software or GraphPad PRISM

4.3 Whole-field analysis of the effect of modulators of Myc-tFT ratio.

Medium- or high-throughput screening relies on the ability to identify active compounds, termed “hits”, from testing a large library of compounds, at a single concentration. To minimise false positive or negatives, this process is dependent on the quality and reproducibility of the assay used to screen the compounds. In order to define the “suitability” or goodness of an assay, Zhang, Chung, and Oldenburg (1999) defined a screening window coefficient, called Z' (Z-prime or Z-factor), which reflects the dynamic range and variability of the assay signal. The Z' is calculated according to the equation:

$$Z' = 1 - \frac{3\sigma_{c+} + 3\sigma_{c-}}{|\mu_{c+} - \mu_{c-}|}$$

where 3σ is defined as three standard deviations and μ is the mean of the positive (c+) or negative (c-) controls. According to Zhang, Chung, and Oldenburg (1999), Z' values are always ≤ 1 and define the goodness of the assay according to the following ranges:

$Z'=1 \Rightarrow$ An ideal assay

$1 > Z' \geq 0.5 \Rightarrow$ An optimal assay

$0.5 > Z' > 0 \Rightarrow$ A marginal assay

$Z'=0 \Rightarrow$ A “yes/no” type of assay

$Z' \leq 0 \Rightarrow$ Non-suitable for screening

Z' is routinely used in AstraZeneca to identify successful assays to be used in their screening platforms. Their internal parameters are that assays with $Z' < 0.4$ are failed, and only assays with a $Z' \geq 0.6$ can be employed in high-throughput assays.

4.3. Whole-field analysis of the effect of modulators of Myc-tFT ratio.

4.3.1 Assessing the goodness of the Myc-tFT assay through artificial stabilization of Myc

In order to define a Z' , a stimulator control (c+) needs to be established against which to measure changes in tFT ratio. For this, I used proteasome inhibitor MG132, whose effect on Myc-tFT had been shown in **Chapter 3**. Vehicle control DMSO would provide the negative control (c-). U2OS FRT/TO Myc-tFT cells were processed according to the workflow shown in **Figure 4.8**, using these controls.

For each experiment, two treatment plates were dosed according to the layout shown in **Figure 4.9 A**, and a control plate was left untreated. The column-wise dosing allows testing of the reproducibility of the measured effect of treatment and any edge effects that could arise. Results in **Figure 4.9 B**, where the ratio is visualised according to a colour gradient, clearly display an increase in Myc-tFT ratio in MG132-treated columns, which is not present in the untreated control plate, **Figure 4.9 C**. No edge effect was recorded in either treated or untreated plates. The effect of MG132 is also apparent in **Figure 4.9 D** where the ratio of each well is plotted by column. MG132-treated wells (in red) displayed an average tFT ratio $tFT=0.77$ (± 0.058 Standard deviation(SD)) while DMSO-treated wells showed greater variability and a tFT ratio averaging $tFT=0.38$ (± 0.055 SD) (**Table 4.1**). In the control plate (**Figure 4.9 E**, **Table 4.1**), wells in the same position as the DMSO and MG132-treatment both had an average ratio of $tFT=0.36$ ($\pm 0.056-0.06$ SD). MG132 treatment also had the effect of increasing the number of Selected Objects, which is expected as cells with low-level expression of Myc-tFT would start becoming positive as a consequence of protein accumulation. Recorded intensity of both channels also increases, with the Channel 3 intensity increasing more than Channel 2, as indicated by the increased ratio. Finally, a Z' factor is calculated by the Genedata Screener software as $Z'=0.1245$ and $Z'=0.1049$ for the treated plates (**Table 4.1**). This value becomes negative in the control plate suggesting that the assay can detect differences in treatment but there are variability issues. A true inhibitor control, which causes a decreased ratio, would offer a more appropriate c- than vehicle control (a neutral stimulator) and might give rise to a bigger Z' factor; however, such a compound has yet to be identified in this study. In order to further test the goodness of

Chapter 4. Optimization and application of Myc-tFT stability sensor in a medium-throughput drug screen.

the Myc-tFT assay, I next tested a compound that had proven effective at increasing Myc-tFT in single cell experiments described in **Chapter 3.4**.

	Plate 1		Plate 2		Control Plate (untreated)	
	DMSO	MG132	DMSO	MG132	DMSO	MG132
Selected obj count	216	246	211	244.5	200	193
MEAN_Avg int RatioCh3Ch2 ±Standard deviation	0.3824 ±0.055	0.7701 ±0.058	0.3651 ±0.053	0.677 ±0.04	0.3608 ±0.056	0.3631 ±0.060
MEAN_Avg int Ch2	1013	2117	999.8	2096	908.6	890.1
MEAN_Avg int Ch3	603.2	1877	535.7	1621	486.7	463.4
Z' factor – Ratio	0.1245		0.1049		-202.5	

Table 4.1: **Myc-tFT assay goodness as assessed in a Stimulator and Neutral control setting.** Table reporting representative data of n=3 experiments, referring to the plates described in Figure 4.9.

Selected Object count: Average number of Hoechst- and mNeonGreen-positive nuclei per condition.

MEAN_AvgIntRatioCh3Ch2: Mean of the average well tFT ratio per condition.

MEAN_AvgIntCh2 or Ch3: Mean of the average well Channel 2 (mNeonGreen) or Channel 3 (mCherry) intensity per condition.

4.3. Whole-field analysis of the effect of modulators of Myc-tFT ratio.

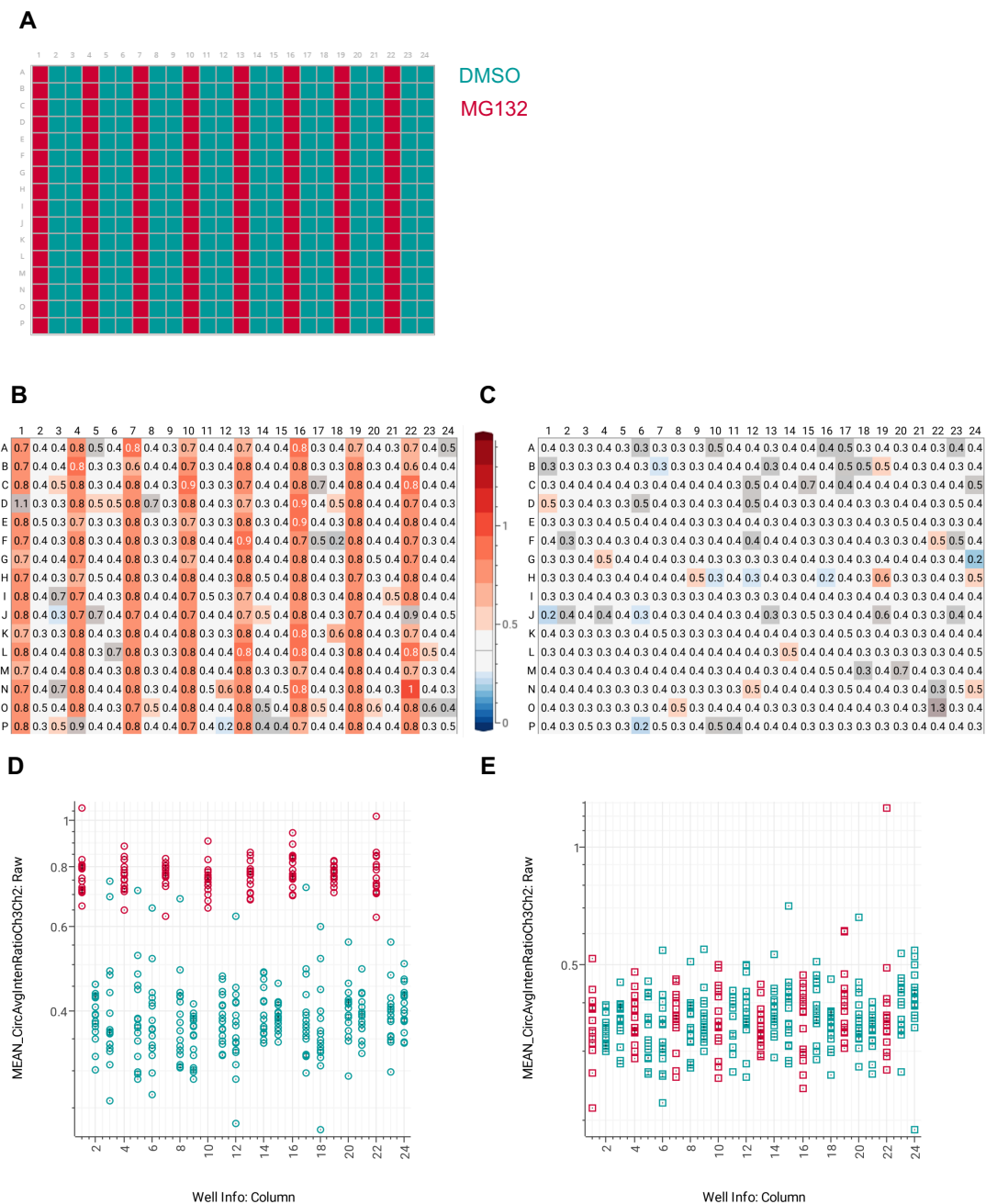


Figure 4.9: **Establishing a stimulator control.** Data from plates of U2OS FRT/TO Myc-tFT treated according to the plate layout or untreated. Representative of n=3 experiments.

- A Compound dosing layout. Cells were treated with Stimulator Control MG132 ($C_f=4.2\mu\text{M}$) or Neutral Control DMSO in columns.
- B Representative treated plate displaying tFT ratio per well. Ratio is displayed in a gradient according to the colour scale. n=2 plates per experiment.
- C Representative untreated plate displaying tFT ratio per well. Ratio is displayed in a gradient according to the colour scale. n=1 plate per experiment.
- D,E Scatter plot of the average tFT ratio per well plotted against plate column. Data of representative treated plate (D), untreated control plate (E).

4.3.2 Challenging the robustness of Myc-tFT assay with with a known modulator of Myc.

As the next step, I challenged the assay with a compound I have previously shown to positively modulate Myc-tFT ratio, GSK3 β inhibitor CHIR99021. I would also note again that GSK3 β is proposed to be physiological regulator of Myc stability (Blake et al., 2019; Gregory, Qi, and Hann, 2003).

Using the established workflow described in the previous **Section 4.3.1**, I treated columns of a 384-well plate with either MG132 (Cf=4.2 μ M), CHIR99021 (Cf=3 μ M) or DMSO, according to the layout in **Figure 4.10 A**. These concentrations had been used in **Chapter 3**.

Once again, the effect of MG132 is marked, (tFT=0.75, representative treated plate in **Figure 4.10 B**). CHIR99021, instead results in a slight increase of the mean ratio (tFT=0.40) as shown in **Table 4.2** and in the scatter plot of **Figure 4.10 D**. However, the spread of the data for CHIR99021-treated wells overlaps with the spread of DMSO, although the distribution is shifted towards a higher ratio. This yields a Z' factor of close to 0, slightly negative in the case of the second plate (Plate 1 Z' =0.029, Plate 2 Z' =-0.018, as reported in **Table 4.2**). No column effect is seen in the untreated plate, Z' could not be measured here (**Figure 4.10 C, E**). This experiment was repeated a total of three times with two treatment plates per experiment; each repeat confirmed low Z' values and an effect of CHIR99021.

An additional analysis was performed where neutral control (DMSO) minimal value is set at 0 and the maximal value of the stimulator control (MG132) is set as 100 (their average values were calculated accordingly). This allows to define the effect of CHIR99021 on a percentage scale (**Table 4.2**, normalised MEAN_AvgIntRatioCh3Ch2) which is approximately 8%. It is worth noting that work by Blake et al. (2019), in which a different fluorescent-based screening method for modulators of Myc is described, employs the same normalisation and only hits with an effect of more than 30% are considered for further characterisation.

4.3. Whole-field analysis of the effect of modulators of Myc-tFT ratio.

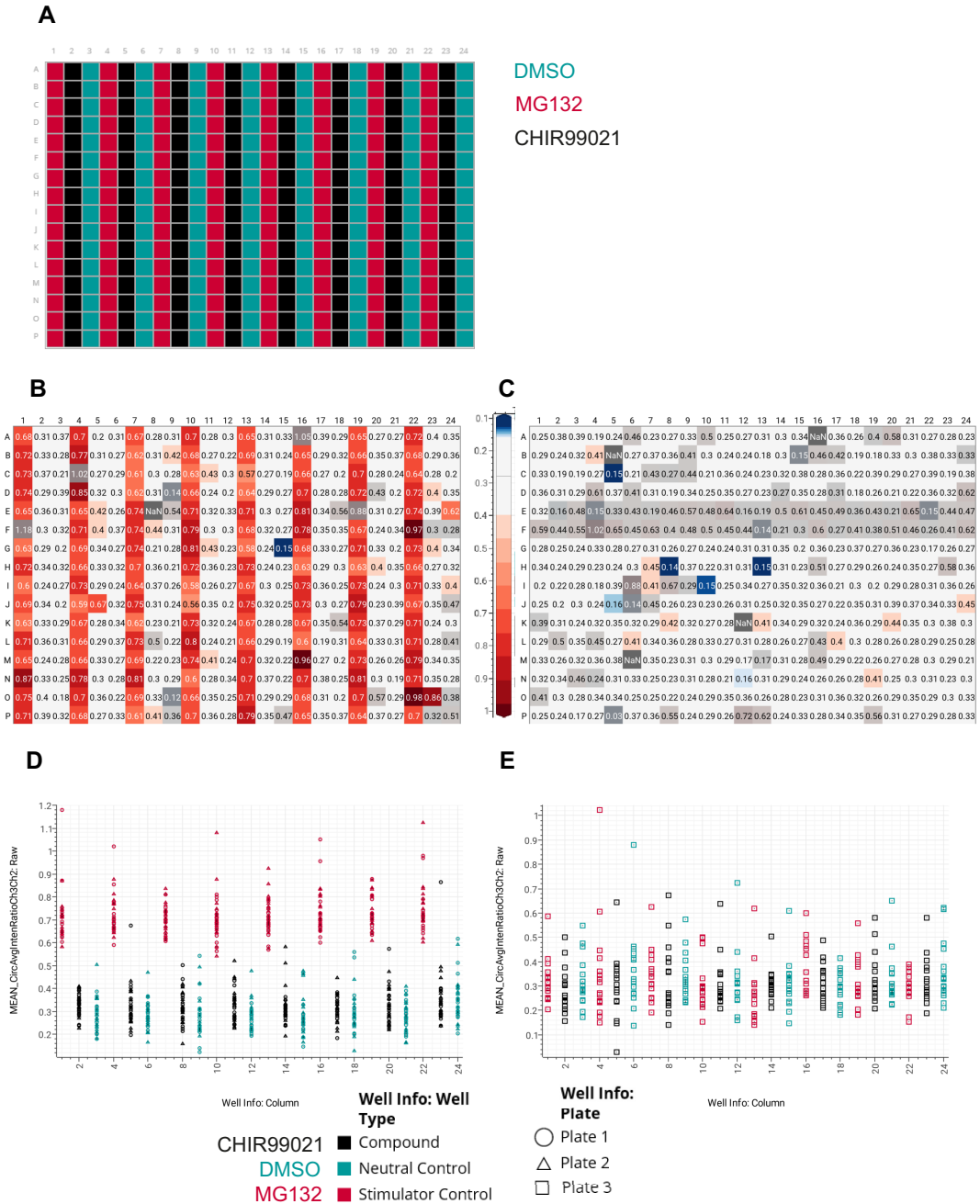


Figure 4.10: Testing an intermediate stimulator, CHIR99021. Data from plates of U2OS FRT/TO Myc-tFT treated according to the plate layout or untreated. Representative of n=3 experiments.

A Compound dosing layout. Cells were treated with Stimulator Control MG132 ($C_f=4.2\mu\text{M}$), compound CHIR99021 ($C_f=3\mu\text{M}$) or Neutral Control DMSO in columns.

B Representative treated plate displaying tFT ratio per well. Ratio is displayed in a gradient according to the colour scale. n=2 plates per experiment.

C Representative untreated plate displaying tFT ratio per well. Ratio is displayed in a gradient according to the colour scale. n=1 plate per experiment.

D,E Scatter plot of the average tFT ratio per well plotted against plate column. Pooled data of two treated plates (D), untreated control plate (E).

Chapter 4. Optimization and application of Myc-tFT stability sensor in a medium-throughput drug screen.

	Plate 1			Plate 2			Control Plate (untreated)		
	DMSO	MG132	CHIR99021	DMSO	MG132	CHIR99021	DMSO	MG132	CHIR99021
Selected obj. count	156.1	165.1	161.5	163.8	179	168.3	180	192	189.5
MEAN_Avg. int RatioCh3Ch2 (Raw)	0.3625	0.7527	0.395	0.3778	0.7634	0.4072	0.3079	0.29	0.2969
MEAN_Avg. int RatioCh3Ch2 (Normalised)	0.1895	99.7	8.47	0.2949	99.23	7.84	0	100	163
MEAN_Avg. int Ch2	1724	3047	1890	1632	3004	1769	1440	1486	1470
MEAN_Avg. int Ch3	1152	2742	1260	1101	2696	1177	767.7	780.3	773.7
Z' factor – Ratio	0.029			-0.018			-135.3		

Table 4.2: **Myc-tFT assay goodness decreases when assessing effect of CHIR99021.** Table reporting representative data of n=3 experiments, referring to the plates described in Figure 4.9.

Selected Object count: Average number of Hoechst- and mNeonGreen-positive nuclei per condition.

MEAN_AvgIntRatioCh3Ch2 Raw: Mean of the average well tFT ratio per condition (raw values).

MEAN_AvgIntRatioCh3Ch2 Normalised: Mean of the average well tFT ratio per condition (Normalised values). For normalisation purposes, Neutral control values were set close to 0 and Stimulator control to 100 to yield a percentage activity of the compound.

MEAN_AvgIntCh2 or Ch3: Mean of the average well Channel 2 (mNeonGreen) or Channel 3 (mCherry) intensity per condition.

4.3. Whole-field analysis of the effect of modulators of Myc-tFT ratio.

Taken together, these results along those of the previous section indicate that with these control compounds, the Z' of the Myc-tFT assay is close to zero, meaning that its variability limits its application as a quantitative assay. However the Z' score suggests that the assay could be used with a “yes/no” qualitative screening approach, to evaluate the presence or absence of an effect of compounds on Myc stability.

To further investigate the impact of the distribution of the data on the goodness of the assay and verify whether the Myc-tFT can be employed to generate dose-response curves, I treated U2OS FRT/TO Myc-tFT cells with varying concentrations of MG132 or CHIR99021. Each plate contained 3 replicate dose-response curve plates, stimulator control (MG132, $C_f=4.2\mu\text{M}$) and neutral control (DMSO) wells. Two plates were treated, imaged and acquired in the same experiment which in turn was repeated three times. Results from a representative experiment are depicted in **Figure 4.11**, which show the ability of the Myc-tFT assay to report on increase in Myc stability induced in a dose-response manner by proteasomal inhibition (MG132 $AC_{50}=0.5\mu\text{M}$) but not for more subtle (and biologically relevant) changes such as that induced by CHIR99021. It is worth noting that the variability within replicate concentrations of MG132 corresponds to the range in which CHIR99021, and probably other compounds, might be having an effect. This means that compounds that do not cause such a great increase/decrease in stability as MG132 will not be identified as hits in a screen, in accordance with the low Z' value of the assay.

Finally, I wanted to test if single-dose data analysed by student t-test would result in statistically significant changes in Myc stability when treated with either compound. Taking the average population tFT ratios of wells from experiments described at the beginning of this section and depicted in **Figure 4.10**, I generated scatter plots of the data in GraphPad Prism and performed statistical analysis with Student's t-Test. Results, shown in **Figure 4.12 A** display a significant effect of MG132 and CHIR99021 when compared to DMSO and analysed with a student t-test ($p\leq 0.0001$ for both treatments). Data from equivalent wells in an untreated plate (**Figure 4.12 B**) record no significant difference when analysed with the same test (MG132 to DMSO columns $p=0.8951$,

Chapter 4. Optimization and application of Myc-tFT stability sensor in a medium-throughput drug screen.

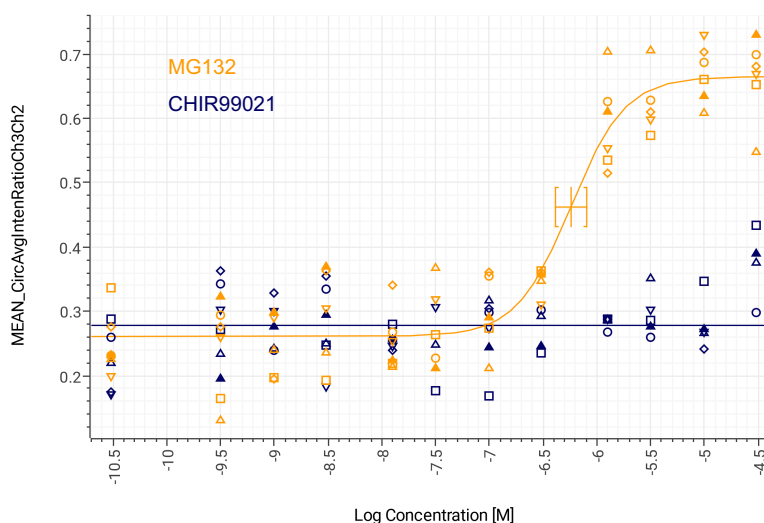


Figure 4.11: **Dose response curves for MG132 and CHIR99021.** Data from plates of U2OS FRT/TO Myc-tFT treated with increasing concentrations of MG132 or CHIR99021, each in triplicate per plate. Representative of n=3 experiments.

CHIR99021 to DMSO columns $p=0.9058$). Therefore, the assay works to generate statistically-significant data but the low Z' factor and distribution of the data precludes the use of the assay in the intended screening programme.

Overall these data supports the notion that Myc-tFT assay could be used to screen compounds dosed at a single dose, however carrying out the analysis at a whole-field level would require too many wells per compound to have sufficient repeats to perform meaningful statistical analysis. For this reason, I next tested a small list of known regulators of Myc stability, by single-cell analysis using the imaging set up I have optimised in this Chapter.

4.3. Whole-field analysis of the effect of modulators of Myc-tFT ratio.

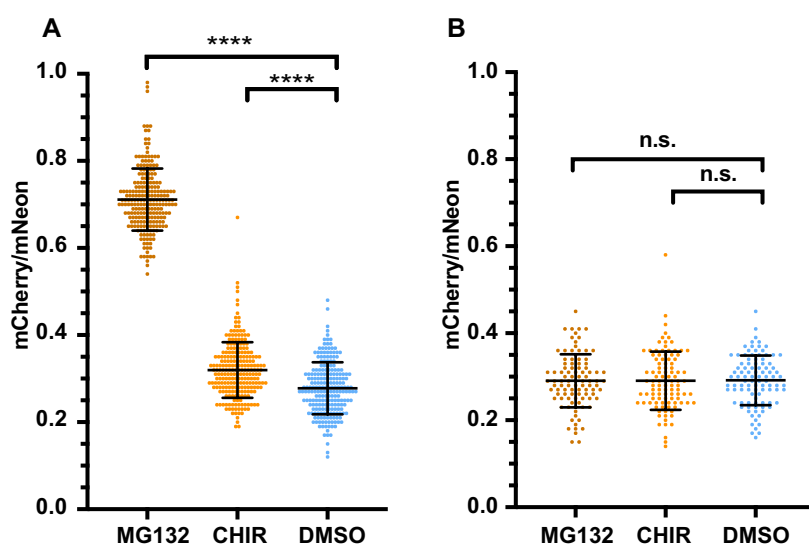


Plate 3 - control

Figure 4.12: Effects of MG132, CHIR99021 by student t-test. Data from plates of U2OS FRT/TO Myc-tFT treated according to the plate layout or untreated in Figure 4.10, analysed by student t-test. Each dot represents the average tFT ratio reading from a well. Representative of n=3 experiments.

A Scatter plot showing the effects of MG132 (Cf=4.2 μ M) or CHIR99021 (Cf=3 μ M) on Myc-tFT ratio compared to DMSO. Data pooled from two separate plates. Each point represents a well. ****= $p \leq 0.0001$ by student t-test.

B Scatter plot showing the tFT ratio of equivalent MG132, CHIR99021, DMSO wells on an untreated plate. Each point represents a well. n.s.=non significant.

4.4 Single-cell analysis of the effect of modulators of Myc stability on the Myc-tFT ratio.

In order to test if the assay was suitable for a single-dose “yes/no” effect screen I applied a medium-throughput screen with the previously outlined workflow, in which I dosed compounds that inhibit proteins whose activity is known to affect Myc stability.

Compounds used for this screen are detailed below and in **Table 4.3** where compound target and reported effect on Myc stability are annotated.

Firstly, CHIR99021, a well established GSK3 β inhibitor, has been shown in this and previous sections to positively modulate Myc stability. This is also seen in work by Blake et al. (2019) and with another inhibitor of GSK3 β by (Gregory, Qi, and Hann, 2003). As described in the introduction, Myc is phosphorylated by GSK3 β on threonine 58 which is a key phosphorylation site for recognition by E3 ligase FBW7 (Welcker et al., 2004; Yada et al., 2004).

ERK1/2 inhibition by SCH772984 has been shown to decrease Myc stability in work by (Hayes et al., 2016; Vaseva et al., 2018). In addition to this compound, I utilised an AstraZeneca-developed ERK inhibitor. In their internal screen for ERK1/2 inhibitors, this compound had resulted more potent than SCH772984. Upon mitogenic signalling, ERK1/2 phosphorylate Myc at serine 62 yielding a phosphorylation that stabilizes and leads to Myc accumulation early in the cell cycle. This phosphorylation is required for subsequent recognition and phosphorylation of Myc by GSK3 β (Sears et al., 1999, 2000).

Ca²⁺/calmodulin-dependent protein kinase II γ (CAMKII) also phosphorylates Myc at S62 and indeed its inhibition by KN-93 is reported to yield decreased Myc levels, as described by (Gu et al., 2017).

USP28 is a de-ubiquitinating enzyme that has been reported to counter ubiquitination by FBW7 (Popov et al., 2007) leading to Myc stabilisation. Work conducted by

4.4. Single-cell analysis of the effect of modulators of Myc stability on the Myc-tFT ratio.

AstraZeneca described an USP28 inhibitor that negatively affects Myc stability (Wrigley et al., 2017), although at high concentrations (measured effect on Myc is above 20 μ M).

Finally, USP14 is a deubiquitinating enzymes associated with the proteasome and is critical for maintenance of proteostasis. Its effect on Myc has not been investigated, however, due to its role in rescuing proteins from degradation by the proteasome (Hu et al., 2005; Koulich, Li, and DeMartino, 2007), it provided an interesting candidate compounds that could, in principle decrease Myc stability via pathways that are GSK3 β and FBW7 independent. In order to test this, USP14 inhibitor IU1-47 (Wang et al., 2018) was employed.

Compound target	Compound name	Effect on Myc stability
GSK3 β inhibitor	CHIR 99021	Increase
ERK1/2 inhibitor	AZ ERK inhibitor	Decrease
ERK1/2 inhibitor	SCH772984	Decrease
Proteosome inhibitor	MG132	Increase
USP28 inhibitor	AZ1	Decrease
USP14 inhibitor	IU1-47	Decrease
CAMIIK inhibitor	KN-93	Decrease

Table 4.3: **Compounds used in this study.** List of compounds that inhibit known regulators of Myc stability and their reported effect on Myc.

4.4.1 Single-dose screening: 10 μ M

Differently to the set up described in the previous section, where the average tFT ratio of all the Selected Objects in the field was plotted, tFT ratios for each Selected Object in a field were exported from the image analysis performed on HCS studio.

tFT values below 0 and above 1 were excluded. Negative tFT ratios could arise in cells with weak Myc-tFT expression and lower mCherry signal than the intensity of background noise. Conversely, ratios greater than 1 could be found in cells with weak Myc-tFT expression, where the mNeonGreen signal was still strong enough to exceed thresholding but differing background noise intensity in the two channels would

Chapter 4. Optimization and application of Myc-tFT stability sensor in a medium-throughput drug screen.

yield an mCherry signal that is slightly higher than the mNeonGreen, giving the false impression of a stable pool of Myc. Due to the automated nature of the image analysis, manual exclusion of these cells could not be carried out, generating a need for gating Myc-tFT values.

Cells were dosed with $10\mu\text{M}$ of the compounds listed above, with the exception of MG132, which had previously shown a significant effect at a final concentration of $4.2\mu\text{M}$, and AZ1 ($\text{Cf}=30\mu\text{M}$), which is reported to have an effect on Myc at concentrations greater of $20\mu\text{M}$ and was used at the highest dose dispensable by the acoustic dispenser whilst maintaining low DMSO concentration. Each compound was dosed in triplicate within a plate and two plates were treated per experiment. Each experiment was repeated in triplicate. Representative results from a dosed plate demonstrate the assay's ability to measure significant changes in Myc-tFT ratio (**Figure 4.13**), however there was great variability in the spread of the data.

4.4. Single-cell analysis of the effect of modulators of Myc stability on the Myc-tFT ratio.

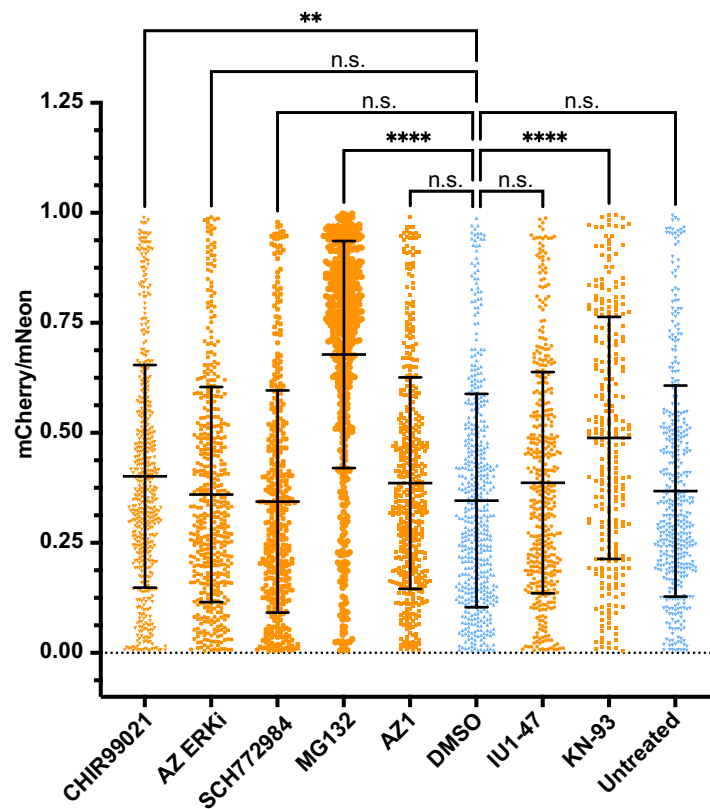


Figure 4.13: **Single-dose ($10\mu\text{M}$) medium-throughput screen of modifiers of Myc stability.** Scatter plot of data from a representative plate of U2OS FRT/TO Myc-tFT treated with compounds listed in table 4.3 at $10\mu\text{M}$ with the exception of MG132 ($C_f=4.2\mu\text{M}$) and AZ1 ($C_f=30\mu\text{M}$); analysed by One-way ANOVA for comparison with DMSO. Each dot represents the ratio for a single cell. Mean and SD are displayed. Representative of $n=2$ plates per experiment and $n=3$ experiments. n.s.= non significant $p>0.05$, $**=p\leq 0.001$, $**** = p\leq 0.0001$

Chapter 4. Optimization and application of Myc-tFT stability sensor in a medium-throughput drug screen.

Statistical analyses of the data from 3 replicates are summarised in **Table 4.4**. Notwithstanding an accurate and consistent effect of MG132, no other compound at these tested concentrations displayed reliable and reproducible effects on Myc-tFT ratios. Indeed the variability was not only recorded across experiments but, more problematically, between plates of the same experiments which are treated and imaged in parallel. Interestingly, KN-93 showed highly significant effect in positively modulating Myc-tFT ratio in three out of five plates. The variability in the data might have been masking any effect of the compounds on Myc stability (as shown by the inconsistency in KN-93 effect), therefore the assay was reproduced with a higher concentration of the compounds.

	EXP 1	EXP 2		EXP 3	
Plate	1	1	2	1	2
CHIR99021	n.s.	*	**	n.s.	****
AZ ERKi	n.s.	n.s.	n.s.	n.s.	n.s.
SCH772984	*	n.s.	n.s.	n.s.	n.s.
MG132	****	****	****	****	****
AZ1	n.s.	n.s.	n.s.	****	****
IU1-47	n.s.	*	n.s.	n.s.	n.s.
KN-93	n.s.	****	****	n.s.	****
Untreated	n.s.	n.s.	n.s.	n.s.	*

Table 4.4: Effect of modulators of Myc stability, dosed at 10 μ M, across multiple experimental repeats. List of compounds that inhibit known regulators of Myc stability and their measured effect on Myc-tFT ratio (red=decrease, green=increase). Final concentration of compounds was 10 μ M with the exception of MG132 (Cf=4.2 μ M) and AZ1 (Cf=30 μ M). Data is analysed for comparison with DMSO by One-way ANOVA. n.s.= non significant $p>0.05$, * = $p\leq 0.05$, ** = $p\leq 0.01$, *** = $p\leq 0.001$, **** = $p\leq 0.0001$

4.4. Single-cell analysis of the effect of modulators of Myc stability on the Myc-tFT ratio.

4.4.2 Single-dose screening: 30 μ M

In a final effort to test the potential use of the Myc-tFT assay for screening, I decided to test the effect of these same compounds at an elevated dose of 30 μ M.

A representative result from one of the plates assayed can be seen in **Figure 4.14** where, once more, the spread of the data is extremely large. At this concentration, the effect of KN-93 is very apparent, as treatment with this compound causes the distribution of the data to resemble the effect yielded by MG132.

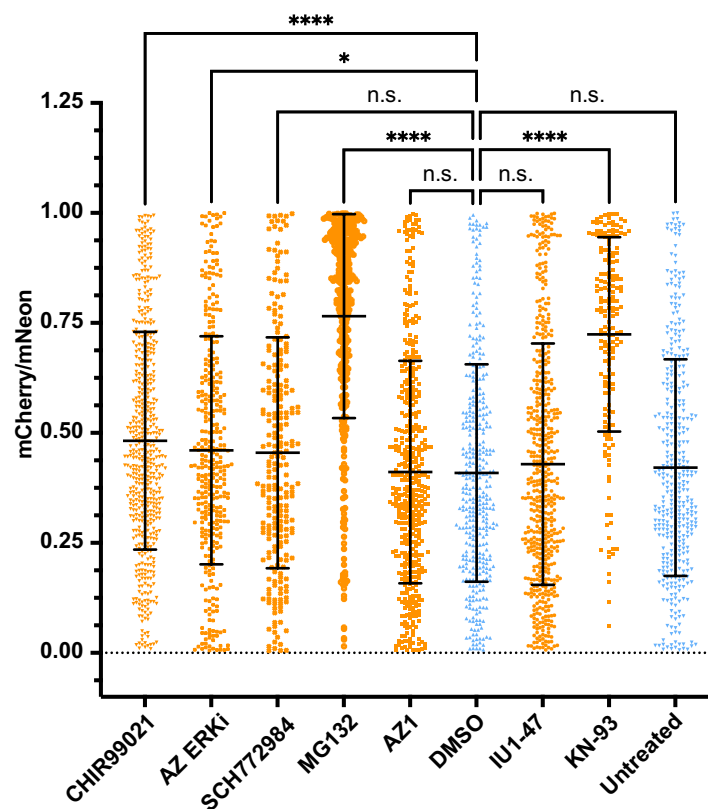


Figure 4.14: **Single dose (30 μ M) screen of modifiers of Myc stability** Scatter plot of data from a representative plate of U2OS FRT/TO Myc-tFT treated at 30 μ M with the exception of MG132 (Cf=4.2 μ M), with compounds listed in table 4.3, analysed by One-way ANOVA for comparison with DMSO. Each dot represents the ratio for a single cell. Mean and SD are displayed. Representative of n=2 plates per experiment and n=3 experiments. n.s.= non significant $p>0.05$, * = $p\leq 0.05$, **** = $p\leq 0.0001$

Indeed the effect of KN-93, when dosed at 30 μ M is reproducibly highly statistically significant ($p<0.0001$), as highlighted in **Table 4.5**. This strong increase in stability of Myc brought about by KN-93 is in contrast to the effect reported in the work that originally identified CAMKII as a modulator of Myc, where CAMKII inhibition is

Chapter 4. Optimization and application of Myc-tFT stability sensor in a medium-throughput drug screen.

shown to decrease Myc stability. Indeed, in this work the effect on Myc is consistent by chemical inhibition and gene knock-out in animal models of T cell lymphoma (Gu et al., 2017), as assessed by immunoblot. Notably, the reduction in Myc stability reported by (Gu et al., 2017) is recorded after 10 μ M treatment of KN-93, while the same concentration of KN-93 in U2OS results in increased Myc-tFT ratio, with higher reproducibility at 30 μ M.

This discrepancy is likely due to differences in CAMKII's role in Myc stability in our cellular context (osteosarcoma). Additionally, the effect reported by (Gu et al., 2017) is based on inhibition of CAMKII γ isoform. The results reported in this work could be due to inhibition of other isoforms, whose effect on Myc has not been described.

It is also possible that the increased Myc stability derives from off-target effects of KN-93 on other proteins that interact with Myc or on biological processes that would have the downstream effect of positively modulating Myc stability.

While this latter explanation is plausible, it does not invalidate our findings, and further investigations into the role of CAMKII in Myc regulation in our cellular context, for example by knock-down of CAMKII, could support these results.

No other compound used in this medium-throughput screen demonstrated reliable and consistent effect on Myc-tFT, even at 30 μ M (**Table 4.5**).

4.4. Single-cell analysis of the effect of modulators of Myc stability on the Myc-tFT ratio.

Plate	EXP 1		EXP 2		EXP 3
	1	2	1	2	1
CHIR99021	*	****	**	n.s.	n.s.
AZ ERKi	n.s.	*	n.s.	n.s.	n.s.
SCH772984	n.s.	n.s.	*	n.s.	n.s.
MG132	****	****	****	****	****
AZ1	n.s.	n.s.	n.s.	****	n.s.
IU1-47	*	n.s.	n.s.	n.s.	n.s.
KN-93	****	****	****	****	****
Untreated	n.s.	n.s.	**	****	*

Table 4.5: **Effect of modulators of Myc stability, dosed at 30 μ M, across multiple experimental repeats.** List of compounds that inhibit known regulators of Myc stability and their measured effect on Myc-tFT ratio (red=decrease, green=increase). Final concentration of compounds was 30 μ M with the exception of MG132 (Cf=4.2 μ M) Data is analysed for comparison with DMSO by One-way ANOVA. n.s.= non significant $p>0.05$, * = $p\leq 0.05$, ** = $p\leq 0.01$, *** = $p\leq 0.002$, **** = $p\leq 0.0001$

4.5 Chapter Summary

To summarise, the work outlined in this chapter can be concluded as follows:

- **The use of the Myc-tFT assay was optimized and established for use in an medium-throughput pipeline:** specifically, seeding density, cell growth imaging media, imaging and image analysis conditions were characterised in detail resulting in an accurate, efficient and semi-automated pipeline for the measurement of Myc-tFT ratio.
- **The Myc-tFT assay was adapted to whole-field analysis and Z' factor was determined:** The effect of previously characterised compounds MG132 and CHIR99021 were used in whole-field analysis experiments to test the reproducibility of the assay and assign a measure of goodness to the assay as measured by the Z'. While the effect of MG132 was evident, the variability in the data of untreated wells caused the assay to perform poorly. The assay would have undoubtedly benefitted from a Inhibitor control compound that had yet to be identified in this assay. Nevertheless, the goodness of the assay was unsatisfactory when assessed by Z', but displayed significant effects of both compounds when the data was analysed using student's t-test. This approach is not suitable for determining dose-response curves or for whole-field analysis so the assay's use was changed to analyse single-cell data.
- **Single-cell analysis of Myc-tFT ratio was employed in a medium-throughput single-dose compound screen:** The Myc-tFT assay was deemed better suited to single-cell analysis of Myc-tFT ratio, such as was described in the first results chapter, but in the higher through-put pipeline described in this chapter. The assay was challenged in a medium-throughput screen of known regulators of Myc dosed at a single dose (10 or 30 μ M) and the effect compared to DMSO by one-way analysis of variance (ANOVA). This yielded highly variable results due to the great variability of the single-cell Myc-tFT ratios recorded in each field. No compound successfully or reproducibly decreased Myc-tFT ratio and only

4.5. Chapter Summary

CAMKII inhibitor KN-93 demonstrated consistent, highly-significant increase in Myc-tFT ratio.

In conclusion, the great variability in single-cell Myc-tFT ratio was a hindrance for the deployment of this assay as a medium-throughput screening tool as hit identification was unreliable. For this reason, high-throughput screening of AstraZeneca's compound library was not pursued as the risk/reward was too great and chances of obtaining consistent and significant hits too low.

Chapter 4. Optimization and application of Myc-tFT stability sensor in a medium-throughput drug screen.

Chapter 5

Discovering the source of variability in the Myc-tFT assay

5.1 Introduction

In the previous chapter, the Myc-tFT assay was adapted to the medium-throughput format typically used for drug discovery at AstraZeneca. While this work revealed potential effects of CAMKII inhibitor KN-93, which positively modulated Myc stability, it most importantly highlighted the great variability in tFT ratios of cells, which prevented its use for the identification of novel compounds modulating Myc stability. As a consequence of this, the next step was to identify the cause of cell-to-cell variability in Myc-tFT ratios, with the ultimate goal of reducing the variability to yield a more reliable assay better suited to drug screening. The investigation into the source of the variability will be the topic of this and the following chapter (**Chapters 5 and 6**).

The first step to understanding the source of the variability in the assay was to assess how the tFT ratio developed over time after induction of expression of Myc-tTF. This would provide some indication of the parameters giving rise to variable tFT ratios.

Therefore I set out to:

1. **Evaluate the evolution of Myc-tFT signal over time in asynchronous cells:** how Myc-tFT ratios change over time had yet to be characterised and elucidated. The effect of a modulator of Myc stability over time was also to be evaluated.

2. **Assess the contribution of the cell cycle to changes in Myc-tFT levels:** the impact of cell cycle regulation of Myc was to be established by cell cycle arrest at different phases.
3. **Appraise the contribution of protein synthesis and post-translational regulation to alterations in Myc-tFT levels:** how post-translational regulation of Myc at key residues and changes in protein synthesis could affect Myc-tFT readings needed further research.

5.2 Time-resolved analysis of Myc-tFT in asynchronous cells

5.2.1 Myc-tFT ratio exhibits cell autonomous oscillations with a periodicity of 24 hours

In order to evaluate the contribution of Myc biology to the variability detected in the medium-throughput assay, U2OS FRT/TO Myc-tFT were filmed every hour over 48 hours from Myc-tFT induction with Doxycycline (DOX). This revealed great variability in Myc-tFT levels and stability over the course of an individual cell's life span, as evidenced in **Figure 5.1**, which shows an asynchronous cell followed through time at an hourly rate, across two cell divisions. From the panel it is evident that Myc-tFT accumulates as a result of induction by DOX. Following first cell division, the levels of Myc-tFT between the daughter cells evolve independently (end of row 2 and rows 3, 4). The bottom daughter cell maintained low levels of Myc-tFT after first-cell division, whereas, the top daughter cells preserved high Myc-tFT levels. Both daughter cells divide once more in a second round of cell division (row 5). The daughter cells resulting from the division of the weakly-expressing bottom daughter cell, maintain low levels of Myc-tFT. The top daughter cell from the first division maintains its high Myc-tFT levels into the second round of division (row 5) but, once more, its daughter cells have differing levels of Myc-tFT with the daughter cell to the left displaying higher Myc-tFT levels to begin with which decay through time (rows 5-8) and the daughter cell to the right maintaining low Myc-tFT levels at the start but increasing over time (also rows 5-8).

5.2. Time-resolved analysis of Myc-tFT in asynchronous cells

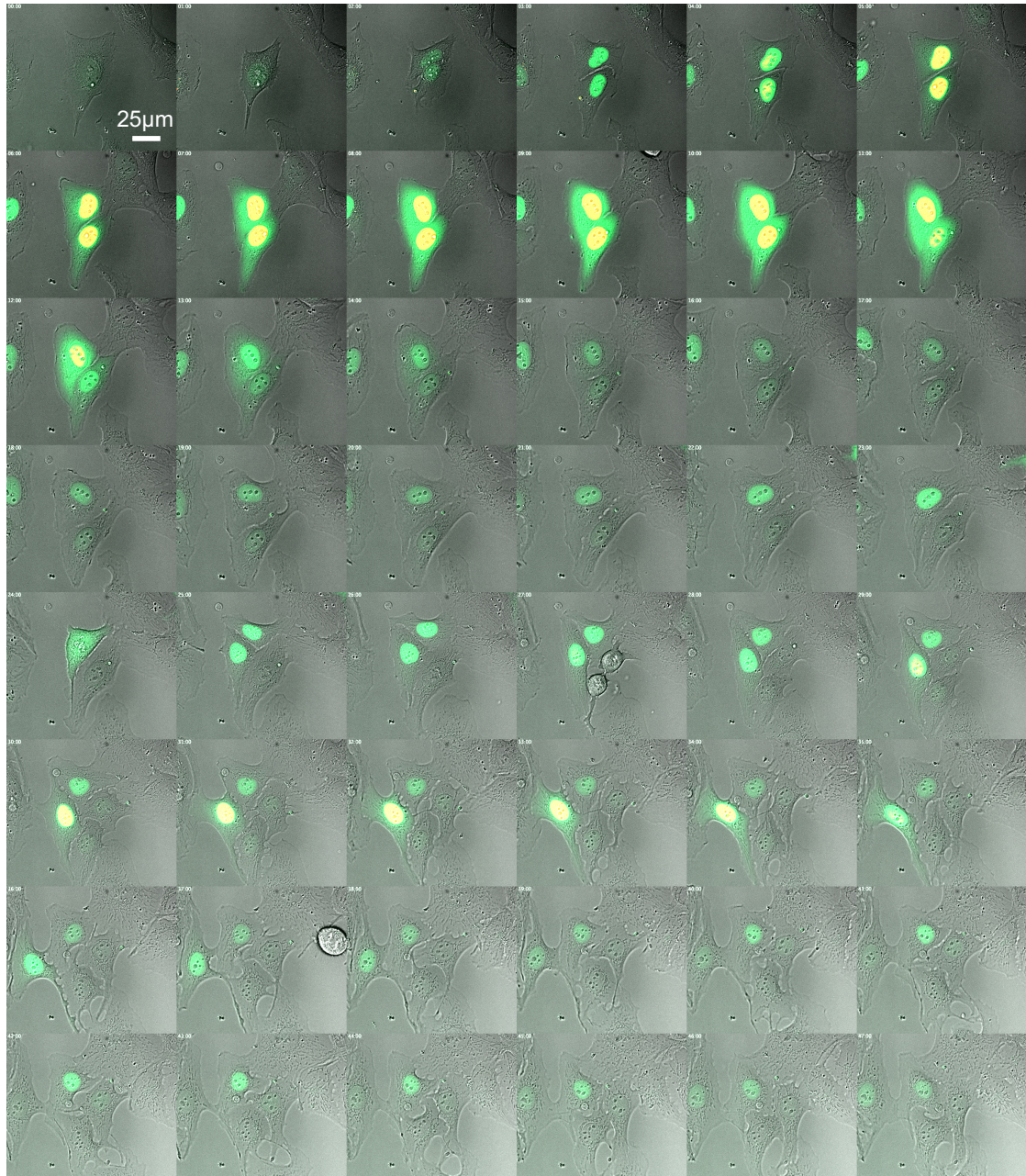


Figure 5.1: **Panel images of a single Myc-tFT expressing cell over time.** Panel illustrating the changes in Myc-tFT levels within the life cycle of a cell. Panels are from images taken an hour apart. Images are a composite of channels 490, 550 and Differential Interference Contrast (DIC).

Chapter 5. Discovering the source of variability in the Myc-tFT assay

Signal from cells like these were followed through time using the Multi_Measurement macro described in the Materials and Methods section (**Chapter 2**), which allowed me to manually follow each cell through time and measure relative fluorescent units (RFU, background-corrected signal) of mNeonGreen and mCherry through time. This was then used to produce the tFT ratio for each time point, which, when plotted on a time vs ratio graph, described the evolution of the ratio of each cell through time. An example of such a graph is shown in **Figure 5.2**.

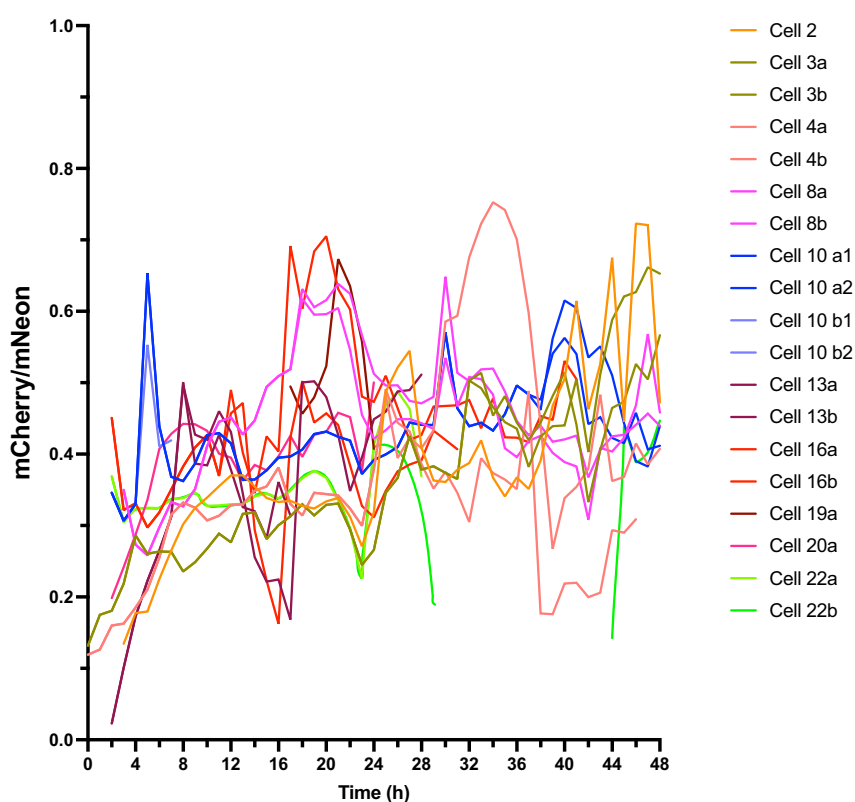


Figure 5.2: **Time-resolved traces of changes in Myc-tFT ratio.** Representative (of $n=3$) data of Myc-tFT ratios of a number of cells undergoing the cell cycle. a and b refer to daughter cells.

The single-cell analysis of Myc-tFT ratio over time echoes the variability in mCherry / mNeonGreen of different cells in a field that was previously described, whereby at any given time point the cells have varying ranges of tFT ratio. In addition the data highlighted the tFT ratio of any single-cell varies substantially through time, for example Cell 3 displays a ratio of ~ 0.2 at the four hour mark, and ~ 0.5 or ~ 0.6 at the 48h mark depending on daughter cell (Cell 3 a and b respectively).

5.2. Time-resolved analysis of Myc-tFT in asynchronous cells

To further the investigation into the source of the variability, the changes in mNeonGreen through time were also considered. RFU of mNeonGreen signal of the same cells used for analysis in **Figure 5.2**, were plotted as displayed in **Figure 5.3** (representative data).

It is evident that there are great differences in maximum mNeonGreen levels reached by different traces (**Figure 5.3 A**), whereby most cells were recorded to have values below 1000 RFU, a couple had values close to 2000 RFU and one cell 4500 RFU. When looking more closely within the range where most traces lie (**Figure 5.3 B**), it can be evidently seen that the mNeonGreen signal is not stable, but rather increases and decreases with time. For many cells, the levels increased and decreased twice in 48 hour, in an oscillatory fashion, as highlighted in the traces with thicker lines in **Figure 5.3 B**.

mCherry RFU traces showed a very similar pattern to their mNeonGreen RFU counterparts, indicating that the magnitude of the oscillations observed in protein level of Myc-tFT **Figures 5.3 and 5.4** dwarfed the changes in stability reported upon by the mCherry/mNeonGreen ratio (**Figure 5.2**).

Importantly, tFTs were designed to measure protein stability at steady state of proteostasis, whereby synthesis and degradation rates are constant. Perturbations of the steady state can then be measured in compound or genetic screens, however the control condition should be at steady state. The oscillations that were consistently measured across all experimental settings, showed that Myc-tFT was not at steady state. For this reason, in subsequent experiments, the mCherry/mNeonGreen ratio might be reported but only tentative conclusions can be drawn from this. For completeness, RFU of both FPs is reported, but it is necessary to highlight that mNeonGreen offered the best read-out of changes in Myc-tFT levels as it is fast-folding (one-step maturation kinetics as opposed to two-step of mCherry), and, consequently, had a more optimal signal:noise ratio and greater range of signal.

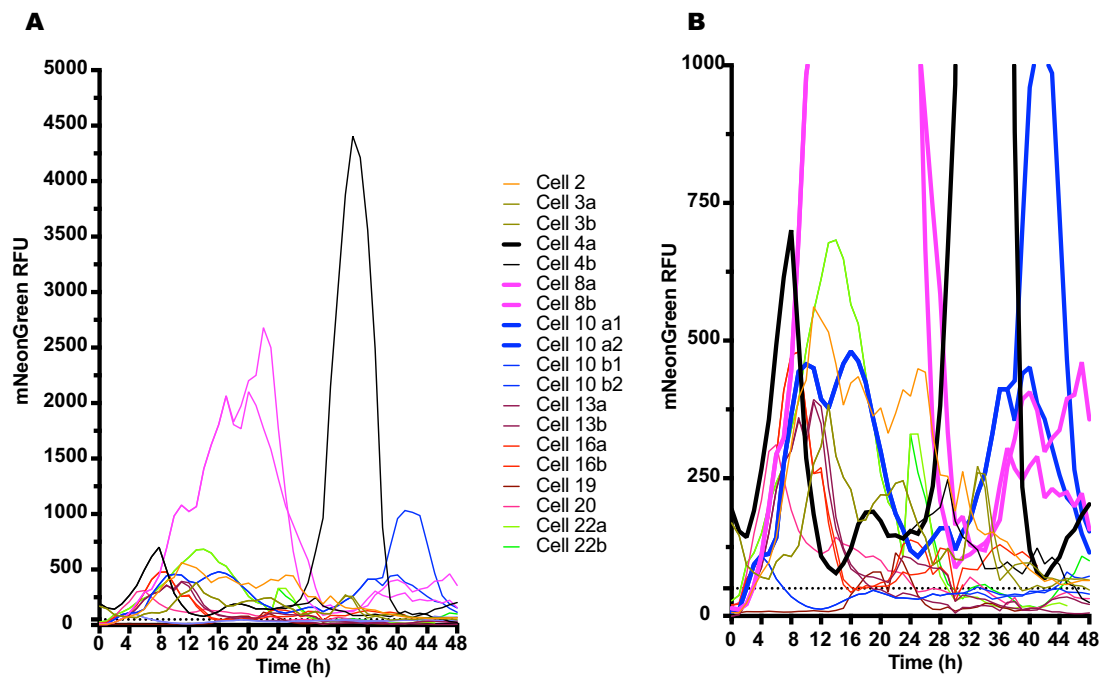


Figure 5.3: **Time-resolved traces of changes in mNeonGreen over time.** Representative (of $n=3$) data of mNeonGreen relative fluorescence units (RFU) of a number of cells undergoing the cell cycle. These are the corresponding mNeonGreen levels to the Myc-tFT ratios of the cells displayed in **Figure 5.2**.

A mNeonGreen levels of asynchronous Myc-tFT cells.

B As in A but focusing into mNeonGreen values between 0 and 1000 RFU. Some traces are highlighted with increased line thickness.

5.2. Time-resolved analysis of Myc-tFT in asynchronous cells

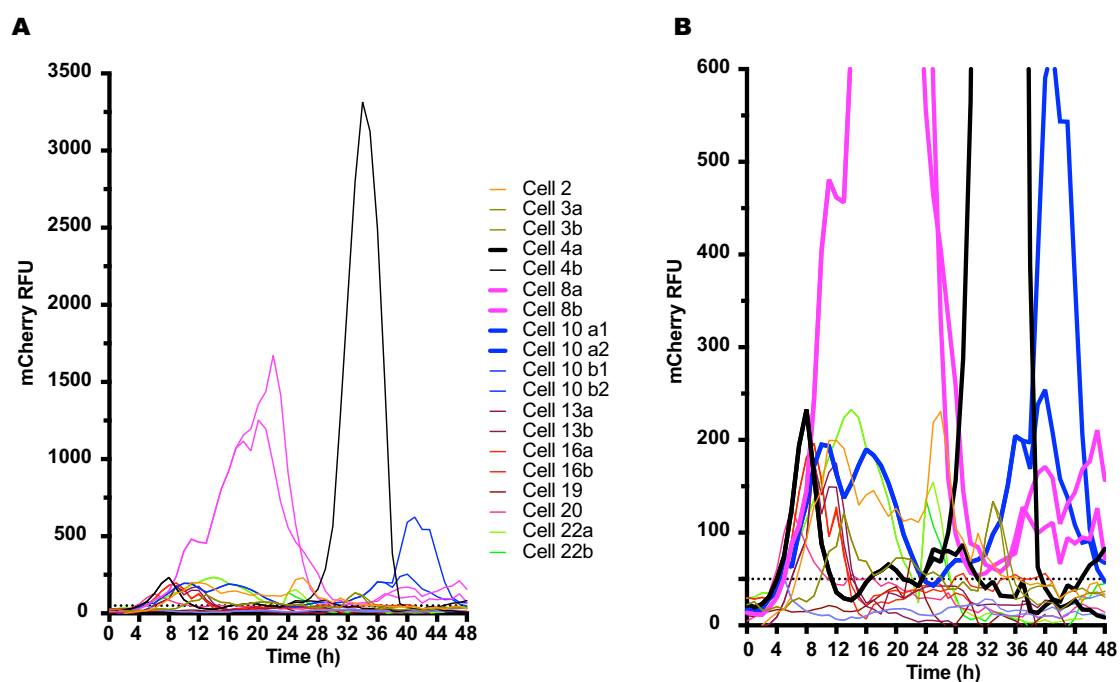


Figure 5.4: **Time-resolved traces of changes in mCherry.** Representative (of $n=3$) data of mCherry relative fluorescence units (RFU) of a number of cells undergoing the cell cycle. These are the corresponding mCherry levels to the Myc-tFT ratio and mNeonGreen signal of the cells displayed in **Figure 5.2 and 5.3**.

A mCherry levels of asynchronous Myc-tFT cells.

B As in A but focusing into mCherry values between 0 and 1000 RFU. Some traces are highlighted with increased line thickness show an oscillatory pattern every 24 hours.

Chapter 5. Discovering the source of variability in the Myc-tFT assay

This preliminary investigation into how the Myc-tFT ratio changed over time in asynchronous cells shed some light into the possible reason for the observed variability in the assay, which appeared to be cell-autonomous regulation of Myc-tFT levels that differ between cells in a field, and even between daughter cells following mitosis, and not an intrinsic limitation of the assay. The oscillation of mCherry/mNeon ratio indicated that the stability of Myc-tFT was changing over time, but at this stage it was not possible to conclude whether stability changes were sufficient to give rise to the observed magnitude of oscillation in total Myc-tFT levels, or whether expression (synthesis) of Myc-tFT was also a variable influencing the behaviour of the Myc-tFT reporter. Furthermore, the experimental set up with asynchronous cells was sub-optimal due to the complexity of the manual analysis where individual daughter cells were followed through time after cell division.

5.3 Time-resolved analysis of Myc-tFT in cells synchronised for cell cycle

The preliminary data suggested that the oscillations in Myc levels could be the source of the variability in the single time-point assay. Since they occur twice in 48 hours (like cell division of U2OS cells), I set out to investigate the contribution of the cell cycle to the observed oscillatory behaviour of the Myc-tFT tool. To address this, I performed time-lapse imaging and analysis of cells arrested in different phases of the cell cycle, first by inhibition of cyclin-dependent kinase 1 (CDK1) activity that drives the cell cycle oscillator, and then by inhibition of DNA replication to arrest cells in S phase.

5.3.1 Myc-tFT oscillations are independent of CDK activity

CDK1, together with the Anaphase-promoting complex/cyclosome (APC/C), is the key driver of the cell cycle oscillator. To assess its contribution to Myc-tFT oscillations U2OS FRT/TO Myc-tFT cells were co-treated with DOX and RO3306 (Cf=10 μ M), a CDK inhibitor that induces arrest in late G2 phase of the cell cycle (since CDK1 activity is required for mitotic entry). Cells were imaged every hour for 48 hours from induction

5.3. Time-resolved analysis of Myc-tFT in cells synchronised for cell cycle

and changes in mNeonGreen, mCherry RFU were measured over time.

Representative data from these experiments is shown in **Figure 5.5**. The treatment resulted in a rapid increase in Myc-tFT ratio in all cells but with evident variability (**Figure 5.5A, C**). This increase in Myc-tFT stability was not a result of accumulation of Myc as the levels of mNeonGreen and mCherry both continued oscillating, as reported by the RFU of individual traces (**Figure 5.5 B**) and average traces (**Figure 5.5 C**).

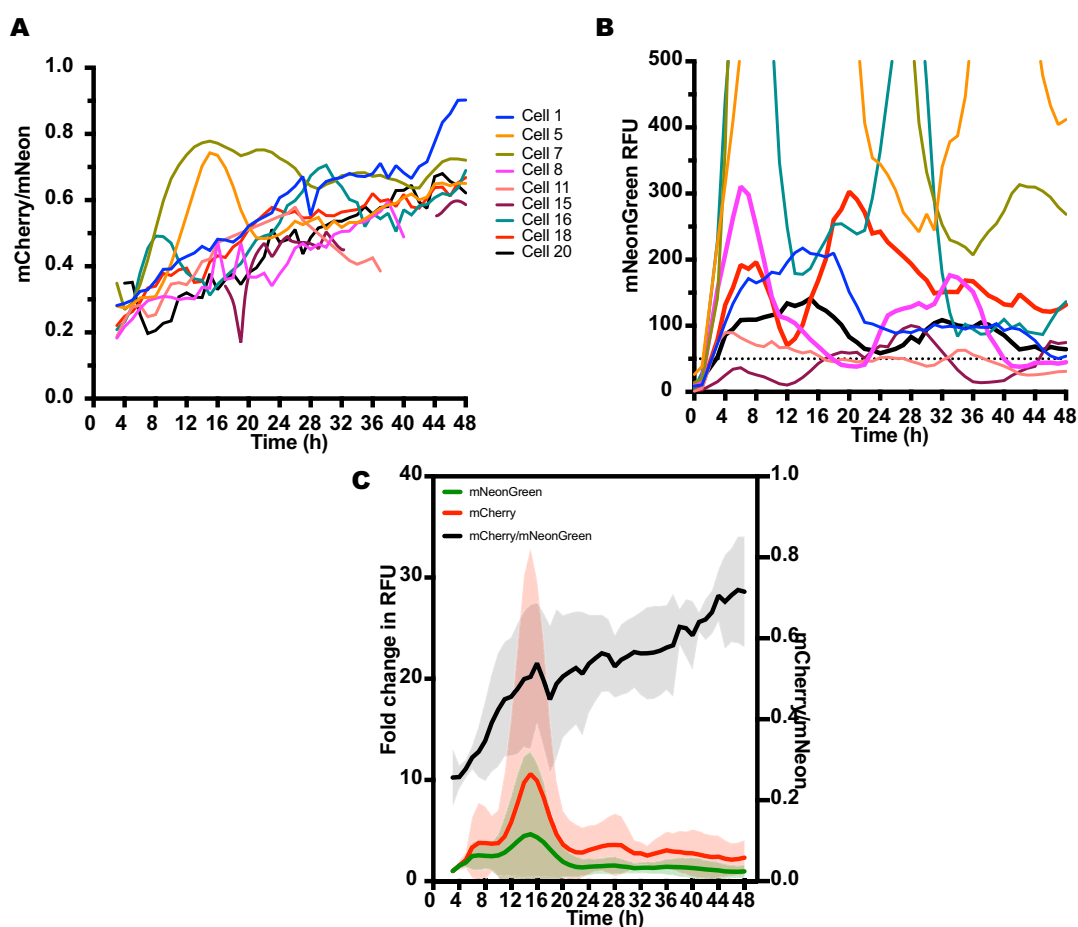


Figure 5.5: **Time-resolved traces of cells treated with RO3306 for arrest in G2.** U2OS FRT/TO Myc-tFT cells were treated with RO3306 ($C_f=10\mu\text{M}$) to induce arrest in G2 phase:

- A Myc-tFT ratio of individual cells arrested in G2
- B mNeonGreen traces of individual cells
- C Average curve of mNeonGreen (green line), mCherry (red line) RFU (left Y axis) and tFT ratio (right Y axis) with standard deviations indicated by light shading.

While these results confirmed the initial observation that the oscillations in Myc-

Chapter 5. Discovering the source of variability in the Myc-tFT assay

tFT levels were not due to cells progressing through the cell cycle, this protocol for synchronisation was sub-optimal as cell toxicity was recorded in the later stages of the recording. This would be unsuitable for co-treatment with other compounds used to further dissect the source of the oscillations.

5.3.2 Myc-tFT oscillates robustly in S-phase arrested cells

To avoid the toxicity seen with cells arrested in G2 phase, another synchronisation protocol was tested. Cells were arrested at the G1/S-phase boundary by double-thymidine block (synchronisation protocol detailed in the Methods section) and imaged. Briefly, an initial overnight incubation with Thymidine enriched cells in G1/S, however this would only arrest cells that had not yet passed S-phase during the incubation and cells in G2-M would have continued cycling. To ensure robust synchronisation cells were released from thymidine pressure for 12 hours and then Thymidine was added again, at the start of the movie, for 48 hours. Average curves and standard deviation of asynchronous versus S-phase arrested cells were plotted for both mNeonGreen and mCherry levels and for the tFT ratio (**Figure 5.6 A and B respectively**). This method for data visualisation allowed for clearer visualisation of the overall trend in how the cells behaved over time, whilst also displaying the variability in Myc-tFT levels via standard deviations. The data in **Figure 5.6**, where oscillations in Myc-tFT levels could be seen regardless of S-phase arrest, allowed to exclude the cell cycle as the source of the oscillations. Furthermore, S-phase arrest proved an optimal cell-cycle synchronisation protocol as it did not affect Myc-tFT ratios over time, which are comparable to those seen in asynchronous cells, and in which oscillations in Myc-tFT can be recorded. I could, therefore, use this experimental setup to begin investigating the source of the oscillations without the complication of tracking daughter cells after division and in absence of any cell cycle affect on Myc expression.

5.4. Contribution of synthesis rates and post-translational regulation on Myc-tFT oscillations

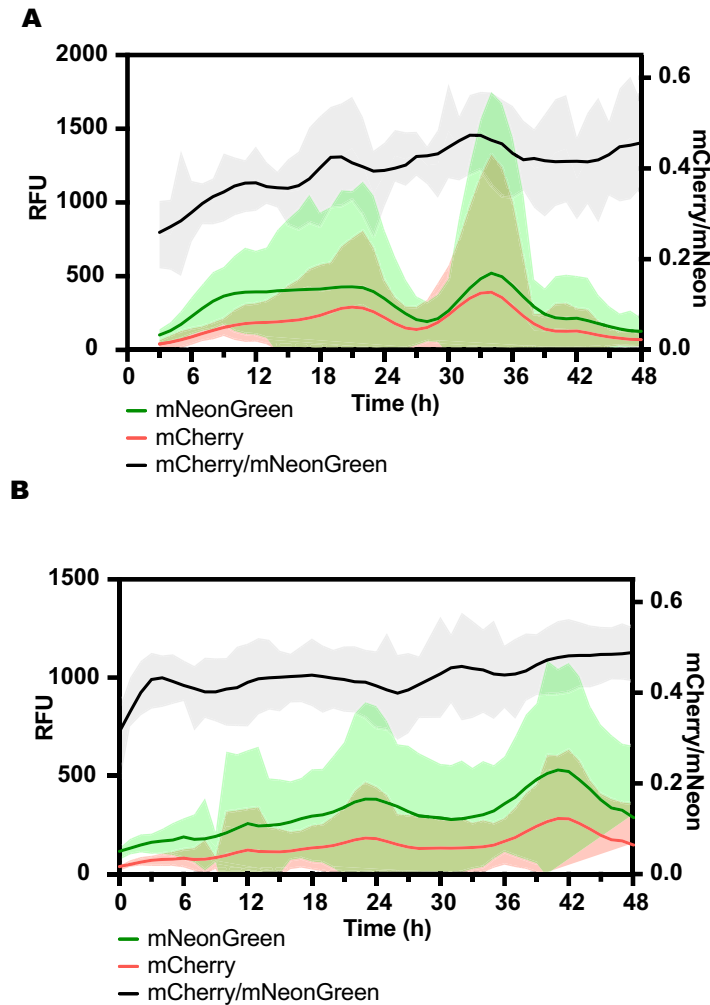


Figure 5.6: **Average of time-resolved traces of cells undergoing cell division or arrested in S-phase.** Average curve of mNeonGreen, mCherry RFU (left Y axis) and tFT ratio (right Y axis) with standard deviation (light shading) of:

- A asynchronous cells
- B Cells arrested in S-phase by double Thymidine block

5.4 Contribution of synthesis rates and post-translational regulation on Myc-tFT oscillations

Having excluded the cell cycle as the cause of the observed oscillations in Myc-tFT, the other known 24 hour clock that could give rise to rhythmic behaviour is the

Chapter 5. Discovering the source of variability in the Myc-tFT assay

circadian clock, and regulation of endogenous Myc expression by the circadian clock has previously been described. This is thought to be transcriptional regulation through the E-boxes in the Myc promoter. Since Myc-tFT expression was driven through an E-box-independent exogenous promoter, it seemed unlikely that the oscillations were driven through a circadian affect on transcription and the preferred hypothesis was that the oscillations were driven through altered protein stability, a hypothesis that will be discussed in detail in **Chapter 6**. Nonetheless it was important to test whether alterations in protein synthesis, or post-translational mechanisms, were responsible for the behaviour of Myc-tFT.

5.4.1 Oscillations are independent of protein synthesis rates

In order to address the contribution of protein synthesis to the oscillations observed, the effect of inhibiting translation rates on Myc-tFT levels was evaluated. This was achieved by treating asynchronous and S-phase arrested cells with the mTOR inhibitor TORin1. The TORin1 concentration used in this experiment ($C_f=2.5\mu\text{M}$) had been shown to be effective at significantly reducing protein translation in U2OS cells in experiments conducted by Dr. Begum Akman in the Lindon lab (data not shown).

Confirming the previous results, DMSO treated cells showed a wide variability in tFT ratio in cells that both did and did not divide in the experimental setting. These were grouped separately of each other as clearly undergoing different biological processes of cell cycle arrest and progression (**Figure 5.7 A and B respectively**). In both cases, variability in Myc-tFT ratio is seen but, once more, fluorescence intensities for individual channels displayed oscillatory patterns (two full oscillations could not be recorded due to the analysis being less than 48 hours). This is shown in panel images of a cell that does not undergo cell division in **Figure 5.7 C**.

5.4. Contribution of synthesis rates and post-translational regulation on Myc-tFT oscillations

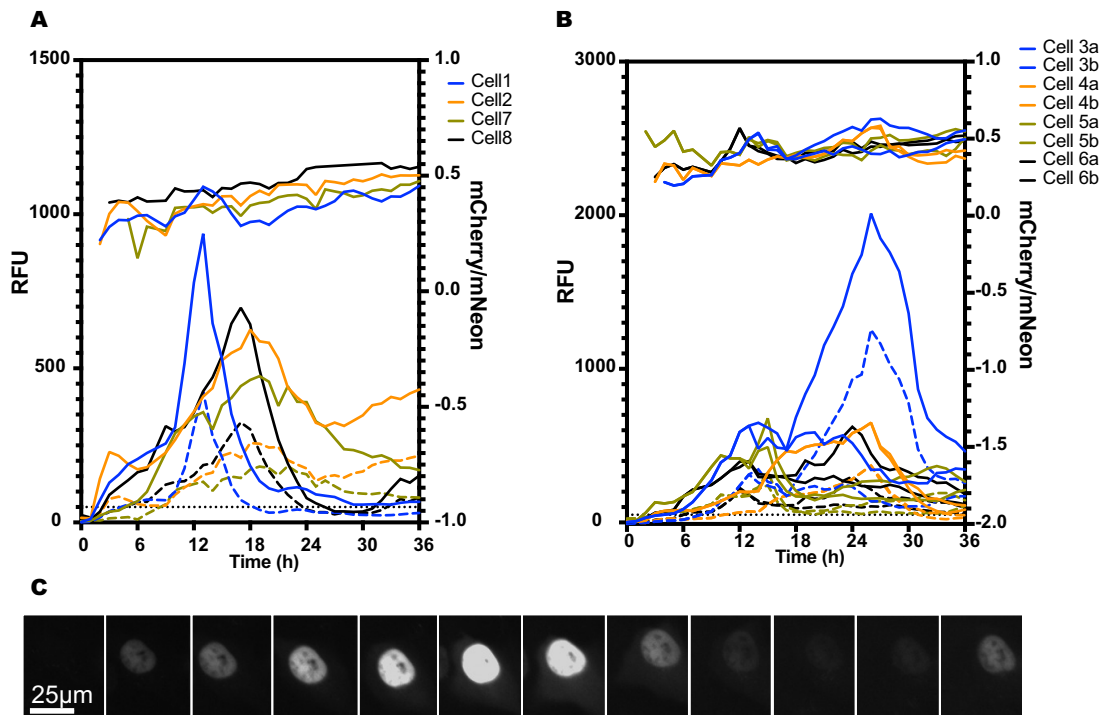


Figure 5.7: **Time-resolved traces of cells treated with DMSO.** Representative traces of mNeonGreen (left Y axis), mCherry (left Y axis, dotted line) and Myc-tFT ratio (top curves, Right Y axis) for cells that:

- A Do not undergo cell division during the length of the filming
- B Undergo cell division during the length of the filming.
- C Representative images of mNeonGreen signal of a non-dividing cell over time. Images were 3 hours apart, starting from addition of DMSO at time 0.

Chapter 5. Discovering the source of variability in the Myc-tFT assay

asynchronous cells treated with TORin1 from Myc-tFT induction, appeared to have reduced capacity to accumulate Myc-tFT as evidenced by the lower mNeonGreen levels (**Figure 5.8 A and B**) when compared to DMSO-treated cells (**Figure 5.7**). In the tFT system FastFP levels allow monitoring of protein synthesis, so reduced mNeonGreen accumulation post-induction is in accordance with the reduced protein translation rates yielded by mTOR inhibition. Myc-tFT ratios in non-dividing cells increased from ~ 0.3 to ~ 0.55 . Importantly, oscillations in mNeonGreen and mCherry persisted in TORin1-treated cells.

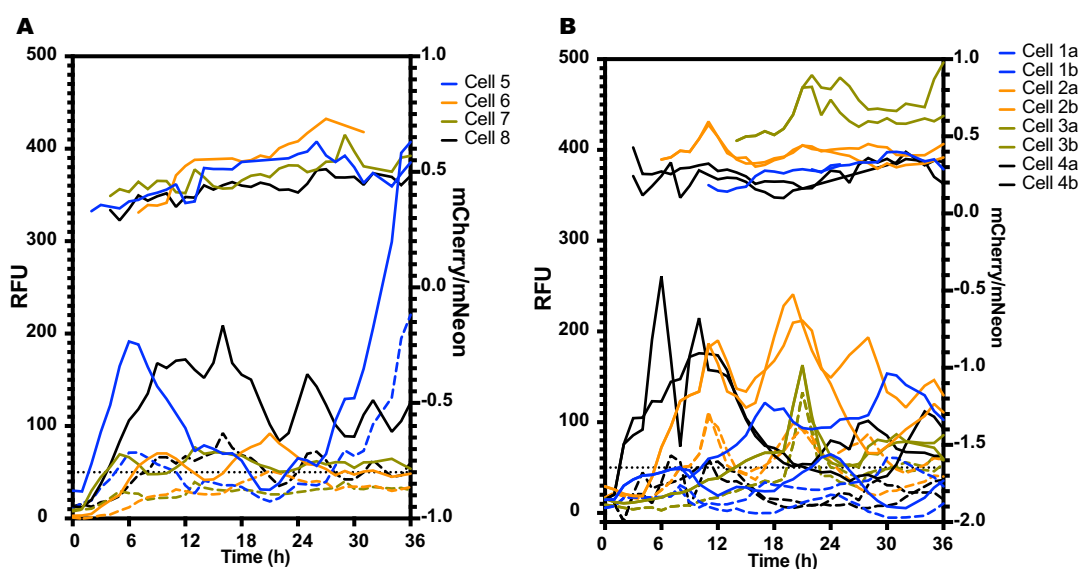


Figure 5.8: **Time-resolved traces of cells treated with TORin.** Representative traces of mNeonGreen (left Y axis), mCherry (left Y axis, dotted line) and Myc-tFT ratio (Right Y axis) for cells treated with mTOR inhibitor TORin ($C_f=2.5\mu\text{M}$) that:

- A Do not undergo cell division during the length of the movie
- B Undergo cell division during the length of the movie.

This experiment was then repeated in cells arrested by thymidine treatment. Myc-tFT cells were treated with DOX, and DMSO or TORin1 following double thymidine block synchronisation and imaged for 48 hours. Cells were followed through time and fold changes in Myc-tFT levels were calculated, by normalising the RFU of each time point to that of the first time point where cells had an mNeonGreen signal of 50 over background. TORin1 treatment did not stop the oscillations in Myc-tFT from occurring as evident when comparing the single cell traces of DMSO and TORin1, **Figure 5.9 A**

5.4. Contribution of synthesis rates and post-translational regulation on Myc-tFT oscillations

and C respectively, or the average curves, Figure 5.9 B and D respectively.

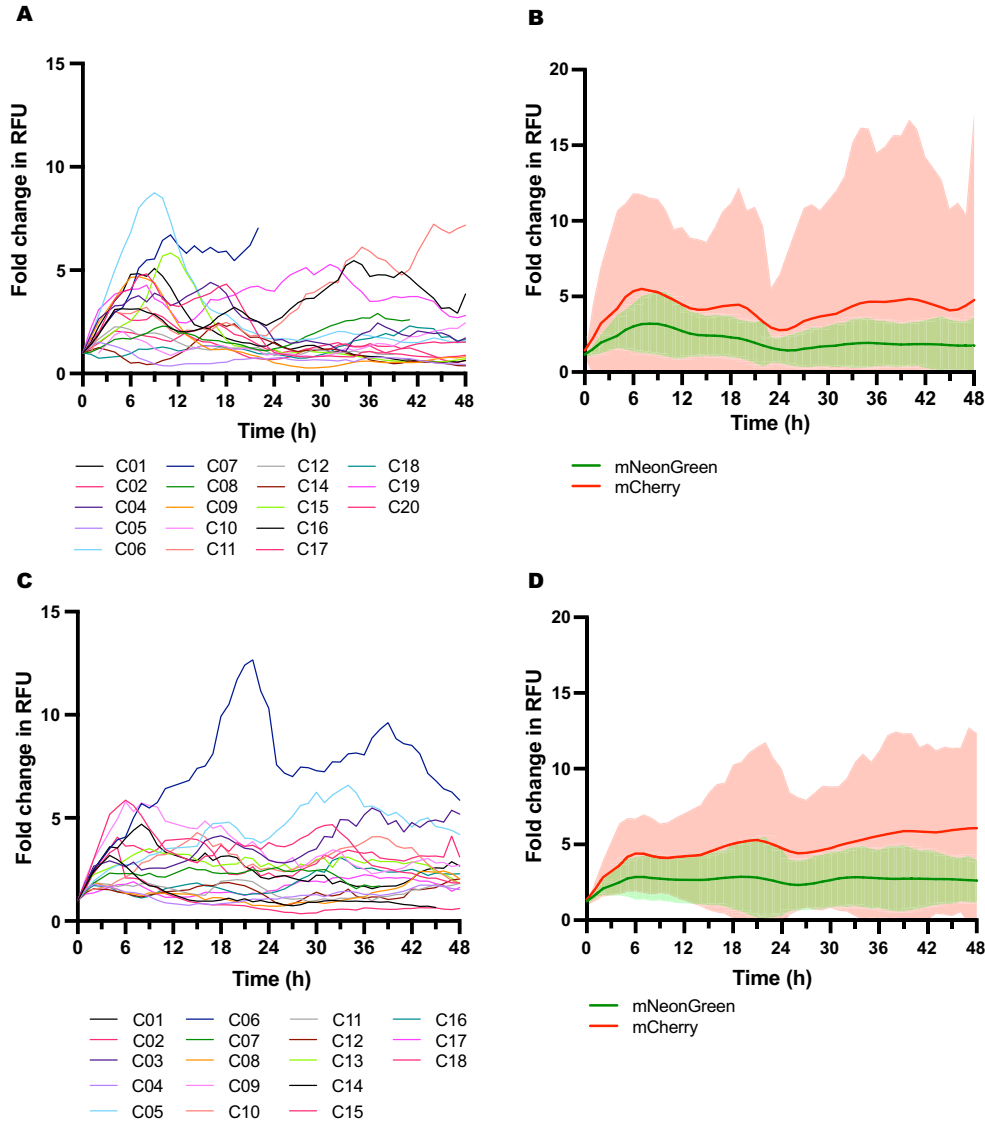


Figure 5.9: Inhibition of protein translation rates by TORin1 does not abolish oscillations in S-phase arrested cells. Representative data of U2OS FRT/TO Myc-tFT cells synchronised in S-phase and treated with DMSO or TORin1 ($C_f=2.5\mu\text{M}$):

- A Single-cell traces of fold change in mNeonGreen RFU of cells treated with DMSO.
- B Average traces of fold change in mNeonGreen and mCherry RFU of cells treated with DMSO, with SD (light shading).
- C Single-cell traces of fold change in mNeonGreen RFU of cells treated with TORin1.
- D Average traces of fold change in mNeonGreen and mCherry RFU of cells treated with TORin1, with SD (light shading).

Chapter 5. Discovering the source of variability in the Myc-tFT assay

These results confirm the observation originally made in asynchronous cells. This suggests that reduction in protein translation rates does not abolish the oscillations, although it is important to consider that protein synthesis was not completely halted but rather reduced, so limited contribution of protein synthesis to the observed oscillations cannot be ruled out.

5.4.2 Post-translational regulation of Myc-tFT oscillations

Having excluded changes in protein synthesis rate as the source of the oscillations, the role of post-translational regulation of Myc-tFT in the generation of these oscillations was next evaluated. To do this, the effect of pharmacological and genetic inhibition of phosphorylation of T58 of Myc, a key residue of the FBW7-recognised phosphodegron, was evaluated.

5.4.2.1 GSK3 β inhibition blocks Myc-tTF oscillation to increase Myc-tFT stability

Pharmacological inhibition of T58 phosphorylation was carried out through inhibition of the kinase responsible for phosphorylating Myc-tFT at this site, GSK3 β . This was achieved through the use of GSK3 β inhibitor CHIR99021, as described in **Chapters 3 and 4**. Once more, the effect of CHIR99021-treatment was evaluated in asynchronous and G1/S-transition arrested cells. CHIR99021 treatment would also allow me to understand the impact of the cell-autonomous regulation of Myc-tFT levels on cells treated with Myc stability modulators.

U2OS FRT/TO Myc-tFT cells were treated with DOX, and DMSO or CHIR99021 (Cf=3 μ M), and imaged every hour for 48 hours. Due to observed toxicity that arose around 36 hours into the filming, cells were tracked through time until that time point.

Cells treated with CHIR99021 were also analysed separately based on whether they had undergone cell division within the 36 hours of filming (**Figure 5.10 A and B**). Once more, the traces for the two fluorescent proteins displayed oscillatory behaviour. The increase in tFT ratio is greater in the CHIR99021-treated cells (initial tFT ratio of non-dividing cells \sim 0.2 and final ratio \sim 0.7) compared to DMSO-treated cells (initial

5.4. Contribution of synthesis rates and post-translational regulation on Myc-tFT oscillations

tFT ratio of non-dividing cells ~ 0.2 and final ratio ~ 0.5). This is consistent with results in previous chapters that showed positive modulation of Myc stability by CHIR99021.

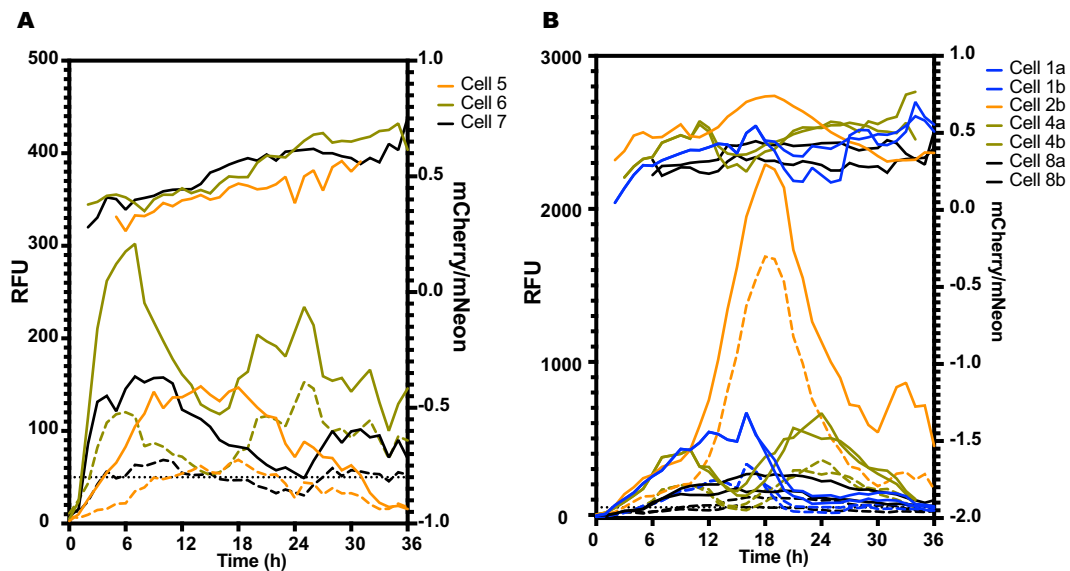


Figure 5.10: **Time-resolved traces of cells treated with CHIR99021.** Representative traces of mNeonGreen (left Y axis), mCherry (left Y axis, dotted line) and Myc-tFT ratio (top curves, Right Y axis) for cells treated with CHIR99021 ($C_f=3\mu M$) that:

- A Do not undergo cell division during the length of the filming
- B Undergo cell division during the length of the filming.

In both DMSO and CHIR99021-treated cells (Figure 5.7 and 5.10 respectively), the amplitude of the RFU was very different between cells that do undergo cell division, which reach higher RFU values, versus those that do not. This difference appears to be greater in CHIR99021-treated cells than DMSO-treated cells. This could be due to the fact that Myc levels are modulated to increase during the cell cycle. Specifically Myc stability increases up until S-phase, as reported by (Sears et al., 1999, Sears et al., 2000), where GSK3 β phosphorylation of Myc leads to FBW7-dependent Myc degradation. Inhibition of Myc T58 phosphorylation by CHIR99021 would have greater effects on cells undergoing the cell cycle than in cells exiting the cell cycle. Nonetheless, I was also able to show differential regulation of Myc stability in cells treated or untreated with CHIR99021, recapitulating the data shown in previous chapters.

Chapter 5. Discovering the source of variability in the Myc-tFT assay

I next performed this experiment in cells arrested in thymidine according to the previously described protocol. Briefly, U2OS FRT/TO Myc-tFT cells were treated with DOX and GSK3 β inhibitor CHIR99021 (Cf=3 μ M) or vehicle control DMSO, following double thymidine block synchronisation; and imaged for 48 hours. As previously noted, there is great difference in signal of both FPs in different cells. To circumvent this problem, for each cell analysed, the RFU of each time point was normalised to the RFU of the first time point where cells had an mNeonGreen signal of 50 over background, yielding fold change in RFU. Resulting data for individual cell traces and average traces of cells treated with DMSO are described in **Figure 5.11 A and B**. These showed oscillations in mNeonGreen and mCherry. In contrast to this, data from CHIR99021-treated cells exhibited abolished oscillations in favour of rapid accumulation and plateau of Myc-tFT at threshold levels **Figure 5.11 C and D**. Interestingly, the threshold of Myc-tFT at which the accumulation reached plateau was notably different in differing cells (**Figure 5.11 C**). These results appear quite different to the effect of CHIR99021 treatment in asynchronous cells. This could be due to the fact that Myc phosphorylation by GSK3 β occurs in late G1 to S-phase of the cell cycle (Sears et al., 1999, Sears et al., 2000), a condition that is enriched in this experimental set up.

5.4. Contribution of synthesis rates and post-translational regulation on Myc-tFT oscillations

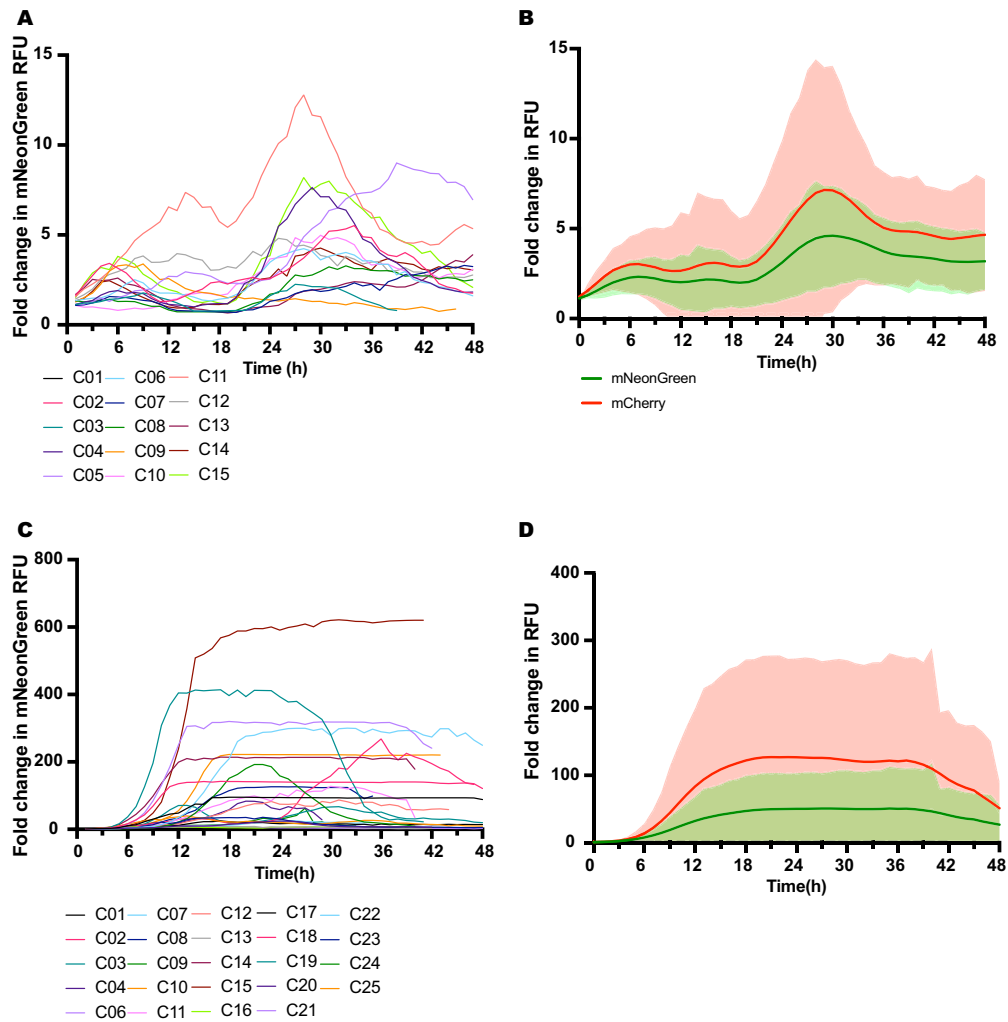


Figure 5.11: **Inhibition of GSK3 β by CHIR99021 leads to time-dependent accumulation of Myc-tFT.** Representative data of U2OS FRT/TO Myc-tFT cells synchronised in S-phase and treated with DMSO or CHIR99021 ($C_f=3\mu M$):

- A Single cell traces of fold change in mNeonGreen RFU of DMSO-treated cells.
- B Average traces of fold change in mNeonGreen and mCherry RFU of DMSO-treated cells, with standard deviations (SD, light shading).
- C Single cell traces of fold change in mNeonGreen RFU of CHIR99021-treated cells.
- D Average traces of fold change in mNeonGreen and mCherry RFU of CHIR99021-treated cells, with SD (light shading).

5.4.2.2 T58A mutation reduces amplitude of Myc-tFT oscillations

To further evaluate the contribution of T58 phosphorylation on Myc-tFT oscillations, S-phase arrested U2OS FRT/TO cells expressing wild-type (WT) or non-phosphorylatable T58A mutant Myc-tFT were compared. As with previous experiments, WT Myc-tFT produced consistent oscillations in both FPs (**Figure 5.12 A**). Myc T58A-tFT displayed reduced fold-changes in RFU, where the maximum fold change in mNeonGreen levels reached was ~ 1.1 , compared to those recorded with the WT, where the maximum fold change in mNeonGreen RFU reached was ~ 3.3 , (**Figure 5.12 B**). Importantly, some degree of oscillation with the mutant was recorded even if at lower RFU fold-changes (**Figure 5.12 C**).

Building on the experiments reported in this section, we can conclude that post-translational regulation of Myc-tFT via T58 phosphorylation does indeed contribute to the oscillations described in this chapter.

5.4. Contribution of synthesis rates and post-translational regulation on Myc-tFT oscillations

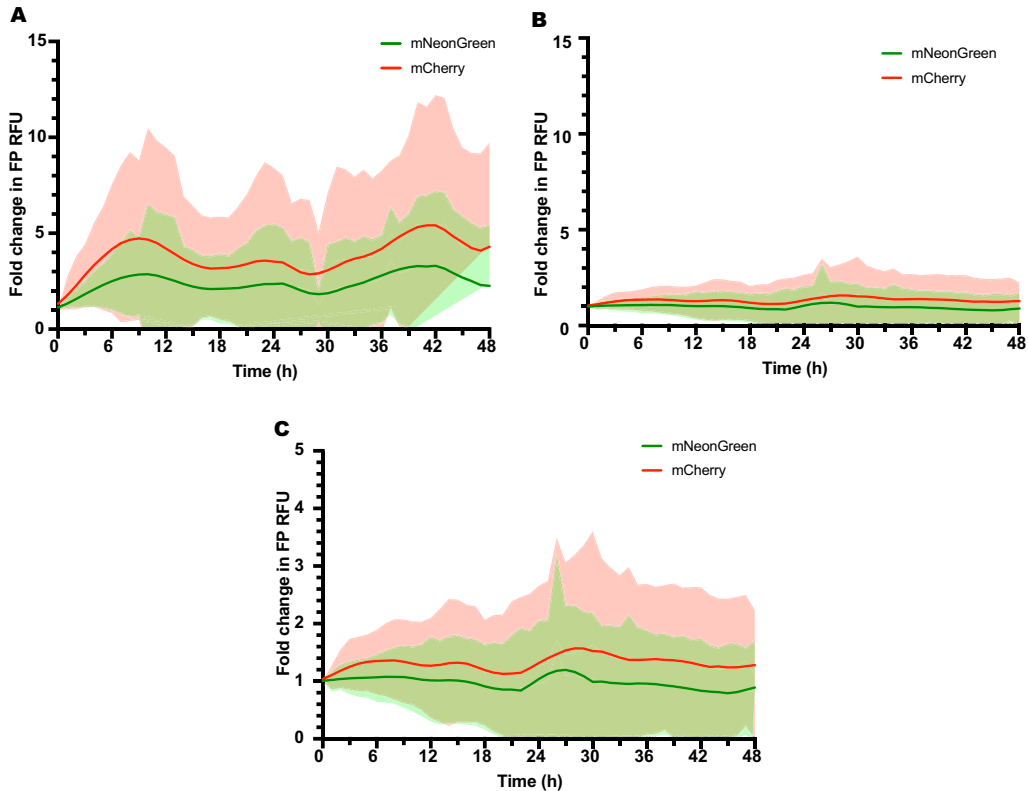


Figure 5.12: **Mutation of T58 in Myc-tFT to non-phosphorylatable T58A dampened the oscillations.** Representative data of U2OS FRT/TO WT or T58A Myc-tFT cells synchronised in S-phase:

- A Average traces of fold change in mNeonGreen and mCherry RFU of WT Myc-tFT cells with SD (light shading).
- B Average traces of fold change in mNeonGreen and mCherry RFU of Myc T58A-tFT cells with SD (light shading).
- C Like B but with smaller Y axis range.

5.5 Chapter summary

The findings of the chapter are concluded as follows:

- **The variability recorded in single time point analysis of Myc-tFT ratio is not due to an intrinsic limitation in the assay, but rather cell-autonomous regulation of Myc-tFT:** Time-lapse imaging of Myc-tFT expression and regulation from induction revealed that there is differential regulation of Myc-tFT across different cells in the field and between daughter cells. This points to a cell-autonomous biological process that regulates Myc-tFT levels. Synchronisation or abolition of this process should, therefore reduce the variability in Myc-tFT ratios.
- **The cell-autonomous process drives Myc-tFT levels to oscillate at a standard rate:** Myc-tFT levels increase and decrease over time with a periodicity of ~ 24 hours.
- **The cell-autonomous process that regulates Myc-tFT stability is not the cell cycle:** Data from asynchronous cells which undergo spontaneous cell cycle arrest and from cells arrested in G2 or S-phase demonstrate that the oscillations in Myc-tFT persist regardless of cell cycle progression.
- **Myc-tFT stability is positively modulated by CHIR99021 over time:** Data from Chapters 3 and 4, in which Myc-tFT is stabilised post-treatment with GSK3 β inhibitor CHIR99021, is once more confirmed through time-lapse recordings in both asynchronous and S-phase arrested cells. It is important to note that the effect of CHIR99021 as assessed in previous chapters was following short incubation with the compound (1, 2 or 3 hours), which resulted in increased Myc stability, although the extent of this effect was not consistent. The data shown in this chapter support the fact that a longer treatment with CHIR99021 would have yielded more significant effects on Myc stability.
- **Post-translational regulation of Myc-tFT affects Myc-tFT oscillations more than changes in rate of protein synthesis:** Taking together the effect of inhibiting T58

5.5. Chapter summary

phosphorylation by pharmacological inhibition or mutation of the residue, which in both cases affects or disrupts the oscillations, leads to the conclusion that post-translational modifications of Myc-tFT play an essential role in the generation of these oscillations, and that phosphorylation of T58 at least partially contributes to the robustness of the phenotype seen. On the other hand, reduction of protein synthesis rate does not appear to have an effect on Myc-tFT oscillations.

Chapter 5. Discovering the source of variability in the Myc-tFT assay

Chapter 6

Circadian rhythms contribute to periodic post-translational regulation of Myc-tFT

6.1 Introduction

The previous chapter began the investigation into the source of the variability observed in the medium-throughput Myc-tFT assay. In it, I described cell-autonomous regulation of Myc-tFT which produced oscillations in its levels that had an estimated periodicity of 24 hours. The oscillations persisted despite cells being arrested in different stages of the cell cycle, suggesting that the cell cycle was not the cell-autonomous biological process that was giving rise to the oscillations. An alternative biological process with a 24-hour periodicity, the circadian rhythm, presented an alternative candidate. This chapter describes the work undertaken to evaluate circadian control of Myc-tFT.

6.1.1 The transcriptional/post-translational delayed feedback loop (TTFL) model of the circadian cycle

Circadian rhythms are cyclical biological processes with a ~24-hour periodicity which tune other biological processes to the light / dark cycles of day and night, and influence the behaviour and physiology of multiple organisms. The fundamental timekeeping unit of circadian rhythms is the cell, as circadian regulation of gene expression and cellular processes is maintained *ex vivo* in mammalian cells. It is also present in other eukaryotes such as plants and fungi. In mammals, the hypothalamic suprachiasmatic nucleus (SCN) is responsible for synchronising these cell-autonomous peripheral clocks at the organism level through neuronal and hormonal cues and has, therefore, been referred to as the 'master pacemaker'. The principal process for cellular timekeeping in cells is rhythmic control of gene expression executed by the transcriptional/post-translational delayed feedback loop (TTFL) (illustrated in the left panel of **Figure 6.1**). In cultured cell that lack the co-ordination by the SCN, circadian rhythms are asynchronous across the cell population but can be entrained by external cues. This feedback system is a balance of transcriptional activation and repression carried out by members of the bHLH family of transcription factors, BMAL1 and CLOCK and their cognate protein products PER1/2 (Period 1 and 2) and CRY1/2 (Cryptochrome 1 and 2). Briefly, BMAL1 and CLOCK transcription factors promote transcription of effector proteins CRY and PER which then heterodimerize in the cytoplasm, and then shuttle to the nucleus where they inhibit BMAL1-CLOCK-driven transcription. Hence, BMAL1 and CLOCK accumulation leads to expression of their negative regulators CRY and PER that reduce BMAL1 and CLOCK activity and, consequently, their own expression allowing another cycle of BMAL1 and CLOCK accumulation. REV-ERB (α and β) are also products of BMAL1 and CLOCK-driven transcription and in turn suppress BMAL1 (*ARNTL*) expression. These cyclical loops of transcriptional activity and repression occur with a periodicity of ~ 24 hours (Burchett, Knudsen-Clark, and Altman, 2021; O'Neill, Maywood, and Hastings, 2013; Takahashi, 2017; Wong and O'Neill, 2018).

6.1.2 The post-translational oscillator model of circadian rhythm establishment and maintenance

An alternative theory of circadian regulation is that post-translational modifications feed back into the TTFL and the two processes together produce robust circadian rhythms of protein abundance. This theory is reviewed in work by Wong and O'Neill (2018), and is supported by several key observations. Many publications report that only a proportion of the cycling proteome have corresponding cycling transcripts, and delays in the cycling of transcriptional products compared to their protein counterparts have also been reported. There is also much evidence for circadian timekeeping in the absence of transcriptional control. Most notably, circadian rhythms have been reported in red blood cells (RBC) which do not have transcriptional capacity as they lack a nucleus and genomic material. Peroxiredoxin, the main anti-oxidant enzyme in RBC, displays oscillatory levels which are driven by modulation of its hyperoxidative state which is preferentially bound by the 20S subunit of the proteasome (Cho et al., 2014; O'Neill and Reddy, 2011). This supports the notion that regulation of protein levels by PTMs is equally important for circadian rhythm maintenance. In the post-translational model for generation of circadian rhythms, it is the cycling activity of the clock components that determines the rhythmicity and this is conferred by PTMs of the clock components. Phosphorylation is a key process for the integration of the post-translational signal to the transcriptional and translational signals. Phosphorylation of clock genes by Casein Kinase 1 and 2, GSK3 (α and β) and dephosphorylation by PP1 have been implicated in regulation of nuclear translocation of clock components, regulation of their transcriptional or translational activity, and hyperphosphorylation has been shown to induce degradation of the clock proteins by the UPS. Overall, the post-translational model integrates evidence for a self-sustained timekeeping mechanism that acts through post-translational processing to yield ~ 24 -hour periodicity in enzyme activity. TTFL components receive timing information from the oscillations in biochemical processes in the form of PTMs and entrain transcription of clock genes and their targets. This, in turn, confers robustness to the transduction of timing information and rhythmic regulation of the expression of those enzymes that dictate the timing in the first instance.

6.1.3 Myc and the circadian rhythm

Myc and clock transcription factors BMAL1 and CLOCK are members of the bHLH family of transcription factors and recognise the same DNA sequence, the E-box. The relationship between these transcription factors is not limited to their similarities, but rather they share a bidirectional relationship that has been mainly observed in cancer. While there is little information on how Myc and the circadian rhythms should interact in a non-cancerous context, there is plenty of evidence that supports the role of deregulated Myc in disrupting the circadian rhythm, illustrated in the right-hand-side panel of **Figure 6.1**. Deregulated Myc has been reported to suppress BMAL1 expression in U2OS cells by up-regulating REV-ERB α and β (Altman et al., 2017) and by binding and antagonising MIZ-1, which would otherwise transcriptionally up-regulate BMAL1 and CLOCK (Shostak et al., 2016, 2017). Myc also occupies the promoters of molecular clocks like PER1 to suppress their induction by BMAL1-CLOCK (Repouskou and Prombona, 2016). Finally, in embryonic stem cells, Myc has been reported to impede PER-CRY shuttling to the nucleus (Umemura et al., 2014).

Circadian rhythms have also been implicated in the regulation of Myc. Indeed, disruption of the clock de-represses and up-regulates Myc. This has been shown in mouse liver of a chronic jet lag model, which displayed upregulated Myc activity and expression, and in lung tumour models with mutation of *Per2* or deletion of *Arntl* (BMAL1) resulting in upregulated Myc (Burchett, Knudsen-Clark, and Altman, 2021). The control of Myc expression by the circadian rhythm has been shown in neuroblastoma models by Repouskou and Prombona (2016), where oscillations in the mRNA and protein levels are reported to be controlled post-transcriptionally. There is limited knowledge on post-translational regulation of Myc by circadian rhythms. Huber et al. (2016) showed post-translational regulation of Myc in mouse fibroblasts, human lung cancer (A549) and colon cancer cell lines (SW480), and a mouse model of lymphoma. According to this work, CRY2 recognises pT58 of Myc and recruits it to E3 ligase FBXL3 for degradation.

Considering the greater evidence for transcriptional/translational control of Myc by circadian rhythms, and since expression of the Myc-tFT is driven from the constitutive

CMV promoter I did not expect to see any circadian effect on transcription. Therefore I focused on investigating whether post-translational circadian regulation might be responsible for the observed oscillations of Myc-tFT.

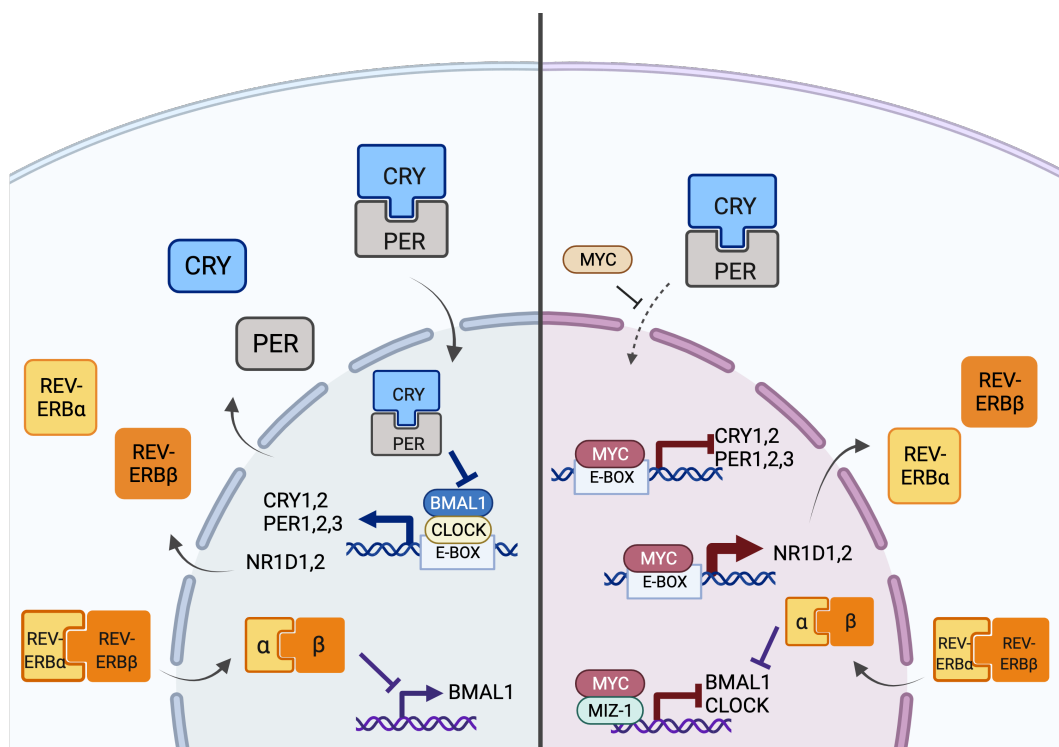


Figure 6.1: **Schematic representation of the transcriptional/post-translational delayed feedback loop (TTFL) (Left) and how Myc disrupts it (Right).** *Left:* The TTFL model of circadian regulation describes BMAL1 and CLOCK bHLH transcription factors that upon accumulation lead to the transcription of their negative regulators Cryptochrome and Period and REV-ERB α and β which in turn inhibit BMAL1 and CLOCK activity, leading to the reduced levels of these transcription factors and of the negative regulators themselves. *Right:* Myc is shown to disrupt the TTFL in different ways. First, it occupies the CRY and PER promoters, inhibiting their transcription. It has also been reported that in embryonic stem cells, Myc impedes PER shuttling to the nucleus. Myc also amplifies expression of REV-ERB α and β , which in turn represses BMAL1 and CLOCK expression. Finally, Myc binds to MIZ-1 and antagonises MIZ-1-induced transcription of BMAL1 and CLOCK genes.

6.2 Circadian synchronisation of U2OS FRT/TO Myc-tFT cells leads to synchronised oscillations in Myc-tFT levels

6.2.1 Synchronisation by Dexamethasone

To assess whether circadian rhythms were contributing to Myc-tFT oscillations, I first tested whether circadian synchronisation by Dexamethasone addition would synchronise Myc-tFT oscillations, according to the protocol detailed in the Materials and Methods chapter. Cells were treated with DMSO or Dexamethasone ($C_f=0.1\mu\text{M}$) and filmed over 96 hours. To reduce proliferation rates, filming medium with 1% FBS was used throughout the imaging process. Individual cells were followed through time and fold changes in mNeonGreen levels were calculated. Representative data is illustrated in **Figure 6.2** where the asynchronous oscillations of Myc-tFT cells treated with DMSO are in contrast with the synchronicity of those treated with Dexamethasone.

Following advice from Dr. John O'Neill (Laboratory of Molecular Biology, University of Cambridge), non-normalised mNeonGreen RFU was detrended by subtraction of the 24 hour rolling average from the RFU, and a damped cosine wave curve fitting was applied. Detrending consists of removing from the data set the effects of trend, allowing for visualisation of only the variation in values from the trend and identification of cyclical patterns such as the oscillations recorded in Myc-tFT levels. An example of this analysis applied to the data from an individual cell is presented in **Figure 6.3 A** where each individual data point is the detrended mNeonGreen RFU for that time point and to which the damped cosine wave curve fitting was applied. Fitted curves were averaged in GraphPad Prism to generate the average curve with the standard error of the mean (SEM) (**Figure 6.3 B**). This is in stark contrast to the result from the curve fitting applied to asynchronous, DMSO treated cells (all from the same field, shown in **Figure 6.3 C**), to which no average or whole-field curves could be fitted.

This experiment demonstrated that circadian synchronisation of Myc-tFT can be achieved to yield data that could be fitted with a curve from which parameters like amplitude and period could be extracted. Given the promising results, a more ro-

6.2. Circadian synchronisation of U2OS FRT/TO Myc-tFT cells leads to synchronised oscillations in Myc-tFT levels

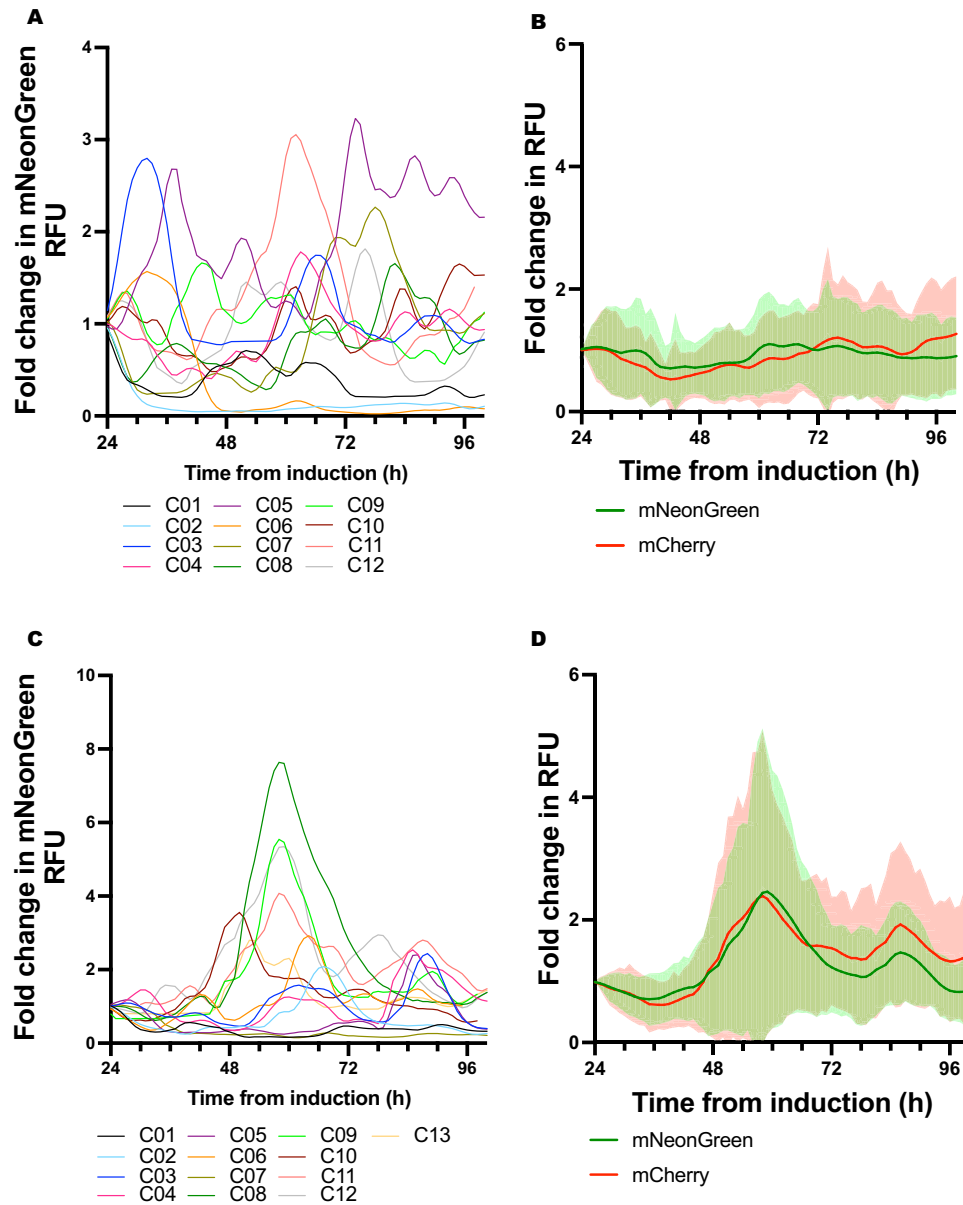


Figure 6.2: Cells treated with Dexamethasone displayed synchronous oscillations. Representative data of U2OS FRT/TO Myc-tFT cells whose circadian rhythms were synchronised by Dexamethasone treatment ($C_f=0.1\mu\text{M}$) or asynchronous in DMSO vehicle control:

- A Single-cell traces of fold change in mNeonGreen RFU of cells treated with DMSO.
- B Average traces of fold change in mNeonGreen and mCherry RFU of cells treated with DMSO.
- C Single-cell traces of fold change in mNeonGreen RFU of cells treated with Dexamethasone.
- D Average traces of fold change in mNeonGreen and mCherry RFU of cells treated with Dexamethasone.

Chapter 6. Circadian rhythms contribute to periodic post-translational regulation of Myc-tFT

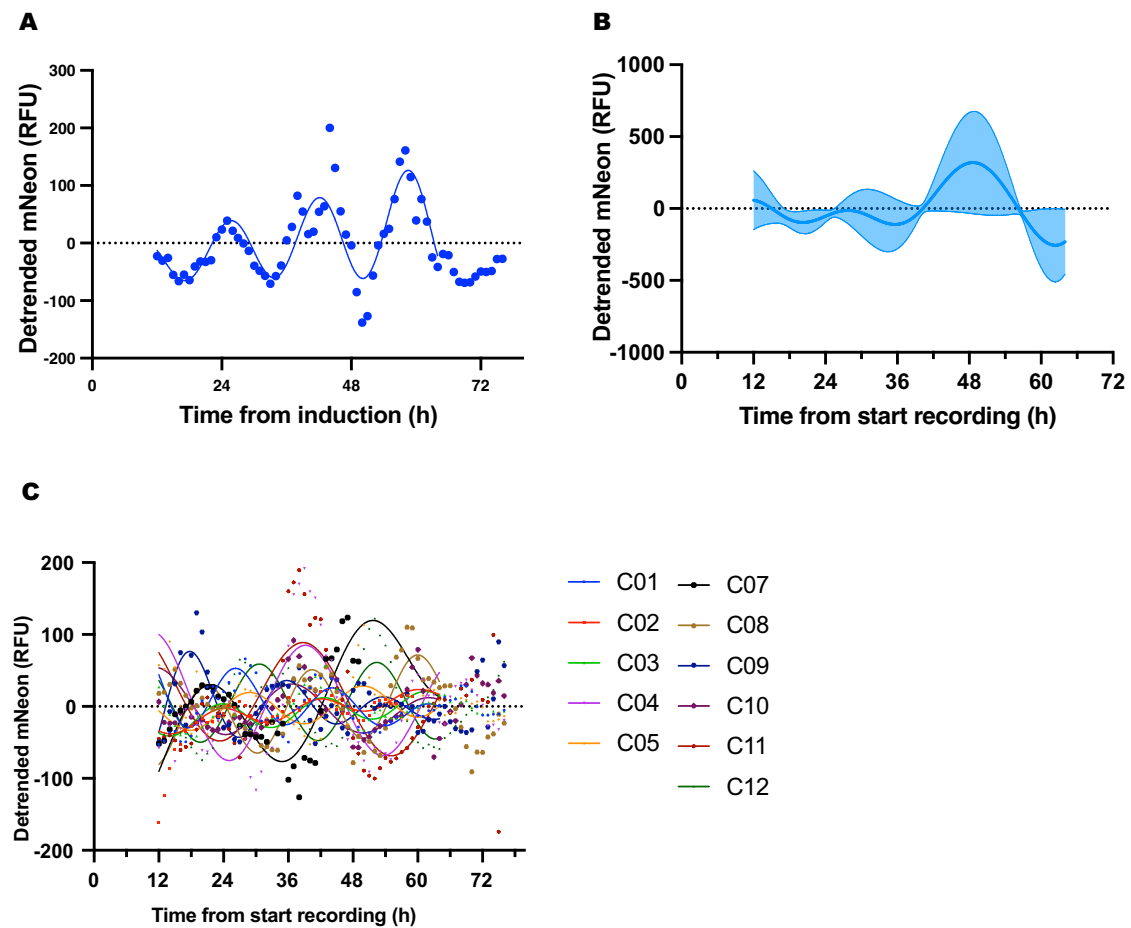


Figure 6.3: **Detrended data of Myc-tFT RFU curve-fitted with a damped cosine wave.** Representative detrended RFU data of U2OS FRT/TO Myc-tFT cells whose circadian rhythms were synchronised by Dexamethasone treatment ($C_f=0.1\mu\text{M}$):

- A Detrended data from C10 from **Figure 6.2** (individual points) and its modelled curve.
- B Average curve (line) and Standard error of the mean (SEM - shaded area) of fitted detrended RFU curves of cells treated with Dexamethasone.
- C Detrended data from **Figure 6.2 A** of cells treated with DMSO and their modelled curve

6.2. Circadian synchronisation of U2OS FRT/TO Myc-tFT cells leads to synchronised oscillations in Myc-tFT levels

bust synchronisation method was tested as Dexamethasone treatment is predicted to synchronise only a fraction of the cell population (Dr. John O'Neill, personal communication).

6.2.2 Synchronisation by temperature cycling

A more robust synchronisation method for circadian synchronisation was tested. This method consisted in culturing cells to confluency (in growth media supplemented with 10% FBS) between temperatures of 37°C and 32°C for 12 hour intervals over 4 days (Putker et al., 2021). On the fourth day, at the end of the last temperature cycle, cells were washed in PBS and the media was replaced with filming media supplemented with 1% FBS and DOX. Cells were then imaged every hour for 96 hours. This protocol yielded synchronous oscillations of Myc-tFT levels that were now synchronous enough to be visible by eye in whole field images as shown in **Figure 6.4**.

Chapter 6. Circadian rhythms contribute to periodic post-translational regulation of Myc-tFT

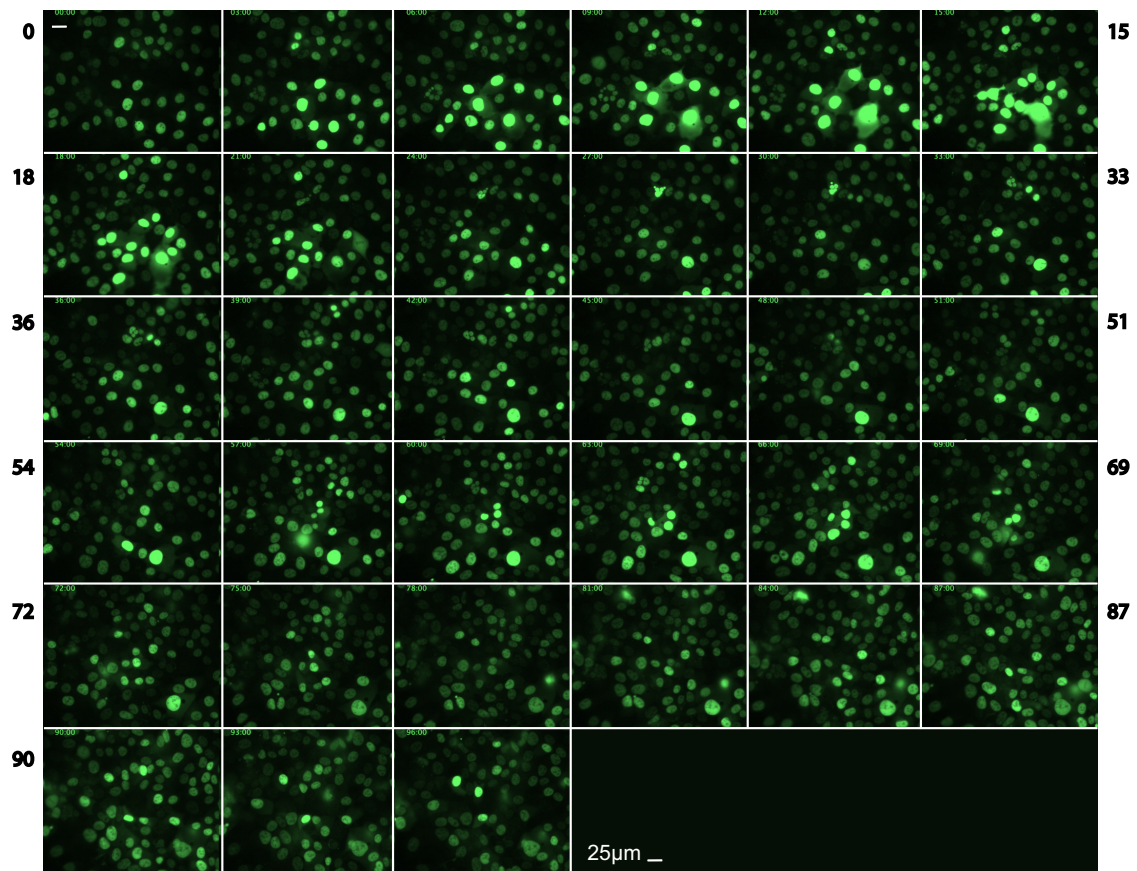


Figure 6.4: **Panel images of U2OS FRT/TO Myc-tFT cells synchronised by temperature cycling.** Images of the mNeonGreen signal of circadian synchronised cells which were imaged every hour for 96 hours. In this image, 3 hours lapsed between one panel and the next. To the left and right of the panels are time stamps of the first and last panels in the row.

6.2. Circadian synchronisation of U2OS FRT/TO Myc-tFT cells leads to synchronised oscillations in Myc-tFT levels

Analysis of mNeonGreen signal at the whole field level, whereby the average intensity of the field of cells was measured and corrected for background, evidenced robust synchronisation the cell population in each field (**Figure 6.5 A**) and between fields (**Figure 6.5 B**).

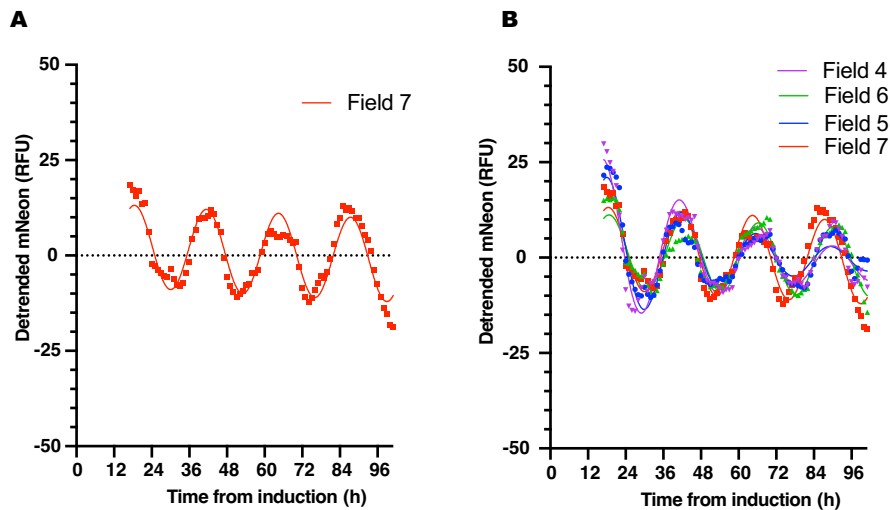


Figure 6.5: Temperature cycling synchronisation yields clear oscillations of cells in a field, and of multiple fields in the same well. Representative detrended RFU data of U2OS FRT/TO Myc-tFT cells:

A Detrended data generated by whole-field analysis of mNeonGreen RFU.

B As A but with each trace representing a different field of cells.

From fitted curves like the ones displayed in **Figure 6.5 A and B**, period and amplitude information were extrapolated and can also be pooled across experiments to generate an average curve with SEM. **Figure 6.6** summarises such information from experimental repeats. Myc-tFT oscillations display robust oscillations following circadian synchronisation (**Figure 6.6 A**) with an average period of 24 hours **Figure 6.6 B** and decreasing amplitude. While the oscillations synchronised consistently, the amplitude of the oscillations was variable, as shown by the individual points in **Figure 6.6 C** which each represent an amplitude reading from a field of Myc-tFT cells. This might reflect the phenomenon described in the previous chapter by which the amount of Myc-tFT that can accumulate in different cells is quite varied. The reason for this has yet to be determined.

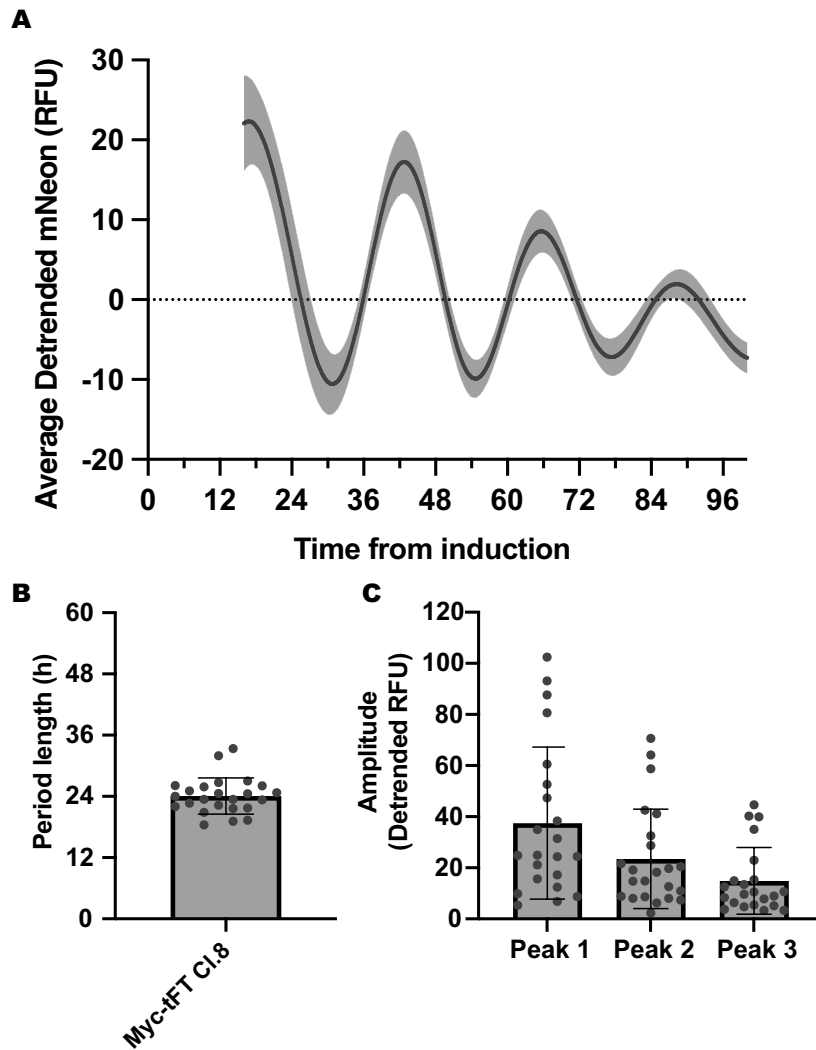


Figure 6.6: **Synchronised oscillations of Myc-tFT have a period of 24h and decreasing amplitude.** Average detrended RFU of curves fitted to data from experimental repeats:

- A Average detrended curve for Myc-tFT oscillations.
- B Average period length (h) of Myc-tFT oscillations (each dot is the period of a curve generated from one field of cells).
- C Average amplitude (detrended RFU) of the first three peaks in Myc-tFT oscillations (each dot is the amplitude of a peak of a curve generated from one field of cells).

6.2. Circadian synchronisation of U2OS FRT/TO Myc-tFT cells leads to synchronised oscillations in Myc-tFT levels

6.2.2.1 Synchronised Myc oscillations are observed by immunoblotting following circadian synchronisation

Given the strong synchronisation achieved with the temperature cycling protocol, it was important to assess whether oscillations in Myc-tFT could be parallel to changes in core members of the TTFL. Cells were synchronised as described and samples were collected and stored at the indicated times. All lysates were prepared together once the sample collection was completed to ensure uniform lysis of the samples. Lysates were then processed for immunoblotting.

Changes in Myc-tFT levels were detectable by immunoblotting as measured both with anti-Myc and anti-HA antibodies (an HA tag is present at the C-terminus of Myc-tFT). Changes in BMAL1 levels, as a biomarker for circadian rhythms, were also assessed, with its levels increasing over time. This might be the result of media changes at time 0h or indirectly of Myc-tFT induction. Oscillations in both Myc-tFT and BMAL1 (from 36 hours onward) were detected after quantification of blots and normalisation against GAPDH, which does not display circadian regulation (**Figure 6.7 A and B**). Because of the possibility that expression of exogenous Myc might have been affecting circadian cycles, as well as being regulated by the cycle, I decided to confirm regulation by temperature cycling of endogenous Myc. I used the lung cancer cell line A549 since these cells express endogenous Myc detectable by immunoblot and had been described in a study investigating Myc interaction with clock protein CRY2 (Huber et al., 2016). To achieve this, cells were synchronised by temperature cycling and extracts were made at the appropriate time points. Lysates were processed for immunoblotting. The results highlight substantial changes in endogenous Myc over time (**Figure 6.8 A**). Myc accumulates in the first 24 hours due to a media change at 0h post-synchronisation. This is a common response to mitogen activation that leads to rapid Myc accumulation. For this reason, the time points relevant to our study were from 36 hours onwards, where Myc levels decreased from 36h to 48h, increased again at 60h and drop once more at 72h. This closely recapitulates the trend in BMAL1 levels in the same cellular extracts (depicted and quantified in **Figure 6.8 A and B**). These data demonstrated that not only Myc-tFT but also endogenous Myc, expressed in another cellular context,

Chapter 6. Circadian rhythms contribute to periodic post-translational regulation of Myc-tFT

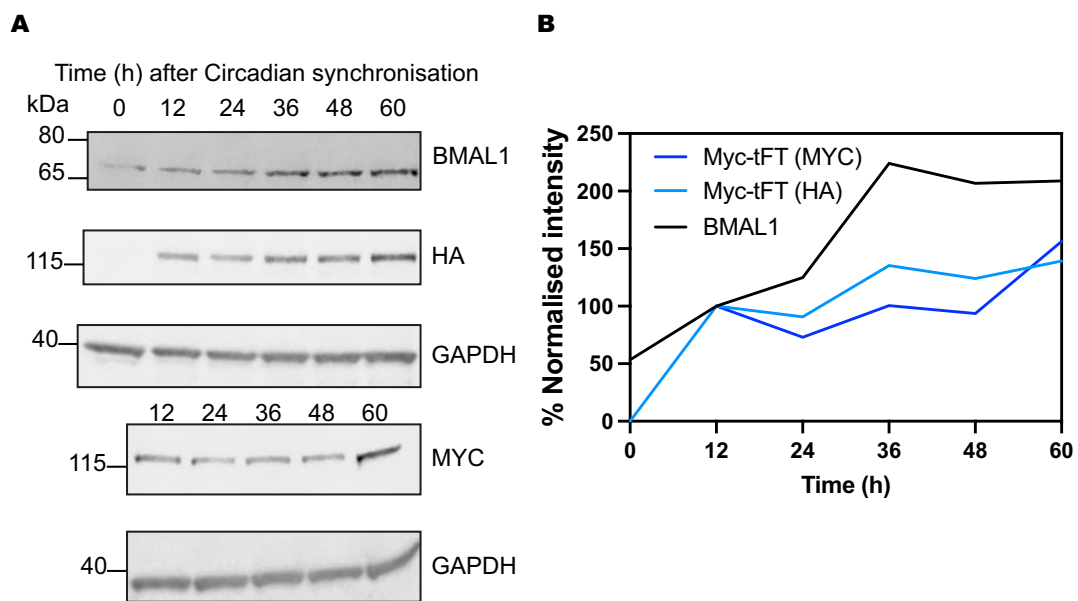


Figure 6.7: **Myc-tFT oscillations are detectable by immunoblotting following circadian synchronisation.** U2OS FRT/TO Myc-tFT cells were synchronised by temperature cycling and samples were collected for lysate extraction at the described time points post-synchronisation:

A Immunoblots probed with antibodies against BMAL1, Myc-tFT (HA and MYC antibodies) and GAPDH control.

B Quantification of immunoblotting data. Signal from each antibody was first normalised to GAPDH signal and then to its 12 hour time point.

6.2. Circadian synchronisation of U2OS FRT/TO Myc-tFT cells leads to synchronised oscillations in Myc-tFT levels

oscillates following circadian synchronisation. Huber et al. (2016) report destabilisation of Myc by CRY2 and FBXL3 in this lung cancer model, and propose that CRY2-mediated regulation of Myc could play a role in reinforcing circadian amplitude. However they do not monitor changes in Myc levels over time. Our finding supports their hypothesis for circadian-dependent Myc regulation in this cell line.

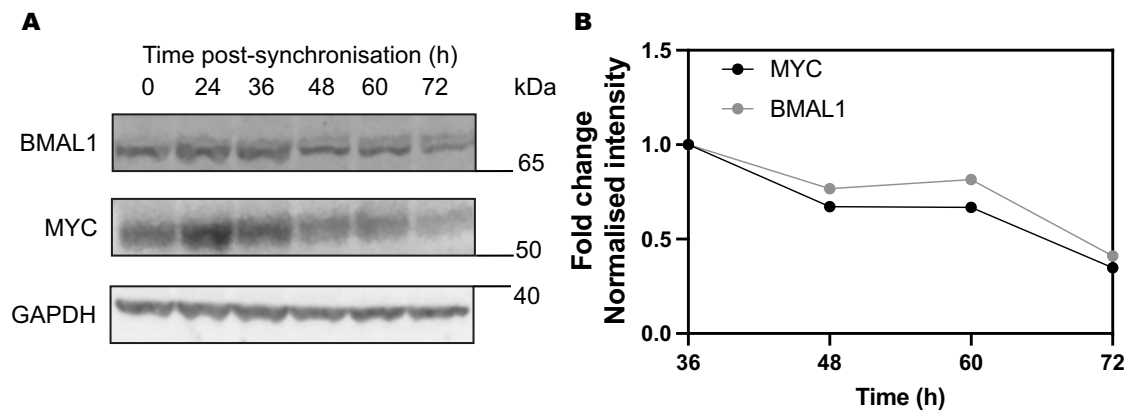


Figure 6.8: **Endogenous Myc levels of A549 cells oscillate following circadian synchronisation** A549 cells (lung cancer cell line) were synchronised by temperature cycling and samples were collected for lysate extraction at the described time points post-synchronisation:

- A Immunoblots probed with antibodies against BMAL1, Myc and GAPDH control.
- B Quantification of immunoblotting data signal from each antibody was first normalised to GAPDH signal and then to its 36h time point.

6.3 Post-translational regulation of Myc-tFT contributes to its circadian regulation.

Having established that circadian synchronisation resulted in synchronised oscillations of Myc-tFT levels, I set out to investigate whether the underlying process regulating this was transcriptional, translational, post-translational or a combination. It is important to reiterate that expression of Myc-tFT was driven from a constitutively active promoter, and that reduction in rates of translation by TORin1, as described in the previous chapter, consistently failed to interrupt the oscillations. These facts pointed to a major role for post-translational regulation in Myc-tFT oscillations.

6.3.1 Myc-tFT mRNA expression

Many studies in the literature report oscillating Myc mRNA levels upon intact circadian regulation. In our system, Myc-tFT is not under the control of the endogenous Myc promoter so regulation of expression of Myc and Myc-tFT would be expected to be different. Nonetheless, I investigated Myc-tFT mRNA levels in circadian synchronised cells, considering that these might also oscillate, in particular taking into account the possible existence of several non-canonical E-boxes (CANNTG) in the CMV promoter (at positions 228, 243, 252 and 540). RT-qPCR analysis of Myc-tFT mRNA was conducted. U2OS FRT/TO Myc-tFT cells were synchronised and cells were collected at 0, 12, 18, 24, 30 and 36 hours and then processed for mRNA extraction. mRNA levels were quantified using One-Step RT-qPCR with primers amplifying mCherry mRNA as a proxy for Myc-tFT expression and hPER2 for comparison with a clock gene. These were normalised to hActin mRNA. mCherry mRNA levels increased uniformly over time (**Figure 6.9**). Unfortunately, it was not possible to interpret this result as evidence of lack of oscillation in Myc-tFT mRNA, since the positive control, hPER2 did not oscillate either. This was not consistent with the reported changes in mRNA levels of hPER2 in U2OS cells reported in the work by Altman et al. (2015). This could be due to disruption in the expression pattern of hPER2 by Myc as reported by Altman et al. (2015), however since control extracts from cells without Myc-tFT expression (-DOX) were lacking,

6.3. Post-translational regulation of Myc-tFT contributes to its circadian regulation.

conclusions could not be drawn. Unfortunately, due to lack of time, this experiment was not repeated with the necessary control. Given that oscillations in BMAL1 were detected by immunoblot following 36 hours, lysates collection at further timepoints might reveal oscillations in hPER2 and, possibly, Myc-tFT. These experiments were deemed inconclusive with regards to establishing the contribution of transcriptional changes to Myc oscillations.

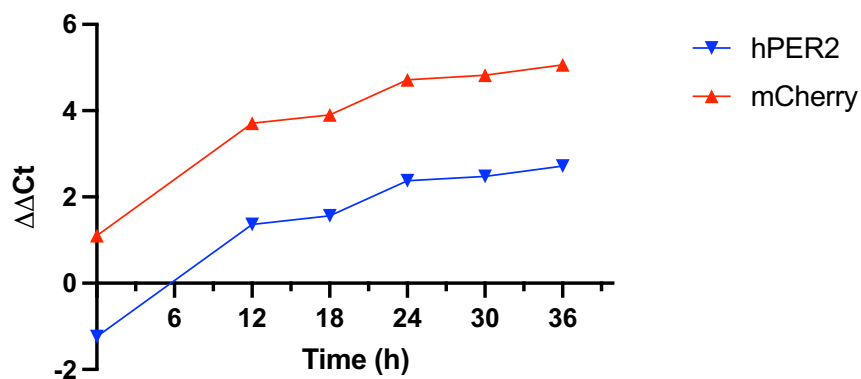


Figure 6.9: Myc-tFT PER2 mRNA levels in Myc-tFT cells. U2OS FRT/TO Myc-tFT cells were synchronised by temperature cycling and samples were collected for mRNA extraction at the described time points post-synchronisation. Myc-tFT mRNA from three biological repeats was evaluated using primers that bound to the mCherry sequence (designed by Roberta Cacioppo).

6.3.2 Oscillations are more robust in the presence of wild-type Myc

I next investigated the contribution of post-translational regulation on the Myc-tFT oscillations. Huber et al. (2016) highlighted the key role of T58 for post-translational regulation of Myc by the circadian rhythm in A549 cells. Having confirmed that Myc does indeed oscillate in A549 cells, I hypothesised that Myc-tFT could be regulated in the same way by CRY2, which interacts preferentially with Myc when T58 phosphorylation is present. For this reason, I compared WT Myc-tFT with Myc T58A-tFT. Two clones of the T58A line were analysed, one that had been used in previous experiments and showed detectable levels of Myc-tFT in the absence of doxycycline (Clone 9), and another that responded appropriately to induction by doxycycline (Clone 5). All cells were circadian synchronised according to the temperature cycling protocol and imaged over 96 hours. Representative panel images of Myc T58A-tFT Cl5 mNeonGreen signal post-synchronisation are displayed in **Figure 6.10**. Detrended data was curve-fitted and an average of the fitted curves (with SEM) was generated (**Figure 6.11 A**). Both WT and T58A cell lines displayed oscillations with a periodicity of 24h over repeated biological experiments (**Figure 6.11 B**). A difference between the cell lines, however, existed in the amplitude of the oscillations, which were significantly greater in the WT (37.5 mean \pm 29.8 detrended RFU of the first peak) than in the two T58A clones (11.6 mean \pm 6.1 Detrended RFU for Cl.9 and 3.7 mean \pm 1.5 for Cl.5), as illustrated in **Figure 6.11 C**. Furthermore, WT Myc-tFT displayed decrease in the average amplitude of the oscillations (Peak 1= 27.5, Peak 2= 23.5, Peak 3= 14.9), while Myc T58A-tFT showed smaller changes in average amplitude over time (Clone 9: Peak 1=11.6 Peak2=8.5, Peak 3=6.1; Clone 5: Peak 1=3.3, Peak 2=5.4, Peak 3=6.4). Differences in amplitude between the two T58A clones could have been due to the clonal differences mentioned above, however Myc-tFT expression levels and ratios between the clones was comparable (**Figure 6.12**). These data highlights that the WT Myc-tFT is expressed at higher levels than the T58A mutant, which might correlate to the higher amplitude in the oscillations of the WT. The lower expression and amplitude of the T58A mutants might indicate a lower tolerance threshold for Myc T58A-tFT accumulation. From these results it can be concluded that there is a key role for PTMs in Myc-tFT oscillations. However due to the

6.3. Post-translational regulation of Myc-tFT contributes to its circadian regulation.

fact that Myc T58A-tFT oscillates, CRY2-FBXL3-mediated regulation of Myc-tFT does not appear to be the mechanism driving the oscillations. Personal communications from Dr. John O'Neill highlighted a lack of detectable CRY2 protein in U2OS cells in his own work. This suggests that CRY2 is not involved in Myc-tFT oscillations.

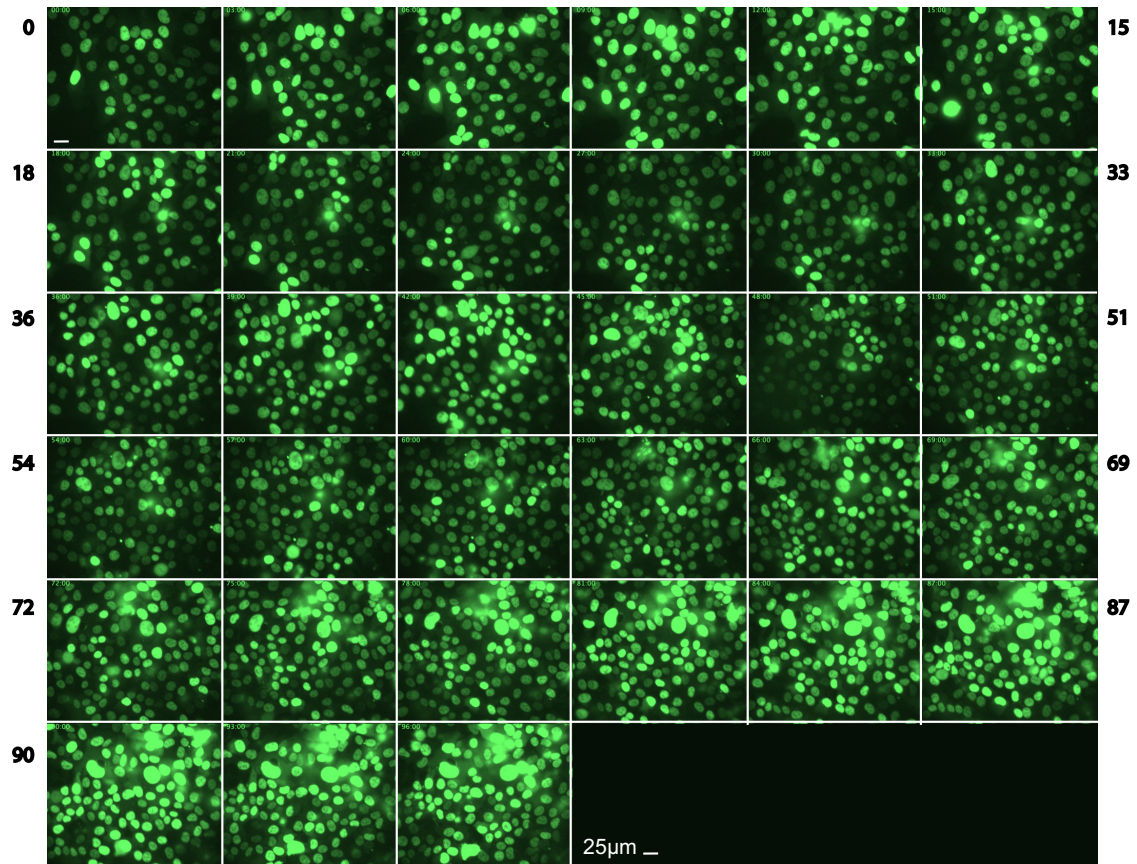


Figure 6.10: **Panel images of U2OS FRT/TO Myc T58A-tFT Clone 5 cells synchronised by temperature cycling.** Images of the mNeonGreen signal of circadian synchronised cells which were imaged every hour for 96 hours. In this panel, 3 hours lapsed between one figure and the next. To the left and right of the panels are time stamps of the first and last panels in the row.

Chapter 6. Circadian rhythms contribute to periodic post-translational regulation of Myc-tFT

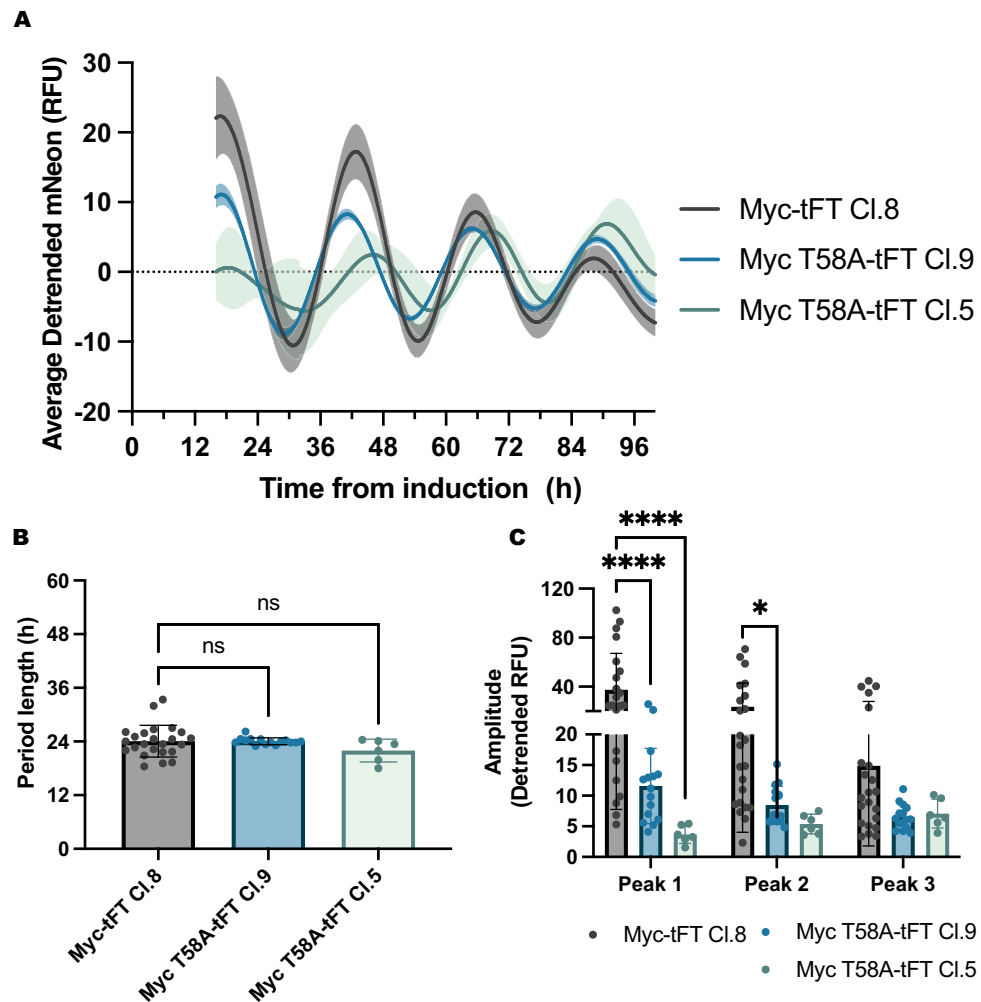


Figure 6.11: Mutation of T58 of Myc to block phosphorylation results in oscillations of decreased amplitude but period length is maintained. Average detrended RFU of curves fitted to data from experimental repeats. Data from U2OS FRT/TO Myc-tFT (WT- grey) or two different clones of Myc T58A-tFT (Cl.9 and 5, blue and green respectively):

- A Average detrended curve for Myc-tFT oscillations.
- B Average period (h) of Myc-tFT oscillations (each dot is the period of a curve generated from one field of cells).
- C Average amplitude (detrended RFU) of the first three peaks in Myc-tFT oscillations (each dot is the amplitude of a peak of a curve generated from one field of cells).

6.3. Post-translational regulation of Myc-tFT contributes to its circadian regulation.

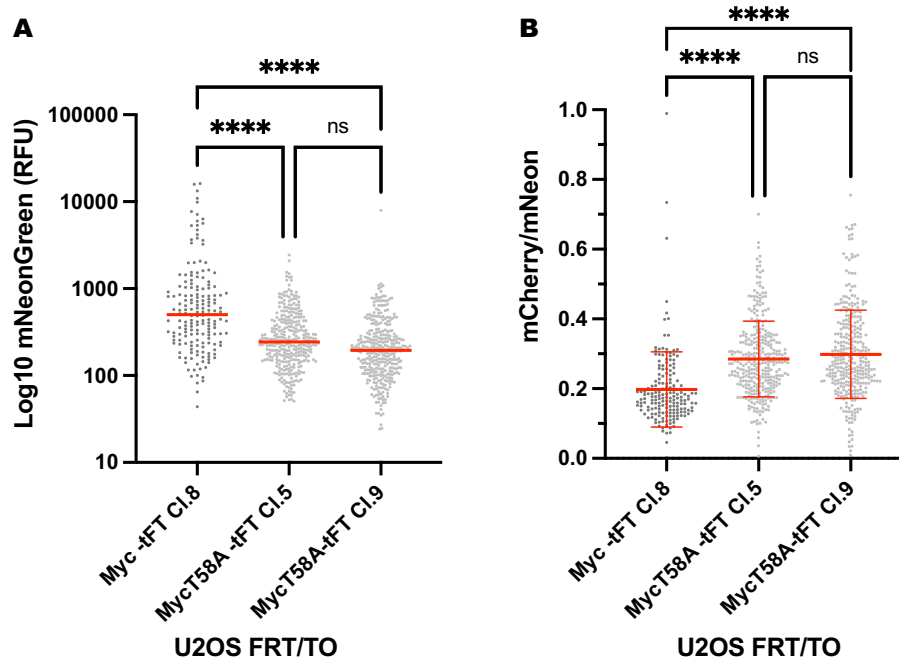


Figure 6.12: mNeonGreen levels and Myc-tFT ratios of Myc-tFT clones. Comparison of Myc-tFT constructs in asynchronous U2OS FRT/TO Myc-tFT (WT and T58A) clones (ns= non significant; ****= $p \leq 0.0001$):

A mNeonGreen levels (RFU) (median in red).

B Myc-tFT ratio (mean and SD in red).

Chapter 6. Circadian rhythms contribute to periodic post-translational regulation of Myc-tFT

Having observed that oscillations persist in a more stable version of Myc-tFT, changes in the tFT construct alone (mCherry-mNeonGreen) were monitored, in search of a negative control for the oscillations observed with WT and T58A versions of Myc. All cell lines were circadian synchronised and imaged over 96h, with imaging data processed as in the previous experiments. Surprisingly, tFT level appeared to also oscillate over time, as depicted in the panel images of **Figure 6.13** and in the graphs **Figure 6.14 A**. However, when period was compared, tFT oscillated at a period 10h greater than that of either WT or T58A Myc-tFT constructs, **Figure 6.14 B**. tFT oscillation amplitude was comparable to that of the T58A cell lines, **Figure 6.14 C**. The oscillations recorded were unexpected as tFT was predicted to increase and stabilise over time, since this is a fusion of exogenous fluorescent proteins with no functional output in cells.

6.3. Post-translational regulation of Myc-tFT contributes to its circadian regulation.

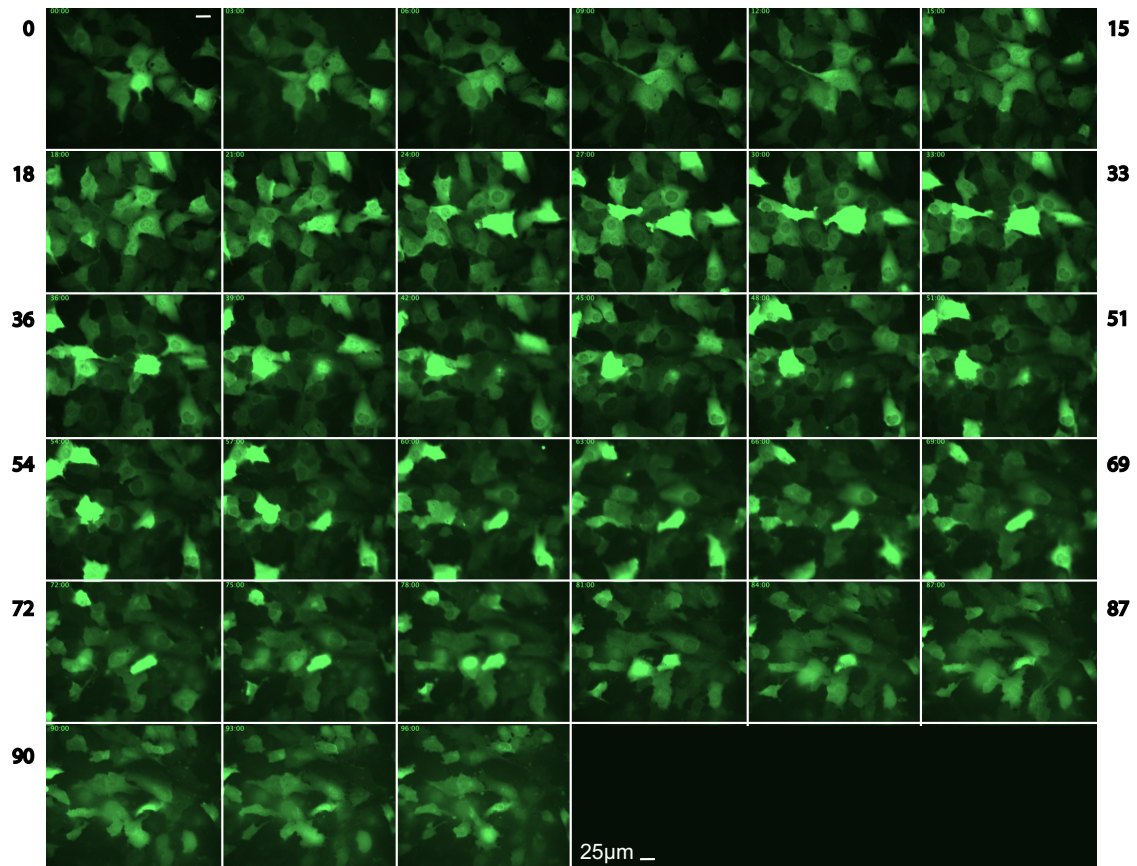


Figure 6.13: **Panel images of U2OS FRT/TO tFT Clone 1 cells synchronised by temperature cycling.** Images of the mNeonGreen signal of circadian synchronised cells which were imaged every hour for 96 hours. In this panel, 3 hours lapsed between one figure and the next. To the left and right of the panels are time stamps of the first and last panels in the row.

Chapter 6. Circadian rhythms contribute to periodic post-translational regulation of Myc-tFT

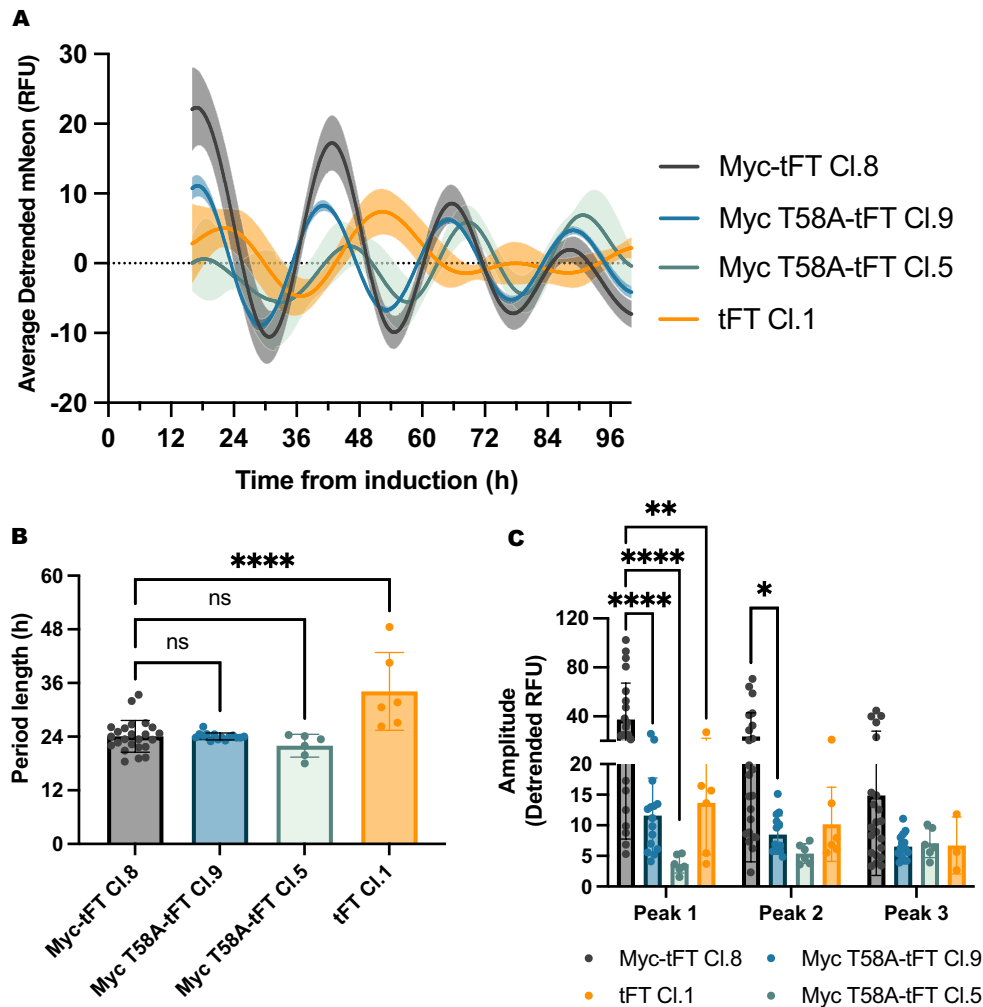


Figure 6.14: Expression of tFT alone results in oscillations with a greater period than those recorded in Myc-tFT lines. Average detrended RFU of fitted curves. Data from U2OS FRT/TO Myc-tFT (WT- grey) or two different clones of Myc T58A-tFT (Cl.9 and 5, blue and green respectively) and tFT (orange):

- A Average detrended curve for oscillations of different tFT constructs .
- B Average period (h) of oscillations of tFT constructs (each dot is the period of a curve generated from one field of cells).
- C Average amplitude (detrended RFU) of the first three peaks in oscillations of tFT constructs (each dot is the amplitude of a peak of a curve generated from one field of cells).

6.3. Post-translational regulation of Myc-tFT contributes to its circadian regulation.

A possible explanation for the increased period seen with the tFT construct could be that tFT is a stable protein whose levels would respond more slowly than Myc-tFT to changes in transcription or degradation rates. I had previously assessed tFT stability to be greater than Myc-tFT by measurement of the tFT ratio, however extrapolation of protein half-lives from this measurement is not possible. To address this, I performed Cycloheximide (CHX)-chase experiments, whereby I incubated U2OS FRT/TO expressing tFT cells with CHX for 3, 6, 9 or 12 hours to block synthesis of new protein and compared the decay in protein levels to untreated cells by immunoblotting (Figure 6.15). Surprisingly, the tFT protein, which is much more stable than Myc-tFT, showed a relatively short half-life of under 3 hours.

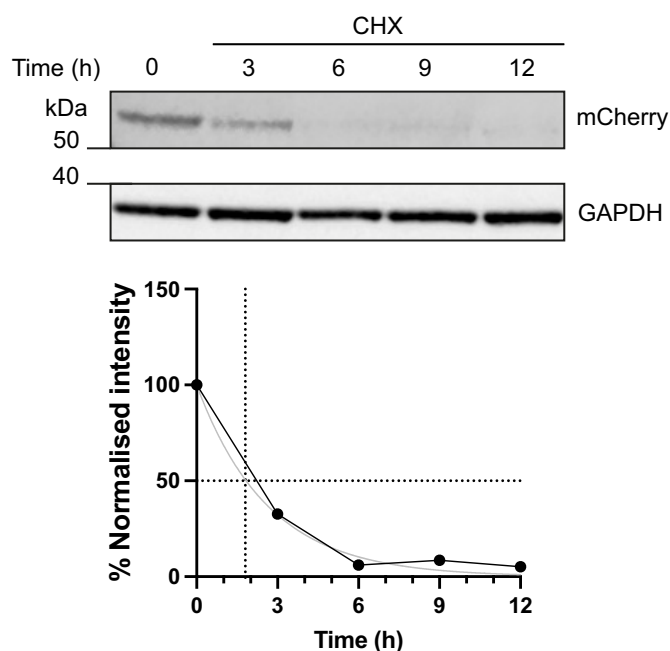


Figure 6.15: **CHX-chase experiments of tFT cells.** U2OS FRT/TO tFT Clone 1 (Cl.1) cells were treated with Cycloheximide for the described periods, and then cells were collected for lysates. Detection of the tFT constructs was achieved with the use of an antibody against mCherry.

In light of this result we concluded that global changes in rate of protein synthesis and degradation in response to circadian synchronisation were contributing factors to the oscillations recorded. Nonetheless, what these data did elucidate is the fact that the most robust oscillations in any tFT construct were recorded in the presence of WT Myc. Post-translational modifications seemed to contribute greatly to the differences

Chapter 6. Circadian rhythms contribute to periodic post-translational regulation of Myc-tFT

recorded. Specifically, it appeared that periodicity was determined by the presence of Myc and not its phosphorylation state at T58. What this phosphorylation site did influence was the amplitude of the oscillations, which were far greater in the WT construct.

6.3.3 The oscillations in Myc-tFT appear independent of Myc-tFT activity

An outstanding question was whether Myc-tFT activity contributed to the oscillations recorded. To investigate this, Myc-tFT cells were treated with Myc inhibitor KJ-Pyr-9 (Cf=10 μ M) following temperature cycling synchronisation and from imaging onset. In parallel, a BrdU assay was carried out to demonstrate inhibition of Myc-tFT by KJ-Pyr-9. As shown in **Figure 6.16 A**, KJ-Pyr-9 was indeed able to significantly reduce Myc-tFT-driven proliferation following induction with DOX. Having established KJ-Pyr-9's ability to inhibit Myc-tFT, time-lapse imaging data from cells treated with the inhibitor or DMSO were compared. The curve-fitted data (**Figure 6.16 B**) revealed that, although a reduction in Myc-tFT activity was recorded in the proliferation assay, no significant changes in periodicity (**Figure 6.16 C**) or reduction in amplitude of Myc-TFT oscillations were measured. Rather, there appears to be a small increase in amplitude with KJ-Pyr-9 treatment, although the difference was not statistically significant (**Figure 6.16 D**). From these data, I excluded the contribution of Myc-tFT activity to its oscillations. These data could be confirmed by treatment with other inhibitors.

6.3. Post-translational regulation of Myc-tFT contributes to its circadian regulation.

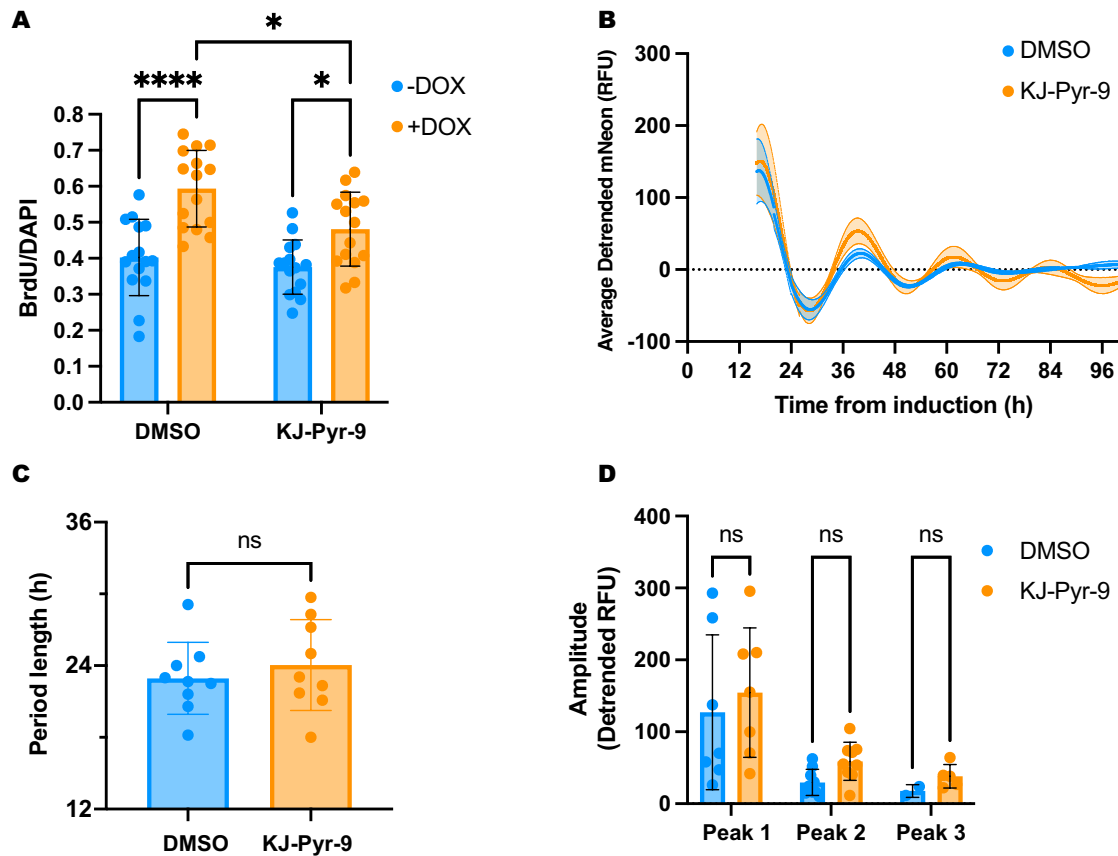


Figure 6.16: **Inhibition of Myc-tFT by KJ-Pyr-9 does not affect Myc-tFT oscillations.** U2OS FRT/TO Myc-tFT were treated with Myc inhibitor KJ-Pyr-9 ($C_f=10\mu M$):

- A Inhibition of Myc by KJ-Pyr-9 was assessed by BrdU assay where serum starved Myc-tFT cells were co-treated for 24 hours with DMSO or KJ-Pyr-9 in the presence of absence of DOX, prior to a 2h BrdU pulse.
- B Average detrended curve of fitted data for oscillations of Myc-tFT treated with DMSO or KJ-Pyr-9
- C Period length of Myc-tFT oscillations in cells treated with the Myc inhibitor or vehicle control.
- D Average amplitude of each peak of oscillating Myc-tFT treated with DMSO or KJ-Pyr-9.

6.3.4 GSK3 β regulates Myc-tFT oscillations independently of T58

Given the established role GSK3 β plays in Myc-tFT post-translational regulation, as well as its ability to confer robustness to circadian rhythms according to the post-translational oscillator model, I formulated an hypothesis whereby GSK3 β 's regulation of Myc-tFT via T58 phosphorylation, could be entraining Myc-tFT levels to circadian rhythms. This phosphorylation site also appeared to influence the amplitude of Myc-tFT oscillations (**Section 6.3.2**). To test this I decided to investigate the effect of GSK3 β in circadian synchronised cells using the GSK3 β inhibitor CHIR99021. To assess whether any possible effect of GSK3 β inhibition on Myc-tFT would reflect direct phosphorylation of Myc T58 by the kinase, I performed the experiment in parallel in the context of WT and T58A-tFT.

U2OS FRT/TO Myc-tFT and Myc T58A-tFT (Cl.5) were synchronised by temperature cycling, then expression of the constructs was induced via Doxycycline treatment, and cells were imaged every hour. 72 hours into the filming, at a point predicted to be a trough in Myc-tFT levels based on previous data, both cell lines were treated with DMSO or CHIR99021 (Cf=3 μ M). Recording progressed to 96 hours.

The results are displayed in **Figure 6.17**, where average curves from fitted data are shown in **panels A and C**, and average curves from non-fitted detrended data are illustrated in **panels B and D**. The reason for displaying the data in these two different ways is that the curve fitting struggled to recapitulate the increase in amplitude in the oscillation post CHIR99021 treatment, which instead is more evident in the non-fitted data. Prior to 72 hours, both WT and T58A displayed three oscillations and a trough at 72 hours. Dosing with CHIR99021, but not DMSO led to an increased amplitude of the following peak in both WT and T58A mutant. These data supports the notion that GSK3 β plays a role in circadian-dependent Myc-tFT oscillations, but did not support the initial hypothesis that this effect is mediated through phosphorylation on T58. Whether this is due to indirect regulation of the circadian processes that dictate Myc oscillations, or directly but through phosphorylation at a different residue, remains unknown.

6.3. Post-translational regulation of Myc-tFT contributes to its circadian regulation.

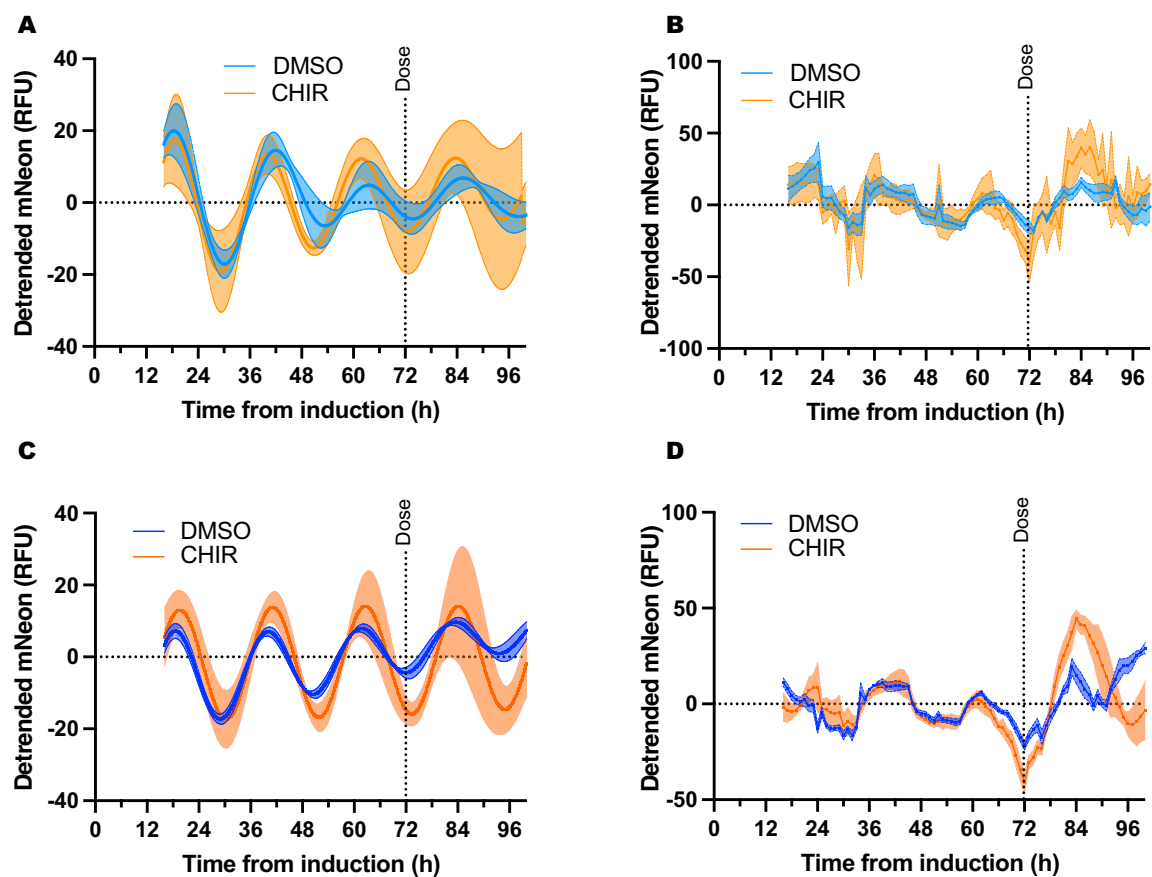


Figure 6.17: **Inhibition of GSK3 β by CHIR99021 resets oscillations of WT and T58A Myc-tFT.** U2OS FRT/TO Myc-tFT (WT- light blue and orange) or Myc T58A-tFT (dark blue and orange) were circadian synchronised and imaged every hour for 96 hours. 72 hours into the movie, CHIR99021 ($C_f=3\mu\text{M}$; orange) or DMSO (blue) were added to the wells:

- A Average detrended curve of fitted data for oscillations of Myc-tFT treated with DMSO or CHIR99021.
- B Average detrended curve of non-fitted data for Myc-tFT treated with DMSO or CHIR99021.
- C Average detrended curve of fitted data for oscillations of Myc T58A-tFT treated with DMSO or CHIR99021.
- D Average detrended curve of non-fitted data for Myc T58A-tFT treated with DMSO or CHIR99021.

6.4 The variability in Myc-tFT ratio is reduced following circadian synchronisation

Although the mechanism for Myc-tFT regulation by the circadian rhythm remained elusive, enough evidence was gathered to support the notion that some of the variability in tFT measurements, after induction of Myc-tFT expression in my clonal cell populations, was due to circadian-mediated post-translational regulation of Myc-tFT. Therefore it was hypothesised that circadian synchronisation of cell populations should remove some of the variability in tFT ratios and improve the Myc-tFT assay. To evaluate if circadian synchronisation improved the Myc-tFT assay, I performed an experiment where synchronised and asynchronous cells were treated at different time points with a few of the compounds that had been used in the AstraZeneca screen, specifically DMSO, CHIR99021 (Cf=10 μ M), KN-93 (Cf=10 μ M) or MG132 (Cf=4.2 μ M). For each timepoint duplicate wells were treated and imaged.

Briefly, Myc-tFT cells were seeded on Day 1 for synchronisation and temperature cycled for 4 days. On Day 3, asynchronous cells were seeded and incubated overnight at 37°C. On day 4 both asynchronous and synchronised cells were washed twice with PBS and media was changed to filming media with 1% FBS and DOX for Myc-tFT induction. On day 5, cells were dosed at time points corresponding to a trough or at a peak in mNeonGreen in synchronised cells, as shown in **Figure 6.18** and according to the data previously described. Specifically, 27 hours after DOX induction, cells were dosed with compounds; at 30h cells were imaged. This was repeated 12 hours later on another plate of cells with cells dosed at 39h and imaged at 42h.

6.4. The variability in Myc-tFT ratio is reduced following circadian synchronisation

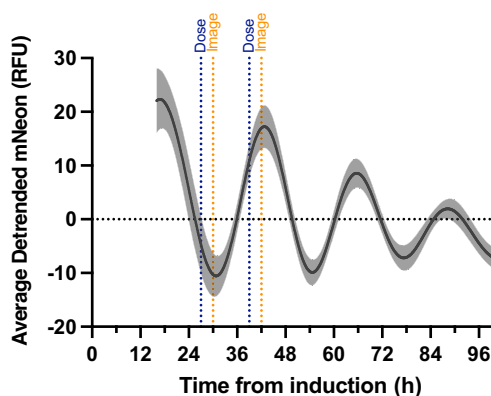


Figure 6.18: **Illustration of dosing regime in synchronised cells.** U2OS FRT/TO Myc-tFT cells were synchronised by temperature cycling and Myc-tFT expression was induced. 27h and 39h post induction cells were dosed with DMSO, CHIR99021 (Cf=10 μ M), KN-93 (Cf=10 μ M) or MG132 (Cf=4.2 μ M). Cells were imaged at 30h and 42h post-induction to correspond to trough (30h) and peak (42h) of circadian oscillation. In parallel, Myc-tFT was induced in asynchronous cells which were also treated at the same timepoints (not shown).

Firstly, control-treated cells in asynchronous and synchronised conditions were compared to evaluate the effect of circadian synchronisation on Myc-tFT readout. As depicted in the scatter plot of **Figure 6.19**, Myc-tFT ratios in asynchronous cells were significantly higher than those in synchronised conditions ($p \leq 0.0001$) at 30h and 42h. No significant differences in ratio were recorded between timepoints of cells synchronised with the same protocol.

The plots represented in **Figure 6.20** display the results from the 30h timepoint imaging, with Myc-tFT ratios for each treatment in duplicate (**Figure 6.20 A**) and for pooled replicate data (**Figure 6.20 B**). Different data distribution within and between the replicates is more apparent in the asynchronous cells than the synchronised, specifically in the case of DMSO and KN-93. This suggests better quality data could be generated following circadian synchronisation.

Variability in pooled data was quantified by descriptive statistics such as mean, standard deviation and sample variance (**Table 6.1**). From the table, it was clear that ratios in asynchronous DMSO and CHIR99021-treated cells are higher than those of synchronised cells, while KN-93 ratios were higher in the synchronised cells, and MG132 was comparable. When sample variance was compared, this is notably reduced in synchronised DMSO and CHIR99021-treated cells compared to asynchronous cells

Chapter 6. Circadian rhythms contribute to periodic post-translational regulation of Myc-tFT

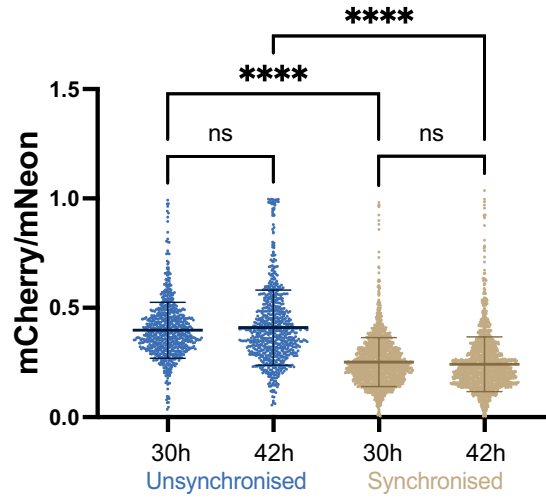


Figure 6.19: **Myc-tFT ratio is significantly lower in synchronised cells.** Data from asynchronous and synchronised U2OS FRT/TO Myc-tFT cells DMSO-treated with DMSO at 30 or 42 hours post-induction. Effect of synchronisation was compared by Ordinary One-Way ANOVA. ns= non significant; ****= $p \leq 0.0001$

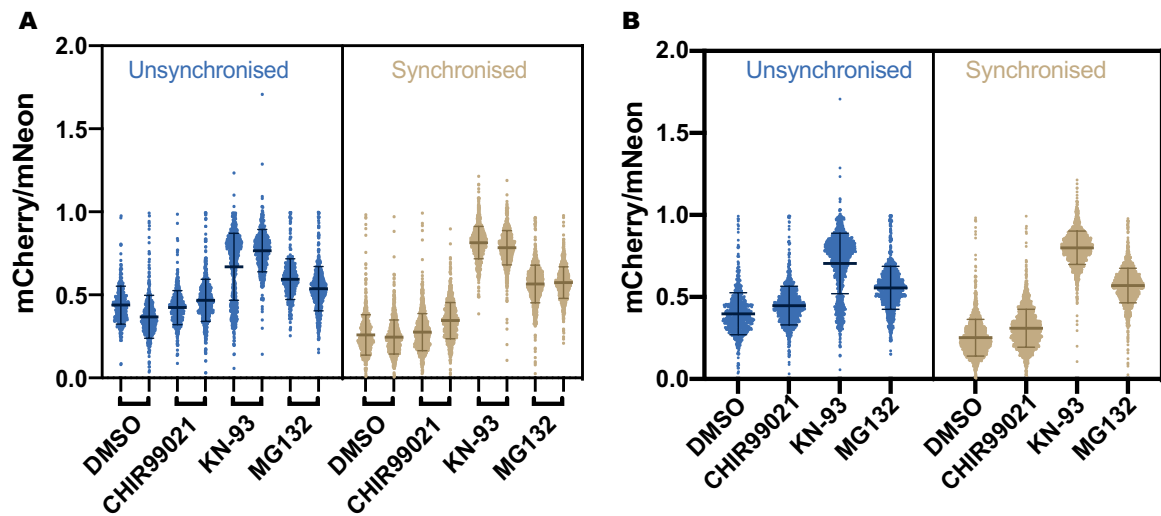


Figure 6.20: **Variability in Myc-tFT read out is reduced in synchronised compared to asynchronous cells treated 30h post-induction.** U2OS FRT/TO Myc-tFT synchronised or asynchronous were treated with DMSO, CHIR99021 ($Cf=10\mu M$), KN-93 ($Cf=10\mu M$) or MG132 ($Cf=4.2\mu M$) 27h post-induction and imaged 30h post-induction.

- A Scatter plot displaying the distribution, mean and standard deviation of replicate wells of asynchronous or synchronised cells treated with the small molecules detailed above.
- B Scatter plot displaying the distribution, mean and standard deviation of pooled data of asynchronous or synchronised cells treated with the small molecules detailed above.

6.4. The variability in Myc-tFT ratio is reduced following circadian synchronisation

dosed with the same compounds. Sample variance also decreased following circadian synchronisation in cells treated with KN-93 and MG132. To further quantify the improvement of the assay's variability I performed Z' analysis between DMSO and MG132 of each synchronisation condition. While the Z' values are negative, there is a 3-fold increase in the Z' of synchronised cells, indicating that the data improved.

	Unsynchronised				Synchronised			
	DMSO	CHIR99021	KN-93	MG132	DMSO	CHIR99021	KN-93	MG132
Mean tFT ratio	0.3976	0.4473	0.7048	0.5559	0.2519	0.3088	0.7996	0.5697
Std. Deviation	0.1279	0.1179	0.1841	0.1314	0.1115	0.1156	0.1017	0.1049
ANOVA		****	****	****		****	****	****
Sample Variance	0.016	0.014	0.034	0.017	0.012	0.013	0.010	0.011
Z'	-3.914				-1.043			

Table 6.1: **Descriptive statistics for cells imaged 30h post-induction.** Descriptive statistics to compare the effect of treatments in asynchronous and synchronised cells on Myc-tFT ratios as calculated using GraphPad Prism or Microsoft Excel. ****= $p \leq 0.0001$

The data from the 42 hour timepoint is presented in **Figure 6.21**. At the 42h timepoint, as at 30h, the spread of the data was clearly greater in the asynchronous when compared to the in the synchronised cells. This is evident when looking at individual duplicates (**Figure 6.21 A**), and the pooled data (**Figure 6.21 B**). Once more, the noise in the asynchronous data is most evident in DMSO and CHIR99021-treated cells. As an example, from descriptive statistics summarised in **Table 6.2**, asynchronous CHIR99021 had a higher ratio with a greater SD (mean tFT=0.46 \pm 0.16 SD) compared to the synchronised data (mean tFT=0.29 \pm 0.11 SD). The Myc-tFT ratio of DMSO and CHIR99021-treated cells is lower in synchronised than asynchronous cells, and it is higher in KN-93-treated synchronised versus asynchronous cells. The effect of MG132 treatment on the Myc-tFT ratio of synchronised and asynchronous cells is comparable. The consistent difference in the effect of synchronisation on treatment with CHIR99021 and KN-93 might be due to inhibition of kinases that act preferentially on a state of Myc (pS62 and pT58) which could be under the control of the circadian cycle, generating a response to inhibition of the cell population that is more complete in synchronised cells.

Chapter 6. Circadian rhythms contribute to periodic post-translational regulation of Myc-tFT

MG132 treatment, on the other hand, affects Myc-tFT indirectly through inhibition of global protein turnover, and might therefore be less susceptible to changes in PTM of Myc-tFT in asynchronous or synchronised conditions.

Synchronisation results in a smaller overlap in data between, for example, DMSO-, KN-93- or MG132-treated cells than asynchronous cells, giving rise to an improved Z' ($Z' = -1.109$) for synchronised cells compared to asynchronous cells ($Z' = -3.948$). **Table 6.2** indicates that the variability in the data, as measured by sample variance is reduced in each synchronised condition compared to the asynchronous equivalent.

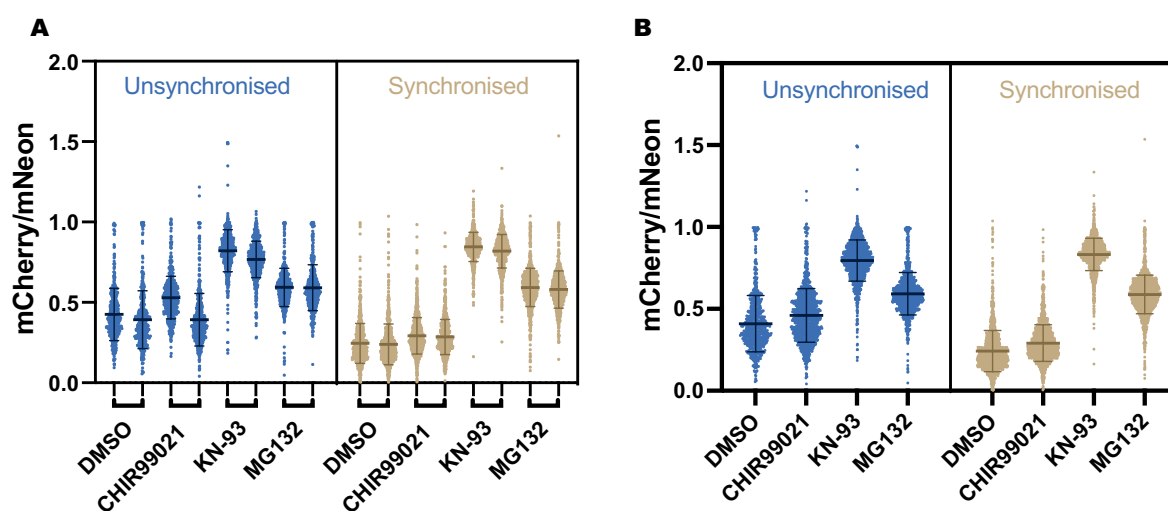


Figure 6.21: **Variability in Myc-tFT read out is reduced in synchronised compared to asynchronous cells treated 42h post-induction.** U2OS FRT/TO Myc-tFT synchronised or asynchronous were treated with DMSO, CHIR99021 (Cf=10 μ M), KN-93 (Cf=10 μ M) or MG132 (Cf=4.2 μ M) 39h post-induction and imaged 42h post-induction.

- A Scatter plot displaying the distribution, mean and standard deviation of replicate wells of asynchronous or synchronised cells treated with the small molecules detailed above.
- B Scatter plot displaying the distribution, mean and standard deviation of pooled data of asynchronous or synchronised cells treated with the small molecules detailed above.

Taken together, the data demonstrates a reduction in the variability of the Myc-tFT assay following circadian synchronisation.

6.4. The variability in Myc-tFT ratio is reduced following circadian synchronisation

	Unsynchronised				Synchronised			
	DMSO	CHIR99021	KN-93	MG132	DMSO	CHIR99021	KN-93	MG132
Mean tFT ratio	0.4093	0.4601	0.7951	0.5924	0.2422	0.2911	0.8321	0.5877
Std. Deviation	0.1722	0.1641	0.1257	0.1298	0.1252	0.1118	0.09867	0.1177
ANOVA		****	****	****		****	****	****
Sample Variance	0.030	0.027	0.016	0.017	0.016	0.013	0.010	0.014
Z'	-3.948				-1.109			

Table 6.2: **Descriptive statistics for cells imaged 42h post-induction.** Descriptive statistics to compare treatments of asynchronous and synchronised cells as calculated using GraphPad Prism or Microsoft Excel. ****= $p \leq 0.0001$

6.5 Chapter summary

The findings of this chapter can be concluded as follows:

- **Circadian synchronisation of U2OS FRT/TO Myc-tFT cells led to synchronised oscillation of Myc-tFT levels:** The circadian rhythm was identified as the cell-autonomous process that could synchronise Myc-tFT oscillations. Two synchronisation methods were tested, by dexamethasone and temperature cycling, and the latter resulted in robust synchronisation of the oscillations at the cell-population level. While this method proved fairly labour-intensive and required 4 days of preparation to achieve appropriate synchronisation prior to the start of experiments, it offered many advantages. It simplified image analysis, allowing the assessment of the oscillations with other techniques. The data analysis of the oscillations also benefitted from the synchronous oscillations, as data could be detrended, curve fitted and pooled across experiments, with results consistent across repeats. From the curve fitting, quantifiable and comparable measures of the oscillation could be obtained, like periodicity and amplitude. Myc-tFT cells were recorded to have oscillations in Myc-tFT with a period of 24 hours and decreasing in amplitude over time.
- **Oscillations in endogenous Myc can be observed in a different cellular context following circadian synchronisation:** Oscillating Myc in circadian synchronised A549 lung cancer cells was recorded for the first time in this study. This supports the notion that the observed oscillation seen with Myc-tFT is not unique to the model developed in this study. This observation should be further investigated in other cellular models of Myc and in other well-established models of Myc like the Myc-ER system.
- **Protein synthesis is not the main contributing process to Myc-tFT oscillations:** The contribution of protein synthesis and post-translational regulation of Myc-tFT to the oscillation was investigated. Work to address transcriptional and translational regulation of Myc-tFT was inconclusive. Experiments from the

previous chapter, where rates of protein synthesis in asynchronous and cell-cycle arrested cells were reduced by mTOR inhibition, consistently exhibited oscillations in Myc-tFT levels. Oscillations were recorded in tFT expressing cells, however these displayed an increased period of 36 hours. Taken together, this suggests that there is some contribution of global changes in protein synthesis rates to the observed oscillations, but this phenomenon did not account for the robust oscillations observed in Myc-tFT.

- **Post-translational modifications of Myc confer robustness to its oscillations:** Comparison of the oscillations observed in WT Myc-tFT to those of the Myc T58A-tFT version or the tFT alone, demonstrate that the presence of WT Myc-tFT confers robustness to the oscillations. Amplitude of the oscillations was reduced in the context of Myc T58A-tFT and tFT, while the period of the oscillations increased greatly in the tFT.
- **Myc-tFT oscillations are unaffected by inhibition of Myc-tFT activity:** An outstanding question was whether Myc-tFT activity was regulating the oscillations by modulation of its expression directly or indirectly through global changes in transcription. CHIP data from **Chapter 3** showed no enrichment of Myc-tFT at its CMV promoter, ruling out direct regulation of its own expression. Inhibition of Myc-tFT activity by Myc inhibitor KJ-Pyr-9 did not result in changes in Myc-tFT oscillations suggesting the oscillations are not being regulated by global changes in transcription rates by Myc. This should be confirmed with other inhibitors and in other cell models and with circadian markers..
- **Inhibition of GSK3 β by CHIR99021 results in an increased oscillation amplitude but this is independent of T58 phosphorylation:** Myc is known to be phosphorylated at T58 by GSK3 β , a kinase that plays an important role in circadian rhythm maintenance. I had hypothesised that GSK3 β could be entraining Myc to circadian rhythms through post-translational modification at this key residue. While this hypothesis was disproved by the fact that Myc T58A-tFT also displayed increased oscillation amplitude following CHIR99021 treatment,

Chapter 6. Circadian rhythms contribute to periodic post-translational regulation of Myc-tFT

this suggests that the kinase does contribute to the robustness of the oscillations. Whether that is through direct phosphorylation at another residue in Myc or indirectly, remains to be elucidated.

- **Variability in Myc-tFT ratios are reduced by circadian synchronisation:** The final experiments demonstrated that circadian synchronisation greatly reduced the variability in Myc-tFT ratios in cells dosed with small molecule compounds that modulate Myc stability and in those treated with vehicle control. Even though the Z' of the assay remained negative, the experiment demonstrated that circadian rhythms contribute greatly to the variability seen and that this biological process should be taken into account when performing drug screens of modulators of Myc stability.

Chapter 7

General discussion and future perspectives

The transcription factor Myc is a well validated cancer target that, although extensively studied, has so far eluded all efforts aimed at reducing its oncogenic activity. In this body of work, I described the generation, validation and application of a live cell imaging fluorescence-based assay designed to measure changes in Myc stability, for the application of medium-throughput screening for the identification of modulators of Myc stability.

7.1 Tandem Fluorescence Timers for studying Myc stability

7.1.1 Myc-tFT is a novel tool for measuring Myc stability

This work offers first proof-of concept for the use of tandem Fluorescent Timers (tFTs) as an imaging-based assay technology for studying Myc protein stability. Firstly, the appropriate combination of fluorophores was tested and selected, resulting in a Myc-mCherry-mNeonGreen tFT construct. This construct was able to report on changes in Myc stability induced by proteasomal inhibition. Importantly, Myc-tFT was shown to be subject to the same post-translational regulation as endogenous Myc, specifically phosphorylation of Threonine 58, resulting in a construct possessing the same half-life

Chapter 7. General discussion and future perspectives

as endogenous Myc. An alternative tool for studying Myc stability was published during the course of this investigation, which employed a GFP-tagged version of Myc, co-expressed with DsRed from the same transcript, allowing normalisation to translational efficiency of the construct (Blake et al., 2019). The aim of their study was to identify, through a compound screen of kinase inhibitors, novel kinase-dependent mechanisms of Myc protein regulation in the context of KRAS-mutant pancreatic cancer. Unlike the Myc-tFT tool, the one described in this paper presented increased stability of the tagged Myc with Myc-GFP still visibly present after 90 minutes of cycloheximide treatment. The authors note the increased Myc stability but reason that any modulation of the more stable Myc-GFP would result in a greater modulation of endogenous Myc which has a shorter half-life. Myc-tFTs were able to consistently measure changes in Myc stability brought about by inhibition of T58 phosphorylation both by indirect inhibition of the kinase responsible for this phosphorylation ($GSK3\beta$), and through mutation of the residue. Surprisingly, in spite of Myc-tFT possessing two fluorophores at its C-terminus, the region required for Myc-DNA binding, these did not inhibit binding ability, and Myc-tFT proved able to bind DNA at the promoter of a well-established Myc target and to execute its proliferation-promoting functions upon induction. Furthermore, Myc-tFT accumulation by $GSK3\beta$ inhibition in S-phase arrested cells led to apoptosis (**Figure 7.1**), a well-established effect of Myc accumulation in cells with intact pro-apoptotic responses (Murphy et al., 2008).

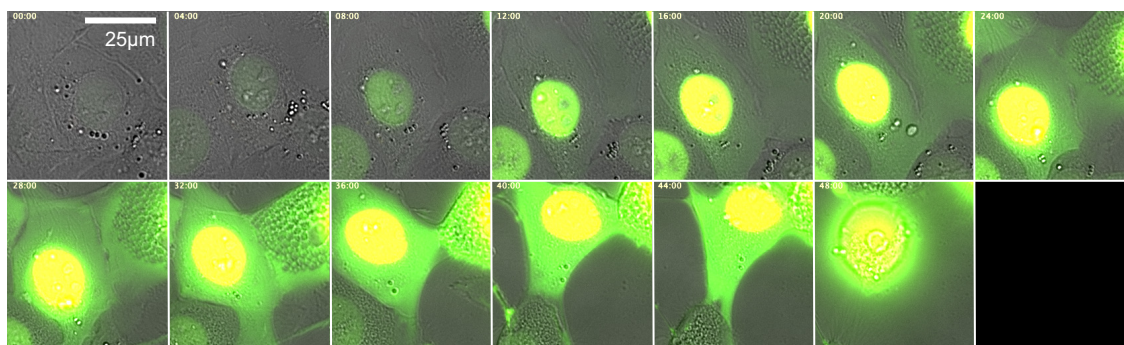


Figure 7.1: Inhibition of $GSK3\beta$ in S-phase arrested cells leads to Myc-tFT accumulation and apoptosis. Myc-tFT expressing U2OS cells arrested in S-phase were treated with $GSK3\beta$ inhibitor CHIR99021 ($Cf=3\mu M$), which lead to rapid increase in Myc-tFT levels and apoptosis.

Finally, Myc-tFT was adapted to a medium-throughput, semi-automated drug

7.1. Tandem Fluorescence Timers for studying Myc stability

screen and was challenged against industry standards for assay robustness and data quality. While the assay was able to report on changes in Myc stability, the variability in Myc-tFT ratios recorded impeded further use of the assay. The variability hindered not only whole-field analysis of Myc-tFT cells treated with drug compounds, but also single-cell analysis, making even qualitative data interpretation challenging.

7.1.2 Different methods for Myc-tFT assay image analysis

Image analysis is a crucial aspect of the Myc-tFT assay. In this work, two approaches to imaging and image analysis were taken: single time point and time-lapse imaging, manual and semi-automated analysis. Both image analysis modes have distinct advantages and disadvantages worth discussing.

7.1.2.1 Manual image analysis on ImageJ

Chapter 3 first described the use of a plug-in for ImageJ, designed by Andrew Ying, to track the changes in Myc-tFT levels and ratios through time and for measurement of images of cells from a single time-point. An advantage offered by this method is that it allows for manual selection of the cells in the imaged field to be analysed, allowing the exclusion of outliers from the image analysis. For example, cells with different morphology from the rest of the cell population (e.g. senescent or dying cells), cells where either or both FP signals were saturated, cells with tFT ratios above one but very low Myc-tFT expression, and cells with negative ratios due to a negative mCherry value, could all be excluded manually. This method for image analysis can be used to measure changes in Myc-tFT levels over time, as the user can accurately follow cells through time. Limitations of this method are that manual analysis can easily be biased by the user, if object selection isn't rigorous, but also it is very time consuming, especially in the case of time-resolved experiments, and, therefore, it is the rate-limiting step in the application of the Myc-tFT assay in house. For the experiments described in Chapters 5 and 6, in which individual cells are tracked through 48 to 96 hours, despite a large amount of imaging data being generated, it was only possible to analyse and interpret a portion of the data. Synchronisation of the oscillations greatly benefitted the

Chapter 7. General discussion and future perspectives

assay and an ROI the size of the field was used instead of the plug-in tool to measure changes in fluorescence at the level of the whole field. This greatly reduced the time required for image analysis and all gathered data was analysed.

7.1.2.2 Semi-automated image analysis on HCS studio

In Chapter 4 I showed that the assay could be adapted to a miniaturised and semi-automated imaging format. The assay was upscaled from 4 wells of an imaging dish to a 384-well plate which offered many advantages, primarily more opportunity for technical replicates. While the difference in the fluorescence levels of both FP between cells was at first problematic for segmentation and object identification, treatment of cells with Hoechst allowed for even segmentation of nuclei and offered a better segmentation of the nuclear area than that produced by the circular region of interest generated by the ImageJ plug-in. Additionally, integrating imaging optimisation into a semi-automated platform that simultaneously acquired images and applied image analysis parameters greatly improved the time required to set up and analyse a Myc-tFT assay experiment. Nonetheless, some issues with the semi-automated image analysis arose, specifically, the need for gating the Myc-tFT ratios to exclude the outliers described in the section above. While gating should not be an issue, but rather an opportunity to create a standard set of rules for data analysis to avoid user-bias, as data values are used to include/exclude cells rather than human decisions, and would allow multiple people to create identical results, a robust and reliable assay is needed for gating to work. In the case of the Myc-tFT assay, ratios below 0 were sometimes generated by the imaging software due to inappropriate selection of cells with a negative mCherry value that resulted from differences in background subtraction in areas with high levels of noise. Ratios above 1 were also excluded as these often arose from cells with very low levels of Myc-tFT expression that barely passed the threshold and that displayed higher fluorescence readings in the red than the green. Alternatively, cells in which either or both fluorescence channels were saturated would also result in ratios greater than 1 but this ratio did not accurately represent a measurement of stability. These cases, which are excluded by the user during the manual analysis, can be excluded in

7.1. Tandem Fluorescence Timers for studying Myc stability

the process of image analysis through gating the values, when single-cell analysis is used. However, gating resulted in underestimated effect of certain compounds. For example, the effects of KN-93 were even greater than those reported in the first screen (Chapter 4) when repeated and analysed by manual image analysis (Chapter 6). Where average readings from all cells in the well were taken, these cells that could provide inappropriate readings could not be excluded from analysis. It is important to note that the higher number of cells in the field and the technical replicates in the 384-well plate would contain enough cells to greatly outweigh any of these outliers. Finally, the lack of semi-automated method for single cell-tracking and analysis of time-lapse imaging experiments is another drawback. In Chapters 5 and 6, I described manual analysis of cells through time. For this I had to revert to manual analysis, partly due to a lack of access to AstraZeneca facilities during the COVID-19 pandemic, partly because tracking of individual cells through time is a process that is very difficult to automate. This was especially true for analysis of Myc-tFT levels in cells undergoing cell division. Additionally, since the semi-automated method relied heavily on nuclear segmentation by Hoechst, a DNA intercalating agent, repeated excitation of the Hoechst signal in a time-resolved set up would likely result in toxicity from DNA damage.

An ideal image analysis pipeline would allow for both snapshot analysis, like the HCS studio, and time-resolved analysis without the use of DNA markers. Machine learning approaches would greatly benefit time-lapse based studies as automated cell tracking and nuclear segmentation based on bright-field images would reduce image analysis time and user bias in selection of representative cells in the field. It would also allow for time-resolved analysis of evolving and differing cellular profiles which could then be synchronised and compared **in silico**.

7.2 A medium-throughput screen of modulators of Myc stability identified KN-93 as a positive modulator

In Chapter 4, I described the use of the Myc-tFT assay for a medium-throughput screen of compounds were already known to inhibit modulators of Myc stability, which demonstrated a strong positive modulation of Myc-tFT stability by CAMKII inhibitor KN-93. While this result was initially overshadowed by the issue of the variability in the assay, the effect was confirmed following circadian synchronisation, a condition in which the variability in the Myc-tFT ratio was improved. It is important to note that the effect was recorded and confirmed only by measuring the effect of KN-93 on Myc-tFT ratios, therefore, this should be confirmed by immunoblotting to verify if Myc-tFT accumulation is seen post KN-93 treatment and by CHX-chase experiments to measure changes in Myc-tFT half-life. The original report of CAMKII modulation described decreased Myc stability following inhibition of CAMKII with KN-93, which contrasts with the finding of this work. CAMKII is a signal-transducing kinase that is activated upon increased Ca^{2+} concentrations in the cytoplasm. It plays different roles in various tissues like the heart, where it couples excitation contraction and transcription of cardiomyocytes (Beckendorf, Hoogenhof, and Backs, 2018), in the brain, where it has been implicated in long-term potentiation and memory formation (Lisman, Yasuda, and Raghavachari, 2012), and in T cells activation (Lin et al., 2005). Gu et al. (2016) have also shown that CAMKII activation and overexpression promotes self-renewal of leukemia stem cells. Its role in osteosarcoma cells has not been described. The different cellular contexts in which these studies were undertaken (T-cell lymphoma and U2OS) could be contributing to the discrepancy. The work by Gu et al. (2017) reports that the destabilising effect that they encountered in their study was mediated by the γ isoform of the kinase. According to the Human Protein Atlas (<http://www.proteinatlas.org>) (Karlsson et al., 2021; Thul et al., 2017), low level expression of the α and β isoforms, and higher expression of the γ isoform can be found in U2OS. The latter is the more ubiquitously expressed isoform across cell lines. This suggests that if the KN-93 effect we consistently observed was in fact mediated by CAMKII inhibition, it would likely

7.2. A medium-throughput screen of modulators of Myc stability identified KN-93 as a positive modulator

be through the γ isoform. Based on the experiments carried out in T Cell lymphoma in the work by Gu et al. (2017), gene silencing and over-expression of CAMKII isoforms in U2OS cells expressing Myc-tFT should be performed to confirm whether CAMKII γ is indeed responsible for promoting the recorded stabilisation of Myc-tFT. The reported residue phosphorylated by CAMKII is S62, so inhibition of phosphorylation of this residue on Myc-tFT by KN-93 or by gene silencing of CAMKII γ should be confirmed in U2OS cells. It is important to note that the authors, in line with the current understanding of Myc regulation at the time of publishing, suggested that the pS62 positively stabilises Myc and proposed that CAMKII activity maintains high pS62 levels, concomitant or not with pT58, impeding dephosphorylation of the S residue and therefore, recognition of the single-phosphorylated T58 by FBW7. Recent findings by Welcker et al. (2022) show that pS62 and pT58 are recognised together by FBW7 and that indeed binding to the E3 ligase is increased by the double phosphorylation. Their data questions the stabilising effect of S62 phosphorylation via the FBW7 pathway and suggest that findings that claim that inhibition of pS62 destabilise Myc, report on FBW7-independent modulation of Myc. This opens a novel interpretation of our data. If KN-93 does indeed reduce the levels of pS62 Myc-tFT, which should be first confirmed, then this could be decreasing Myc-tFT binding to FBW7, therefore leading to its accumulation.

A role for CAMKII activity in circadian rhythm maintenance has been described in the SCN with kinase-dead mutant rats exhibiting reduced SCN clock stability under dark-dark cycles compared to WT mice. This was reflected in desynchronisation of PER2:LUC oscillations in the SCN slices of mutant CAMKII mice (Kon et al., 2014). Increasing concentrations of KN-93 were also shown to reduce the period in BMAL1:LUC reporter oscillations in rat fibroblasts, with oscillations nearly ablated at $10\mu\text{M}$ and lost at $20\mu\text{M}$ (Kon et al., 2015). The reduced variability in Myc-tFT ratios in synchronised cells treated with KN-93 could be due to synchronous oscillating activity of KN-93 post circadian synchronisation. In one of the replicates of the 30 hour treatment a portion of the cells appeared to be unaffected by the treatment with the inhibitor, possibly signalling cells at a different phase of the circadian cycle that would not have active

CAMKII to inhibit. Furthermore, KN-93's effect on Myc could be through inhibition of CAMKII-driven entrainment of Myc to the circadian rhythms. Time lapse-imaging experiments to evaluate the role of CAMKII on Myc-tFT oscillations should be carried out both by pharmacological inhibition of the kinase and gene silencing. If this were to result in ablation of the Myc-tFT oscillation it might lead to the stabilisation of Myc-tFT as reported by the increased ratio.

7.3 Time-resolved analysis of the Myc-tFT signal revealed oscillating Myc-tFT levels

Following the shortcoming of the Myc-tFT assay in the medium-throughput screen, the main focus of the project shifted towards identifying the source of the variability that was preventing successful interpretation of the assay data. Time-lapse imaging experiments were carried out to investigate how the Myc-tFT signal and ratio evolved over time. This investigation, the subject of Chapters 5 and 6, brought to light several aspects of Myc-tFT regulation that had not been considered previously.

7.3.1 Myc-tFT levels are regulated by a cell-autonomous process

Time-lapse imaging of unsynchronised and untreated U2OS FRT/TO Myc-tFT cells recapitulated the different Myc-tFT ratio within cells in the field that had been previously observed during the single-time point imaging procedures used for screening. It also revealed that Myc-tFT levels increase and decrease over the life-span of a cell, and often differed between daughter cells generating from the same cell division. Although this observation was not followed up in depth, it is worth discussing. Asymmetric distribution of Myc levels was described by Verbist et al. (2016) in activated T lymphocytes. Specifically, levels of a Myc-GFP knock in fusion were monitored after first and second cell division in activated T-cell lymphocytes. Myc-GFP levels diverged dramatically between the daughter cells in the first round of division, with the highest Myc-GFP levels present in the daughter cells expressing higher levels of CD8 and lower in the daughter cell expressing lower levels of CD8, a transmembrane glycoprotein

7.3. Time-resolved analysis of the Myc-tFT signal revealed oscillating Myc-tFT levels

that acts as a co-receptor of the T-cell receptor, and is a marker for asymmetric cell division in T-cells. This correlation was then lost in the second round of division. This asymmetric expression correlated with proximity to the antigen presenting cells, indeed the proximal daughter cell expressed high levels of CD8 and inherited higher levels of Myc-GFP. In this study, asymmetric cell division was inhibited by mTORC1 inhibition via rapamycin and TORin2 and by translational inhibition via cycloheximide. Inhibition of GSK3 β (via CHIR911), the proteasome (via MG132) and transcription (via actinomycin D) did not affect the asymmetric division of Myc between CD8 high or low cells. This supported a role for mTOR's translational regulation of Myc in Myc asymmetric regulation post cell division. The authors then proceeded to show that asymmetric segregation of Myc impacted the transcriptional profile and metabolic processes of the daughter cells, with increased glycolysis in Myc^{high} cells. Finally, Myc^{high} T cells *in vivo* proliferated faster than Myc^{low} cells which, contrarily showed slower proliferation upon primary immune response but persisted longer into the secondary immune response. While the work by Verbist et al. (2016) provides evidence for the role of Myc regulation in T cell activation and maturation, which is a different context to the one discussed in this dissertation, it also offered some insight into what could be regulating asymmetric regulation of Myc in our cells. In their work, the authors detail that Myc levels became asymmetric following cytokinesis and nuclear envelope reformation, suggesting that asymmetric division of Myc regulators between daughter cells could be responsible for the differing levels of Myc. This observation is unlikely to be true in the Myc-tFT context as the average half-life of Myc-tFT is less than 30 minutes, and circadian-dependent changes in Myc-tFT regulation are the major determinants of Myc-tFT levels in the cells. It is, therefore, more plausible, based on our findings, that the conditions in each daughter cell, perhaps involving differential entrainment of the circadian cycle, determine the level of expression of Myc-tFT achieved in each daughter cell following cell division. Having performed experiments with mTOR inhibitor TORin1, some preliminary information on the role of this enzyme on Myc-tFT asymmetric regulation could be drawn. As shown in **Figure 7.2**, TORin1 treatment did not appear to affect asymmetric regulation of Myc-tFT between daughter cells. This is a preliminary obser-

Chapter 7. General discussion and future perspectives

vation which should be scored over a greater number of cells to verify whether there is a reduction in asymmetric regulatory events. It is important to note that the work by Verbist et al. (2016) demonstrates that asymmetric Myc levels are maintained by translational processes downstream of mTOR, and not post-translational regulation. While translational regulation could be driving asymmetric Myc-tFT regulation, it is important to account for the differences between the two systems in which asymmetric regulation of Myc have been described. The Myc-tFT is over-expressed under a CMV promoter that drives expression of Myc's coding sequence. The system employed by Verbist et al. (2016) consists of a knock-in GFP system whereby Myc's endogenous promoter and UTRs are maintained in the fusion and, therefore, Myc-GFP is under the transcriptional and translational control of endogenous Myc. The work described in T cells shows clear implication of asymmetric regulation of Myc in generation of primary or secondary immune responses. While the reason for the effect of asymmetric division of Myc in U2OS might be unclear, this should be evaluated. Firstly, differing cell fates should be assessed and this would benefit from the identification of a marker for the asymmetric division. It is important to note that Myc-tFT is not static within daughter cells, but rather oscillates, suggesting that what is regulating this cell-autonomous asymmetric regulation of Myc is not cell cycle dependent. Like the paper described above, chemical or genetic perturbation should be carried out in the form of drug treatments or siRNAs to dissect the biological processes and key players that could be contributing to this phenomenon. Contributions of transcription and translation to asymmetric Myc-tFT division should be assessed. The use of cycloheximide and actinomycin D could be used as described above, however these treatments would cause cellular stress and apoptosis, affecting any possible observation in Myc regulation. High content automated imaging could be used to track daughter cells for cell fate and with other markers to elucidate this multi-factorial problem. The contribution of post-translational regulation should also be investigated by proteasomal inhibition, or silencing of known Myc regulators, such as GSK3 β and FBW7. Asymmetric division of Myc regulators, like GSK3 β , should be assessed, together with PTM state of Myc between daughter cells.

7.3. Time-resolved analysis of the Myc-tFT signal revealed oscillating Myc-tFT levels

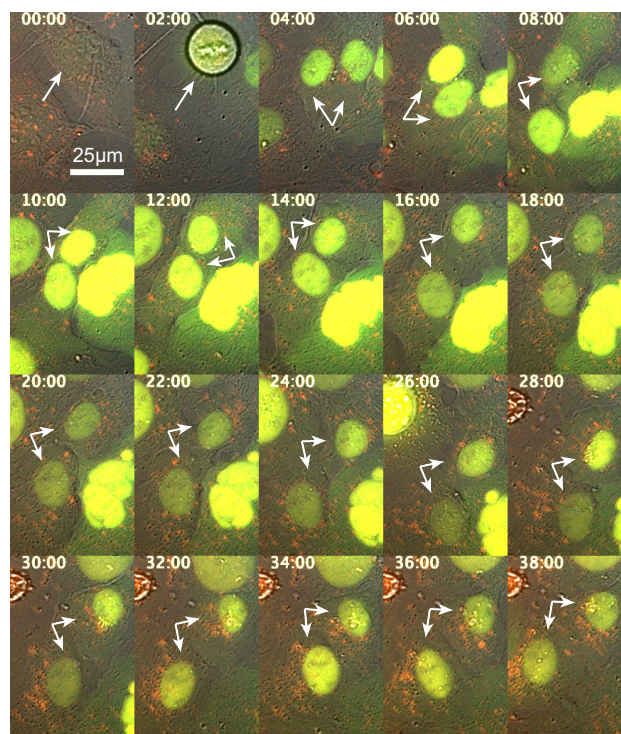


Figure 7.2: Inhibition of mTOR in unsynchronised cells does not impede asymmetric regulation of Myc-tFT between daughter cells. Myc-tFT expressing U2OS cells were treated with mTORC1 and 2 inhibitor TORin1 ($C_f=2.5\mu M$) and imaged over time. At 4 hours, daughter cells of a single division at 2 hours are indicated by arrows and in remaining frames.

Chapter 7. General discussion and future perspectives

Finally, Myc-tFT levels in S-phase arrested cells seemed to accumulate at different levels upon stabilisation by GSK3 β inhibition with CHIR99021. Indeed single cell traces revealed that most cells accumulated Myc before reaching a plateau state and undergoing apoptosis. This seems to suggest that oscillating of Myc-tFT levels can be tolerated by cells, and that GSK3 β inhibition, by blocking oscillations, drives Myc-tFT levels past the pro-apoptotic threshold of Myc. Murphy et al. (2008) described the ability of low levels of Myc to induce proliferation and prime cells for a pro-apoptotic response that can be triggered by other sub-apoptotic stimuli. Consequently, what might be determining the differing threshold of Myc-tFT levels reached by cells could be the amount of sub-apoptotic stimuli that the individual cells have already gathered. In this experimental setup, cells are arrested at the G1/S-phase by double thymidine block, which halts DNA replication, giving rise to sub-apoptotic lesions that could be co-operating with increasing Myc levels to yield apoptosis following Myc-tFT stabilisation. Importantly, while Myc-tFT is stabilised in unsynchronised cells treated with a GSK3 β inhibitor, this accumulation and cell death is not recorded within 36 hours from induction and treatment. In the same amount of time, S-phase arrested cells treated with the same inhibitor, at the same concentration, rapidly increase Myc-tFT levels and undergo apoptosis. This should be further investigated by looking at pro-apoptotic markers, such as DNA-damage markers, p19 and p53, in S-phase arrested cells treated with CHIR99021 to evaluate a correlation between these markers and the levels of Myc-tFT that individual cells reach.

Taking together the asymmetric regulation of Myc-tFT between daughter cells following cell division and the differential capacity for cells to accumulate Myc-tFT, we can conclude that there is a cell-autonomous process that is driving Myc-tFT regulation at the single cell level.

7.3.2 Oscillations in Myc-tFT levels are cell-cycle independent

The variability in Myc-tFT ratio was shown to derive from oscillations in Myc-tFT levels, most accurately reported by mNeonGreen fluorescence, which appeared to have a

7.3. Time-resolved analysis of the Myc-tFT signal revealed oscillating Myc-tFT levels

24 hour period. While some synchronisation in the oscillations can be attributed to induction of Myc-tFT by Doxycycline, the oscillations in unsynchronised cells remained largely unsynchronised. Having noted differential regulation of Myc-tFT between daughter cells, the cell cycle offered a candidate cell-autonomous process that could be regulating the oscillations in Myc-tFT levels. Myc-tFT oscillations were recorded in both dividing and non-dividing cells in unsynchronised imaging conditions, first suggesting that the cell cycle might not be the cell-autonomous driver for the oscillations. This observation was confirmed by arresting cells in late G2 and in G1/S-phase by CDK1 and DNA replication inhibition, respectively. Myc-tFT oscillations were neither abolished nor synchronised under these conditions, confirming that another cell-autonomous process was driving these oscillations. Furthermore, reduced translational rates resulting from mTOR inhibition did not abolish the oscillations. Conversely, modulation of Myc-tFT phosphorylation by GSK3 β inhibition and T58A mutation respectively resulted in Myc-tFT accumulation with abolishment of the oscillations and reduction of the oscillations by several folds of magnitude. These data preliminarily supports a key role of post-translational regulation of Myc in regulation of Myc-tFT oscillations.

7.3.3 Myc-tFT oscillations can be synchronised by circadian synchronisation

The circadian rhythm, another cell-autonomous process with 24 hour periodicity, offered an alternative biological process that could be regulating Myc oscillations. As described in the introduction to Chapter 6, the circadian rhythm is a process of timekeeping that in mammalian cells regulates biological processes to the day/night cycle. While the SCN directs and synchronises biological processes at the organism levels, individual cells have the intrinsic capacity for timekeeping. Circadian rhythm maintenance in individual cells has been largely attributed to the feedback loop consisting of the cycling of BMAL1-CLOCK levels and activity which drive the expression of their negative regulators, CRY and PER proteins, which in turn inhibit BMAL1-CLOCK activity, thereby rhythmically reducing their own expression. These cycles can be synchronised in cells presenting intact circadian rhythms by treatment with Dexamethasone or by growing cells under

Chapter 7. General discussion and future perspectives

cycling temperatures of 37°C and 32°C, alternating every 12 hours. U2OS cells, the cellular model used in this work, have been employed in circadian rhythm studies (Altman et al., 2015; Burke et al., 2015) and are reported to have intact circadian rhythms. On this premise, the contribution of circadian rhythms to Myc-tFT oscillations in U2OS cells was evaluated by harnessing both circadian synchronisation methods. Both synchronisation by Dexamethasone treatment and temperature cycling resulted in synchronisation of Myc-tFT oscillations at the population level, with temperature cycling resulting in a more robust synchronisation. Traces from single-cell and whole-field analysis were detrended by removal of the 24 hour rolling average, and curve fitting of a cosine curve was applied. This generated measurable values of period and amplitude which confirmed that Myc-tFT oscillations at the single-cell and population levels oscillated with a 24 hour periodicity, and illustrated that the amplitude of the oscillations decreased over time. It is worth noting that there is some variability in the amplitude of the Myc-tFT oscillations across imaging fields and experiments. While circadian synchronisation undoubtedly improved the variability in the Myc-tFT assay, reducing the variability in the amplitude would probably further reduce the variability in ratios.

Following synchronisation, oscillating levels of Myc-tFT in U2OS cells and endogenous Myc in A549 cells were measured by immunoblotting and compared to BMAL1 levels in the same extracts. While the immunoblotting data supports appropriate synchronisation of the TTFL as measured by oscillations in BMAL1 levels in our Myc-tFT expressing cells, no measured oscillations in PER2 mRNA levels were recorded. This could be due to Myc-tFT induction, as Myc has been shown to disrupt circadian rhythms (Altman et al., 2015; Altman et al., 2017), however the lack of a control without Myc-tFT induction renders this a hypothesis which should be confirmed. While work to generate U2OS FRT/TO Myc-tFT cells expressing bioluminescence reporters of TTFL activity was initiated, due to COVID-19 these were not validated in time to provide substantial proof of circadian integrity in our model, generating a substantial gap in our model. Future work should highly prioritise the validation of intact circadian rhythms in these cells and evaluate the impact of induction of the

7.3. Time-resolved analysis of the Myc-tFT signal revealed oscillating Myc-tFT levels

Myc stability sensor on the TTFL. Work by Altman et al. (2015) shows that active Myc-ER (treated with 4-hydroxytamoxifen) led to increased expression of circadian genes, and reduced oscillations in a BMAL1:Luc reporter. While they report that the oscillations are profoundly ablated by Myc activity, some degree of oscillation is still recorded so the oscillations might be dampened, instead of ablated, by Myc activity. Dampening of oscillations of circadian proteins has been reported in the context of disruption of the TTFL. Specifically, Putker et al. (2021) demonstrated that oscillations in TTFL activity as reported by a bioluminescence reporter of the *NR1D1* promoter (BMAL1), were greatly dampened but still intact following knockout of Cryptochrome with or without concomitant PER knock out. Therefore, CRY proteins play a central role in promoting oscillating TTFL activity, however they are not essential for the cell-intrinsic capacity of daily timekeeping. Consequently, it is plausible that Myc-ER activity reduced the amplitude of circadian rhythms by disrupting the TTFL. It is important to note that disruption of the TTFL does not abolish circadian rhythms, as postulated by the post-translational model of circadian rhythm maintenance (O'Neill, Maywood, and Hastings, 2013). Several studies implicate GSK3 and CK in regulating the activity of core clock components through PTM that support the TTFL in translating enzymatic timing cues in transcriptional response. These findings signal that an intact post-translational mechanism in cells lacking the canonical transcriptional feedback, which in wild-type cells confers robust circadian rhythmicity to PER levels, is sufficient to maintain cellular timekeeping. Oscillations in PER2 levels were affected by inhibition of GSK3 and CK in both WT and CRY-deficient mouse fibroblast, indicating that these kinases are involved in regulation of the post-translational rhythm reported by PER2 levels (Putker et al., 2021). It is, therefore, important to establish the role of Myc-tFT activity in regulating expression as well as activity of core clock genes like BMAL1 and PER2 in these cells and verify if Myc-tFT dampens the oscillations in the TTFL while retaining intact circadian rhythms. If this is indeed the case, then it is plausible that the proteostasis mechanisms that maintain circadian rhythms intact in the context of disrupted TTFL loops are also regulating Myc-tFT to generate the oscillations we recorded in this work. For this reason, the contribution of GSK3 β and CK to Myc-tFT

oscillations should be evaluated in parallel.

7.3.4 Post-translational regulation of Myc-tFT contributes to its oscillating levels

The contribution of protein synthesis and post-translational regulation to Myc-tFT oscillations was investigated in this study.

In the context of S-phase arrest, reduction in translation rates following mTOR inhibition with TORin did not result in abolition of the oscillations. This should be repeated in the context of circadian synchronisation, where the amplitude of the oscillations is likely to be diminished following TORin treatment. Contribution of transcription was evaluated by measurement of Myc-tFT mRNA levels over time in circadian synchronised cells. These data did not show oscillation in Myc-tFT mRNA. Transcriptional contribution to Myc-tFT oscillations could be further investigated by treating circadian-synchronised Myc-tFT expressing cells with a sub-saturating dose of Cycloheximide or switching to a TET-OFF system where addition of Doxycycline or tetracycline would yield repression of CMV-driven expression. This work should be performed in parallel to Systems Biology studies where changes to parameters of synthesis rates and degradation can be modelled and outcomes predicted.

Amplitude of Myc-tFT oscillation was altered in the context of non-phosphorylatable Myc T58A-tFT, where the amplitude decreased. The differences in Myc-tFT expression between WT and T58A mutants could account for the differing amplitude readings, however if the amplitude of the oscillations were linked to Myc-tFT expression levels, it would suggest Myc's transcriptional activity contributes to the generation and maintenance of the oscillations. This does not align with the findings that describe no effect of Myc-tFT inhibition on the period or amplitude of its oscillations. Cells expressing only the two FPs in tandem (tFT construct) also displayed oscillations. While this might suggest a circadian regulation of the proteome that is not specific to Myc, the increase in tFT oscillation period, which showed a 10 hour increase compared to those recorded in Myc-tFT, supported the need for post-translational regulation of Myc-tFT for robust oscillations. Furthermore, inhibition of GSK3 β with CHIR99021

7.3. Time-resolved analysis of the Myc-tFT signal revealed oscillating Myc-tFT levels

resulted in an increase in amplitude of circadian synchronised cells expressing cycling Myc-tFT, both WT and T58A. The initial hypothesis whereby phosphorylation of T58 by GSK3 β , a known regulator of Myc and contributor to post-translationally-driven circadian timekeeping, and consequent FBW7-mediated degradation of Myc would result in entrainment of Myc levels not to the cell-cycle but to the circadian cycle, was rejected. These results did not altogether negate the role of GSK3 β in Myc-tFT oscillation maintenance, but rather proposed an indirect modulation of Myc by the kinase. The recent identification of a second phosphodegron site in Myc (at residues T244 and T248) by Welcker et al. (2022) allowed us to reshape our hypothesis. In this study, the authors demonstrate that a second phosphodegron, also recognised by FBW7, was present. Interestingly, their data demonstrates that the role of the two phosphodegrons in mediating Myc-dependent degradation varies in the context of endogenous or over-expressed Myc. Specifically, FBW7 monomers can recognise either phosphodegron site, leading to ubiquitination and degradation of Myc. Indeed T58A, which had been previously reported as a version of Myc non-degradable by FBW7, was indeed bound and degraded by FBW7 when phosphorylation of T244 and T248 was in place. Conversely, in the context of endogenous Myc, both phosphodegrons are needed to allow FBW7 dimers to bind and degrade Myc. The authors do not investigate which kinases are responsible for the phosphorylation of priming T248 phosphorylation, which is analogous to the priming pS62, or the secondary phosphorylation at T244, which is essential for FBW7-mediated degradation in the context of T58A. Given that GSK3 most commonly targets the pre-phosphorylated sequence, S/T-X-X-X-S/T(P) (Beurel, Grieco, and Jope, 2015) (X is any amino acid), and that the T58 and T244 phosphodegron sites are similar (T58: TPPLSP; T244: TPPTTS), the kinase could be responsible for the phosphorylation of T244 post priming of pT248. To confirm this, phosphorylation state of T244 in WT and T58A Myc should first be investigated with and without concomitant inhibition of GSK3. Welcker et al. (2022) describe a novel antibody for detection of pT244. Since both WT and T58A mutant Myc-tFT display oscillatory behaviour, and their amplitude is affected by GSK3 β inhibition, there might be a role for modulation of T244 phosphorylation, perhaps by GSK3 β in the generating

Chapter 7. General discussion and future perspectives

the oscillations. A double mutant of Myc-tFT, T58A and T244A should be generated and its oscillations post-circadian synchronisation should be assessed. If the lack of double phosphorylation results in disruption of the oscillations then a role for FBW7-dependent degradation in timely cyclical degradation of Myc could be postulated. These data could then be confirmed by genetic silencing of FBW7 in a context of WT Myc-tFT. If T244 phosphorylation is indeed GSK3 β dependent and mutation of both phosphodegrons abolishes Myc-tFT oscillation then, this would confirm Myc entrainment to the circadian rhythms by GSK3-FBW7.

7.3.5 Circadian synchronisation reduced the variability in Myc-tFT ratios

The portion of this study that focussed on circadian-driven regulation of Myc stemmed from the need to identify the source of the variability in Myc-tFT ratios observed in the medium-throughput screen of modifiers of Myc stability. While the mechanism of circadian regulation of Myc-tFT remains unresolved and offers many interesting avenues of research, circadian synchronisation of U2OS FRT/TO Myc-tFT cells did indeed result in reduced variability in Myc-tFT signal. Unfortunately, I was not able to return to AstraZeneca and challenge the circadian synchronised Myc-tFT assay on the screening platform described in Chapter 4. However, using the imaging platform available in our lab, circadian synchronisation proved able to significantly reduce the variability in Myc-tFT ratio and reduced the Myc-tFT ratio values themselves in DMSO treated cells at two intervals 12 hours apart. While the measured variance decreased in synchronised cells and the Z-factor improved almost four-fold, the latter remained negative. Given the reduced amplitude in oscillations of the T58A version of the Myc-tFT construct, this might offer a better screening tool than WT Myc-tFT as it appeared to be a version of Myc that is less subject to the circadian cytoplasmic oscillator. If indeed the double T58A and T244A mutant were to show abolition of the oscillations, then this would offer another version of Myc for screening, as long as these PTMs don't overlap with those required in clinically relevant pathways. Considering FBW7 mutations occur in cancer to hinder its tumour suppressor activity, screening with versions of Myc that are resistant to FBW7 degradation might offer a disease-relevant screening approach.

7.4. Future work and concluding remarks

In order to satisfy the original aim of this work, the Myc-tFT assay could be performed in cell lines where there is no cytoplasmic oscillator. Cells without intact circadian rhythms might offer reduced variability in Myc-tFT readings. The state of circadian rhythms in these cell lines should be first verified using a *NR1D1:Luciferase* reporter and once this is confirmed Myc-tFT signal evolution should be evaluated. A Flp-In system could then be generated in any candidate cell lines as this offers the advantages of a switchable Myc system. For example, Flp-In T-REX HeLa and HEK293 exist and offer tetracycline-inducible systems. Modulation of candidate circadian regulators of Myc could be tested in both contexts of intact and non- circadian rhythms. Any hits derived from a screen of modulators of Myc stability in a context of disrupted circadian rhythms should be tested in U2OS FRT/TO Myc-tFT cells to investigate the effect of the modulation in a circadian context. Vulnerability to Myc modulation in both contexts would offer interesting insights and novel targeting approaches.

7.4 Future work and concluding remarks

The original aim of this work was to design an assay able to measure changes in Myc stability at the single-cell level. While this study was underway, Blake et al. (2019) described an alternative approach which consisted of Myc-GFP and DsRed generated from the same transcript but resulting in two separate proteins due to an IRES (internal ribosome entry site) site in between the two coding sequences. This approach was successful in identifying both positive and negative modulators of Myc stability in the context of KRAS-mutant pancreatic cancer. Based on the information gathered in our work, Blake's assay could be improved by switching the green FP from GFP to mNeonGreen, which does not stabilise Myc, and possibly making the assay more sensitive. The screening approach. used by (Blake et al., 2019) is FACS sorting but the assay described in their work, with some improvements, could also be applied for live cell imaging. DsRed, which has a reported maturation time of 1600 min (Lambert, 2019) could be substituted with another FP with faster maturation time (like mCherry), and an NLS sequence could be added to have co-localisation in the nucleus for ease of image analysis segmentation. Recently, HiBit assays have become a popular tool

Chapter 7. General discussion and future perspectives

for measuring modulation of protein levels, and more specifically degradation. This technique, developed by Promega, consists of tagging the POI with a HiBit - an 11 amino acid peptide that binds with high affinity to LgBiT, a larger subunit, obtaining luciferase activity when bound in complex (Schwinn et al., 2018). While this system is highly sensitive and well-suited for high-throughput screening, it does not offer snapshot information on protein stability, unlike the tFTs, but rather requires time-resolved data to obtain this information. Furthermore, it does not offer single-cell information so with this approach the cell-autonomous circadian regulation of Myc that is described in this work would not have come to light unless circadian synchronisation were applied.

During the course of this investigation the Myc stability sensor developed into a novel tool to study the relationship between Myc and the circadian rhythm. Some outstanding questions remain and should be addressed in future work. The consequence of oscillations in Myc and its entrainment to the circadian rhythm remain undefined. Time-course experiments to monitor the mRNA levels of Myc targets following circadian synchronisation could evaluate if Myc targets are consequently entrained. The phenotypic outcome of Myc oscillations and their disruption remain uncharacterised and would offer necessary information on the interplay between circadian rhythms and Myc. The sensitivity to Myc inhibition of cells that do and do not have intact circadian rhythms might be different, and this could offer a novel classification of tumour types which are more susceptible to Myc inhibition or targeted degradation. Furthermore, if circadian rhythms are intact, candidate modulators might not be exerting their effect on Myc directly, but rather indirectly through modulation of circadian processes.

Finally, unsynchronised oscillations (regardless of source) have the potential to confound efforts to develop and run medium- to high-throughput experiments in drug research (where protein levels are being measured), due to the miniaturisation, scale and robustness required in industry. For this reason, the impact of oscillating biological process should be accounted for in assay design. In the context of intact circadian rhythms, candidate molecules interfering with the circadian rhythm might exert indirect effects on Myc stability, and conversely, the cell autonomous oscillation

7.4. Future work and concluding remarks

in Myc might mask the effect of candidate molecules tested on an unsynchronized population of cells. My work, therefore, demonstrates that circadian synchronisation could be an important addition to screens for modulators of Myc stability, with the potential for identification of new candidate drugs.

Chapter 7. General discussion and future perspectives

References

- Adhikary, Sovana et al. (2005). "The ubiquitin ligase HectH9 regulates transcriptional activation by Myc and is essential for tumor cell proliferation." eng. In: *Cell* 123.3, pp. 409–421. ISSN: 0092-8674 (Print); 0092-8674 (Linking). DOI: 10.1016/j.cell.2005.08.016.
- Agarwal, Ekta et al. (2019). "Myc Regulation of a Mitochondrial Trafficking Network Mediates Tumor Cell Invasion and Metastasis". In: *Molecular and Cellular Biology* 39.14. ISSN: 0270-7306. DOI: 10.1128/MCB.00109-19. eprint: <https://mcb.asm.org/content/39/14/e00109-19.full.pdf>.
- Alber, Andrea Brigitta et al. (2018). "Single Live Cell Monitoring of Protein Turnover Reveals Intercellular Variability and Cell-Cycle Dependence of Degradation Rates". In: *Molecular Cell* 71.6, 1079–1091.e9. ISSN: 1097-2765. DOI: <https://doi.org/10.1016/j.molcel.2018.07.023>.
- Allen-Petersen, Brittany L. and Rosalie C. Sears (2019). "Mission Possible: Advances in MYC Therapeutic Targeting in Cancer". In: *BioDrugs* 33.5, pp. 539–553. DOI: 10.1007/s40259-019-00370-5.
- Altman, Brian J et al. (Dec. 2015). "MYC Disrupts the Circadian Clock and Metabolism in Cancer Cells". In: *Cell metabolism* 22.6, pp. 1009–1019. DOI: 10.1016/j.cmet.2015.09.003.
- Altman, Brian J. et al. (2017). "Correspondence: Oncogenic MYC persistently upregulates the molecular clock component REV-ERB α ". In: *Nature Communications* 8.1, p. 14862. DOI: 10.1038/ncomms14862.
- Amati, Bruno et al. (1992). "Transcriptional activation by the human c-Myc oncoprotein in yeast requires interaction with Max". In: *Nature* 359.6394, pp. 423–426. DOI: 10.1038/359423a0.
- Amati, Bruno et al. (1993). "Oncogenic activity of the c-Myc protein requires dimerization with Max". In: *Cell* 72.2, pp. 233–245. ISSN: 0092-8674. DOI: [https://doi.org/10.1016/0092-8674\(93\)90663-B](https://doi.org/10.1016/0092-8674(93)90663-B).
- Andrieu, Guillaume, Anna C Belkina, and Gerald V Denis (2016). "Clinical trials for BET inhibitors run ahead of the science." eng. In: *Drug Discov Today Technol* 19, pp. 45–50. ISSN: 1740-6749 (Electronic); 1740-6749 (Linking). DOI: 10.1016/j.ddtec.2016.06.004.
- Bahram, Fuad et al. (Mar. 2000). "c-Myc hot spot mutations in lymphomas result in inefficient ubiquitination and decreased proteasome-mediated turnover". In: *Blood* 95.6, pp. 2104–2110. ISSN: 0006-4971. DOI: 10.1182/blood.V95.6.2104. eprint: <https://ashpublications.org/blood/article-pdf/95/6/2104/1663256/2104.pdf>.
- Balleza, Enrique, J Mark Kim, and Philippe Cluzel (2018). "Systematic characterization of maturation time of fluorescent proteins in living cells." eng. In: *Nat Methods* 15.1, pp. 47–51. ISSN: 1548-7105 (Electronic); 1548-7091 (Print); 1548-7091 (Linking). DOI: 10.1038/nmeth.4509.
- Barry, Joseph D et al. (2016). "TimerQuant: a modelling approach to tandem fluorescent timer design and data interpretation for measuring protein turnover in embryos." eng. In: *Development* 143.1, pp. 174–179. ISSN: 1477-9129 (Electronic); 0950-1991 (Print); 0950-1991 (Linking). DOI: 10.1242/dev.125971.
- Bartolomé, Fernando and Andrey Y. Abramov (2015). "Measurement of Mitochondrial NADH and FAD Autofluorescence in Live Cells". In: *Mitochondrial Medicine: Volume I, Probing Mitochondrial Function*. Ed. by Volkmar Weissig and Marvin Edeas. New York, NY: Springer New York, pp. 263–270. ISBN: 978-1-4939-2257-4. DOI: 10.1007/978-1-4939-2257-4_{ }23.
- Baudino, Troy A. et al. (Oct. 2002). "c-Myc is essential for vasculogenesis and angiogenesis during development and tumor progression". In: *Genes & Development* 16.19, pp. 2530–2543.
- Beaulieu, Marie-Eve, Francisco Castillo, and Laura Soucek (2020). "Structural and Biophysical Insights into the Function of the Intrinsically Disordered Myc Oncoprotein." eng. In: *Cells* 9.4. ISSN: 2073-4409 (Electronic); 2073-4409 (Linking). DOI: 10.3390/cells9041038.
- Beckendorf, Jan, Maarten M G van den Hoogenhof, and Johannes Backs (2018). "Physiological and unappreciated roles of CaMKII in the heart." eng. In: *Basic Res Cardiol* 113.4, p. 29. ISSN: 1435-1803 (Electronic); 0300-8428 (Print); 0300-8428 (Linking). DOI: 10.1007/s00395-018-0688-8.
- Beer, Shelly et al. (Sept. 2004). "Developmental Context Determines Latency of MYC-Induced Tumorigenesis". In: *PLOS Biology* 2.11. DOI: 10.1371/journal.pbio.0020332.
- Beijersbergen, R.L. et al. (1994). "Interaction of c-Myc with the pRb-related protein p107 results in inhibition of c-Myc-mediated transactivation." In: *The EMBO Journal* 13.17, pp. 4080–4086. DOI: 10.1002/j.1460-

References

- 2075.1994.tb06725.x. eprint: <https://www.embopress.org/doi/pdf/10.1002/j.1460-2075.1994.tb06725.x>.
- Beurel, Eleonore, Steven F. Grieco, and Richard S. Jope (2015). "Glycogen synthase kinase-3 (GSK3): Regulation, actions, and diseases". In: *Pharmacology Therapeutics* 148, pp. 114–131. issn: 0163-7258. doi: <https://doi.org/10.1016/j.pharmthera.2014.11.016>.
- Blake, Devon R et al. (2019). "Application of a MYC degradation screen identifies sensitivity to CDK9 inhibitors in KRAS-mutant pancreatic cancer." eng. In: *Sci Signal* 12.590. issn: 1937-9145 (Electronic); 1945-0877 (Print); 1945-0877 (Linking). doi: 10.1126/scisignal.aav7259.
- Bouchard, Caroline et al. (Aug. 2001). "Regulation of cyclin D2 gene expression by the Myc/Max/Mad network: Myc-dependent TRRAP recruitment and histone acetylation at the cyclin D2 promoter". In: *Genes & Development* 15.16, pp. 2042–2047.
- Brockmann, Markus et al. (2013). "Small Molecule Inhibitors of Aurora-A Induce Proteasomal Degradation of N-Myc in Childhood Neuroblastoma". In: *Cancer Cell* 24.1, pp. 75–89. issn: 1535-6108. doi: <https://doi.org/10.1016/j.ccr.2013.05.005>.
- Brooks, Tracy A. and Laurence H. Hurley (2010). "Targeting MYC Expression through G-Quadruplexes". In: *Genes & Cancer* 1.6. PMID: 21113409, pp. 641–649. doi: 10.1177/1947601910377493. eprint: <https://doi.org/10.1177/1947601910377493>.
- Burchett, Jamison B., Amelia M. Knudsen-Clark, and Brian J. Altman (2021). "MYC Ran Up the Clock: The Complex Interplay between MYC and the Molecular Circadian Clock in Cancer". In: *International Journal of Molecular Sciences* 22.14. issn: 1422-0067. doi: 10.3390/ijms22147761.
- Burke, Tina M. et al. (2015). "Effects of caffeine on the human circadian clock in vivo and in vitro". In: *Science Translational Medicine* 7.305, 305ra146–305ra146. doi: 10.1126/scitranslmed.aac5125. eprint: <https://www.science.org/doi/pdf/10.1126/scitranslmed.aac5125>.
- Campaner, Stefano et al. (2010). "Cdk2 suppresses cellular senescence induced by the c-myc oncogene." eng. In: *Nat Cell Biol* 12.1, pp. 54–59. issn: 1476-4679 (Electronic); 1465-7392 (Linking). doi: 10.1038/ncb2004.
- Campbell, Kirsteen J and Robert J White (2014). "MYC regulation of cell growth through control of transcription by RNA polymerases I and III." eng. In: *Cold Spring Harb Perspect Med* 4.5. issn: 2157-1422 (Electronic); 2157-1422 (Linking). doi: 10.1101/cshperspect.a018408.
- Cancer - NHS (2019).
- Carroll, Patrick A. et al. (2018). "The MYC transcription factor network: balancing metabolism, proliferation and oncogenesis". In: *Frontiers of Medicine* 12.4, pp. 412–425. doi: 10.1007/s11684-018-0650-z.
- Casey, Stephanie C., Virginie Baylot, and Dean W. Felsher (2017). "MYC: Master Regulator of Immune Privilege". In: *Trends in Immunology* 38.4, pp. 298–305. issn: 1471-4906. doi: <https://doi.org/10.1016/j.it.2017.01.002>.
- Casey, Stephanie C. et al. (2016). "MYC regulates the antitumor immune response through CD47 and PD-L1". In: *Science* 352.6282, pp. 227–231. issn: 0036-8075. doi: 10.1126/science.aac9935. eprint: <https://science.sciencemag.org/content/352/6282/227.full.pdf>.
- Cerni, Christa (2000). "Telomeres, telomerase, and myc. An update". In: *Mutation Research/Reviews in Mutation Research* 462.1, pp. 31–47. issn: 1383-5742. doi: [https://doi.org/10.1016/S1383-5742\(99\)00091-5](https://doi.org/10.1016/S1383-5742(99)00091-5).
- Chang, Kyle et al. (2013). "The Cancer Genome Atlas Pan-Cancer analysis project". In: *Nature Genetics* 45.10, pp. 1113–1120. doi: 10.1038/ng.2764.
- Chen, Chang-Rung, Yibin Kang, and Joan Massagué (2001). "Defective repression of c-myc in breast cancer cells: A loss at the core of the transforming growth factor β growth arrest program". In: *Proceedings of the National Academy of Sciences* 98.3, pp. 992–999. issn: 0027-8424. doi: 10.1073/pnas.98.3.992. eprint: <https://www.pnas.org/content/98/3/992.full.pdf>.
- Cho, Chun-Seok et al. (2014). "Circadian rhythm of hyperoxidized peroxiredoxin II is determined by hemoglobin autoxidation and the 20S proteasome in red blood cells". In: *Proceedings of the National Academy of Sciences* 111.33, pp. 12043–12048. doi: 10.1073/pnas.1401100111. eprint: <https://www.pnas.org/doi/pdf/10.1073/pnas.1401100111>.
- Cianfanelli, Valentina et al. (2015). "AMBRA1 links autophagy to cell proliferation and tumorigenesis by promoting c-Myc dephosphorylation and degradation". In: *Nature Cell Biology* 17.1, pp. 20–30. doi: 10.1038/ncb3072.
- Cichon, Magdalena A. et al. (2016). "MYC Is a Crucial Mediator of TGF β -Induced Invasion in Basal Breast Cancer". In: *Cancer Research* 76.12, pp. 3520–3530. issn: 0008-5472. doi: 10.1158/0008-5472.CAN-15-3465. eprint: <https://cancerres.aacrjournals.org/content/76/12/3520.full.pdf>.
- Ciehanover, A, Y Hod, and A Hershko (1978). "A heat-stable polypeptide component of an ATP-dependent proteolytic system from reticulocytes." eng. In: *Biochem Biophys Res Commun* 81.4, pp. 1100–1105. issn: 0006-291X (Print); 0006-291X (Linking). doi: 10.1016/0006-291x(78)91249-4.

References

- Clausen, Lene et al. (2019). "Protein stability and degradation in health and disease." eng. In: *Adv Protein Chem Struct Biol* 114, pp. 61–83. issn: 1876-1631 (Electronic); 1876-1623 (Linking). doi: 10.1016/bs.apcsb.2018.09.002.
- Cole, Nelson B. (2013). "Site-Specific Protein Labeling with SNAP-Tags". In: *Current Protocols in Protein Science* 73.1, pp. 30.1.1–30.1.16. doi: 10.1002/0471140864.ps3001s73. eprint: <https://currentprotocols.onlinelibrary.wiley.com/doi/pdf/10.1002/0471140864.ps3001s73>.
- Conacci-Sorrell, Maralice, Lisa McFerrin, and Robert N. Eisenman (Jan. 2014). "An Overview of MYC and Its Interactome". In: *Cold Spring Harbor Perspectives in Medicine* 4.1.
- Conacci-Sorrell, Maralice, Celine Ngouenet, and Robert N. Eisenman (2010). "Myc-Nick: A Cytoplasmic Cleavage Product of Myc that Promotes α -Tubulin Acetylation and Cell Differentiation". In: *Cell* 142.3, pp. 480–493. issn: 0092-8674. doi: <https://doi.org/10.1016/j.cell.2010.06.037>.
- Csibi, Alfredo et al. (2014). "The mTORC1/S6K1 Pathway Regulates Glutamine Metabolism through the eIF4B-Dependent Control of c-Myc Translation". In: *Current Biology* 24.19, pp. 2274–2280. issn: 0960-9822. doi: <https://doi.org/10.1016/j.cub.2014.08.007>.
- Dang, Chi V. (2012). "MYC on the Path to Cancer". In: *Cell* 149.1, pp. 22–35. issn: 0092-8674. doi: <https://doi.org/10.1016/j.cell.2012.03.003>.
- Dang, Chi V. et al. (2017). "Drugging the 'undruggable' cancer targets". In: *Nature Reviews Cancer* 17.8, pp. 502–508. doi: 10.1038/nrc.2017.36.
- Dauch, Daniel et al. (2016). "A MYC–aurora kinase A protein complex represents an actionable drug target in p53-altered liver cancer". In: *Nature Medicine* 22.7, pp. 744–753. doi: 10.1038/nm.4107.
- Delmore, Jake E et al. (2011). "BET bromodomain inhibition as a therapeutic strategy to target c-Myc." eng. In: *Cell* 146.6, pp. 904–917. issn: 1097-4172 (Electronic); 0092-8674 (Print); 0092-8674 (Linking). doi: 10.1016/j.cell.2011.08.017.
- Delpuech, Oona et al. (2007). "Induction of Mxi1-SR α by FOXO3a Contributes to Repression of Myc-Dependent Gene Expression". In: *Molecular and Cellular Biology* 27.13, pp. 4917–4930. issn: 0270-7306. doi: 10.1128/MCB.01789-06. eprint: <https://mcb.asm.org/content/27/13/4917.full.pdf>.
- Deribe, Yonathan Lissanu, Tony Pawson, and Ivan Dikic (2010). "Post-translational modifications in signal integration." eng. In: *Nat Struct Mol Biol* 17.6, pp. 666–672. issn: 1545-9985 (Electronic); 1545-9985 (Linking). doi: 10.1038/nsmb.1842.
- Dominguez-Sola, David and Jean Gautier (June 2014). "MYC and the Control of DNA Replication". In: *Cold Spring Harbor Perspectives in Medicine* 4.6.
- Donà, Erika et al. (2013). "Directional tissue migration through a self-generated chemokine gradient." eng. In: *Nature* 503.7475, pp. 285–289. issn: 1476-4687 (Electronic); 0028-0836 (Linking). doi: 10.1038/nature12635.
- Dong, Peng et al. (2014). "Division of labour between Myc and G1 cyclins in cell cycle commitment and pace control". In: *Nature Communications* 5.1, p. 4750. doi: 10.1038/ncomms5750.
- Drygin, Denis et al. (2008). "Quarfloxin (CX-3543) disrupts the Nucleolin/ rDNA quadruplex complexes, inhibits the elongation by RNA Polymerase I and exhibits potent antitumor activity in models of cancer". In: *Cancer Research* 68.9 Supplement, pp. 3301–3301. issn: 0008-5472. eprint: <https://cancerres.aacrjournals.org/content>.
- Duesberg, P H, K Bister, and P K Vogt (1977). "The RNA of avian acute leukemia virus MC29." In: *Proceedings of the National Academy of Sciences* 74.10, pp. 4320–4324. issn: 0027-8424. doi: 10.1073/pnas.74.10.4320. eprint: <https://www.pnas.org/content/74/10/4320.full.pdf>.
- Eden, Eran et al. (2011). "Proteome Half-Life Dynamics in Living Human Cells". In: *Science* 331.6018, pp. 764–768. issn: 0036-8075. doi: 10.1126/science.1199784. eprint: <https://science.sciencemag.org/content/331/6018/764.full.pdf>.
- Eldeeb, Mohamed A. et al. (2019). "A molecular toolbox for studying protein degradation in mammalian cells". In: *Journal of Neurochemistry* 151.4, pp. 520–533. doi: 10.1111/jnc.14838. eprint: <https://onlinelibrary.wiley.com/doi/pdf/10.1111/jnc.14838>.
- Evan, Gerard I. et al. (1992). "Induction of apoptosis in fibroblasts by c-myc protein". In: *Cell* 69.1, pp. 119–128. issn: 0092-8674. doi: [https://doi.org/10.1016/0092-8674\(92\)90123-T](https://doi.org/10.1016/0092-8674(92)90123-T).
- Felsher, Dean W. and J. Michael Bishop (1999). "Reversible Tumorigenesis by MYC in Hematopoietic Lineages". In: *Molecular Cell* 4.2, pp. 199–207. issn: 1097-2765. doi: [https://doi.org/10.1016/S1097-2765\(00\)80367-6](https://doi.org/10.1016/S1097-2765(00)80367-6).
- Felsher, Dean W. et al. (2000). "Overexpression of MYC causes p53-dependent G2 arrest of normal fibroblasts". In: *Proceedings of the National Academy of Sciences* 97.19, pp. 10544–10548. issn: 0027-8424. doi: 10.1073/pnas.190327097. eprint: <https://www.pnas.org/content/97/19/10544.full.pdf>.
- Foley, Kevin P and Robert N Eisenman (1999). "Two MAD tails: what the recent knockouts of Mad1 and Mxi1 tell us about the MYC/MAX/MAD network". In: *Biochimica et Biophysica Acta (BBA) - Reviews on Cancer* 1423.3, pp. M37–M47. issn: 0304-419X. doi: [https://doi.org/10.1016/S0304-419X\(99\)00012-8](https://doi.org/10.1016/S0304-419X(99)00012-8).

References

- Gabay, Meital, Yulin Li, and Dean W. Felsner (June 2014). "MYC Activation Is a Hallmark of Cancer Initiation and Maintenance". In: *Cold Spring Harbor Perspectives in Medicine* 4.6. DOI: 10.1101/cshperspect.a014241.
- Gautier, Arnaud et al. (2008). "An Engineered Protein Tag for Multiprotein Labeling in Living Cells". In: *Chemistry Biology* 15.2, pp. 128–136. ISSN: 1074-5521. DOI: <https://doi.org/10.1016/j.chembiol.2008.01.007>.
- Giardino Torchia, Maria Letizia and Jonathan D. Ashwell (Oct. 2018). "Getting MAD at MYC". In: *Proceedings of the National Academy of Sciences* 115.40, p. 9821. DOI: 10.1073/pnas.1813867115.
- Gouw, Marc et al. (Nov. 2017). "The eukaryotic linear motif resource – 2018 update". In: *Nucleic Acids Research* 46.D1, pp. D428–D434. ISSN: 0305-1048. DOI: 10.1093/nar/gkx1077. eprint: <https://academic.oup.com/nar/article-pdf/46/D1/D428/23162234/gkx1077.pdf>.
- Grandori, Carla et al. (2000). "The Myc/Max/Mad Network and the Transcriptional Control of Cell Behavior". In: *Annual Review of Cell and Developmental Biology* 16.1. PMID: 11031250, pp. 653–699. DOI: 10.1146/annurev.cellbio.16.1.653. eprint: <https://doi.org/10.1146/annurev.cellbio.16.1.653>.
- Gregory, Mark A. and Stephen R. Hann (2000). "c-Myc Proteolysis by the Ubiquitin-Proteasome Pathway: Stabilization of c-Myc in Burkitt's Lymphoma Cells". In: *Molecular and Cellular Biology* 20.7, pp. 2423–2435. ISSN: 0270-7306. DOI: 10.1128/MCB.20.7.2423-2435.2000. eprint: <https://mcb.asm.org/content/20/7/2423.full.pdf>.
- Gregory, Mark A., Ying Qi, and Stephen R. Hann (2003). "Phosphorylation by Glycogen Synthase Kinase-3 Controls c-Myc Proteolysis and Subnuclear Localization". In: *Journal of Biological Chemistry* 278.51, pp. 51606–51612. DOI: 10.1074/jbc.M310722200.
- Gu, Y. et al. (2016). "Aberrant activation of CaMKII γ accelerates chronic myeloid leukemia blast crisis". In: *Leukemia* 30.6, pp. 1282–1289. DOI: 10.1038/leu.2016.53.
- Gu, Ying et al. (2017). "Stabilization of the c-Myc Protein by CAMKII γ Promotes T Cell Lymphoma." eng. In: *Cancer Cell* 32.1, pp. 115–128. ISSN: 1878-3686 (Electronic); 1535-6108 (Print); 1535-6108 (Linking). DOI: 10.1016/j.ccell.2017.06.001.
- Han, Huiying et al. (2019). "Small-Molecule MYC Inhibitors Suppress Tumor Growth and Enhance Immunotherapy". In: *Cancer Cell* 36.5, 483–497. ISSN: 1535-6108. DOI: <https://doi.org/10.1016/j.ccell.2019.10.001>.
- Hanahan, Douglas and Robert A Weinberg (2000). "The Hallmarks of Cancer". In: *Cell* 100.1, pp. 57–70. ISSN: 0092-8674. DOI: [https://doi.org/10.1016/S0092-8674\(00\)81683-9](https://doi.org/10.1016/S0092-8674(00)81683-9).
- Hanahan, Douglas and Robert A. Weinberg (2011). "Hallmarks of Cancer: The Next Generation". In: *Cell* 144.5, pp. 646–674. ISSN: 0092-8674. DOI: <https://doi.org/10.1016/j.cell.2011.02.013>.
- Hart, Jonathan R et al. (2014). "Inhibitor of MYC identified in a Kröhnke pyridine library." eng. In: *Proc Natl Acad Sci U S A* 111.34, pp. 12556–12561. ISSN: 1091-6490 (Electronic); 0027-8424 (Print); 0027-8424 (Linking). DOI: 10.1073/pnas.1319488111.
- Hartl, F. Ulrich, Andreas Bracher, and Manajit Hayer-Hartl (2011). "Molecular chaperones in protein folding and proteostasis". In: *Nature* 475.7356, pp. 324–332. DOI: 10.1038/nature10317.
- Hashiguchi, Taylor et al. (2019). "Cyclin-Dependent Kinase-9 Is a Therapeutic Target in MYC-Expressing Diffuse Large B-Cell Lymphoma." eng. In: *Mol Cancer Ther* 18.9, pp. 1520–1532. ISSN: 1538-8514 (Electronic); 1535-7163 (Linking). DOI: 10.1158/1535-7163.MCT-18-1023.
- Hayes, Tikvah K. et al. (2016). "Long-Term ERK Inhibition in KRAS-Mutant Pancreatic Cancer Is Associated with MYC Degradation and Senescence-like Growth Suppression". In: *Cancer Cell* 29.1, pp. 75–89. ISSN: 1535-6108. DOI: <https://doi.org/10.1016/j.ccell.2015.11.011>.
- Hermeking, Heiko et al. (2000). "Identification of CDK4 as a target of c-MYC". In: *Proceedings of the National Academy of Sciences* 97.5, pp. 2229–2234. ISSN: 0027-8424. DOI: 10.1073/pnas.050586197. eprint: <https://www.pnas.org/content/97/5/2229.full.pdf>.
- Hershko, A, A Ciechanover, and I A Rose (1979). "Resolution of the ATP-dependent proteolytic system from reticulocytes: a component that interacts with ATP." eng. In: *Proc Natl Acad Sci U S A* 76.7, pp. 3107–3110. ISSN: 0027-8424 (Print); 1091-6490 (Electronic); 0027-8424 (Linking). DOI: 10.1073/pnas.76.7.3107.
- Hershko, A et al. (1980). "Proposed role of ATP in protein breakdown: conjugation of protein with multiple chains of the polypeptide of ATP-dependent proteolysis." eng. In: *Proc Natl Acad Sci U S A* 77.4, pp. 1783–1786. ISSN: 0027-8424 (Print); 1091-6490 (Electronic); 0027-8424 (Linking). DOI: 10.1073/pnas.77.4.1783.
- Hsieh, Annie L and Chi V Dang (2016). "MYC, Metabolic Synthetic Lethality, and Cancer." eng. In: *Recent Results Cancer Res* 207, pp. 73–91. ISSN: 0080-0015 (Print); 0080-0015 (Linking). DOI: 10.1007/978-3-319-42118-6_{_}4.
- Hu, Min et al. (2005). "Structure and mechanisms of the proteasome-associated deubiquitinating enzyme USP14". In: *The EMBO Journal* 24.21, pp. 3747–3756. DOI: <https://doi.org/10.1038/sj.emboj.7600832>. eprint: <https://www.embopress.org/doi/pdf/10.1038/sj.emboj.7600832>.

References

- Huber, Anne-Laure et al. (2016). "CRY2 and FBXL3 Cooperatively Degrade c-MYC". In: *Molecular Cell* 64.4, pp. 774–789. doi: 10.1016/j.molcel.2016.10.012.
- Huynh, Hung et al. (2003). "Over-expression of the mitogen-activated protein kinase (MAPK) kinase (MEK)-MAPK in hepatocellular carcinoma: Its role in tumor progression and apoptosis". In: *BMC Gastroenterology* 3.1, p. 19. doi: 10.1186/1471-230X-3-19.
- Hydbring, Per et al. (2010). "Phosphorylation by Cdk2 is required for Myc to repress Ras-induced senescence in cotransformation." eng. In: *Proc Natl Acad Sci U S A* 107.1, pp. 58–63. issn: 1091-6490 (Electronic); 0027-8424 (Print); 0027-8424 (Linking). doi: 10.1073/pnas.0900121106.
- Jensen, Kim Steen et al. (2011). "FoxO3A promotes metabolic adaptation to hypoxia by antagonizing Myc function". In: *The EMBO Journal* 30.22, pp. 4554–4570. doi: 10.1038/emboj.2011.323. eprint: <https://www.embopress.org/doi/pdf/10.1038/emboj.2011.323>.
- Jiang, Hao et al. (2009). "Stabilizers of the Max homodimer identified in virtual ligand screening inhibit Myc function." eng. In: *Mol Pharmacol* 76.3, pp. 491–502. issn: 1521-0111 (Electronic); 0026-895X (Print); 0026-895X (Linking). doi: 10.1124/mol.109.054858.
- Jung, Kwan-Young et al. (2015). "Perturbation of the c-Myc-Max protein-protein interaction via synthetic α -helix mimetics." eng. In: *J Med Chem* 58.7, pp. 3002–3024. issn: 1520-4804 (Electronic); 0022-2623 (Print); 0022-2623 (Linking). doi: 10.1021/jm501440q.
- Karlsson, Max et al. (2021). "A single-cell type transcriptomics map of human tissues". In: *Science Advances* 7.31, eabh2169. doi: 10.1126/sciadv.abh2169. eprint: <https://www.science.org/doi/pdf/10.1126/sciadv.abh2169>.
- Kato, G J et al. (1990). "An amino-terminal c-myc domain required for neoplastic transformation activates transcription." In: *Molecular and Cellular Biology* 10.11, pp. 5914–5920. issn: 0270-7306. doi: 10.1128/MCB.10.11.5914. eprint: <https://mcb.asm.org/content/10/11/5914.full.pdf>.
- Keppeler, Antje et al. (2003). "A general method for the covalent labeling of fusion proteins with small molecules in vivo". In: *Nature Biotechnology* 21.1, pp. 86–89. doi: 10.1038/nbt765.
- Khmelniskii, Anton et al. (2012). "Tandem fluorescent protein timers for in vivo analysis of protein dynamics". In: *Nature Biotechnology* 30.7, pp. 708–714. doi: 10.1038/nbt.2281.
- Khmelniskii, Anton et al. (2016). "Incomplete proteasomal degradation of green fluorescent proteins in the context of tandem fluorescent protein timers". In: *Molecular Biology of the Cell* 27.2. PMID: 26609072, pp. 360–370. doi: 10.1091/mbc.e15-07-0525. eprint: <https://doi.org/10.1091/mbc.e15-07-0525>.
- Kim, So Young et al. (2003). "Skp2 regulates Myc protein stability and activity." eng. In: *Mol Cell* 11.5, pp. 1177–1188. issn: 1097-2765 (Print); 1097-2765 (Linking). doi: 10.1016/s1097-2765(03)00173-4.
- Kon, Naohiro et al. (May 2014). "CaMKII is essential for the cellular clock and coupling between morning and evening behavioral rhythms". In: *Genes & Development* 28.10, pp. 1101–1110. doi: 10.1101/gad.237511.114.
- Kon, Naohiro et al. (July 2015). "Cell-based inhibitor screening identifies multiple protein kinases important for circadian clock oscillations". In: *Communicative & Integrative Biology* 8.4, e982405. doi: 10.4161/19420889.2014.982405.
- Kortlever, Roderik M. et al. (2017). "Myc Cooperates with Ras by Programming Inflammation and Immune Suppression". In: *Cell* 171.6, 1301–1315.e14. issn: 0092-8674. doi: <https://doi.org/10.1016/j.cell.2017.11.013>.
- Koulich, Elena, Xiaohua Li, and George N. DeMartino (2007). "Relative Structural and Functional Roles of Multiple Ubiquitylating Proteins Associated with Mammalian 26S Proteasome". In: *Molecular Biology of the Cell* 19.3, pp. 1072–1082. doi: 10.1091/mbc.e07-10-1040.
- Lambert, Talley J. (2019). "FPbase: a community-editable fluorescent protein database". In: *Nature Methods* 16.4, pp. 277–278. doi: 10.1038/s41592-019-0352-8.
- Lancho, Olga and Daniel Herranz (2018). "The MYC Enhancer-ome: Long-Range Transcriptional Regulation of MYC in Cancer". In: *Trends in Cancer* 4.12, pp. 810–822. issn: 2405-8033. doi: <https://doi.org/10.1016/j.trecan.2018.10.003>.
- Li, Lian et al. (2016). "Time-staggered delivery of docetaxel and H1-S6A,F8A peptide for sequential dual-strike chemotherapy through tumor priming and nuclear targeting." eng. In: *J Control Release* 232, pp. 62–74. issn: 1873-4995 (Electronic); 0168-3659 (Linking). doi: 10.1016/j.jconrel.2016.04.021.
- Lin, Meei Yun et al. (2005). "A Pivotal Role for the Multifunctional Calcium/Calmodulin-Dependent Protein Kinase II in T Cells: From Activation to Unresponsiveness". In: *The Journal of Immunology* 174.9, pp. 5583–5592. issn: 0022-1767. doi: 10.4049/jimmunol.174.9.5583. eprint: <https://www.jimmunol.org/content/174/9/5583.full.pdf>.
- Lindon, Catherine (2008). "Control of mitotic exit and cytokinesis by the APC/C." eng. In: *Biochem Soc Trans* 36.Pt 3, pp. 405–410. issn: 0300-5127 (Print); 0300-5127 (Linking). doi: 10.1042/BST0360405.
- Lindon, Catherine, Rhys Grant, and Mingwei Min (2015). "Ubiquitin-Mediated Degradation of Aurora Kinases." eng. In: *Front Oncol* 5, p. 307. issn: 2234-943X (Print); 2234-943X (Electronic); 2234-943X (Linking). doi: 10.3389/fonc.2015.00307.

References

- Lindquist, Susan L and Jeffery W Kelly (2011). "Chemical and biological approaches for adapting proteostasis to ameliorate protein misfolding and aggregation diseases: progress and prognosis." eng. In: *Cold Spring Harb Perspect Biol* 3.12. ISSN: 1943-0264 (Electronic); 1943-0264 (Linking). doi: 10.1101/cshperspect.a004507.
- Lisman, John, Ryohei Yasuda, and Sridhar Raghavachari (2012). "Mechanisms of CaMKII action in long-term potentiation." eng. In: *Nat Rev Neurosci* 13.3, pp. 169–182. ISSN: 1471-0048 (Electronic); 1471-003X (Print); 1471-003X (Linking). doi: 10.1038/nrn3192.
- Liu, Hong et al. (2012). "MYC suppresses cancer metastasis by direct transcriptional silencing of αv and $\beta 3$ integrin subunits". In: *Nature Cell Biology* 14.6, pp. 567–574. doi: 10.1038/ncb2491.
- Ma, Li et al. (2010). "miR-9, a MYC/MYCN-activated microRNA, regulates E-cadherin and cancer metastasis". In: *Nature Cell Biology* 12.3, pp. 247–256. doi: 10.1038/ncb2024.
- Ma, X. et al. (2017). "Myc suppresses tumor invasion and cell migration by inhibiting JNK signaling". In: *Oncogene* 36.22, pp. 3159–3167. doi: 10.1038/onc.2016.463.
- Macek, Pavel et al. (June 2018). "Myc phosphorylation in its basic helix–loop–helix region destabilizes transient α -helical structures, disrupting Max and DNA binding". In: *Journal of Biological Chemistry* 293.24, pp. 9301–9310.
- Marampon, Francesco, Carmela Ciccarelli, and Bianca M. Zani (2006). "Down-regulation of c-Myc following MEK/ERK inhibition halts the expression of malignant phenotype in rhabdomyosarcoma and in non muscle-derived human tumors". In: *Molecular Cancer* 5.1, p. 31. doi: 10.1186/1476-4598-5-31.
- Marinkovic, Dragan et al. (2004). "Reversible lymphomagenesis in conditionally c-MYC expressing mice". In: *International Journal of Cancer* 110.3, pp. 336–342. doi: 10.1002/ijc.20099. eprint: <https://onlinelibrary.wiley.com/doi/pdf/10.1002/ijc.20099>.
- McMahon, Steven B. (July 2014). "MYC and the Control of Apoptosis". In: *Cold Spring Harbor Perspectives in Medicine* 4.7.
- McShane, Erik et al. (2016). "Kinetic Analysis of Protein Stability Reveals Age-Dependent Degradation". In: *Cell* 167.3, 803–815.e21. ISSN: 0092-8674. doi: <https://doi.org/10.1016/j.cell.2016.09.015>.
- Min, Mingwei and Catherine Lindon (2012). "Substrate targeting by the ubiquitin-proteasome system in mitosis." eng. In: *Semin Cell Dev Biol* 23.5, pp. 482–491. ISSN: 1096-3634 (Electronic); 1084-9521 (Linking). doi: 10.1016/j.semcdb.2012.01.015.
- Mo, Hao and Marie Henriksson (2006). "Identification of small molecules that induce apoptosis in a Myc-dependent manner and inhibit Myc-driven transformation". In: *Proceedings of the National Academy of Sciences* 103.16, pp. 6344–6349. doi: 10.1073/pnas.0601418103. eprint: <https://www.pnas.org/content/103/16/6344.full.pdf>.
- Molina, Julian R. and Alex A. Adjei (2006). "The Ras/Raf/MAPK Pathway". In: *Journal of Thoracic Oncology* 1.1, pp. 7–9. doi: 10.1016/S1556-0864(15)31506-9.
- Montagne, Martin et al. (Feb. 2012). "The Max b-HLH-LZ Can Transduce into Cells and Inhibit c-Myc Transcriptional Activities". In: *PLOS ONE* 7.2, pp. 1–9. doi: 10.1371/journal.pone.0032172.
- Murphy, Daniel J. et al. (2008). "Distinct Thresholds Govern Myc's Biological Output In Vivo". In: *Cancer Cell* 14.6, pp. 447–457. ISSN: 1535-6108. doi: <https://doi.org/10.1016/j.ccr.2008.10.018>.
- Nair, Satish K. and Stephen K. Burley (2003). "X-Ray Structures of Myc-Max and Mad-Max Recognizing DNA: Molecular Bases of Regulation by Proto-Oncogenic Transcription Factors". In: *Cell* 112.2, pp. 193–205. ISSN: 0092-8674. doi: [https://doi.org/10.1016/S0092-8674\(02\)01284-9](https://doi.org/10.1016/S0092-8674(02)01284-9).
- Nandi, Dipankar et al. (2006). "The ubiquitin-proteasome system." eng. In: *J Biosci* 31.1, pp. 137–155. ISSN: 0250-5991 (Print); 0250-5991 (Linking). doi: 10.1007/BF02705243.
- Oft, Martin, Rosemary J. Akhurst, and Allan Balmain (2002). "Metastasis is driven by sequential elevation of H-ras and Smad2 levels". In: *Nature Cell Biology* 4.7, pp. 487–494. doi: 10.1038/ncb807.
- Oh, Jang-Hyun, Shun-Jia Chen, and Alexander Varshavsky (Nov. 2017). "A reference-based protein degradation assay without global translation inhibitors". In: *Journal of Biological Chemistry*.
- Olenych, Scott G. et al. (2007). "The Fluorescent Protein Color Palette". In: *Current Protocols in Cell Biology* 36.1, pp. 21.5.1–21.5.34. doi: <https://doi.org/10.1002/0471143030.cb2105s36>. eprint: <https://currentprotocols.onlinelibrary.wiley.com/doi/pdf/10.1002/0471143030.cb2105s36>.
- O'Neill, John S, Elizabeth S Maywood, and Michael H Hastings (2013). "Cellular mechanisms of circadian pacemaking: beyond transcriptional loops." eng. In: *Handb Exp Pharmacol* 217, pp. 67–103. ISSN: 0171-2004 (Print); 0171-2004 (Linking). doi: 10.1007/978-3-642-25950-0{_}4.
- O'Neill, John S. and Akhilesh B. Reddy (2011). "Circadian clocks in human red blood cells". In: *Nature* 469.7331, pp. 498–503. doi: 10.1038/nature09702.
- Ottis, Philipp and Craig M. Crews (Apr. 2017). "Proteolysis-Targeting Chimeras: Induced Protein Degradation as a Therapeutic Strategy". In: *ACS Chemical Biology* 12.4, pp. 892–898. doi: 10.1021/acscchembio.6b01068.
- Otto, Tobias et al. (2009). "Stabilization of N-Myc Is a Critical Function of Aurora A in Human Neuroblastoma". In: *Cancer Cell* 15.1, pp. 67–78. ISSN: 1535-6108. doi: <https://doi.org/10.1016/j.ccr.2008.12.005>.

References

- Partanen, Johanna I., Anni I. Nieminen, and Juha Klefstrom (2009). "3D view to tumor suppression: lkb1, polarity and the arrest of oncogenic c-myc". In: *Cell Cycle* 8.5. PMID: 19221484, pp. 716–724. doi: 10.4161/cc.8.5.7786. eprint: <https://doi.org/10.4161/cc.8.5.7786>.
- Partanen, Johanna I. et al. (2007). "Suppression of oncogenic properties of c-Myc by LKB1-controlled epithelial organization". In: *Proceedings of the National Academy of Sciences* 104.37, pp. 14694–14699. issn: 0027-8424. doi: 10.1073/pnas.0704677104. eprint: <https://www.pnas.org/content/104/37/14694.full.pdf>.
- Patel, Jagruti H et al. (2004). "The c-MYC oncoprotein is a substrate of the acetyltransferases hGCN5/PCAF and TIP60." eng. In: *Mol Cell Biol* 24.24, pp. 10826–10834. issn: 0270-7306 (Print); 1098-5549 (Electronic); 0270-7306 (Linking). doi: 10.1128/MCB.24.24.10826-10834.2004.
- Pelengaris, Stella et al. (1999). "Reversible Activation of c-Myc in Skin: Induction of a Complex Neoplastic Phenotype by a Single Oncogenic Lesion". In: *Molecular Cell* 3.5, pp. 565–577. issn: 1097-2765. doi: [https://doi.org/10.1016/S1097-2765\(00\)80350-0](https://doi.org/10.1016/S1097-2765(00)80350-0).
- Peter, Stefanie et al. (2014). "Tumor cell-specific inhibition of MYC function using small molecule inhibitors of the HUWE1 ubiquitin ligase." eng. In: *EMBO Mol Med* 6.12, pp. 1525–1541. issn: 1757-4684 (Electronic); 1757-4676 (Print); 1757-4676 (Linking). doi: 10.15252/emmm.201403927.
- Pietenpol, Jennifer A. et al. (1990). "TGF- β 1 inhibition of c-myc transcription and growth in keratinocytes is abrogated by viral transforming proteins with pRB binding domains". In: *Cell* 61.5, pp. 777–785. issn: 0092-8674. doi: [https://doi.org/10.1016/0092-8674\(90\)90188-K](https://doi.org/10.1016/0092-8674(90)90188-K).
- Popov, Nikita et al. (2007). "The ubiquitin-specific protease USP28 is required for MYC stability." eng. In: *Nat Cell Biol* 9.7, pp. 765–774. issn: 1465-7392 (Print); 1465-7392 (Linking). doi: 10.1038/ncb1601.
- Popov, Nikita et al. (2010). "Ubiquitylation of the amino terminus of Myc by SCF β -TrCP antagonizes SCFFbw7-mediated turnover". In: *Nature Cell Biology* 12.10, pp. 973–981. doi: 10.1038/ncb2104.
- Putker, Marrit et al. (2021). "CRYPTOCHROMES confer robustness, not rhythmicity, to circadian time-keeping". In: *The EMBO Journal* 40.7, e106745. doi: <https://doi.org/10.15252/emboj.2020106745>. eprint: <https://www.embopress.org/doi/pdf/10.15252/emboj.2020106745>.
- Raina, Kanak et al. (2016). "PROTAC-induced BET protein degradation as a therapy for castration-resistant prostate cancer". In: *Proceedings of the National Academy of Sciences* 113.26, pp. 7124–7129. issn: 0027-8424. doi: 10.1073/pnas.1521738113. eprint: <https://www.pnas.org/content/113/26/7124.full.pdf>.
- Rakhra, Kavya et al. (2010). "CD4+ T Cells Contribute to the Remodeling of the Microenvironment Required for Sustained Tumor Regression upon Oncogene Inactivation". In: *Cancer Cell* 18.5, pp. 485–498. issn: 1535-6108. doi: <https://doi.org/10.1016/j.ccr.2010.10.002>.
- Rapp, Ulf R. et al. (June 2009). "Myc Is a Metastasis Gene for Non-Small-Cell Lung Cancer". In: *PLOS ONE* 4.6, pp. 1–16. doi: 10.1371/journal.pone.0006029.
- Repouskou, Anastasia and Anastasia Prombona (2016). "c-MYC targets the central oscillator gene Per1 and is regulated by the circadian clock at the post-transcriptional level". In: *Biochimica et Biophysica Acta (BBA) - Gene Regulatory Mechanisms* 1859.4, pp. 541–552. issn: 1874-9399. doi: <https://doi.org/10.1016/j.bbagr.2016.02.001>.
- Richards, Mark W. et al. (2016). "Structural basis of N-Myc binding by Aurora-A and its destabilization by kinase inhibitors". In: *Proceedings of the National Academy of Sciences* 113.48, pp. 13726–13731. issn: 0027-8424. doi: 10.1073/pnas.1610626113. eprint: <https://www.pnas.org/content/113/48/13726.full.pdf>.
- Roberts, Karen et al. (2016). "Implementation and Challenges of Direct Acoustic Dosing into Cell-Based Assays". In: *Journal of Laboratory Automation* 21.1. PMID: 26169025, pp. 76–89. doi: 10.1177/2211068215595212. eprint: <https://doi.org/10.1177/2211068215595212>.
- Sakamuro, Daitoku et al. (1996). "BIN1 is a novel MYC-interacting protein with features of a tumour suppressor". In: *Nature Genetics* 14.1, pp. 69–77. doi: 10.1038/ng0996-69.
- Salghetti, Simone E. et al. (2000). "Functional overlap of sequences that activate transcription and signal ubiquitin-mediated proteolysis". In: *Proceedings of the National Academy of Sciences* 97.7, pp. 3118–3123. issn: 0027-8424. doi: 10.1073/pnas.97.7.3118. eprint: <https://www.pnas.org/content/97/7/3118.full.pdf>.
- Savino, Mauro et al. (July 2011). "The Action Mechanism of the Myc Inhibitor Termed Omomyc May Give Clues on How to Target Myc for Cancer Therapy". In: *PLOS ONE* 6.7, pp. 1–16. doi: 10.1371/journal.pone.0022284.
- Schaub, Franz X. et al. (2018). "Pan-cancer Alterations of the MYC Oncogene and Its Proximal Network across the Cancer Genome Atlas". In: *Cell Systems* 6.3, 282–300.e2. issn: 2405-4712. doi: <https://doi.org/10.1016/j.cels.2018.03.003>.
- Schwinn, Marie K. et al. (2018). "CRISPR-Mediated Tagging of Endogenous Proteins with a Luminescent Peptide". In: *ACS Chemical Biology* 13.2. PMID: 28892606, pp. 467–474. doi: 10.1021/acscchembio.7b00549. eprint: <https://doi.org/10.1021/acscchembio.7b00549>.
- Sears, Rosalie et al. (1999). "Ras Enhances Myc Protein Stability". In: *Molecular Cell* 3.2, pp. 169–179. issn: 1097-2765. doi: [https://doi.org/10.1016/S1097-2765\(00\)80308-1](https://doi.org/10.1016/S1097-2765(00)80308-1).

References

- Sears, Rosalie et al. (Oct. 2000). "Multiple Ras-dependent phosphorylation pathways regulate Myc protein stability". In: *Genes & Development* 14.19, pp. 2501–2514.
- Serrano-Gomez, Silvia Juliana, Mazvita Maziveyi, and Suresh K Alahari (2016). "Regulation of epithelial-mesenchymal transition through epigenetic and post-translational modifications." eng. In: *Mol Cancer* 15, p. 18. issn: 1476-4598 (Electronic); 1476-4598 (Linking). doi: 10.1186/s12943-016-0502-x.
- Shaaf, Hanan et al. (2016). "Modified gold nanoparticles for intracellular delivery of anti-liver cancer siRNA." eng. In: *Int J Pharm* 504.1-2, pp. 125–133. issn: 1873-3476 (Electronic); 0378-5173 (Linking). doi: 10.1016/j.ijpharm.2016.03.051.
- Shachaf, Catherine M. et al. (2004). "MYC inactivation uncovers pluripotent differentiation and tumour dormancy in hepatocellular cancer". In: *Nature* 431.7012, pp. 1112–1117. doi: 10.1038/nature03043.
- Shchors, Ksenya et al. (Sept. 2006). "The Myc-dependent angiogenic switch in tumors is mediated by interleukin 1 β ". In: *Genes & Development* 20.18, pp. 2527–2538.
- Sheiness, D, L Fanshier, and J M Bishop (Nov. 1978). "Identification of nucleotide sequences which may encode the oncogenic capacity of avian retrovirus MC29." In: *Journal of Virology* 28.2, p. 600.
- Shostak, Anton et al. (2016). "MYC/MIZ1-dependent gene repression inversely coordinates the circadian clock with cell cycle and proliferation". In: *Nature Communications* 7.1, p. 11807. doi: 10.1038/ncomms11807.
- Shostak, Anton et al. (2017). "Correspondence: Reply to 'Oncogenic MYC persistently upregulates the molecular clock component REV-ERB α '". In: *Nature Communications* 8.1, p. 14918. doi: 10.1038/ncomms14918.
- Simon, Einav and Daniel Kornitzer (2014). "Pulse-chase analysis to measure protein degradation." eng. In: *Methods Enzymol* 536, pp. 65–75. issn: 1557-7988 (Electronic); 0076-6879 (Linking). doi: 10.1016/B978-0-12-420070-8.00006-4.
- Smith, A P et al. (2009). "A positive role for Myc in TGF β -induced Snail transcription and epithelial-to-mesenchymal transition". In: *Oncogene* 28.3, pp. 422–430. doi: 10.1038/onc.2008.395.
- Sodir, Nicole M. et al. (May 2011). "Endogenous Myc maintains the tumor microenvironment". In: *Genes & Development* 25.9, pp. 907–916.
- Soucek, L et al. (1998). "Design and properties of a Myc derivative that efficiently homodimerizes." eng. In: *Oncogene* 17.19, pp. 2463–2472. issn: 0950-9232 (Print); 0950-9232 (Linking). doi: 10.1038/sj.onc.1202199.
- Soucek, Laura and Gerard I Evan (2010). "The ups and downs of Myc biology". In: *Current Opinion in Genetics Development* 20.1. Genetic and cellular mechanisms of oncogenesis, pp. 91–95. issn: 0959-437X. doi: <https://doi.org/10.1016/j.gde.2009.11.001>.
- Soucek, Laura et al. (2008). "Modelling Myc inhibition as a cancer therapy". In: *Nature* 455.7213, pp. 679–683. doi: 10.1038/nature07260.
- Stine, Zachary E. et al. (2015). "MYC, Metabolism, and Cancer". In: *Cancer Discovery* 5.10, pp. 1024–1039. issn: 2159-8274. doi: 10.1158/2159-8290.CD-15-0507. eprint: <https://cancerdiscovery.aacrjournals.org/content/5/10/1024.full.pdf>.
- Sun, Xiao-Xin, Rosalie C Sears, and Mu-Shui Dai (2015). "Deubiquitinating c-Myc: USP36 steps up in the nucleolus." eng. In: *Cell Cycle* 14.24, pp. 3786–3793. issn: 1551-4005 (Electronic); 1538-4101 (Print); 1551-4005 (Linking). doi: 10.1080/15384101.2015.1093713.
- Sun, Xiao-Xin et al. (2015). "The nucleolar ubiquitin-specific protease USP36 deubiquitinates and stabilizes c-Myc." eng. In: *Proc Natl Acad Sci U S A* 112.12, pp. 3734–3739. issn: 1091-6490 (Electronic); 0027-8424 (Print); 0027-8424 (Linking). doi: 10.1073/pnas.1411713112.
- Swatek, Kirby N and David Komander (2016). "Ubiquitin modifications". In: *Cell Research* 26.4, pp. 399–422. doi: 10.1038/cr.2016.39.
- Takahashi, Joseph S. (2017). "Transcriptional architecture of the mammalian circadian clock". In: *Nature Reviews Genetics* 18.3, pp. 164–179. doi: 10.1038/nrg.2016.150.
- Takahashi, Kazutoshi and Shinya Yamanaka (2006). "Induction of Pluripotent Stem Cells from Mouse Embryonic and Adult Fibroblast Cultures by Defined Factors". In: *Cell* 126.4, pp. 663–676. issn: 0092-8674. doi: <https://doi.org/10.1016/j.cell.2006.07.024>.
- Takahashi, Kazutoshi et al. (2007). "Induction of Pluripotent Stem Cells from Adult Human Fibroblasts by Defined Factors". In: *Cell* 131.5, pp. 861–872. doi: 10.1016/j.cell.2007.11.019.
- Thomas, Lance R. et al. (2015). "Interaction with WDR5 Promotes Target Gene Recognition and Tumorigenesis by MYC". In: *Molecular Cell* 58.3, pp. 440–452. issn: 1097-2765. doi: <https://doi.org/10.1016/j.molcel.2015.02.028>.
- Thul, Peter J. et al. (2017). "A subcellular map of the human proteome". In: *Science* 356.6340, eaal3321. doi: 10.1126/science.aal3321. eprint: <https://www.science.org/doi/pdf/10.1126/science.aal3321>.
- Tomita, Takuya and Andreas Matouschek (2019). "Substrate selection by the proteasome through initiation regions." eng. In: *Protein Sci* 28.7, pp. 1222–1232. issn: 1469-896X (Electronic); 0961-8368 (Print); 0961-8368 (Linking). doi: 10.1002/pro.3642.

References

- Toure, Momar and Craig M. Crews (2016). "Small-Molecule PROTACS: New Approaches to Protein Degradation". In: *Angewandte Chemie International Edition* 55.6, pp. 1966–1973. doi: 10.1002/anie.201507978. eprint: <https://onlinelibrary.wiley.com/doi/pdf/10.1002/anie.201507978>.
- Treisman, Richard (1992). "The serum response element". In: *Trends in Biochemical Sciences* 17.10, pp. 423–426. issn: 0968-0004. doi: [https://doi.org/10.1016/0968-0004\(92\)90013-Y](https://doi.org/10.1016/0968-0004(92)90013-Y).
- Umehura, Yasuhiro et al. (2014). "Transcriptional program of Kpna2/Importin α 2 regulates cellular differentiation-coupled circadian clock development in mammalian cells". In: *Proceedings of the National Academy of Sciences* 111.47, E5039–E5048. doi: 10.1073/pnas.1419272111. eprint: <https://www.pnas.org/doi/pdf/10.1073/pnas.1419272111>.
- Untergasser, Andreas et al. (June 2012). "Primer3—new capabilities and interfaces". In: *Nucleic Acids Research* 40.15, e115–e115. issn: 0305-1048. doi: 10.1093/nar/gks596. eprint: <https://academic.oup.com/nar/article-pdf/40/15/e115/25343564/gks596.pdf>.
- Van Roey, Kim et al. (July 2014). "Short Linear Motifs: Ubiquitous and Functionally Diverse Protein Interaction Modules Directing Cell Regulation". In: *Chemical Reviews* 114.13, pp. 6733–6778. doi: 10.1021/cr400585q.
- Vaseva, Angelina V. et al. (2018). "KRAS Suppression-Induced Degradation of MYC Is Antagonized by a MEK5-ERK5 Compensatory Mechanism". In: *Cancer Cell* 34.5, 807–822.e7. issn: 1535-6108. doi: <https://doi.org/10.1016/j.ccell.2018.10.001>.
- Verbist, Katherine C. et al. (2016). "Metabolic maintenance of cell asymmetry following division in activated T lymphocytes". In: *Nature* 532.7599, pp. 389–393. doi: 10.1038/nature17442.
- Verdine, Gregory L and Loren D Walensky (2007). "The challenge of drugging undruggable targets in cancer: lessons learned from targeting BCL-2 family members." eng. In: *Clin Cancer Res* 13.24, pp. 7264–7270. issn: 1078-0432 (Print); 1078-0432 (Linking). doi: 10.1158/1078-0432.CCR-07-2184.
- von der Lehr, Natalie, Sara Johansson, and Lars-Gunnar Larsson (2003). "Implication of the Ubiquitin/Proteasome System in Myc-Regulated Transcription". In: *Cell Cycle* 2.5, pp. 402–406. doi: 10.4161/cc.2.5.484. eprint: <https://doi.org/10.4161/cc.2.5.484>.
- von der Lehr, Natalie et al. (2003). "The F-box protein Skp2 participates in c-Myc proteosomal degradation and acts as a cofactor for c-Myc-regulated transcription." eng. In: *Mol Cell* 11.5, pp. 1189–1200. issn: 1097-2765 (Print); 1097-2765 (Linking). doi: 10.1016/s1097-2765(03)00193-x.
- Vousden, Karen H (2002). "Switching from life to death: The Miz-ing link between Myc and p53". In: *Cancer Cell* 2.5, pp. 351–352. issn: 1535-6108. doi: [https://doi.org/10.1016/S1535-6108\(02\)00186-1](https://doi.org/10.1016/S1535-6108(02)00186-1).
- Walz, Susanne et al. (July 2014). "Activation and repression by oncogenic MYC shape tumour-specific gene expression profiles". In: *Nature* 511.7510, pp. 483–487. doi: 10.1038/nature13473.
- Wang, Richard et al. (2021). "Selective targeting of non-centrosomal AURKA functions through use of a targeted protein degradation tool." eng. In: *Commun Biol* 4.1, p. 640. issn: 2399-3642 (Electronic); 2399-3642 (Linking). doi: 10.1038/s42003-021-02158-2.
- Wang, Xiaoyan et al. (2011). "Phosphorylation Regulates c-Myc's Oncogenic Activity in the Mammary Gland". In: *Cancer Research* 71.3, pp. 925–936. issn: 0008-5472. doi: 10.1158/0008-5472.CAN-10-1032. eprint: <https://cancerres.aacrjournals.org/content/71/3/925.full.pdf>.
- Wang, Yan et al. (2004). "Synthetic lethal targeting of MYC by activation of the DR5 death receptor pathway." eng. In: *Cancer Cell* 5.5, pp. 501–512. issn: 1535-6108 (Print); 1535-6108 (Linking). doi: 10.1016/s1535-6108(04)00113-8.
- Wang, Yiwei et al. (2018). "Small molecule inhibitors reveal allosteric regulation of USP14 via steric blockade". In: *Cell Research* 28.12, pp. 1186–1194. doi: 10.1038/s41422-018-0091-x.
- Wei, Yong et al. (2019). "Multiple direct interactions of TBP with the MYC oncoprotein". In: *Nature Structural & Molecular Biology* 26.11, pp. 1035–1043. doi: 10.1038/s41594-019-0321-z.
- Welcker, Markus et al. (2004). "The Fbw7 tumor suppressor regulates glycogen synthase kinase 3 phosphorylation-dependent c-Myc protein degradation." eng. In: *Proc Natl Acad Sci U S A* 101.24, pp. 9085–9090. issn: 0027-8424 (Print); 1091-6490 (Electronic); 0027-8424 (Linking). doi: 10.1073/pnas.0402770101.
- Welcker, Markus et al. (2022). "Two diphosphorylated degrons control c-Myc degradation by the Fbw7 tumor suppressor". In: *Science Advances* 8.4, eab17872. doi: 10.1126/sciadv.ab17872.
- Whitfield, Jonathan R., Marie-Eve Beaulieu, and Laura Soucek (2017). "Strategies to Inhibit Myc and Their Clinical Applicability". In: *Frontiers in Cell and Developmental Biology* 5, p. 10. issn: 2296-634X. doi: 10.3389/fcell.2017.00010.
- Wiegner, Armin et al. (2015). "Targeting Translation Initiation Bypasses Signaling Crosstalk Mechanisms That Maintain High MYC Levels in Colorectal Cancer." eng. In: *Cancer Discov* 5.7, pp. 768–781. issn: 2159-8290 (Electronic); 2159-8274 (Print); 2159-8274 (Linking). doi: 10.1158/2159-8290.CD-14-1040.
- Wiese, Katrin E. et al. (Dec. 2013). "The Role of MIZ-1 in MYC-Dependent Tumorigenesis". In: *Cold Spring Harbor Perspectives in Medicine* 3.12.
- Wilson, Anne et al. (Nov. 2004). "c-Myc controls the balance between hematopoietic stem cell self-renewal and differentiation". In: *Genes & Development* 18.22, pp. 2747–2763.

References

- Wolf, Elmar et al. (2015). "Taming of the beast: shaping Myc-dependent amplification". In: *Trends in Cell Biology* 25.4, pp. 241–248. issn: 0962-8924. doi: <https://doi.org/10.1016/j.tcb.2014.10.006>.
- Wolfer, Anita et al. (2010). "MYC regulation of a "poor-prognosis" metastatic cancer cell state". In: *Proceedings of the National Academy of Sciences* 107.8, pp. 3698–3703. issn: 0027-8424. doi: 10.1073/pnas.0914203107. eprint: <https://www.pnas.org/content/107/8/3698.full.pdf>.
- Wong, David Cs and John S O'Neill (2018). "Non-transcriptional processes in circadian rhythm generation." eng. In: *Curr Opin Physiol* 5, pp. 117–132. issn: 2468-8673 (Electronic); 2468-8673 (Linking). doi: 10.1016/j.cophys.2018.10.003.
- World Health Organisation - Cancer (2022).
- Wrigley, Jonathan D et al. (2017). "Identification and Characterization of Dual Inhibitors of the USP25/28 Deubiquitinating Enzyme Subfamily." eng. In: *ACS Chem Biol* 12.12, pp. 3113–3125. issn: 1554-8937 (Electronic); 1554-8929 (Linking). doi: 10.1021/acscchembio.7b00334.
- Yada, Masayoshi et al. (2004). "Phosphorylation-dependent degradation of c-Myc is mediated by the F-box protein Fbw7." eng. In: *EMBO J* 23.10, pp. 2116–2125. issn: 0261-4189 (Print); 1460-2075 (Electronic); 0261-4189 (Linking). doi: 10.1038/sj.emboj.7600217.
- Yeh, Elizabeth et al. (2004). "A signalling pathway controlling c-Myc degradation that impacts oncogenic transformation of human cells". In: *Nature Cell Biology* 6.4, pp. 308–318. doi: 10.1038/ncb1110.
- Yewdell, Jonathan W et al. (2011). "Out with the old, in with the new? Comparing methods for measuring protein degradation". In: *Cell Biology International* 35.5, pp. 457–462. doi: <https://doi.org/10.1042/CBI20110055>. eprint: <https://onlinelibrary.wiley.com/doi/pdf/10.1042/CBI20110055>.
- Yi, Yong Weon et al. (2015). " β -TrCP1 degradation is a novel action mechanism of PI3K/mTOR inhibitors in triple-negative breast cancer cells." eng. In: *Exp Mol Med* 47.2, e143. issn: 2092-6413 (Electronic); 1226-3613 (Print); 1226-3613 (Linking). doi: 10.1038/emm.2014.127.
- Zhang, Hongtao et al. (2019). "Tandem Fluorescent Protein Timers for Noninvasive Relative Protein Lifetime Measurement in Plants". In: *Plant Physiology* 180.2, pp. 718–731. issn: 0032-0889. doi: 10.1104/pp.19.00051. eprint: <http://www.plantphysiol.org/content/180/2/718.full.pdf>.
- Zhang, Ji-Hu, Thomas D. Y. Chung, and Kevin R. Oldenburg (1999). "A Simple Statistical Parameter for Use in Evaluation and Validation of High Throughput Screening Assays". In: *Journal of Biomolecular Screening* 4.2, pp. 67–73. doi: 10.1177/108705719900400206.
- Zhang, Kangling, Francesco Faiola, and Ernest Martinez (2005). "Six lysine residues on c-Myc are direct substrates for acetylation by p300." eng. In: *Biochem Biophys Res Commun* 336.1, pp. 274–280. issn: 0006-291X (Print); 0006-291X (Linking). doi: 10.1016/j.bbrc.2005.08.075.
- Zhang, Lichao and Joshua E Elias (2017). "Relative Protein Quantification Using Tandem Mass Tag Mass Spectrometry." eng. In: *Methods Mol Biol* 1550, pp. 185–198. issn: 1940-6029 (Electronic); 1064-3745 (Linking). doi: 10.1007/978-1-4939-6747-6_{14}.
- Zhang, Yuan et al. (2013). "Combinational delivery of c-myc siRNA and nucleoside analogs in a single, synthetic nanocarrier for targeted cancer therapy." eng. In: *Biomaterials* 34.33, pp. 8459–8468. issn: 1878-5905 (Electronic); 0142-9612 (Print); 0142-9612 (Linking). doi: 10.1016/j.biomaterials.2013.07.050.